Swansea University E-Theses

Growth and functionalisation of zinc oxide nanowires for biosensing applications.

Evans, Jonathan Edward

How to cite:

Evans, Jonathan Edward (2014) *Growth and functionalisation of zinc oxide nanowires for biosensing applications..* thesis, Swansea University.
http://cronfa.swan.ac.uk/Record/cronfa43180

Use policy:

This item is brought to you by Swansea University. Any person downloading material is agreeing to abide by the terms of the repository licence: copies of full text items may be used or reproduced in any format or medium, without prior permission for personal research or study, educational or non-commercial purposes only. The copyright for any work remains with the original author unless otherwise specified. The full-text must not be sold in any format or medium without the formal permission of the copyright holder. Permission for multiple reproductions should be obtained from the original author.

Authors are personally responsible for adhering to copyright and publisher restrictions when uploading content to the repository.

Please link to the metadata record in the Swansea University repository, Cronfa (link given in the citation reference above.)

http://www.swansea.ac.uk/library/researchsupport/ris-support/

Growth and Functionalisation of Zinc Oxide Nanowires for Biosensing Applications

Jonathan Edward Evans

Submitted to Swansea University in fulfilment of the requirements for the degree of Doctor of Philosophy.

Swansea University
September 2014

ProQuest Number: 10821572

All rights reserved

INFORMATION TO ALL USERS
The quality of this reproduction is dependent upon the quality of the copy submitted.

In the unlikely event that the author did not send a complete manuscript
and there are missing pages, these will be noted. Also, if material had to be removed,
a note will indicate the deletion.

ProQuest 10821572

Published by ProQuest LLC (2018). Copyright of the Dissertation is held by the Author.

All rights reserved.
This work is protected against unauthorized copying under Title 17, United States Code
Microform Edition © ProQuest LLC.

ProQuest LLC.
789 East Eisenhower Parkway
P.O. Box 1346
Ann Arbor, MI 48106 – 1346

Abstract

Zinc oxide nanowires have attracted great interest due to their quasi-one dimensional morphology and favourable optical and electrical properties. Although much work has been done on the synthesis of a rich variety of ZnO nanostructures, integration of large numbers of these nanostructures into devices has remained problematic.

Biosensing represents one of the more active areas of nanotechnology, with major interest stemming from the key advantages offered over competing sensor technologies, such as low cost of mass production and reduced packaging dimensions, potentially allowing for the development of point-of-care medical devices.

In this work, high quality zinc oxide nanowires have been grown on industry standard silicon substrates with an emphasis on vertical device incorporation, allowing large numbers of nanowires to be integrated into devices that may be fabricated using mature semiconductor fabrication techniques. Optimum results were obtained by growth on sputter deposited conductive layers, which also offers an attractive method for contacting the base of the nanowire arrays.

These nanowires were subsequently functionalised using glutaraldehyde as a linking molecule between the ZnO surface and a model antibody and also by treating the antibody with EDC/NHS to create a zero-length cross-link between the antibody and nanowire surface. The functionalisation methods were investigated using XPS. Individual nanowires were transferred to allow lateral FET measurements to be conducted using a nanoprobe, where a large spread in resistivity was measured between the as-grown wires. This large wire-to-wire variation has been reported previously, and is thought to be related to changes in surface states between nanowires. However, the wire-to-wire variation was found to be highly dependant on surface functionalisation, with the variation increasing or decreasing depending on the attachment of biomolecules. This has large implications for ensemble ZnO nanowires devices.

Building on these electrical measurements, a novel design for a ensemble nanowire biosensor was proposed, consisting of microchannels capped by top and bottom contacts, through which an analyte may be flown, and hence detected. The feasibility of implementing this sensor design is further explored.

Contents

Abstract i

Table of Contents v

List of Figures vii

List of Tables xvii

Acknowledgements xix

Declaration xx

1 Introduction 1

1.1 Thesis outline 3

2 Literature Review 4

2.1 Zinc Oxide 4

2.1.1 Defect chemistry 6

2.1.2 Zinc oxide nanostructures 7

2.1.3 Synthesis of zinc oxide nanostructures 7

2.1.3.1 Hydrothermal growth 8

2.1.3.2 Vapour-phase growth 9

2.2 Nanowire Field Effect Transistors and Other Devices 13

2.3 Functionalisation and Biosensing 16

2.3.1 Surface Modification 17

2.3.1.1 Immobilisation of Anti-bodies 18

3 Experimental Techniques 20

3.1 Vapour Phase Growth of Zinc Oxide Nanowires 20

3.1.1 Nanowire Growth Optimisation 21

3.2 Device Fabrication 23

3.2.1 Substrate Preparation and Cleaning 23

3.2.2 Photolithography 24

3.2.2.1 Photoresists 24

3.2.2.2 Spin Coating 25

3.2.2.3 Mask Alignment and Exposure 25
3.2.2.4 Development 27
3.2.2.5 Etch-back and Lift-off Processes 27
3.2.3 Wet Etching 28
3.2.4 Dry Etching 29
3.2.4.1 Reactive Ion Etching 30
3.2.5 Deposition Techniques 31
3.2.5.1 Sputtering 32
3.2.5.2 Chemical Vapour Deposition 33
3.2.6 Plasma Cleaning/Ashing 33
3.3 Characterisation 35
3.3.1 Electron Microscopy 35
3.3.2 Atomic Force Microscopy 37
3.3.3 Energy-dispersive X-ray Spectroscopy 40
3.3.4 X-ray Photoelectron Spectroscopy 42
3.3.4.1 Photoemission 42
3.3.4.2 The Three Step Model 44
3.3.4.3 Interpreting XPS Spectra 46
3.3.4.4 XPS at Swansea University 48
3.3.4.5 XPS at the Science City Photoemission Facility 48
3.3.4.6 Analysis of XPS Spectra 49
3.3.5 Auger Electron Spectroscopy 49
3.3.5.1 Analysis of Auger Spectra 52
3.3.6 Photoluminescence Spectroscopy 53
3.3.7 X-ray Diffraction 54
3.3.7.1 Determination of Size and Strain 56
3.3.7.2 Texture Analysis 57

4 Nanowire Growth 59
4.1 Introduction 59
4.2 Seed Layer Assisted Growth 60
4.2.1 Experimental 60
4.2.2 Summary 61
4.3 Roughness Assisted Growth 62
4.3.1 Experimental 62
4.3.2 Results 63
4.3.2.1 Electron microscopy and atomic force microscopy 65
4.3.2.2 X-ray diffraction 67
4.3.2.3 Transmission electron microscopy 69
4.3.2.4 X-ray photoelectron spectroscopy of etched Si 73
4.3.2.5 Photoluminescence spectroscopy 73
4.3.3 Selective Area Growth 75

4.3.4 Summary . . . 76
4.4 Growth on Conductive Thin Films . . . 77
4.4.1 Experimental . . . 77
4.4.2 Results . . . 78
4.4.2.1 Electron microscopy . . . 78
4.4.2.2 X-ray diffraction measurements . . . 80
4.4.2.3 Photoluminescence spectroscopy . . . 88
4.4.2.4 Summary . . . 91
4.5 Summary and Comparison of Vapour-Phase Growth Methods . . . 92

5 Surface Modification and Attachment of Biomolecules to Zinc Oxide Nanowires 93
5.1 Introduction . . . 93
5.1.1 The hCG antibody . . . 95
5.1.2 Glutaraldehyde cross-linking method . . . 95
5.1.3 EDC/NHS zero-length cross-linking method . . . 96
5.1.4 Bovine serum albumin . . . 97
5.2 Experimental . . . 98
5.2.1 Surface Modification . . . 98
5.2.2 Antibody immobilisation via glutaraldehyde - Pathway A . . . 98
5.2.3 Antibody immobilisation via EDC/NHS - Pathway B . . . 98
5.2.4 Blocking of non-specific binding . . . 98
5.2.5 Antigen binding . . . 99
5.2.6 Summary . . . 99
5.3 Electron microscopy . . . 100
5.3.1 Zinc oxide compatibility tests . . . 100
5.3.2 APTES . . . 102
5.3.3 Glutaraldehyde - Pathway A . . . 102
5.3.4 Anti-hCG, BSA and the hCG protein - Pathway A . . . 104
5.3.5 EDC/NHS treated anti-hCG - Pathway B . . . 105
5.4 X-ray Photoelectron Spectroscopy . . . 106
5.4.1 Quantification . . . 106
5.4.2 Peak fitting . . . 110
5.4.3 Valence band scans . . . 118
5.5 Photoluminescence Spectroscopy . . . 121
5.6 Electrical Measurements . . . 123
5.6.1 Back-gated measurements . . . 125
5.6.1.1 Analysis . . . 125
5.6.1.2 Comparison with XPS valence band scans . . . 130
5.6.1.3 Comparison with PL integrated intensity ratio . . . 137
5.6.2 Resistivity Measurements . . . 138
5.7 Chapter Summary . . . 143

6 **Device Fabrication** 145
6.1 Vertical Device Fabrication 145
6.2 Floating Metal Contacts 147
6.2.1 Encapsulation of nanowire arrays 148
6.2.2 Controlled ashing of resist films 149
6.2.3 Planarisation of nanowire array 150
6.2.4 Top contact deposition and patterning 152
6.2.5 Removal of encapsulation layer 152
6.3 Fabrication of a Vertical Nanowire Sensing Device 157
6.3.1 Overview of fabrication process 157
6.3.2 Etching of microchannels 158
6.3.3 Deposition of conductive layer and nanowire growth 162
6.3.4 Deposition of top contact 166
6.4 Chapter Summary 170

7 **Conclusions** 172
7.1 Future Work 174
7.2 Publications 175

Appendices 176

A **List of X-ray Diffraction Peaks** 177

B **Gated Measurements** 180
B.1 *Mathematica* Code and Transistor Characteristics 180
B.2 Propagation of Uncertainty 191

References 194

List of Figures

1.1 Diagram of vertical NW arrays grown in microtrenches. The arrays have been capped with a contact in order to seal the channel. This contact provides the means to apply a potential across the NW array between the top electrode and substrate, allowing the conductometric detection of biomolecules in the channel. The thermally grown SiO_2 layer prevents a short circuit path between the silicon substrate and metal top contact. 2

2.1 Schematic representation of the wurtzite structure with lattice constants a and c. The nearest neighbour distance is denoted b, u is the bond length and α and β are the bond angles. Reproduced from [1]. 5

2.2 The crystal structures of ZnO (a) rocksalt (b) zinc blende (c) wurtzite. The black spheres are oxygen and the grey spheres zinc. Reproduced from [1]. 5

2.3 Comparison of PL emission at (a) 4 K and at (b) RT for nanorods grown on polyethylene-napthalate substrates. Both show a narrow dominant near-band-edge emission (NBE) with a broader deep level emission (DLE) likely produced by a large amount of various donor species. Reproduced from [2]. 6

2.4 Examples of the conjectured location of intrinsic defect states in the wurtzite ZnO band-gap. 7

2.5 SEM images of ZnO nanostructures synthesised by thermal evaporation of solid powders. Reproduced from [3]. 8

2.6 Top-down and cross-sectional SEM images of hydrothermal ZnO NWs comparing morphology grown on (a), (d) Au, (b), (e) Ni and (c), (f) Si substrates. The samples shown in (a), (b) and (c) were all grown together in the same batch of solution, whereas (d), (e) and (f) were grown in separate beakers. Both Au and Si substrates show increased length when grown separately, whilst Ni does not; suggesting that it is the primary inhibitor of ZnO crystal growth. All scale bars are 1 µm. Reproduced from [4]. 9

2.7 Schematic diagram showing the surface-roughness-assisted VS growth mechanism. (a) Zn atoms move freely on a smooth surface and (b) Zn atoms are stuck in pits on a surface, which serve as nucleation sites. Reproduced from [5]. 11

2.8 Self-seeding VS growth mechanism of ZnO NWs on an Si substrate. (a) initial ZnO nucleation with little texturing. (b) epitaxial growth of NWs from seed particles. (c) further *c*-axis growth and additional seeding of *c*-axis aligned NWs. (d) formation of a polycrystalline base growth layer which inhibits poorly aligned NW growth. Reproduced from [6]. 11
2.9 (left) SEM images of ZnO nanowire alignment dependence on the seed layer thickness. The as-deposited Zn layer thicknesses are (a) 10 nm, (b) 20 nm, (c) 30 nm, (d) 50 nm, (e) 70 nm, and (f) 100 nm, respectively. The scale bar is 1 µm. (right) XRD spectra of ZnO seed layer oxidised from varying Zn layer thicknesses. The optimised result is observed from a 30 nm thick oxidised Zn layer. Reproduced from [7]. 12
2.10 Schematic layout of a wrap gate FET. The gate wraps around the base of the wire, and is isolated from the NW by a layer of SiN_x. Reproduced from [8]. 13
2.11 Outline of a silicon nanowire sensor fabrication process: (a) spin-coat monolayer of close-packed nanospheres; (b) reduce nanosphere diameter in oxygen plasma; (c) deposit catalyst material for Si etching and rinse away nanospheres; (d) catalytic, anisotropic etching of Si; (e) embed nanowire array in thick photoresist and etch back in oxygen plasma to reveal nanowire tips; (f) spin-coat second monolayer of close-packed nanospheres; (g) reduce nanosphere diameter in oxygen plasma; and (h) deposit top electrode material and dissolve away nanosphere and photoresist layers. Reproduced from [9]. 14
2.12 Fabrication process of air-bridged top metal contact on vertically aligned SiNWs; (a) formation of thin suspended layer of polystyrene (PS) on the uppermost part of vertical SiNWs, (b) partial removal of PS layer by oxygen plasma etching to expose the tips of SiNWs, and (d) sputter deposition of gold for electrical contact. SEM images of the corresponding sample structure are presented on the right side. Reproduced from [10]. 15
2.13 Schematic illustrations of polysilicon nanowire biosensor fabrication after (a) oxide pillar formation, (b) nanowire plasma etch, (c) metal contact formation, and (d) sensor window opening. The biasing configuration for the biosensor electrical measurements is also shown: (e) cross- sectional SEM image of a fabricated polysilicon nanowire; (f) cross-sectional SEM micrograph of polysilicon nanowires at the corner of a pillar; (g) optical image of a completed nanowire biosensor wafer; (h) high magnification optical image of a fabricated nanowire biosensor through a sensor window. Reproduced from [11]. 17
2.14 Sulfo-NHS plus EDC (carbodiimide) cross-linking reaction scheme. Adapted from [12]. 19

3.1 Schematic of vapour phase nanowire growth set-up. 20
3.2 Thermo Scientific tube furnace. Gas inlet is on the left with Pirani and piezo vacuum gauges mounted on the cross piece. The vacuum hose is connected on the right. 21

3.3 Quartz tube following growth (gas flow from left to right). An alumina source boat is also shown. Condensation of ZnO vapour is seen both upstream and downstream. 22

3.4 Calibration curve of furnace temperature gradient, as measured relative to the centre of the furnace. Measurements were conducted using a type K thermocouple in contact with the alumina furnace tube under ambient conditions. The blue, red and green curves are for furnace temperatures 1100 °C, 1050 °C and 1000 °C, respectively. 22

3.5 The basic steps involved in photolithography. 24

3.6 Spin curves for AZ6612 (**a**) and AZ nLOF 2070 (**b**). Adapted from [13] and [14], respectively. 26

3.7 SUSS MicroTec MA/BA8 Gen3 mask aligner 26

3.8 The result of incorrect developing. In (a), resist still remains on the substrate surface which could result in complete lift-off of a deposited layer or a faulty contact. In (b), over-development has led to undercut of the resist features. This is more common for negative photoresists and can be exploited to avoid resist sidewall coverage during the lift-off process. 28

3.9 The lift-off process performed on a thin film (grey) using a photoresist (pink) as a sacrifical material. 28

3.10 Isotropic and anisotropic (directional) etching. Undercut of the photoresist (pink) is shown in (a). 30

3.11 The Oxford Instruments Plasma Lab 80+ is shown in (a), with a schematic of the parallel plate reactor shown in (b). 31

3.12 Lesker PVD 75. The deposition chamber is located on the top left of the unit in (**a**). A close up of the deposition chamber with the three magnetron sources is shown in (**b**). 33

3.13 The K1050X plasma cleaner is shown in (**a**). The the chamber door is visible in the middle of the unit, with a schematic of the barrel reactor contained inside shown in (**b**). 34

3.14 Diagram of a hot cathode SEM column showing the photomultiplier for electron detection. The condenser lens, apertures and electrostatic and magnetic lenses all serve to collect, collimate and focus the electron beam. The scan coils defect the beam for raster scanning across the sample surface. Reproduced from [15]. 36

3.15 Hitachi S-4800 SEM with angled EDX detector visible on the left of the column. . . 36

3.16 1 µm × 1 µm AFM scan of a ZnO seed layer annealed at 650 °C. The z-range is 10 nm. 37

3.17 Schematic of AFM optics and components. In this set-up, the cantilever and optics are fixed in place and the sample is moved using piezoelectric scanners to form an image and modulate the tip-sample separation. 38

3.18 Diagram showing average (R_a) and RMS (R_q) roughness for a line profile. Levelling the line profile is equivalent to subtraction of the mean line. 38

3.19 JPK NanoWizard II AFM with optical microscope for laser and tip-sample alignment. 39

3.20 Interaction effects due to electron bombardment are shown on the left. A more detailed illustration of the interaction volume is shown on the right. Secondary electron generation and electron induced luminescence occurs close to the sample surface, whereas X-ray generation occurs in a much larger excitation volume. Backscattered electrons are scattered from a penetration distance intermediate between the two. 41

3.21 Relative efficiency of Auger and X-ray emission for K shell vacancies. A similar graph is also found for L shell transitions. 41

3.22 Oxford Instruments X-Max silicon drift detector. 42

3.23 Energy distribution curve for a ZnO nanowire sample, with Auger and core level peaks labelled. 43

3.24 The "‘universal curve"’. Electron inelastic mean free path up to 2000 eV for a range of materials. Adapted from [16]. 44

3.25 VG ESCALab XPS system. The analysis chamber is on the left, with the X-ray source visible and the hemispherical analyser located above the chamber. 48

3.26 Science City Photoemission Facility, University of Warwick. The far system is for angle resolved photoemission spectroscopy (ARPES). 49

3.27 An O1s peak fitted with a Shirley background (brown) and two Gaussian/Lorentzian components (pink and blue). 50

3.28 A diagram of the Auger process, with the primary electron shown in red. A vacancy is created in the 1s level. An electron from the 2s level then fills the 1s hole, with the transition energy coupled to a 2p electron which is emitted. The same process is shown on the right with an energy level diagram. This particular transition would be labelled $KL_1L_{2,3}$. 50

3.29 Omicron LT Nanoprobe equipped with an NanoSAM Auger electron analyser and a Zeiss GEMINI SEM column. Shown prior to bake-out. 51

3.30 AES of the O KLL transition. In **(a)**, the peak is shown without processing. The smoothed and differentiated data is shown in **(b)** 53

3.31 Constructive interference between lattice planes is describes by Bragg's law. Lattice sites and planes are shown in blue and black, respectively. The incident and scattered X-rays are shown in red. 55

3.32 Goniometer showing the axis of rotation. In the current position, the sample stage is at $\psi = \pm 90°$, with the ϕ angle (the rotation of the stage) being arbitrary, depending on how the sample is mounted. 55

3.33 Williamson-Hall plot showing how the strain (ε) and size (D) components are obtained from the peak position (θ) and FWHM (β). 57

4.1 SEM images of poor quality ZnO NW growth obtained during optimisation experiments.It is interesting to note that in (b), not base growth ZnO layer is observed, indicating island type nucleation. 63

4.2 **(a-e)** SEM images of samples A-E respectively **(f-j)** 10 µm × 10 µm AFM scans of samples A-E respectively. Z-range of AFM scans are shown in table 4.2. **(k-o)** Typical line scans from AFM scans f-j respectively. 64
4.3 Power spectral density plot comparing etched samples. 66
4.4 SEM images of resulting NW growth on sample B, which was dry etched using a SF_6/O_2 plasma. 67
4.5 **(a)** XRD 2θ scan of surface enhanced NW growth. **(b)** Williamson-Hall plot of the ZnO diffraction peaks. 68
4.6 XRD pole figure of the (0 0 2) reflection for surface enhanced NW growth. 69
4.7 **(a)** Cross sectional SEM image of cleaved substrate. **(b)**Wide bright-field TEM image of the Si/ZnO NW interface with the locations of figure 4.8a, 4.8b and 4.8c indicated. 70
4.8 HRTEM of the Si/ZnO interface. The angle θ is formed between the Si (0 0 1) substrate lattice planes and *c*-axis (0 0 2) ZnO planes. Amorphous regions are present at the Si/ZnO interface. The SAED pattern in (c) shows poor ZnO crystallinity close to the interface. 71
4.9 XPS survey scan showing removal of weakly bound RIE reaction products following annealing under vacuum at 400 °C. 74
4.10 Normalised PL spectrum averaged over 5 points on the sample. The dashed grey lines show the standard deviation. 74
4.11 Schematic diagram showing the lithography processing steps. (1) Spin coated AZ nLOF 2070 resist, (2) patterned with electron beam (3) developed unexposed area (4) plasma etching (5) removal of patterned resist (6) selectively growth of NWs. . . 75
4.12 **(a)** High magnification SEM image of NWs grown using patterning technique. **(b)** SEM showing an example of patterning with 'Swansea University, Prifysgol Abertawe' excluded from NW growth. 76
4.13 SEM images of ZnO NWs grown on 100 nm sputtered conductive layers viewed normal to the substrate. A noticeable difference in alignment, density and diameter of the NWs can be seen between samples. Molybdenum appears to result in wide dense growth in contrast to the arrays grown on ITO. Catalyst particles are conspicuously absent on the NW tips (confirmed using the BSE and EDX detectors). Note the lower magnification for the Ti sample. 79
4.14 Cross-sectional SEM images of ZnO NWs arrays. The 100 nm sputtered conductive layer and base growth ZnO is visible is some of the images. Evidence of diffusion of aluminium layer into the silicon substrate is visible. It is also apparent that the copper layer has become detached from the silicon substrate. Clear differences in the morphology and density of the NW arrays are visible between samples. 81
4.15 Plots showing relationship between **(a)** base layer growth thickness and NW density **(b)** NW diameter and array height. Error bars left out for clarity (see table 4.5). 82
4.16 XRD 2θ scans of NW growth on the metal layers. A table listing the peaks shown in each figure is found in appendix A. 83

4.17 XRD pole figures of the ZnO (0 0 2) reflection. The linear intensity colour scale is shown in the top right of each figure and allows for a direct comparison between samples. Gas flow direction was from $\phi = 90°$ to $\phi = 270°$ i.e. down the page. 85

4.18 ZnO (0 0 2) X-ray pole figure of ITO on Si_3N_4 showing no symmetric inheritance from the Si substrate. 86

4.19 **(a)** Rocking curves conducted along the furnace gas flow direction ($\phi = 270°$) for the ZnO (0 0 2) reflection. Positive values of χ represent the downstream direction and negative values the upstream direction. This leads to a slight asymmetry in the curves, with a higher degree of texturing observed in the upstream direction, as previously reported in section 4.3.2.2. **(b)** Plot of rocking curve FWHM against maximum peak intensity. The order of magnitude increase in peak intensity with a two-fold decrease in FWHM indicates that peak area, or total quantity of *c*-axis aligned ZnO, is roughly correlated with peak height. 87

4.20 PL spectra of NW arrays grown on metal thin-films, normalised to the NBE excitonic peak and averaged over 5 areas on the sample. The dashed lines show the standard deviation. Notice the different intensity scale for the Al and Mo samples. . 89

4.21 **(a)** Integrated intensity ratio and NBE peak intensity. Fractional integrated intensity ratios indicated that the ZnO is highly defective. This could be attributed to dopants from the sputtered conductive layers used to encourage ZnO nucleation and *c*-axis aligned growth. **(b)** Position of NBE peak, as compared with intrinsic (undoped) bulk ZnO. The effect of dopants from the sputtered conductive layers on the width of the band-gap is complex, due to the presence of mixed zinc-metal and metal oxide phases identified using XRD. 90

5.1 APTES hydrolysis followed by condensation reaction at hydroxylated ZnO surface. 94

5.2 Diagram of the hCG antibody. The heavy and light chains are shown in blue and green, respectively, and are shown linked by disulfide bonds (red). 95

5.3 Schematic of antibody attachment using GA. Adapted from [17]. 96

5.4 Chemical structure of EDC and NHS. Adapted from [12,18]. 96

5.5 Sulfo-NHS plus EDC (carbodiimide) cross-linking reaction scheme. Adapted from [12]. 97

5.6 The two biofunctionalisation processes. APTES is initially used for amine surface termination. The antibody is then either attached using a linking molecule (pathway A), or by activating groups and directly attaching the antibody to the amine terminating surface (pathway B). 99

5.7 SEM images of NW arrays following 24 hour immersion in different concentrations of PBS. Both (a) and (b) are images for the 0.01 M PBS solution, with (b) providing a magnified high contrast image of the rectangular area indicated in (a). Although large scale structures, such as the NWs, are still visible, light pitting of the ZnO surface is seen in these images, whereas the samples immersed in the 0.1 M (c) and 1 M (d) solutions exhibit complete dissociation. 101

5.8 Top down SEM images of NWs following treatment with **(a)** 40% and **(b)** 0.5% APTES in DI. 102
5.9 SEM image of the NWs following treatment with APTES and glutaraldehyde. Some etching of the ZnO surface is observed which can be attributed to the dissociation of ZnO in DI water. 103
5.10 SEM image of GA treated sample following attachment of antibody. 104
5.11 SEM images of GA treated samples following attachment of proteins. 104
5.12 SEM images of EDC/NHS antibody and BSA samples. No etching of the surface is observed, which can be contrasted with the GA samples shown above (figure 5.9). . 105
5.13 Antigen 105
5.14 Relative composition of each sample, as measured using XPS. **(a)** GA treated samples **(b)** EDC/NHS antibody treated samples. 107
5.15 APTES silinization of the ZnO surface resulting in different layer formations. Adapted from [19]. 109
5.16 Normalised XPS spectra of as grown ZnO NWs, NWs treated with APTES and NWs treated with APTES and glutaraldehyde. 112
5.17 Normalised XPS spectra of ZnO NWs progressively treated with glutaraldehyde, the hCG antibody, BSA and the hCG protein. 113
5.18 Normalised XPS spectra of ZnO NWs progressively treated with APTES, the hCG antibody activated using EDAC/NHS, BSA and the hCG protein. 114
5.19 XPS: Elemental composition of each sample by component. The fitted peaks are shown in figures 5.16, 5.17 and 5.18. Table 5.2 shows the approximate fitted peak positions with colour key and commonly attributed hybridisation states. 115
5.20 XPS spectra of the Fermi level energy and valence band maximum of the as-grown ZnO NWs. A valence band position greater than the ZnO band-gap indicates surface metallisation. 118
5.21 Band diagram of surface accumulation with conduction band minimum (E_C), valence band maximum (E_V), Fermi level energy (E_F), surface band bending (ϕ), surface barrier height (ϕ_B), and width of the surface band bending region (W). . . . 120
5.22 Schematic of surface metallisation along length of ZnO NW. Reproduced from [20]. 120
5.23 PL spectra, normalised to the NBE emission, for **(a)** GA antibody immobilised samples (pathway A) **(b)** EDAC antibody immobilised samples (pathway B). The arrows are a guide between progressive attachment steps. 121
5.24 Schematic cross-section of measurement set-up in the lateral FET configuration. The diameter of the NW, thickness of the dielectric layer are and length of the channel are labeled d_{NW}, h and L, respectively. 123
5.25 Nanoprobe SEM image showing two tungsten probes contacting a silanized NW treated with anti-hCG and BSA. A line profile across the wire is shown inset. 124
5.26 I_{ds}–V_g plot for APTES treated NW with V_{ds} = 0.1 V. The transconductance, g_m, is given by the gradient of the linear fit (blue). 127
5.27 Schematic cross-section of a nanowire with corresponding energy band diagram for n-type flatband condition, surface depletion, and surface accumulation. 130

5.28 The three Fermi level approximations for different degeneracy conditions. 131
5.29 Plot of the valence band position relative to the Fermi level as a function of the the carrier concentration (n). 132
5.30 Graph of expected carrier concentration calculated using equation 5.13 based on XPS and PL data (table 5.8). 133
5.31 Fit of Joyce-Dixon approximation (equation 5.15) to data. Note that ΔV_C has subsequently been subtracted from the data and fit. 134
5.32 Graph showing the local increase in carrier concentration with reduced accumulation width. 136
5.33 NW resistivity against integrated intensity ratio between the NBE peak and defect band for **(a)** Pathway A (GA antibody immobilised samples) **(b)** Pathway B (EDAC antibody immobilised samples). 137
5.34 Resistivity-NW diameter plot comprising of 262 IV measurements performed on 46 individual NWs. 138
5.35 Average resistivity of each sample set overlayed with the spread in resistivity. The points show the resistivity values from individual NW measurements. 140
5.36 Average resistance per NW assuming a channel length of 6 μm. 141
5.37 Average resistance per NW assuming a channel length of 6 μm and a NW diameter of 144 nm. 142

6.1 Cross sectional schematic of the floating contact fabrication process. The colours correspond to the following: green - Si substrate, purple - negative photoresist encapsulation layer, blue - metal top contact, orange - positive photoresist etch mask. 147
6.2 SEM images of photoresist forming dome shaped deposits around NW bundles following high speed spin coating. A lower spin speed is necessary to improve film uniformity. 148
6.3 Cross-sectional SEM images of NWs encapsulated in a thick AZ nLOF 2070 photoresist layer. (a) demonstrates a high degree of uniformity across the top of the encapsulation layer. No voids or defects are seen in the film, as shown in (b). 149
6.4 SEM images of cracks formed in photoresist encapsulation layer due to unequal thermal expansion of the substrate/polymer film following O_2 plasma ashing at an RF power of 100 W. These voids would cause problems for top-contact deposition and uniform NW contacting and could, in extreme cases, result in shorts between bottom and top contacts. 149
6.5 Calibration curve for controlled encapsulation layer (AZ nLOF 2070 photoresist) removal as a function of ashing duration conducted in an O_2 plasma at an RF power of 50 W. A slight non-linearity is seen in the ashing rate likely due to sample heating. 150

6.6 Tilted SEM images showing NW array in encapsulation layer following controlled resist ashing. (a) 35° tilted SEM image of cleaved edge of sample following ashing – NWs are seen on the exposed edge of the sample due to the isotropic ashing. The exposed NW tips can be seen in the background. (b) 60° tilted SEM image of exposed NW tips showing variation in NW length and tip protrusion. A subsequent planarisation step is required in order to level NW tips. 151

6.7 SEM images of ultrasonic planarisation of NW arrays. This step will likely been required to increase the density of contacted NWs and more importantly to ensure contact uniformity between individual NWs in the array. 151

6.8 SEM images of Ti top contacts coated with photoresist mask following metal deposition and etching. No NW protrusions are seen from the encapsulation layer as the ZnO has been etched away by the BOE solution. 153

6.9 SEM images of floating Al contacts following removal of the encapsulation layer using plasma ashing. In (a), a lighter boarder is observed around the edge of the contact. This could suggest possible retention of resist in the centre of the contact, although it could also be indicative of etching of the NWs at the extremity of the capped array due to percolation of the etchant solution through the uncapped NW growth. This is supported by the lower density of NW growth at the contact edges observed in (b). (c) demonstrates the uniform contacting to the NW tips resulting from planarisation of the NW arrays. Deposits and residues identified as phosphorous rich using EDX were present on the contacts following removal of the encapsulation layer. These can be observed in (a) and also on the uncontacted etched NWs shown in (d) and indicate the need for an alternative etchant solution. 154

6.10 SEM images of floating Ti contacts following removal of encapsulation layer using P1316 resist stripper. In contrast to the images shown in 6.9, a planarisation step has not been conducted in order to level the NWs following encapsulation and NW tip exposure. This is apparent in (d) and (e), where unequal protrusion of the NWs through the top contact is clearly visible. This will likely create issues with variable contact resistance and quality between individual NWs. (f) shows tapered NW tips damaged due to exposure to the BOE solution used to pattern the Ti top contact. 155

6.11 Model device consisting of a top (grey) and bottom (blue) electrode which form a microfluidic channel containing the NW sensing elements. The bottom contact must be electrically isolated from the Si substrate to prevent a short circuit path between contacts. This may be achieved by pre-sputtering a thin insulating SiO_2 layer prior to contact deposition. 158

6.12 Flow diagram of fabrication process for vertical NW sensing devices. The processes are split into three distinct sections - (1) Formation of microchannels using dry etching. (2) Bottom contact deposition and NW growth. (3) Top contact deposition. 159

6.13 Diagram of first photolithography and etching process to create a trench support structure for the device. The Si substrate is shown in green and the photoresist mask in pink. This process is a typical example of semiconductor etching employing a photoresist mask. 160

6.14 SEM images of etched silicon with the photoresist etch mask still in place. In (a), the undercut of the etch mask is clearly visible. (b) shows surface pitting of the etch mask due to the high etching bias used in RIE. (c) shows a cross-sectional SEM image following photoresist stripping. An undercut of approximately 4 μm is visible. 161

6.15 Diagram showing (a) simultaneous lift-off patterning of bottom contact and insulating SiO_2 layer (blue) and (b) subsequent selective area NW growth. 163

6.16 SEM images of ZnO NWs growth on sputtered SiO_2/Ti layers. (a) demonstrates that despite the presence of an amorphous oxide layer, the NWs still appear highly aligned. This suggests that the oxide layer is still thin enough (50 nm) to allow for symmetric inheritance from the Si substrate (see sections 4.4.2.2). (b) shows a cross-sectional SEM image of the ZnO/Ti/SiO_2/Si interface. The polycrystalline nature of the Ti layer and initial ZnO nucleation is clearly visible. 163

6.17 SEM images of NW growth on device structure showing the difference between unwanted growth on (a) deposited Si_3N_4 and (b) etched Si substrate. In (b), the bottom contact is electrically isolated from the substrate by a thin pre-sputtered SiO_2 layer deposited prior to bottom contact deposition and patterned simultaneously using the lift-off process. This method results in less non-specific ZnO nucleation over the substrate surface. 164

6.18 Top-down SEM image of unwanted ZnO deposits and NW growth on Si and Si sidewalls of etched support structure. This unwanted nucleation is problematic for subsequent processing steps such as encapsulation layer spin coating and top contact deposition. 165

6.19 Top down SEM image of etched structure following bottom contact lift-off. The red circles indicate areas of metal retention due to non-uniform resist coverage on step edges following spin coating. Although these deposits do not interfere directly with the fabrication steps, they result in unwanted nucleation during NW growth that will interfere with subsequent encapsulation layer and top contact deposition (see figure 6.18). 165

6.20 Diagram of top contact deposition and patterning. The Si substrate is shown in green, the bottom contact in light blue, the encapsulated NW array in dark blue, the positive photoresist etch mask in pink and the metal top contact in grey. (b) an initial lift-off layer of positive resist is use to mask the sample from contact deposition. (c) the metal contact is sputtered over the sample. (d) a photoresist etch mask is patterned on top of the metal contact. (e) the metal is etched using wet chemistry and the photoresist and encapsulation layers are removed. 166

6.21 SEM images of NW array and device structure following etching of the ZnO in dilute HCl. The base growth layer allows for a large undercut into the array leading to. (a) shows the bare Si surface and encapsulation layer following etch back. The NW array is just visible inside the encapsulation layer. (b) shows the same device following removal of the encapsulation layer to reveal the damaged NW array. . . . 167
6.22 SEM images of devices following removal of encapsulation layer.The top and bottom contact dimensions vary between images. A slight misalignment is apparent in the top contact etch mask, and consequently the top contact, in all four images. In (a), etching of the array has led to collapse of the top contact and shorting between the bottom and top contacts, which has been exacerbated by the top contact misalignment. Due to the small array size in (b), severe etching has removed most of the nucleated ZnO. In (c), complete removal of the NW array is observed. The top contacts appear fragile in all four images, with some bowing of the contact visible around the array in (d). 168

B.1 Transfer characteristics at $V_{ds} = (0.1\,\text{V})$ 189
B.2 Threshold voltage as a function of drain-source voltage. 190
B.3 I_{ds}–V_g plot for APTES treated NW with $V_{ds} = 0.1\,\text{V}$. The blue bands show the 1σ (68%) confidence interval. 191

List of Tables

3.1 Cleaning procedure for silicon samples. 23
3.2 Wet etchants and etch rates for various materials. 29
3.3 Types of dry etching. 30

4.1 Summary of samples and their processing conditions. 64
4.2 Roughness and NW morphology measurements. 66
4.3 Estimated surface coverage, with peak contribution and atomic % calculated using equation 3.24. 73
4.4 Deposition parameters for conductive thin films. 77
4.5 Table of mean NW densities and dimensions for NWs grown on conductive thin films. The height refers to the average length of the array above the base growth layer (BGL), not the average length of individual NWs. The uncertainty is the standard deviation. 80
4.6 Lattice parameters for wurtzite ZnO NWs grown on different thin films. The c-axis parameter was obtained using the (0 0 2) peak and the a-axis parameter was subsequently obtained using the (1 0 1) peak, except for those marked with an asterix, in which case the (1 0 3) was used. 84

5.1 Binding energy scan range and relative sensitivity factors (RSFs) for core levels. . . 106
5.2 Fitted components for C, O, Zn and N peaks. The legend applies to the components shown in figures 5.16, 5.17 and 5.18 and also to the quantification in figure 5.19. . . 110
5.3 Location of valence band maximum relative to the Fermi level. 119
5.4 Position of the NBE peak as measured using PL. The band-gap, E_g, is obtained following addition of the exciton binding energy (60 meV). 122
5.5 Maximum transconductance and threshold values. 128
5.6 Carrier concentrations for pathway A. 129
5.7 Carrier concentrations for pathway B. 129
5.8 Position of the Fermi level relative to the conduction band ($\xi = E_F - E_C$). 133
5.9 Number of NWs and I-V measumrents for each sample. 139

A.1 XRD peaks for NWs grown on 100 nm sputtered thin films. Peak position indicates the 2θ value. 177

Acknowledgements

I would like to express my gratitude to my supervisor Prof. Steve Wilks, for giving me the opportunity to carry out this research and for his continued guidance and support. In addition, I would like to thank Thierry Maffeis and Owen Guy for their help and expertise.

Thanks to all my friends and colleagues at the Centre for NanoHealth, Department of Engineering and Department of Physics at Swansea University for all their help and for making my time in Swansea much more interesting.

Many thanks to Alex Lord and Michael Ward for conducting the FIB and TEM experiments at Leeds EPSRC Nanoscience and Nanotechnology Facility (LENNF). Also to Marc Walker for providing assistance with the XPS measurements at the Science City Photoemission Facility, University of Warwick. I am also very grateful to Nathan Smith for taking the time to help with the crucial nanoprobe measurements. Thanks to Greg Burwell of Burwell Scientific Ltd for photographing the device fabrication tools. A special thanks to Sofia Teixeira for all her help with the functionalisation chemistry.

Finally, my gratitude to my mother and father for all they have done.

Declaration

This work has not previously been accepted in substance for any degree and is not being concurrently submitted in candidature for any degree.

Signed .... (Candidate)

Date 15/5/15 ....

Statement 1

This thesis is the result of my own investigation except where otherwise stated. Other sources have been acknowledged by footnotes giving explicit references. A bibliography is appended.

Signed .... (Candidate)

Date 15/5/15 ....

Statement 2

I hereby give consent for my thesis, if accepted, to be available for photocopying and for interlibrary loan, and for the title and summary to be made available to outside organizations.

Signed .... (Candidate)

Date 15/5/15 ....

Chapter 1

Introduction

One dimensional (1-D) nanostructures such as nanowires (NWs) and nanotubes have received substantial research interest due to their unique properties and their potential to be implemented into nanoscale sensors, electronics and optoelectronics. In the field of nanosensors, NWs have shown particular promise due to the combination of efficient electron transport and high surface sensitivity – crucially, 1-D nanostructures are the lowest dimensional structures that can be used for the efficient transport of electrons.

Due to the dominant effects of surface modulation on electrical conduction, much effort has been made to integrate NWs into conductometric sensing devices. Biosensing is of particular interest in this area, due to the promise of offering rapid local "point-of-care" detection of low concentrations of biomolecules, which could prove revolutionary in the monitoring, diagnoses and treatment of diseases.

Zinc oxide offers a number of material properties that make it highly suited to nanoscale biosensing applications. Firstly, it is known as a bio-safe and biocompatible material that, owing to its crystal structure, can be grown in a rich variety of high surface area nanostructures. It is also piezoelectric, has natural hydroxyl surface termination and has electrical transport properties that are known to be highly dependant on the adsorption of surface chemical species.

It has previously been reported that large variations exist in the intrinsic electrical properties of similarly grown NWs, likely due to changes at the surface. In particular, conductometric measurements on individual NWs have shown a high degree of instability and variation between NWs. This proves extremely problematic for sensing applications, particularly those involving low concentrations and minor changes in conductance.

This thesis aims to address some of the issues associated with the integration of ZnO NWs into conductometric biosensing devices by outlining a strategy for integrating large numbers of NWs in parallel, in order to mitigate variation and stability issues commonly encountered when dealing with individual NWs. In order to do this, three challenges relating to synthesis, sensing and device integration must be solved:

1. A method must be developed to allow the synthesis of large numbers of NWs, preferably in a state where they can be directly integrated into a device without the need for transfer and manipulation.
2. A process to allow selective conductometric detection of biomolecules through surface attachment must be developed. The effect of this process on the conductive properties of the NWs needs to be thoroughly investigated in order to establish if integration of a large number of NWs into a sensing device is a feasible method for detecting biomolecules.

3. Integration of a large number of NWs into a conductometric sensing device, preferably using mainstream top-down semiconductor fabrication techniques.

The approach undertaken was to grow highly dense vertical arrays of NWs on standard silicon substrates. In order to apply a potential, the tips of the NW arrays need to be contacted. This was to be achieved using a top-contact metallisation process in order to create a "floating" contact, which could also serve to cap the NW array, allowing the possibility of creating a microfluidic channel. Selective sensing was to be achieved using antibody immobilisation. Immunosensors use the specific nature of the antibody-antigen interaction in order to allow selective detection of proteins in complex real world analytes, such as blood and urine. The antibody may be immobilised on the ZnO surface through use of a cross-linking method between metal oxide surface hydroxyls and functional groups present on the antibody. An example of a microfluid sensing device integrating vertically grown NW arrays is shown in figure 1.1.

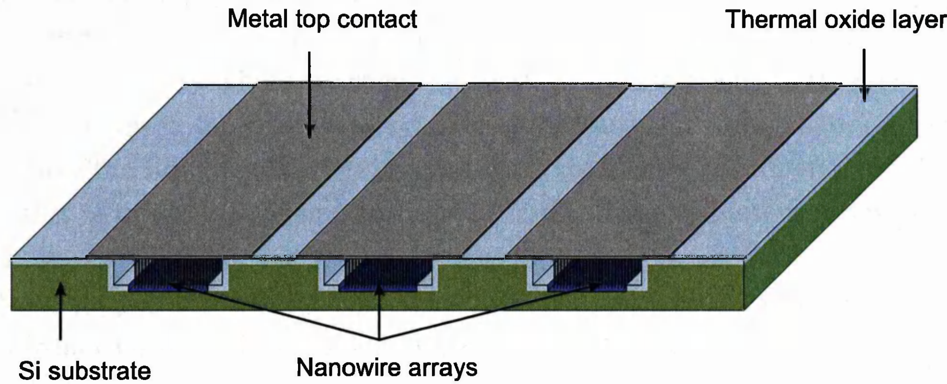

Figure 1.1: Diagram of vertical NW arrays grown in microtrenches. The arrays have been capped with a contact in order to seal the channel. This contact provides the means to apply a potential across the NW array between the top electrode and substrate, allowing the conductometric detection of biomolecules in the channel. The thermally grown SiO_2 layer prevents a short circuit path between the silicon substrate and metal top contact.

1.1 Thesis outline

- Chapter 2 provides a review of the literature on ZnO nanostructures, applications and devices with a focus on nanowire biosensing and novel devices integrating nanowire arrays.
- Experimental methods and characterisation techniques are outline in chapter 3. The vapour phase nanowire growth method is detailed, along with fabrication processes and materials and surface analysis techniques. These techniques are well adapted to characterising the structural, chemical and electrical properties of nanowires.
- In chapter 4, three methods of preparing ZnO nanowire arrays on silicon are investigated with a focus on vertical device integration. The methods consist of seed layer assisted growth, roughness or surface enhanced growth, and growth on sputtered conductive layers.
- Chapter 5 presents surface modification and functionalisation of nanowire arrays for biosensing. A model antibody is immobilised on the ZnO surface using two different approaches. Electron and optical spectroscopy techniques are used to analyse the binding and changes to the surface chemistry. These are combined with nanoscale electrical measurements of individual nanowires in the typical lateral field effect transistor configuration to gain information on how the functionalisation process alters the electrical properties of the nanowires. The results of this and their implications for ZnO nanowire biosensor design are then discussed.
- Chapter 6 proposes a novel design for a ZnO nanowire biosensor, based on information gained from chapter 5. The fabrication process is detailed along with methods for contacting vertical arrays.
- Finally, the conclusions drawn from this work and potential areas for future study are identified in chapter 7.

Chapter 2

Literature Review

This chapter presents a review of zinc oxide (ZnO) nanostructures and the field of nanowire (NW) biosensing with a particular emphasis on recent innovation in device structures. Firstly, some of the material and physical properties of ZnO are outlined. Synthesis of ZnO nanostructures is then discussed, along with methods for growing vapour-phase NWs on differing substrates. Finally, the role of ZnO NWs and related structures in conductometric sensing is discussed.

2.1 Zinc Oxide

Zinc oxide (ZnO) is a wide band-gap semiconductor that has received substantial research interest in applications involving bulk single crystals (SCs) and, more recently, in devices that incorporate the rich variety of ZnO nanostructures that may be synthesised using relatively simple bottom up techniques. Extensive studies have been conducted integrating ZnO nanomaterials into such diverse application as light-emitting diodes [21], photodiodes [22], nanolasers [23], varistors [24], gas sensors [25, 26], dye-sensitized solar cells [27] and more recently, third generation perovskite solar cells [28]. Due to its wide band-gap of around 3.37 eV and large exciton binding energy of 60 meV, ZnO will be important for optical devices operating within the blue and ultraviolet regime, offering the potential to overtake currently used materials such as GaN, due to its low cost of production, simple bulk crystal-growth process and higher exciton binding energy [1]. A renewed interest in ZnO properties and devices has owed much to the development of fabrication techniques allowing the growth of high quality SCs and epitaxial layers.

In ambient conditions, ZnO crystallises in the wurtzite (B4 type) structure. This hexagonal lattice belongs to the space group $P6_3mc$, consisting of two interconnecting sublattices of Zn^{2+} and O^{2-}, with each cation surrounded by a tetrahedra of anions, and vice-versa (figure 2.1).

The lattice parameters of the hexagonal unit cell are $a = 3.2495\,Å$ and $c = 5.2069\,Å$ and the density is $5.605\,g\,cm^{-3}$. This arrangement results in polar symmetry along the hexagonal c-axis, giving rise to a number of the properties of ZnO, including its piezoelectricity and spontaneous polarization. Although the Zn–O bond posses a strong ionic character, the mentioned tetrahedral coordination is usual indicative of sp^3 covalent bonding. Consequently, ZnO lies on the borderline between being classed as a covalent and ionic compound [29]. The four most common terminating faces in bulk wurtzite ZnO SCs are the polar Zn terminating $(0\,0\,0\,1)$ and O terminating $(0\,0\,0\,\bar{1})$ faces (c-axis orientated), and the the non-polar $(1\,1\,\bar{2}\,0)$ (a-axis) and $(1\,0\,\bar{1}\,0)$ faces [29]. These correspond to the fast growth directions in ZnO, and interplay between these fast growth directions is responsible for the rich variety of nanostructures that can be grown using ZnO. Zinc oxide can also crystallise in the less stable cubic zinc blende (B3) and rocksalt phases (B1) (figure

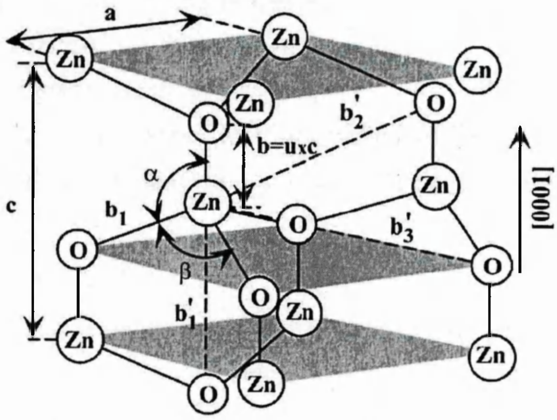

Figure 2.1: Schematic representation of the wurtzite structure with lattice constants a and c. The nearest neighbour distance is denoted b, u is the bond length and α and β are the bond angles. Reproduced from [1].

2.2), although the rocksalt structure is only present at relatively high pressures. The zinc blende phase can be stabilised by growth of ZnO films on cubic substrates, such as silicon [30].

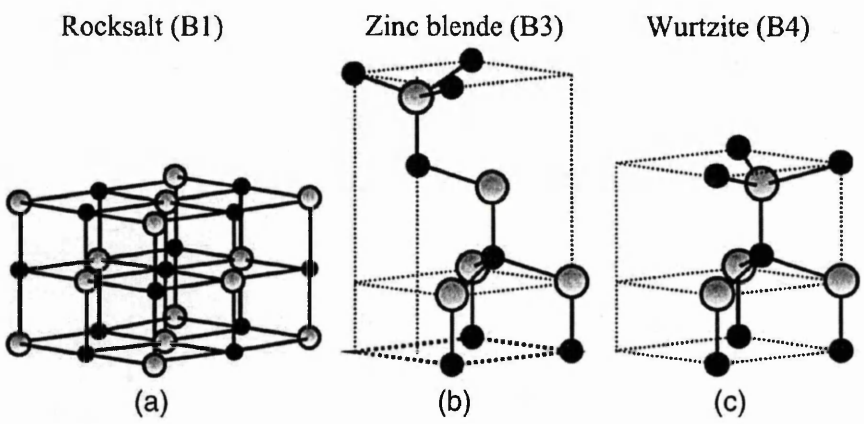

Figure 2.2: The crystal structures of ZnO (a) rocksalt (b) zinc blende (c) wurtzite. The black spheres are oxygen and the grey spheres zinc. Reproduced from [1].

Zinc oxide has shown promise for use in other applications such as fabrication of transparent thin-film transistors and as an alternative transparent conductive oxide (TCO) to indium tin oxide (ITO) and fluorine doped tin oxide (FTO). Careful control of the doping level allows the electrical properties to be changed from insulator through n-type semiconductor to metal while retaining the optical transparency that makes it useful for TCO applications such as flat-panel displays and solar cells. Carrier concentrations as high as $2 \times 10^{21}\,\mathrm{cm}^{-3}$ can be achieved by using heavy substitutional doping of ZnO [1]. However, one important hurdle needs to be overcome before ZnO achieves widespread adoption in optoelectronic devices: the growth of good quality p-type crystals. Despite all the progress that has been made and reports of p-type conductivity in ZnO films using various growth methods and group V dopants (N, P, As, Sb) [1,31], reliable and reproducible high quality p-type conductivity has not yet been achieved, and reports of p-type doping remain controversial. This remains one of the most pivotal topics in current ZnO research. Despite the large number of publications and long history of research on ZnO, some of

the basic material properties also still remain unclear. For example, the nature of the intrinsic n-type conductivity in undoped ZnO is still under some debate. Commonly, the donor states are attributed to intrinsic point defects such as oxygen vacancies [32, 33], zinc interstitials [34, 35] or related defect complexes [36–38]. Other authors have ascribed the conductivity to extrinsic effects, such as non-controllable hydrogen incorporation during growth [35, 37].

2.1.1 Defect chemistry

There are five kinds of intrinsic defects in ZnO films: zinc vacancy V_{Zn}, oxygen vacancy V_O, interstitial zinc Zn_i, interstitial oxygen O_i and antisite oxygen O_{Zn} [39]. Oxygen vacancies occur in three different charge states: neutral (V_O), singly ionised ($V_O^{\bullet}$) and doubly ionised ($V_O^{\bullet\bullet}$), with only singly ionised oxygen vacancies ($V_O^{\bullet}$) acting as so-called luminescent centres [40]. As previously mentioned, ZnO is a direct band-gap semiconductor with a large exciton binding energy that will have important applications in UV optical devices. However, in addition to the UV excitonic emission, ZnO is well known to exhibit a secondary broad visible emission which is commonly ascribed to combinations of native defects and defect clusters [38]. These native defects have been extensively studied in both bulk and nanostructured ZnO using photoluminescence spectroscopy (PL) [40–43], paramagnetic resonance [36,44,45], and positron annihilation spectroscopy [37,41]. A typical PL spectra for ZnO NWs is shown in figure 2.3.

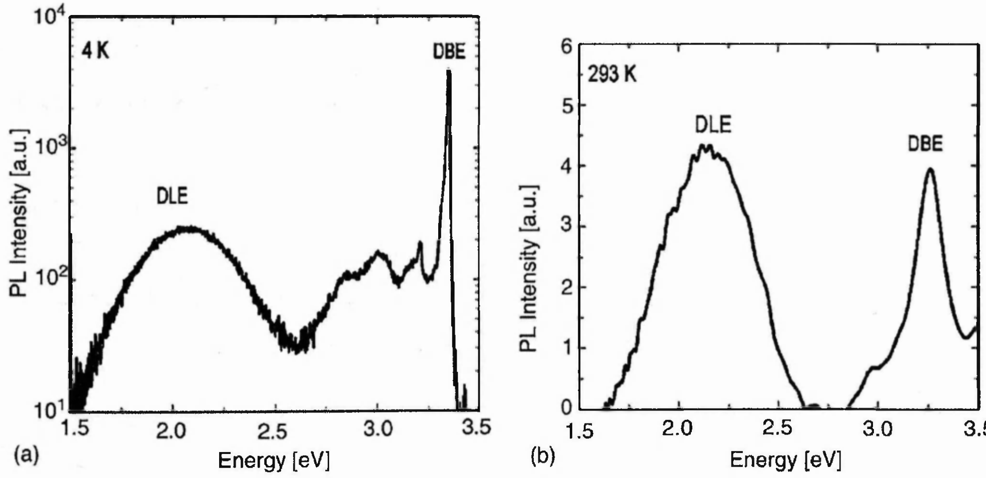

Figure 2.3: Comparison of PL emission at (a) 4 K and at (b) RT for nanorods grown on polyethylene-napthalate substrates. Both show a narrow dominant near-band-edge emission (NBE) with a broader deep level emission (DLE) likely produced by a large amount of various donor species. Reproduced from [2].

The blue-green luminescence remains particularly controversial and is commonly attributed to oxygen vacancies ($V_O^{\bullet}$), although many other interpretations exist [46]. Association with singly ionised oxygen vacancies which act as shallow donors is common [32, 46]. Previous work on the annealing of ZnO in a reducing atmosphere has highlighted increases in this area of the defect band [47, 48]. The orange-red emission centered at around 1.95 eV has been attributed to O_i by Studenikin et al. who also reported an increase in the green emission at the expense of the orange emission following annealing in a reducing atmosphere, which is consistent with a

change from oxygen rich to oxygen deficient ZnO [49]. Oxygen octahedral interstitials (O_i that sit within an octahedral co-ordination of lattice sites) have been calculated to be mobile even at low temperatures. Huang et al. claim the low migration energy barrier and formation energy suggest that O_i^{2-} are responsible for diffusion of oxygen in n-type ZnO [50]. An alternative explanation for the orange luminescence is transition from the conduction band to a monovalent oxygen vacancy ($V_O^{\bullet}$) [51]. Several examples of the location of defect states offered by various authors is shown in figure 2.4.

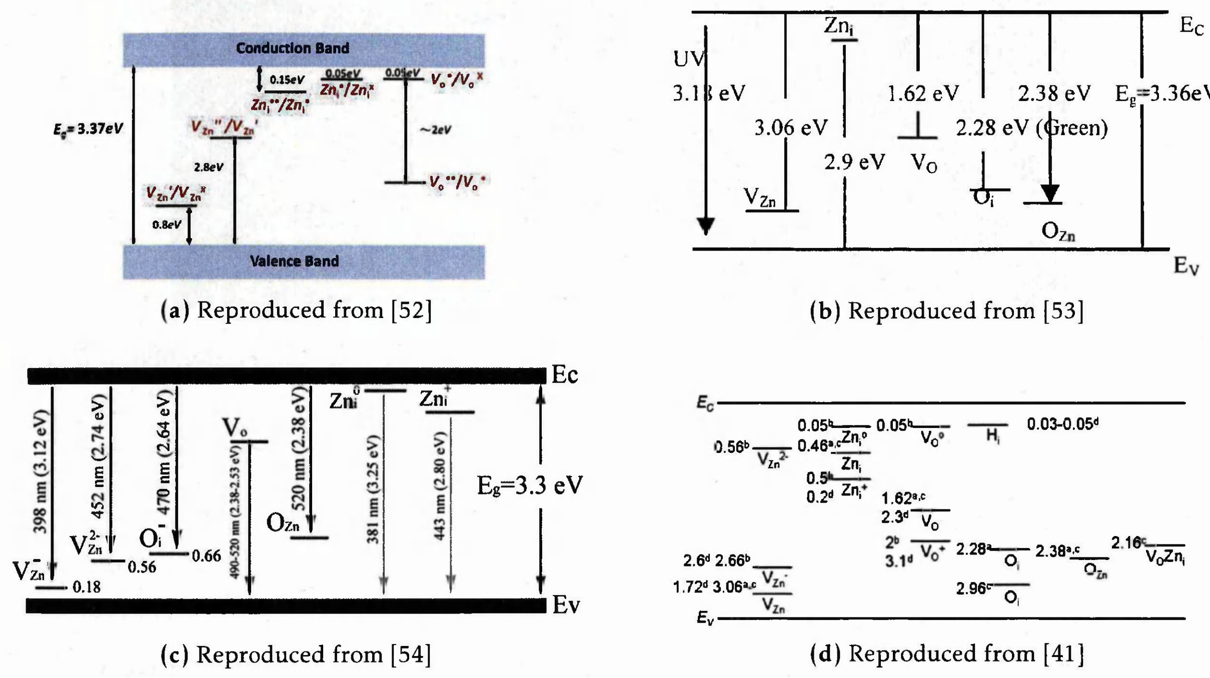

(a) Reproduced from [52]

(b) Reproduced from [53]

(c) Reproduced from [54]

(d) Reproduced from [41]

Figure 2.4: Examples of the conjectured location of intrinsic defect states in the wurtzite ZnO band-gap.

2.1.2 Zinc oxide nanostructures

Nanostructured ZnO has long been studied in the form of polycrystalline layers, deposited using physical vapour or liquid phase deposition techniques [55, 56]. Zinc oxide also crystallises in a variety of complex nanostructures including nanobelts, nanocombs, nanospirals and nanowires, some of which are shown in figure 2.5 [3]. It is also possible, through thermal decomposition of zinc precursors e.g. zinc acetate, to form polycrystalline nanostructures in morphologies unrelated to their crystal structure. This technique has been used to hydrothermally grow layered basic zinc acetate (LBZA) nanosheets which are subsequently pyrolytically decomposed into nanocrystalline ZnO [57].

2.1.3 Synthesis of zinc oxide nanostructures

The most common methods of bottom-up ZnO nanostructure synthesis are high temperature vapour phase and hydrothermal methods, although the term hydrothermal tends to be used as a misnomer, as the term is generally used to describe all elevated temperature liquid phase growth, even at atmospheric pressure. Recently, metal-organic chemical vapour deposition (MOCVD)

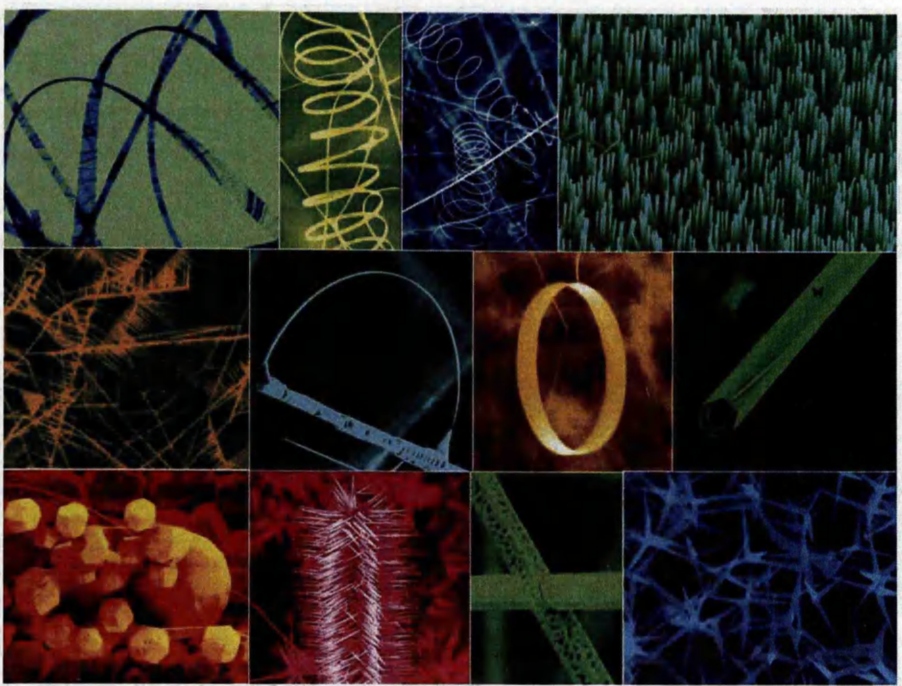

Figure 2.5: SEM images of ZnO nanostructures synthesised by thermal evaporation of solid powders. Reproduced from [3].

[58, 59] has seen an increase in popularity, owing to the high quality nanostructures and easy fabrication of NW quantum structures and heterojunction that can be achieved using this technique [60, 61].

The growth of quasi-one dimensional nanostructures is of particular interest for applications involving dense growth of vertical arrays, such as field emitters, sensors and optoelectronic devices. These applications have been extensively investigated using carbon nanotubes [62–65], however quasi-one dimensional ZnO nanostructures, or nanowires (NWs), offer significant advantages over carbon in terms of synthesis and applications. An immediate advantage is the polar nature of ZnO – the Zn-terminating face is known to be the more chemically active polar face, resulting in faster nucleation along the +*c*-axis, which leads to the growth of dissimilar high aspect ratio structures [66, 67]. In addition, ZnO along with the other metal oxides naturally surfaces terminates in hydroxyl groups, allowing the use of a broad class of well developed functionalisation and blocking chemistries [68]. Finally, and perhaps most importantly, the rich defect chemistry inherent in ZnO and other compound metal oxide semiconductors offers a powerful alternative to substitutional doping for control of optical and electronic properties.

2.1.3.1 Hydrothermal growth

Hydrothermal synthesis provides a commonly used solution phase method for generating ZnO nanostructures, particularly nanorods and nanowires [69–72]. Generally, solution phase reactions occur at temperatures under 200 °C, allowing compatibility with a large range of substrates. Several chemicals are usually added to the growth solution to change the morphology of the resulting nanostructures. Mixtures of zinc nitrate and hexamine are common, which act to fur-

ther inhibit the slow growth directions of ZnO, resulting in high aspect ratio nanostructures or nanowires. Amine compounds can be employed to direct growth along the *c*-axis direction, whereas citrates inhibit *c*-axis growth, resulting in increased relative growth of the *m*-planes and formation of thick rods or plates [73]. The growth velocities during hydrothermal synthesis typically follow the pattern $V(0001) > V(10\bar{1}1) > V(10\bar{1}0)$ [74]. Generally, hydrothermal wires are of a lower aspect ratio than those obtained using vapour phase techniques, and often exhibit a tapered appearance, as shown in figure 2.6.

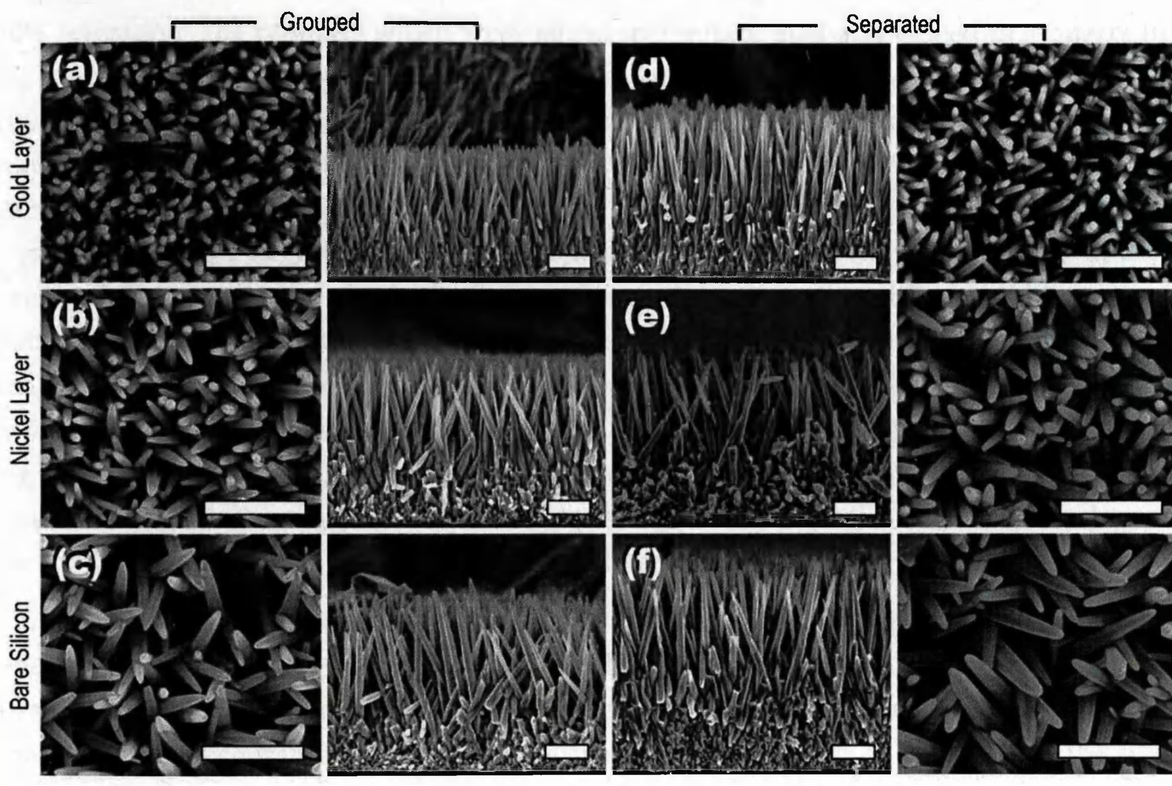

Figure 2.6: Top-down and cross-sectional SEM images of hydrothermal ZnO NWs comparing morphology grown on (a), (d) Au, (b), (e) Ni and (c), (f) Si substrates. The samples shown in (a), (b) and (c) were all grown together in the same batch of solution, whereas (d), (e) and (f) were grown in separate beakers. Both Au and Si substrates show increased length when grown separately, whilst Ni does not; suggesting that it is the primary inhibitor of ZnO crystal growth. All scale bars are 1 µm. Reproduced from [4].

2.1.3.2 Vapour-phase growth

Vapour phase synthesis is probably the most extensively explored approach to the formation of quasi 1-D nanostructures such as whiskers, nanorods and nanowires. Although the exact mechanisms for 1-D growth are complex and not fully understood, this route has been used by many researchers to fabricate ZnO NWs for intrinsic study or for integration into optical and electronic devices. In a typical process, vapour species are first generated by evaporation, chemical reduction and gaseous reaction. These species are subsequently transported using an inert carrier gas and condense onto the surface of a substrate positioned in a cooler portion of the growth apparatus. Commonly, a mixture of ZnO and graphite powder is used to generate the vapour, which undergoes a carbothermal reduction process at relatively low temperature, as shown in equation 5.1 (k_1 and k_2 signify the respective reaction rates). The Zn vapour is re-

oxidised by introduction of a small amount of oxygen into the reaction chamber, either whilst undergoing transport or following condensation on the substrate.

$$ZnO(s) + CO(g) \xrightarrow{k_1} Zn(s) + CO_2(g) \tag{2.1}$$

$$CO_2(g) + C(s) \xrightarrow{k_2} 2CO(g) \tag{2.2}$$

Zinc oxide NWs were first reported by Kong et al. using a powder mixture of 70% zinc and 30% selenium. The powders which were mixed in a quartz boat and placed in a quartz tube in the centre of a tube furnace heated to 1100 °C for 10 hours under a wet oxidation atmosphere at 100 Torr. It was observed that particles of ZnSe formed, with Se serving as a liquid forming agent, resulting in the growth of NWs via the vapour-liquid solid (VLS) mechanism [75]. The VLS mechanism was reported in the 1960s by Wagner and Ellis, who used Au catalysts to grow large single crystal micrometer-sized silicon wires [76]. It was then explored more thoroughly in the early twenty-first century to synthesis single crystal nanostructures using silicon and binary semiconductors such as ZnO and GaN [77]. In its present form, VLS growth of ZnO NWs is usually achieved using Au catalyst particles. This allows selective area growth of the NW by selectively depositing catalyst particles using conventional photolithographic techniques. Selective patterning may also be controlled by using temporary templates such as polystyrene nanospheres. The mechanisms behind catalytic growth are complex and several theories have been used to explain the the nucleation of Zn/ZnO vapour and its interaction with the metal catalyst particle [78,79].

Alternatives to catalytic growth in the vapour phase involve the roughness assisted and seed/buffer layer assisted growth. The absence of metal catalyst particles indicates that growth progresses via a vapour-solid (VS) mechansim, where nucleation of Zn(O) vapour occurs directly onto the substrate without encouragement from an intermediate liquid phase. Alterations to the substrate surface using wet chemical methods have been shown to result in nucleation and growth on lattice matched substrates such as sapphire and on silicon (1 0 0) [5,80]. A proposed mechanism for increased nucleation involves surface irregularities present on the substrate acting to limit the free movement of adsorbed Zn atoms, due to the increased energy barrier associated with migration across the surface (figure 2.7) [5]. This mechanism could also be used to explain nucleation on other non-single crystal surfaces, such as sputtered seed layers [81].

A defect-drive nucleation process has also been used to explain NW growth on α-Al_2O_3 following light surface etching using NaOH. Nanowire growth was found to occur only on chemically treated substrates, despite AFM surface roughness measurements showing similar values before and after etching. Further TEM analysis revealed growth occurring around defective regions of the substrate such as at step edges and dislocations [82].

Seed layers and buffer layers are commonly used on non-lattice matched substrates to instigate growth by (1) providing energetically favourable nucleation sites at the surface of the deposited layer (2) buffering the lattice mismatch between ZnO and the substrate. Jeong et al. investigated the initial growth of ZnO NWs on Si substrates without the use of metal catalysts or any kind of surface preparation [6]. They attributed the growth a self-seeding vapour-solid process, which

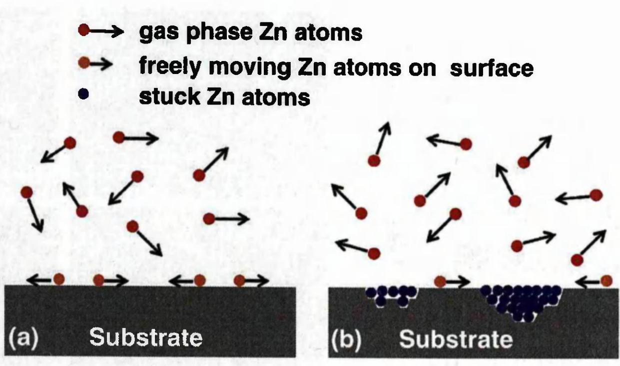

Figure 2.7: Schematic diagram showing the surface-roughness-assisted VS growth mechanism. (a) Zn atoms move freely on a smooth surface and (b) Zn atoms are stuck in pits on a surface, which serve as nucleation sites. Reproduced from [5].

proceeded through four steps: (1) initial formation of ZnO seed without any inherited orientation from the Si substrate, (2) epitaxial growth of NWs from the base growth seeds and formation of additional local seeds, (3) further acceleration of growth along the *c*-axis direction and (4) coalescence of the ZnO seeds to form a layer which promoted growth of aligned ZnO NWs. These steps correspond to diagrams (a-d) in figure 2.8.

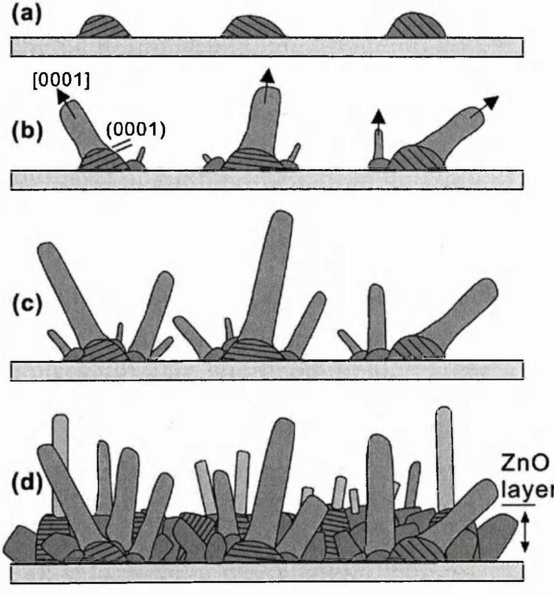

Figure 2.8: Self-seeding VS growth mechanism of ZnO NWs on an Si substrate. (a) initial ZnO nucleation with little texturing. (b) epitaxial growth of NWs from seed particles. (c) further *c*-axis growth and additional seeding of *c*-axis aligned NWs. (d) formation of a polycrystalline base growth layer which inhibits poorly aligned NW growth. Reproduced from [6].

Several studies have been conducted on optimising the crystallographic properties of seed layers for high quality vertically aligned growth [7,83–85]. Cha et al. conducted a CVD growth study on DC sputtered Zn seed layers that were thermally oxidised at 400 °C under ambient conditions. They studied a range of seed layer thicknesses and found using X-ray diffraction (XRD) that strong *c*-axis texturing of the seed layer resulting in highly aligned NW growth (figure 2.9) [7].

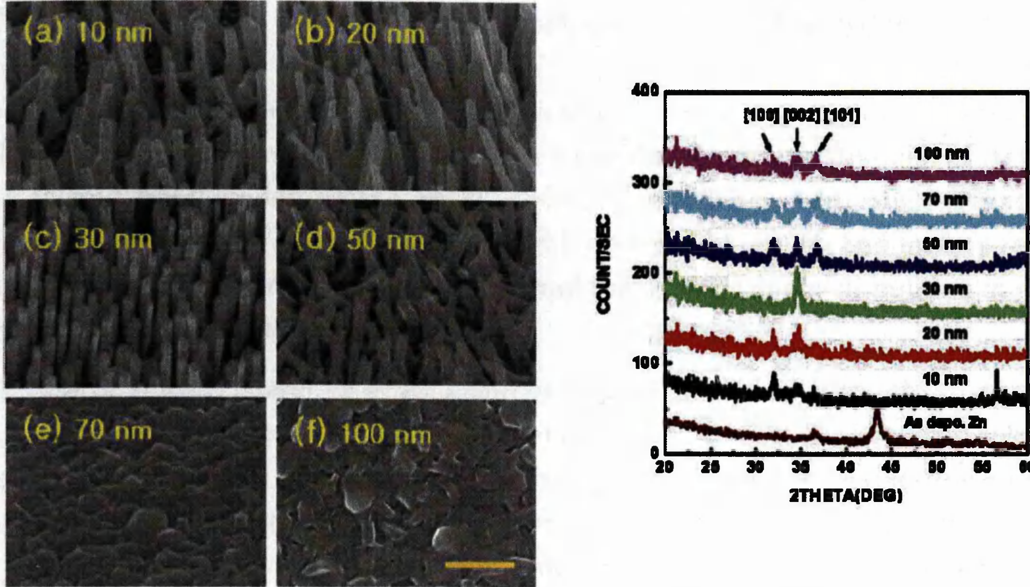

Figure 2.9: (left) SEM images of ZnO nanowire alignment dependence on the seed layer thickness. The as-deposited Zn layer thicknesses are (a) 10 nm, (b) 20 nm, (c) 30 nm, (d) 50 nm, (e) 70 nm, and (f) 100 nm, respectively. The scale bar is 1 µm. (right) XRD spectra of ZnO seed layer oxidised from varying Zn layer thicknesses. The optimised result is observed from a 30 nm thick oxidised Zn layer. Reproduced from [7].

Several issues exist with the high temperature vapour phase growth method. The choice of substrate materials is necessarily limited due to the high temperature and oxidative atmosphere in the furnace. Also, issues with repeatability related to sensitive dependence on initial conditions have been widely reported [77]. Chang et al. demonstrated a vapour trapping method for altering local conditions inside the furnace during growth. A quartz vial was placed downstream and used to create a zinc-rich environment in the system. Electrical measurements were conducted on NWs grown in different locations in the furnace and were found to vary significantly in their electronic properties depending on the local atmospheric conditions, which act to change the relative number of native defect states [86]. This gives an indication of how the structural and electronic properties of NWs grown using vapour phase techniques may vary across larger substrates due to temperature, pressure and oxygen/zinc concentration gradients in the system.

2.2 Nanowire Field Effect Transistors and Other Devices

Quasi-one dimensional nanostructures such as silicon nanowires (Si NWs) and carbon nanotubes (CNTs) have received substantial interest from the research community, although other materials such as GaN and metal oxides (In2O3, SnO2, ZnO) have also been used. The focus on Si NWs and CNTs likely stems from ease of fabrication, well understood doping and mature fabrication and contacting techniques, in the case of silicon, and the unusual and well publicised electronic and material properties, in the case of CNTs.

In the case of silicon, lateral FETs are commonly fabricated using a top-down approach on silicon-on-insulator substrates (SOI) [87]. However, in the case of single crystal NWs grown using bottom-up techniques, fabrication of FETs typically involved some harvesting and transfer step from the growth substrate. For research purposes, this is commonly achieved using crude transfer techniques such as simple mechanical transfer [88] or sonication, suspension in solvent and drop casting [89]. This results in random placement of NWs on the substrate - in order to contact the NWs using industry standard optical lithography, addition alignment processes are typically required [90]. Individual NWs may also be contacted using e-beam lithography or by using specialist nanoscale probing equipment [88], however these techniques are severely limited and unsuitable for scaling.

Vertical arrays have also been integrated into FET devices through the use of complex wrap gates [8,91,92], although problems with leakage between large area gate pads and leakage to the substrate effecting channel pinch off have been reported [8]. A schematic of a wrap gate FET is shown in figure 2.10.

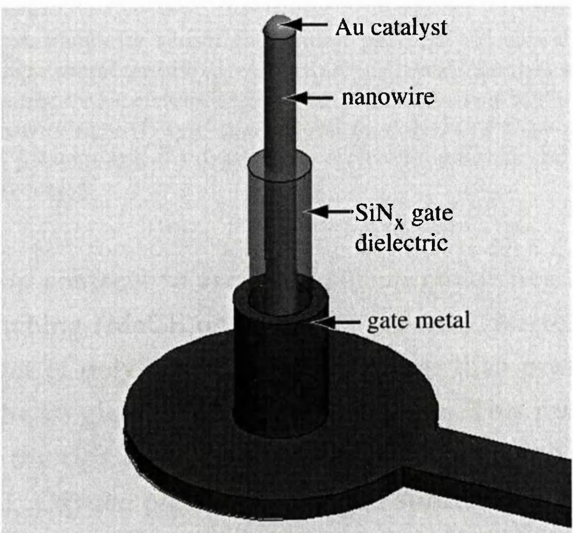

Figure 2.10: Schematic layout of a wrap gate FET. The gate wraps around the base of the wire, and is isolated from the NW by a layer of SiN_x. Reproduced from [8].

Some attempts have been made to avoid the problems associated with conventional lateral FET devices. In et al. identified several problems with chemFET-type sensors incorporating semiconductor NWs. These included slow serial processing of individual devices, unreliable results due

to irreproducible NW dimensions and surface chemistry, size-dependant noise sources such as $1/f$ noise and substrate electrical effects such as trapping-detrapping of charge carriers and adsorbates. Instead, they investigated a design for a gas sensing device employing large parallel arrays of vertical nanowires, intended to average out charge-carrier-dependant noise sources and minimise the deleterious effect of the substrate on NW sensing. The proposed fabrication process is shown in figure 2.11. A top-down metal assisted etching process was used to fabricate the NWs on a silicon substrate. A temporary photoresist encapsulation layer was then used to create a porous top contact to the nanowire array. The device was tested using NO_2 and NH_3 and exhibited a rapid response and an 18% resistance drop at a concentration level of 10 ppb of NO_2. This is amongst the lowest detection threshold reported for SiNW based gas sensors. [9]

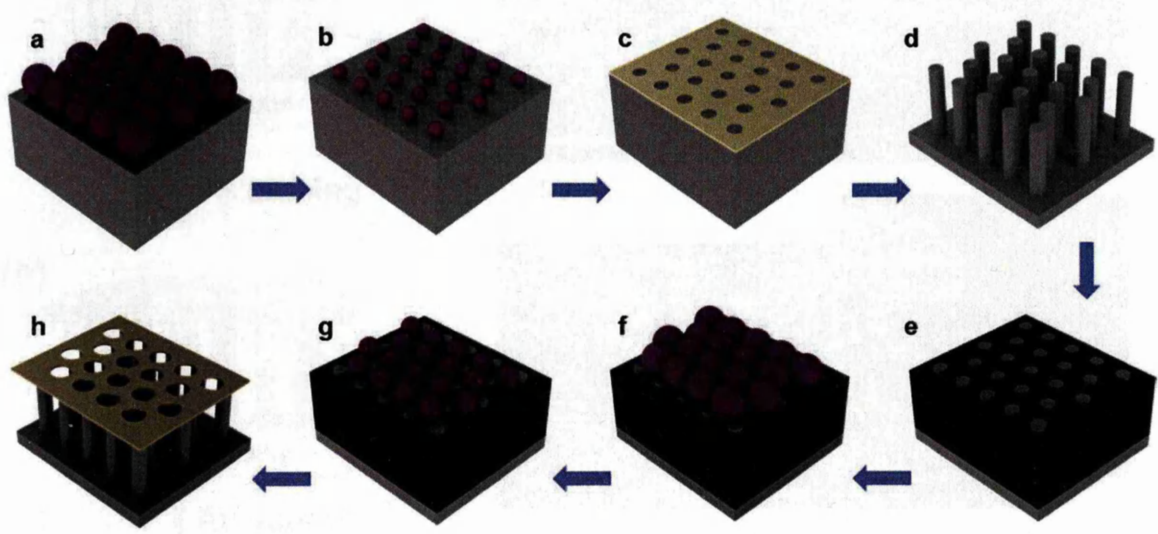

Figure 2.11: Outline of a silicon nanowire sensor fabrication process: (a) spin-coat monolayer of close-packed nanospheres; (b) reduce nanosphere diameter in oxygen plasma; (c) deposit catalyst material for Si etching and rinse away nanospheres; (d) catalytic, anisotropic etching of Si; (e) embed nanowire array in thick photoresist and etch back in oxygen plasma to reveal nanowire tips; (f) spin-coat second monolayer of close-packed nanospheres; (g) reduce nanosphere diameter in oxygen plasma; and (h) deposit top electrode material and dissolve away nanosphere and photoresist layers. Reproduced from [9].

Han et al. fabricated top contacts to arrays of silicon nanowires formed using a top-down metal-assisted chemical etching (MaCE or MacEtch) process. Mirror finished aluminium foil was spin coated with a layer of polystyrene (PS), which was then pressed against the top of the NW array and heated to the PS glass transition temperature. This resulted in a thin suspended layer of PS impregnating the tips of the array. The aluminium foil was etched away using a solution of $CuCl_2$ and HCl. Oxygen plasma ashing and sputter deposition were then employed to create a top contact to the NW tips (figure 2.12). This method has the advantage of avoiding complete encapsulation of the NWs in a support polymer and can be applied to any vertical array, regardless of aspect ratio and density. [10]

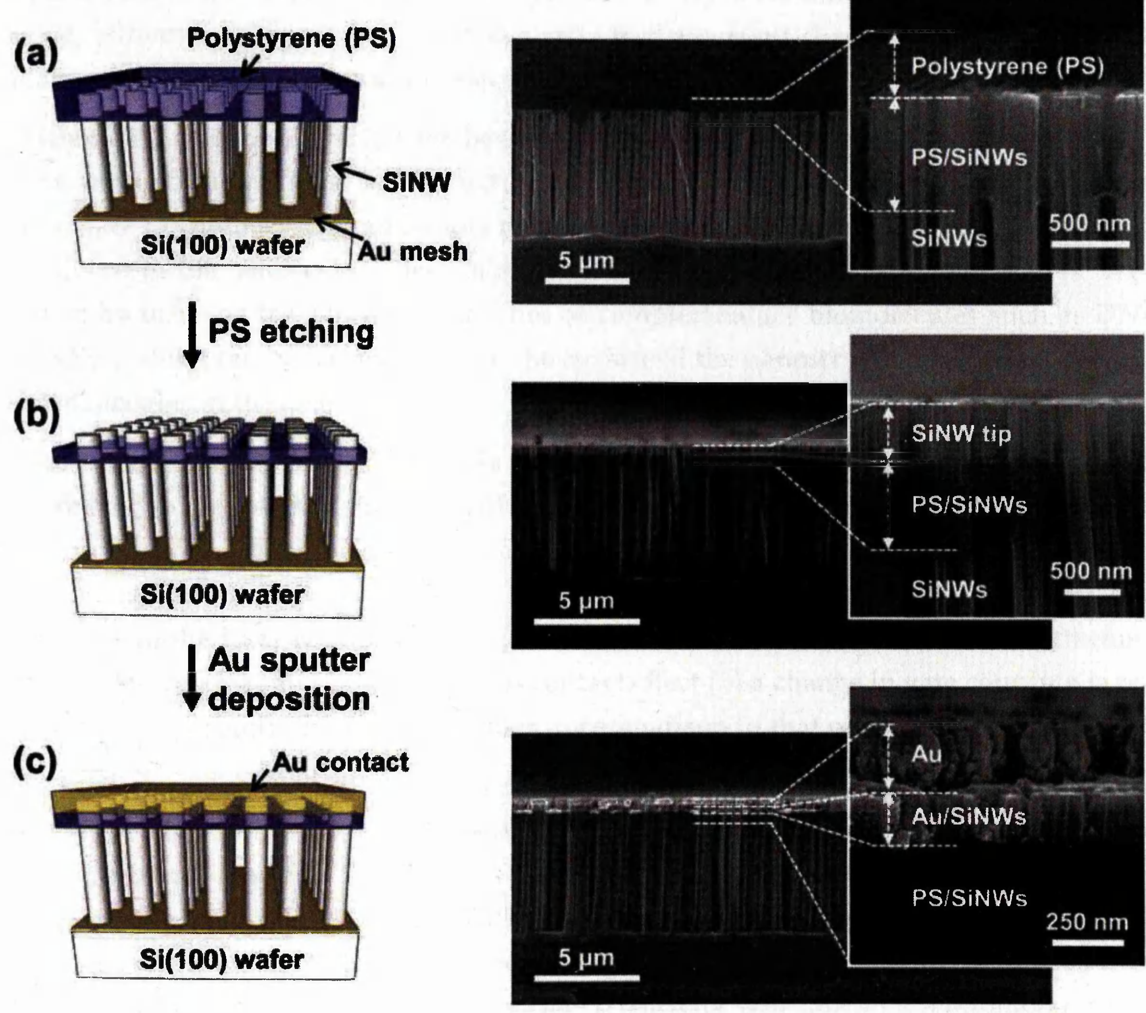

Figure 2.12: Fabrication process of air-bridged top metal contact on vertically aligned SiNWs; (a) formation of thin suspended layer of polystyrene (PS) on the uppermost part of vertical SiNWs, (b) partial removal of PS layer by oxygen plasma etching to expose the tips of SiNWs, and (d) sputter deposition of gold for electrical contact. SEM images of the corresponding sample structure are presented on the right side. Reproduced from [10].

2.3 Functionalisation and Biosensing

The chemresistors (sometimes chemoresistor or chemiresistor) constitute the simplest chemical sensors. They comprise of a sensing element (e.g. a nanotube or nanowire) with a resistance that is a function of analyte exposure. Typically, a voltage is applied across the sensing element and the change in current induced by exposure to a specific analyte concentration is recorded with time. Certain sensor parameters such as sensitivity and response can then be extracted from the temporal resistance characteristics. This type of sensing is commonly known as amperometric sensing, although the same term may also refer to the current characteristics measured during oxidation/reduction reactions at the electrodes during electrochemical sensing.

Although conventional FETs have been previously used as biosensing devices[6], FETs based on one and two dimensional nanostructures offer vast improvements in sensitivity due to their high surface to volume ratio and unique material properties that become salient once dimensions are reduced to the nanoscale. These biosensing devices, commonly called chemFETs, are made selective by utilising the binding properties of complementary biomolecules such as DNA and antibodies, which can be immobilised on the surface of the nanostructures to selectively capture target molecules in the analyte.

The sensing mechanism for NW FETs and NW chemresistors is commonly assumed to be entirely related to the electrostatic gating of the NW channel due to the attachment of biomolecules. In addition, several other mechanisms have been identified that that also contribute to the measured change in conductance [93]: (1) modification of the surface charge and surface states (2) changes to the local workfunction and consequently the band structure from attachment of biomolecules, refereed to as the interfacial contact effect (3) a change in gate coupling is possible due to the low permittivity of biomolecules in comparison to that of the electrolyte.

Early work on SiNW FETs was pioneered by Lieber et al., who were the first to demonstrate label-free detection of biomolecules in solution [94]. Their work relied on the sensing of streptavidin using biotin-modified Si NWs, and selectively was demonstrated by comparing their results with unmodified Si NWs and biotin-modified Si NWs where binding sites had been blocked. Following this work Lieber et al. fabricated a multiplexed sensor for the simultaneous detection of multiple cancer biomarkers. The reported sensitivity was down to femtomolar concentrations [95]. A following up to this work reported detection of individual viruses using monoclonal antibody receptors [96].

As an alternative to expensive SOI substrates, polycrystalline silicon NWs have also been integrated into biosensing devices using chemical vapour deposition of amorphous Si coupled with standard photolithographic patterning techniques. A schematic of the fabrication process is shown in figure 2.13. Following fabrication, the exposed NWs were treated with oxygen plasma, then functionalised using APTES. Succinic acid coupling involving the use of EDC-HCl and sulfo-NHS was used for antibody attachment. [11]

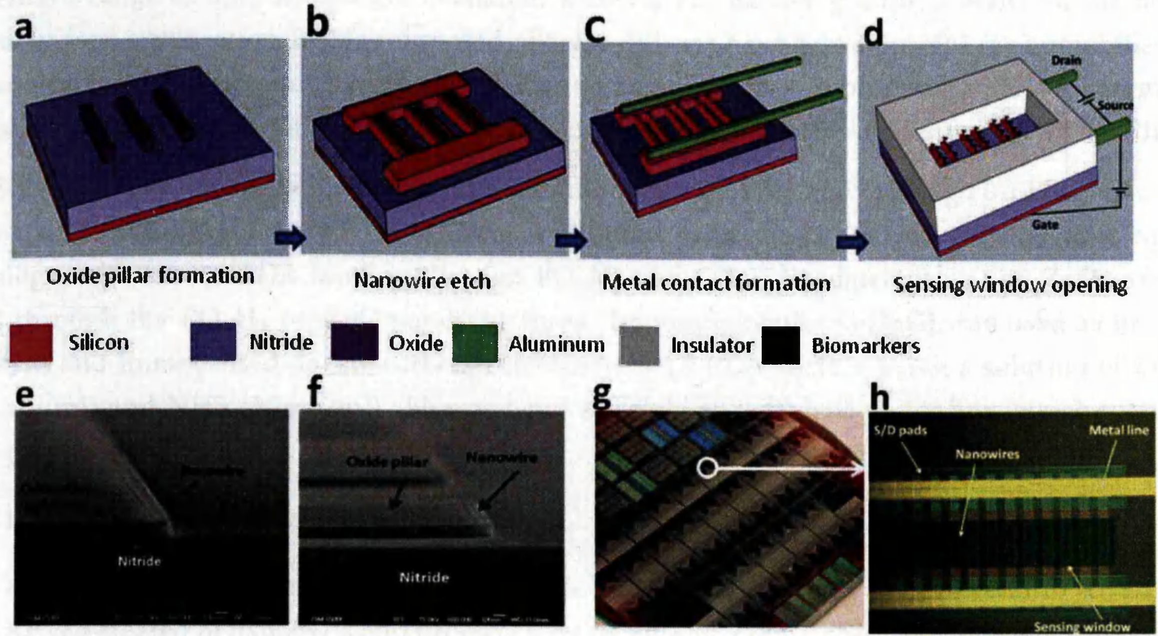

Figure 2.13: Schematic illustrations of polysilicon nanowire biosensor fabrication after (a) oxide pillar formation, (b) nanowire plasma etch, (c) metal contact formation, and (d) sensor window opening. The biasing configuration for the biosensor electrical measurements is also shown: (e) cross- sectional SEM image of a fabricated polysilicon nanowire; (f) cross-sectional SEM micrograph of polysilicon nanowires at the corner of a pillar; (g) optical image of a completed nanowire biosensor wafer; (h) high magnification optical image of a fabricated nanowire biosensor through a sensor window. Reproduced from [11].

2.3.1 Surface Modification

Surface modification involves physical, chemical or biological alterations to surfaces to engineer surface or surface dependant bulk properties of materials. In the context of chemical alterations, surface modification and surface functionalisation are usually used interchangeably, although functionalisation specifically involves changes to native surface functional groups. Common uses of surface modification involve changes to surface energy, adhesion, hydrophobicity, lubricity, increased chemical or corrosion resistance, biocompatibility and attachment of functional groups or biomolecules.

A common way to achieve modification of a surface for the subsequent attachment of biomolecules are self-assembled monolayers (SAMs). Self-assembled monolayers are created by covalently bonding short to medium-sized organic molecules by one end to a surface. This can potentially allow for a complete degree of surface coverage with a high degree of order within the layer. Self-assembled monolayers can be used to introduce controlled chemical functionality at a surface interface without having to resort to crude deposition or physical modification of the underlying bulk material. Further reactions can be carried out exploiting that functionality; in particular, this route can be used to immobilise macromolecules at the interface. [97]

Organosilanes and alkylsilanes (aliphatic organosilanes) are widely used for surface modification, particularly in biological applications as hetero-bifunctional cross-linkers. Since organosilanes react readily with a range of hydroxyl containing materials (such as metal oxides) and an

extensive range of alkylsilanes are available, with varied reactive groups present on the non-immobilised termination, SAMs composed of organosilanes have proved useful for immobilising biomolecules on a range of hydroxyl terminating surfaces [98]. Typical examples of common organosilanes used for biofunctionalisation include APTES, APTMS, AEAPS and GPS [99–101].

Stable SAMs have also been formed on both ZnO wafers and ZnO NWs using 10-phosphonodecanoic acid (10-PDA). The type of binding was found to be dependant on the substrate morphology, with the 10-PDA binding through PO_3H_2 and CO_2H headgroups on the ZnO wafers and through the PO_3H_2 on ZnO nanostructures. Immunoglobulin G (IgG) was used as model protein and immobilised on the carboxyl terminating 10-PDA surface using a solution of EDC (50 mg/ml) and NHS (50 mg/ml). Fluorescence microscopy was used to confirm attachment of the protein. [102]

2.3.1.1 Immobilisation of Anti-bodies

Wu et al. demonstrated the use of glutaraldehyde as a linking molecule between amino terminating APTES treated Si nanobelts and prostate specific antibody (anti-PSA). The amino terminating self-assembled monolayers were formed by immersing the nanobelt FET sample into a solution of 10% aqueous APTES for 30 minutes, then washing with DI water and drying at 120 °C for 30 minutes. No preparatory hydroxylation of the Si nanobelt surface was reported prior to silinization. The device was then treated with glutaraldehyde and the anti-PSA, with BSA used to block non-specific binding sites. The resulting calibration curve was found to be highly linear ($R^2 = 0.984$) with an ultimate detection threshold of 5 pg/ml. Arginine was then used as an intermediate between the amine terminated surface and the glutaraldehyde to increase the number of aldehyde binding sites, resulting in a increased detection threshold of 50 fg/ml. [17]

An alternative to a linking molecule is the use of carbodiimides (carboxyl-to-amine cross-linker groups), which couple carboxyls to primary amines, resulting in the formation of amide. 1-Ethyl-3-(3-dimethylaminopropyl)carbodiimide (EDC or EDAC) or reacts with carboxylic acid groups, activating the carboxyl group to form an active *O*-acylisourea intermediate, allowing coupling between the activated molecule and amino groups in the reaction mixture. An EDC byproduct is released as a soluble urea derivative after being displaced by the nucleophile. The *O*-acylisourea intermediate is unstable in aqueous solutions, making it ineffective in two-step conjugation procedures without increasing the stability of the intermediate using N-hydroxysuccinimide (NHS). This intermediate reacts with a primary amine to form an amide derivative. In the event that no amine is present, hydrolysis of the *O*-acylisourea intermediate results in regeneration of the carboxyls and the release of an N-unsubstituted urea [103]. The reaction process is shown in figure 2.14.

An issue with the activation method is that polymerization is likely to occur because all activated proteins contain carboxyls and amines. Hydrolysis of EDC (middle pathway in figure 2.14) results in recovery of the initial carboxyl group, meaning hydroxylation if a a competing reaction during coupling. Relative reaction rates between the hydroxylation and formation of amide bonds are dependent on temperature, pH and buffer composition. Phosphate buffers, for

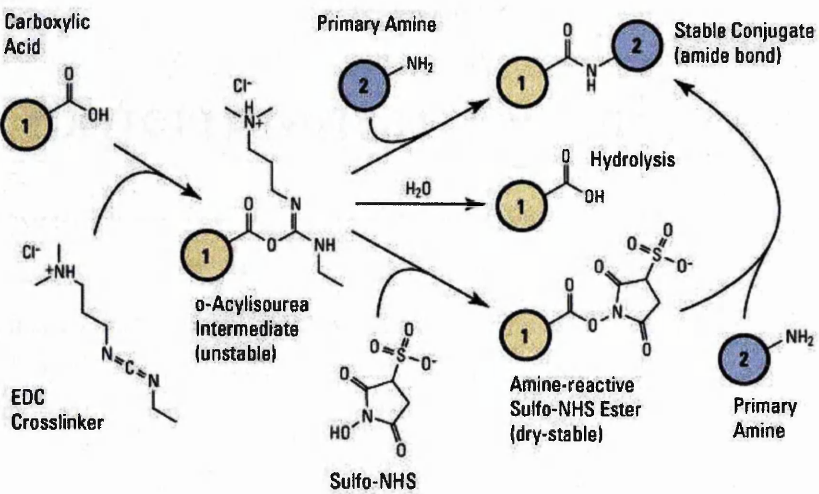

Figure 2.14: Sulfo-NHS plus EDC (carbodiimide) cross-linking reaction scheme. Adapted from [12].

example, reduce the reaction efficiency (amide formation) of the EDC, but increasing the amount of EDC can compensate for the reduced efficiency. Hydrolysis rate increases with increasing pH and occurs more readily in dilute protein solutions. NHS-esters are usually used at 2 to 50 times the molar protein concentration. Typically, the concentration of the cross-linker varies between 0.1 mM to 10 mM. The protein concentration should be greater than 10 µM (between 50 µM and 100 µM is optimal), as more dilute protein solutions result in excessive hydrolysis of the cross-linker [103]. If the concentration of carboxyl groups per mole is known, the recommended molar ratio of EDC:COOH is 2.5 to 1, whereas the corresponding molar ratio of NHS:COOH is 20 to 1 [104].

Chapter 3

Experimental Techniques

In this chapter, nanowire (NW) synthesis as well as the various techniques employed during device fabrication are described, along with specifics of the fabrication equipment used. Subsequently, materials and surface characterisation methods are detailed.

3.1 Vapour Phase Growth of Zinc Oxide Nanowires

Zinc oxide (ZnO) NWs were grown using the vapour transport method in a standard double tube furnace set-up. The source powder and substrates were placed inside a quartz tube, which is then inserted into the alumina (Al_2O_3) furnace tube. Both source powder and samples were contained in alumina combustion boats, with the source boat located at the centre of the quartz tube, and the sample boat positioned downstream in the condensation region. The source was a 1 : 1 mixture of ZnO powder (Alfa Aesar, 99.99%) and graphite powder (Alfa Aesar, -325 mesh, 99.9995%), typically 0.6 g of each, with the graphite catalysing the thermal decomposition of the ZnO, as detailed in section 2.1.3.2. Argon was used as a carrier gas which was mixed with oxygen prior to injection into the tube furnace. The gas flow rates for Ar and O_2 were 100 sccm and 10 sccm, respectively. The growth procedure is summarised below:

1. Load furnace with quartz tube containing source powder and samples.
2. Evacuate furnace tube to a base pressure of 1.5×10^{-2} mbar.
3. Bleed in process gasses and let pressure stabilise at around 7.5×10^{-1} mbar.
4. Ramp up furnace to growth temperature and hold for growth duration.
5. Turn off furnace heater and gas flow. Allow to cool.

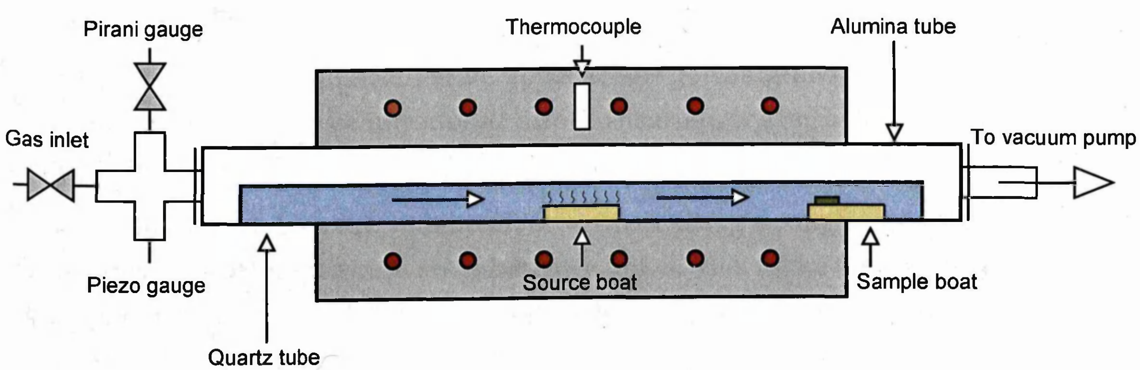

Figure 3.1: Schematic of vapour phase nanowire growth set-up.

The furnace used was a Thermo Scientific F79320-33 (figure 3.2) equipped with a 750 mm alumina tube of inner diameter 50 mm and outer diameter 60 mm. The quartz reaction tube (figure 3.3) measured 610 mm with inner diameter 22 mm and outer diameter 25 mm. The alumina source and sample boats measured 88 mm × 15 mm. Furnace temperature was measured using a thermocouple located outside of the alumina tube in the furnace chamber, with the ramp rate reported as approximately 30 °C/min. An Edwards RV5 rotary vane pump was used to evacuate the chamber.

Figure 3.2: Thermo Scientific tube furnace. Gas inlet is on the left with Pirani and piezo vacuum gauges mounted on the cross piece. The vacuum hose is connected on the right.

3.1.1 Nanowire Growth Optimisation

There are many experimental variables to be considered when optimising the growth of NWs via the vapour transport method. A summary follows:

- Furnace temperature.
- Ratio of ZnO : graphite and total quantity of source powder.
- Source-sample separation and sample temperature.
- Growth and base pressure.
- Gas flow rates and Ar : O_2 ratio (O_2 partial pressure).
- Growth duration.

In addition, there are several alternative approachers to the growth process to consider. For example, process gasses may be introduced prior to heating, or alternatively once the furnace has stabilised at the set-point.

Not all of these variables are independent – when using a single zone furnace the sample separation and sample temperature are inherently linked, due to the temperature gradient across the heating zone (figure 3.4). The metal (oxide) vapour and oxygen partial pressures at the sample will also dependant on sample-source distance. This allows a range of growth conditions to be investigated for a given set of growth parameters, just by varying the sample location relative to the source, with the source remaining fixed at the centre of the tube furnace.

Figure 3.3: Quartz tube following growth (gas flow from left to right). An alumina source boat is also shown. Condensation of ZnO vapour is seen both upstream and downstream.

Rectangular silicon samples of up to 150 mm in length were used to study how nanostructure morphologies differ with source-sample separation. To further complicate matters, the location of the sample relative to the sample boat was found to have an influence on the condensation of vapour. It was necessary to optimise the furnace temperature and source-sample separation for each sample type i.e. for seed layers, conductive layers and for the surface enhanced growth method.

The humidity, pressure and oxygen partial pressure are known to have a profound influence on the nucleation and morphology of metal-oxide nanostructures. Efforts were made to control for the humidity by keeping the furnace evacuated when not in use, and pumping to a consistent base pressure prior to growth.

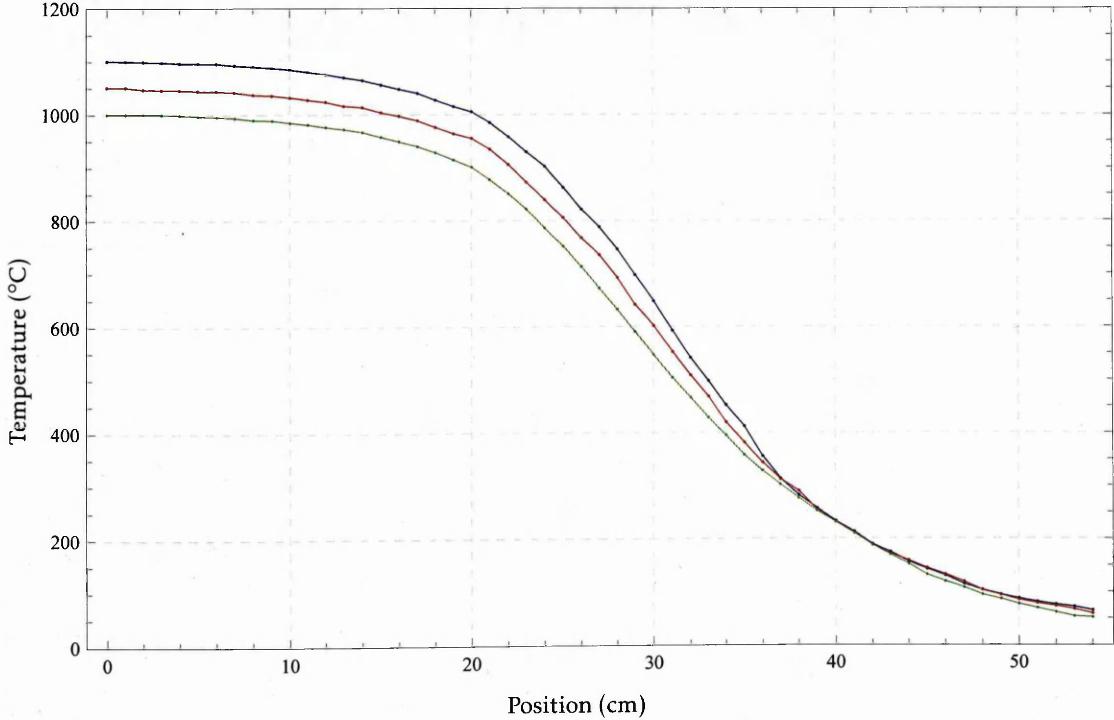

Figure 3.4: Calibration curve of furnace temperature gradient, as measured relative to the centre of the furnace. Measurements were conducted using a type K thermocouple in contact with the alumina furnace tube under ambient conditions. The blue, red and green curves are for furnace temperatures 1100 °C, 1050 °C and 1000 °C, respectively.

3.2 Device Fabrication

The following microfabrication techniques were conducted in the Centre for NanoHealth (CNH) Class 1000 cleanroom, with photolithographic patterning performed in the adjoining Class 100 area.

3.2.1 Substrate Preparation and Cleaning

Devices were fabricated on silicon (1 0 0), due to its prevalent use in the semiconductor industry. The wafer specifications were as follows:

- Diameter: 150mm (6")
- Thickness: 610–640 µm
- Dopant: Phosphorus (n-type)
- Doping concentration: $10^{15}\,cm^{-3}$
- Resistivity: 4–7 Ω cm

Wafers were scored parallel or perpendicular to the wafer flat to provide cleavage along the {1 1 0} direction. Cleaved samples measured 1.5cm × 1.5cm.

Removal of chemical contaminants, biological residues and particulate impurities from the silicon wafer surface is critically important prior to the beginning of processing. Subsequent photolithographic, thin film deposition and NW growth processes make this procedure particularly crucial. The cleaning procedure consists of the following steps:

Table 3.1: Cleaning procedure for silicon samples.

Process	Duration	Notes
Sonicate in acetone	5 minutes	Removes cleaving debris, lipophilic contaiminants and some organic impurities from the wafer surface.
Sonicate in IPA	5 minutes	Removes striations and acetone residue from sample surface.
Piranha clean	15 minutes	Mixture of H_2SO_4 and H_2O_2. Powerful oxidiser that removes organic residues.
HF dip (49%)	-	Dip in HF to remove oxide layer formed during piranha clean.

Samples were transferred directly from acetone into IPA, then blow dried in N_2 following ultrasonic cleaning. The samples were further rinsed in DI water and blow dried in N_2 both after the piranha clean and following the HF dip. Piranha solution is a 5 : 1 mixture of H_2SO_4 to H_2O_2. The solution is self-heating due to the exothermic nature of the reaction, and a further 1 part H_2O_2 was added every 5 minutes to retain the solution temperature. The HF etches the oxide layer formed during the piranha clean, which also contains impurities from the piranha solution. This results in a clean hydrophobic silicon surface.

3.2.2 Photolithography

Photolithography is the process of transferring patterns on a mask on to a thin layer of photosensitive material (photoresist). The resist patterns are not a permanent feature of the device and are removed once the pattern is transferred onto the underlying layers. This pattern transfer is accomplished using etching but patterning can also be achieved using the additive lift-off process.

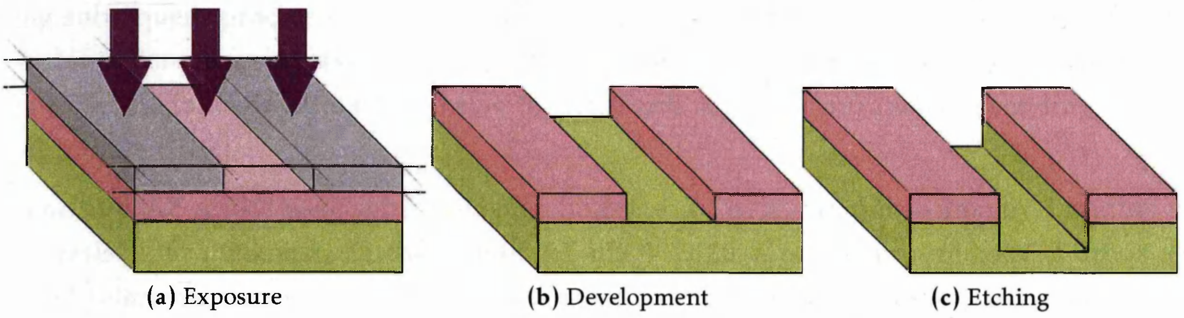

(a) Exposure (b) Development (c) Etching

Figure 3.5: The basic steps involved in photolithography using a positive photoresist. (a) UV contact exposure of a positive photoresist layer (pink) on a substrate (green). The chromium mask is shown in grey. (b) The exposed part of the photoresist is removed using a developer. (c) The substrate is then etched. After, the photoresist may be removed (plasma ashing – section 3.2.6) or may be left for a further processing (lift-off – section 3.2.2.5).

3.2.2.1 Photoresists

Photoresist is a chemical formulation which contains a photoactive material suspended in a solvent. The photoactive compound gives the resist its developer resistance and absorption properties. Exposure to light of a certain wavelength (usually UV) results in one of the following reactions:

- **Positive resist:** Photoactive compound in the exposed portion of the resist undergoes photochemical decomposition. Exposed area becomes soluble to the developer.
- **Negative resist:** Photoactive compound in the exposed portion of the resist cross-links with molecules present in the formulation. Exposed area of the resist coating becomes insoluble to the developer.

The photoresists used in this work were AZ 6612 and AZ nLOF 2070, both purchased from MicroChemicals GmbH. The resin used in the AZ series of photoresists is Novolak, a cresol resin that is synthesized from phenol and formaldehyde. Resist properties are determined from the molecular chain lengths, with long chains increasing thermal stability, developer selectivity and development time at the expense of resin adhesion. The photo active compound (PAC) belongs to the group of diazonaphtho-quinones (DNQ), with the addition of DNQ to Novolak decreasing the alkaline solubility of the resin by an order of magnitude. Following UV exposure (440 nm), the DNQ transforms into a carboxylic acid, increasing the alkaline solubility by more than three orders of magnitude. This is accompanied by absorption of water and the release of nitrogen into the resist film. The solvent used in AZ photoresists is propylene-glycol-mono-methyl-ether-acetate (PGMEA). [105]

Baking of Photoresist Films

Following coating, a baking step is necessary to remove the solvent from the photoresist. This is important for a number of reasons, mainly to dry the resist and to prevent bubbles forming in the film due to nitrogen released during decomposition of DNQ. In addition, accurate soft-baking can help to improve film uniformity and adhesion [106]. When developed, remaining PGMEA solvent converts to acetic acid, increasing the dark erosion of the resist. Also, thermal stability of the resist may be compromised by excess solvent in the film, leading to rounding of resist features during subsequent processing e.g. dry etching. The baking step following coating is known as soft-baking. For AZ resists, typical average PGMEA concentration in the film drops from 20-40%, down to 5-10% following the soft-bake, with initial and final concentrations depending on resist film thickness. [107]

Generally, AZ resists were soft-baked on a hotplate at 110 °C for approximately 1 minute per µm of resist film thickness. In the case of AZ nLOF 2070, a post exposure bake (PEB) is also required following exposure to cross-link the resist, rendering the exposed portion of the film insoluble to the developer. The PEB is largely independent of film thickness, therefore all films were baked on a hot plate at 110 °C for 1 minute 30 seconds.

3.2.2.2 Spin Coating

Spin coating is a technique for the application of thin-films. Fluid or resin is deposited on to a sample and then the sample is spun at high speed. The centrifugal force experienced by the fluid causes it to spread out and fall off of the edge of the sample, leaving a thin-film on the surface. Film thickness will depend on the nature of the fluid or resin (viscosity, drying rate, surface tension, etc...) and the parameters chosen for the spin process (acceleration, rotation speed, duration and deceleration). Also, subtle factors such as air temperature, humidity and air flow around the sample have an effect on film thickness. In general, higher speeds and longer spin times create thinner films.

The spin curves for the AZ resists used in this work are shown in figure 3.6. In the case of AZ6612, samples were spun at 3000 rpm for 45 seconds, with an initial acceleration of 1000 rpm/s. From figure 3.6a, this corresponds to a film thickness of around 1.4 µm. For AZ nLOF 2070, employed mainly as a NW encapsulation layer, spin speed was varied from 2000–3000 rpm to attain desired film thickness with an acceleration of 500 rpm/s and a duration of 30 seconds. This corresponds to a thickness of 6.5–8 µm according to figure 3.6b, although the actual thickness was considerably more, due to the presence of NW arrays inhibiting flow across the sample. See chapter 6 for details.

3.2.2.3 Mask Alignment and Exposure

The wafer is masked, typically using an ultra-flat glass plate patterned with a metal thin film on one side called a photomask, then exposed to light of a given wavelength determined by the absorption spectrum of the resist. Commonly, UV light produced by a high intensity mercury vapour lamp is used.

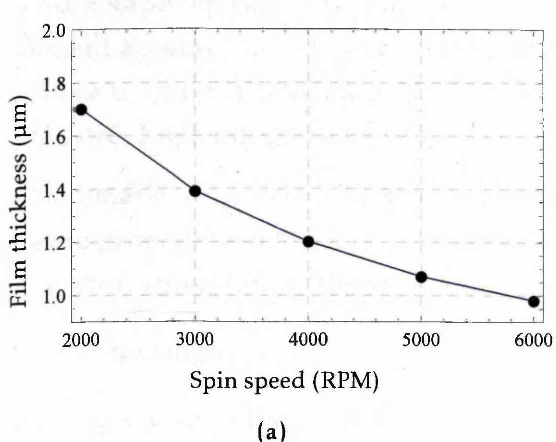

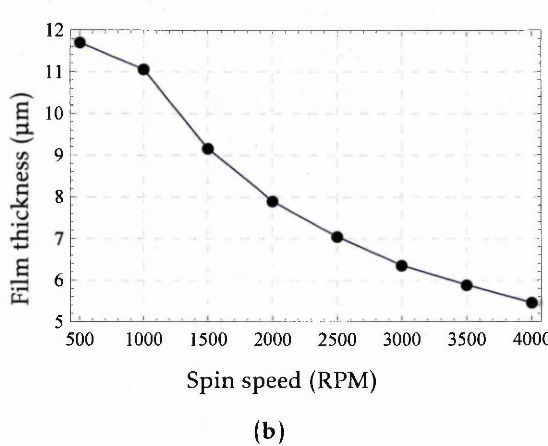

Figure 3.6: Spin curves for AZ6612 (**a**) and AZ nLOF 2070 (**b**). Adapted from [13] and [14], respectively.

Different methods exist for masking the sample, but the simplest method is contact exposure in which the patterned side of the photomask is brought into direct contact with the sample. This has the advantage that diffraction at the edges of features on the mask is minimised. However, masks are especially prone to wear in contact printing and debris from resist coatings can become lodged between the photomask and wafer resulting in incorrect patterning and poor contact in isolated areas. Also, the pronounced edge bead formed at the edges of the substrate during photoresist spinning can be problematic, especially for small samples. Instead, proximity exposure is sometimes preferable. In proximity mode, the thickness of the substrate is taken into account and the sample height adjusted to maintain a fixed gap between mask and sample surface.

Often more than one photolithographic step is required, meaning the sample must be precisely aligned with a different patterns following processing of the previous layer. Masks typically contain registration (or alignment) marks that allow the samples to be precisely aligned under a microscope by means of a moveable stage.

Figure 3.7: SUSS MicroTec MA/BA8 Gen3 mask aligner

A SUSS MicroTec MA/BA8 Gen3 mask aligner equipped with a Ushio 1000W mercury arc lamp was used for exposures (figure 3.7). The machine was operated in proximity mode, with

exposure gaps typically less than 50 µm. Top side alignment (TSA) was done manually, with alignment accuracy limited to approximately ±5 µm, due to the use of small samples. The exposure dose used for AZ6612 was 350 mJ/cm^2, as measured at the h-line (405 nm). For the thicker nLOF 2070, higher doses of up to 750 mJ/cm^2 were used, measured at the i-line (365 nm).

Photomasks were designed using a combination of L-Edit sofware (Tanner EDA) and custom software programmed to output in Caltech Intermediate Format (.CIF). Mask specifications were 5″ x 5″ with chromium patterned on soda-lime glass.

3.2.2.4 Development

Following exposure the photoresist is developed using a solvent. The mechanism for developing is a surface-limited dissolution process that differs drastically between positive and negative resists. For positive resists the selectivity, or difference in etch rate between the exposed and unexposed regions, is generally much greater. For high resolution device fabrication metal-ion free developers are available to prevent metal ion contamination of the wafer.

Immersion of the samples in the developer solution is the most straight forward method of developing, although other methods such as spray and puddle development exist. During immersion development it is important to agitate the sample in order to provide uniform development and to carry away the solution as it dissolves the photoresist. A complex interplay exists between development and previous photolithographic steps. The major variables affecting development time are:

- Photoresist thickness
- Photoresist soft-bake temperature/duration
- Exposure dose
- Developer concentration
- Developer agitation method

For the AZ series of photoresist, AZ 726 MIF developer was used. This is a H_2O based metal ion free developer with 2.38% tetramethylammonium hydroxide (TMAH), that also contains surfactants to improve sample wetting. AZ6612 was developed in a 2 : 1 ratio of AZ 726 to DI water. Development times were on the order of 30-60 seconds. For the thicker AZ nLOF 2070, undiluted developed was used, with the development lasting several minutes. Following development, samples were rinsed in DI water and blow dried with N_2. Features were examined under an optical microscope to confirm proper development without undercut and resist peeling.

3.2.2.5 Etch-back and Lift-off Processes

Following resist patterning, the underlying layer can be etched back using a suitable wet etchant (see section 3.2.3). This requires a high (preferably infinite) selectivity of the underlying device layers compared to the layer requiring patterning.

The lift-off process is an alternative method of patterning thin-films. Following thin-film deposition onto a sacrificial material, such as a patterned photoresist layer, the sample is immersed in a solvent. The photoresist is dissolved, causing the the deposited thin-film to lift-off leaving

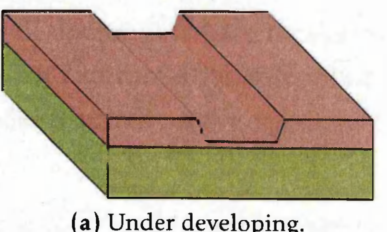

(a) Under developing.

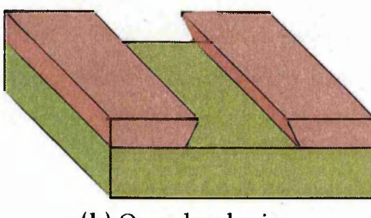

(b) Over developing.

Figure 3.8: The result of incorrect developing. In (a), resist still remains on the substrate surface which could result in complete lift-off of a deposited layer or a faulty contact. In (b), over-development has led to undercut of the resist features. This is more common for negative photoresists and can be exploited to avoid resist sidewall coverage during the lift-off process.

behind exposed areas of the underlying layer.

The main advantage of this technique over the etch-back is substrate compatibility – the underlying layers need only be compatible with the solvent, rather than an etching solution. This allows inert thin-films, such as SiO_2, to be patterned on top of amphoteric layers, for example. However, problems exist with this technique – notably the retention of unwanted parts of the film (commonly referred to as 'ears') and redeposition of lifted off material onto random locations on the sample surface.

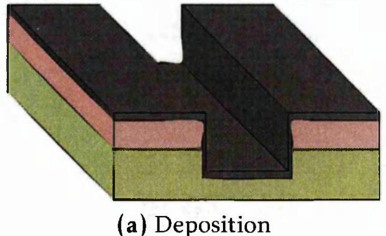

(a) Deposition

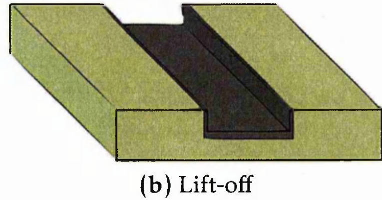

(b) Lift-off

Figure 3.9: The lift-off process performed on a thin film (grey) using a photoresist (pink) as a sacrifical material.

Common solvents, such as acetone, can be used for the lift-off but this is ill advised, as the high vapour pressure tends to lead to striations and redeposition of the lifted off material [108]. Instead, 1-methyl-2-pyrrolidone (NMP) is recommended due to its suitable physical properties: NMP yields a low vapour pressure (no striation formation), strongly solves organic impurities as well as resists, keeps solved particles in solution and can be heated due to its high boiling point (204 °C) [109]. However, since NMP is classified as toxic and teratogenic a safer alternative for routine handling is dimethyl sulfoxide (DMSO). With performance as a photoresists stripper comparable to NMP, DMSO is a highly polar solvent that can also be heated to aid with resist removal (boiling point 189 °C) [108]. In this work, both NMP and DMSO were employed for the lift-off process. A typical process would involve 5-10 minutes of sonicating in ample solvent followed by an additional 5-10 minutes of sonicating in fresh solvent to minimise redeposition. Samples were then rinsed in DI water and blow dried with N_2.

3.2.3 Wet Etching

Liquid-phase (or wet) etching is generally isotropic, although directional wet etching is possible due to etch rates for certain enchants being highly dependant on crystallographic orientation.

This effect is well documented for monocrystalline silicon, with etchants such as potassium hydroxide (KOH) and tetramethylammonium hydroxide (TMAH) frequently employed to create sloped pyramidal features on the wafer surface, due to the reduced etch rate in the {1 1 1} direction [110, 111].

Wet etching is commonly used to pattern thin-films, where etch isotropy and undercut is less problematic. Optimised resist adhesion to the substrate is important to prevent peeling. In this work, wet etching was mainly employed for etching metal contacts. A example of some typical etchants are shown in table 3.2.

Table 3.2: Wet etchants and etch rates for various materials.

Target Material	Etchant	Etch Rate (nm/min)	Source
Silicon	KOH (30%, 80 °C)	1100	[112]
Silicon dioxide	HF (49%)	2300	[112]
	10:1 HF	23	
	25:1 HF	9.7	
	100:1 HF	2.3	
Zinc oxide	Dilute HCl (1%)	500	[113]
	NH_4Cl (10%)	40	[114]
ITO	HCl (29%)	14	[115]
	Aqua regia (33%)	22	
Aluminium	H_3PO_4 (80%) + HNO_3 (5%) + $C_2H_4O_2$ (5%) + H_2O (10%)	530	[112]
Titanium	20:1:1 H_2O : HF (49%) : H_2O_2 (30%)	1100	[112]
Chromium	CR-7 (Cyantek)	170	[112]
Gold	Aqua regia 3:1:2 HCl (37%) : HNO_3 (70%) : H_2O	680	[112]

3.2.4 Dry Etching

Dry etching is an encompassing term for all ion based etching processes and is usually used synonymously with plasma etching. In the semiconductor industry, the move towards dry etch processes was motivated by a need for increased etch uniformity across wafers due to decreased pattern dimensions. Plasma etching includes such sub-technologies as reactive ion etching (RIE) and sputter etching (ion milling). As their names indicate, these techniques rely on both chemical and physical processes.

Basic plasma etching and RIE generally use molecular gasses that contain one or more halogen

Table 3.3: Types of dry etching.

	Plasma etching	Reactive ion etching	Sputter etching
Relative ion energy	Low	Medium	High
Relative selectivity	High	Medium	Low
Directionality	Isotropic	Quasi-isotropic to anisotropic	Highly anisotropic
Pressure	$> 0.1\,\text{mbar}$	$\sim 0.1\,\text{mbar}$	$\ll 0.1\,\text{mbar}$

atoms. These are introduced into the chamber where a glow discharge is initiated, generating ions, radicals and reactive atomic species that combine with oxides, semiconductors and metals to produce volatile by-products. The by-products formed at the sample surface diffuse into the process chamber and are subsequently evacuated by the vacuum system. These chemical processes allow a high degree of selectivity to be achieved as the resists used are necessarily compatible, in the sense that they only react slightly with the plasma species, as compared with the film or substrate being etched. As can be seen in table 3.3, there is generally a compromise between anisotropy and selectivity, with physical ablation processes providing highly directional etching at the expense of material selectivity.

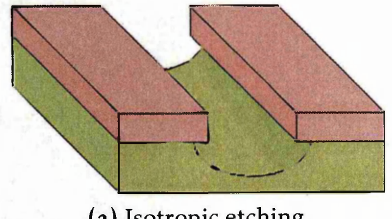

(a) Isotropic etching.

(b) Perfectly anisotropic etching.

Figure 3.10: Isotropic and anisotropic (directional) etching. Undercut of the photoresist (pink) is shown in (a).

3.2.4.1 Reactive Ion Etching

Reactive ion etching (RIE) is a common plasma configuration for dry etching. Reactive ion etching employs highly reactive gases that react with surface atoms and molecules to form volatile species. The actual mechanisms that result in etching are complicated and there are both physical and chemical processes that result in removal of material from the surface. The following processes occur during RIE:

- Active species generation: An electric glow discharge plasma is formed by passing a current through the etch gases at low pressure. This is done by applying a strong RF electromagnetic field to the wafer platter, typically at a frequency of 13.56 MHz. The oscillating field ionises the gases resulting in radicals, positive and negative ions, electrons and neutrals.
- Formation of a DC bias for ion acceleration: The high frequency driven capacitively coupled electrode acquires a negative charge due to high electron mobility. This attracts positive ions towards the electrode.
- Diffusion of plasma generated reactive species from the bulk of the plasma to the material being etched.

- Absorption of reactive radicals into the surface of the sample. This step is assisted by removal of the passivated fluorine surface layer through ion bombardment.
- Reaction step: The sample material reacts with the absorbed atoms to form volatile species.
- Desorption step: The reaction products are sputtered back into the gas phase through ion bombardment.

Etching of Si can be accomplished using fluorine, chlorine and bromine based chemistries. Examples of fluorine based gases include sulphur hexafluoride (SF_6), tetrafluoromethane (CF_4) and trifluoromethane (CHF_3). Common etch rates for these gasses in isolation are 600, 60 and 0.6 nm/min, respectively [116]. In addition, additive gases such as oxygen and argon can be introduced into the plasma. Inert heavy gases, such as argon, increase the physical aspect of the etching process through sputtering, while the addition of oxygen can be used to aid the directionality of the etch through side-wall passivation. It is thought that oxidation of the side-walls prevents fluorine attacking the silicon. This does not occur on horizontal exposed areas of the sample as the oxide layer is sputtered.

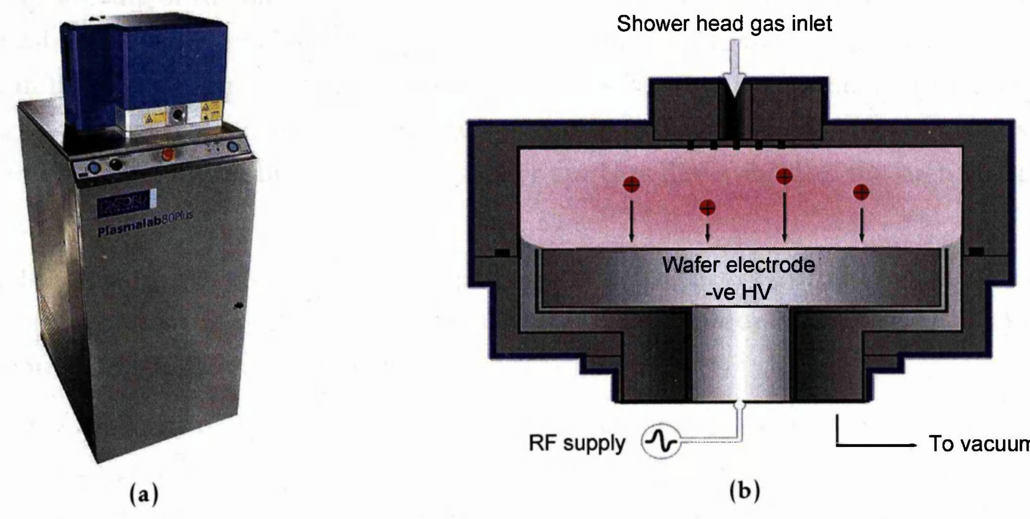

Figure 3.11: The Oxford Instruments Plasma Lab 80+ is shown in (a), with a schematic of the parallel plate reactor shown in (b).

An Oxford Instruments PlasmaLab 80 Plus RIE (figure 3.11a) was used for silicon etching. The system consists of a 13.56 MHz driven parallel plate reactor with a shower head gas inlet, optimised for RIE uniformity (figure 3.11b). A typical Si etch process would use SF_6, CHF_3 and O_2 at flow rates of 30, 10 and 5 sccm, respectively. Chamber pressure would be maintained at 0.1 mbar during the process, with an RF power of 100 W. A process such as this gives an etch rate of around 1 μm/min.

3.2.5 Deposition Techniques

Described in the following sections are several metal, semiconductor and dielectric thin-film deposition techniques. Sputtering and evaporation (not detailed here) are types of physical vapour deposition (PVD), whereas chemical vapour deposition (CVD) refers to the group of techniques utilising reactive precursors as source material.

3.2.5.1 Sputtering

Sputtering is a vacuum deposition technique involving the bombardment of a target material with energetic particles, typically inert argon ions, with energies greater than the surface binding energy of the target. This results in ejection of neutral target atoms which are then incident on a substrate located in the deposition chamber.

For conductive targets, a negative DC bias is applied to the target, resulting in a glow discharge. In order to increase the sputter yield, a magnet located in the sputter gun increases the ionisation density in the vicinity of the target, due to the helical path of the free and secondary electrons in the magnetic field (magnetron sputtering). The ions are accelerated towards the target, resulting in ablation of the target material.

When sputtering low conductivity targets (semiconductors or insulators), AC is employed to discharge the target every half cycle, preventing build up of positive charge on the surface of the deposition source. For frequencies <50 kHz, both electrons and ions are mobile, resulting in alternate sputtering of the target and sample (system ground). At frequencies >50 kHz, electrons are still mobile, however the heavy ions can no longer follow the switching. Instead, a capacitor installed in the deposition source prevents electrons discharging to ground, setting up a DC bias on the target and neutralising positive charge built up from incident ions. Flow of negative charge towards the target is uninhibited, as the capacitor appears like a short to the high frequency RF field.

In reactive sputtering, other gases such as oxygen or nitrogen are introduced into the chamber in order to react with the sputtered target material. This technique is often used in conjunction with RF sputtering in order to retain oxide film stoichiometry.

Due to the presence of a sputtering gas, step coverage is generally increased over evaporation techniques, owing to the decreased mean free path. Film properties and morphologies are vastly different between evaporation and sputtering, with sputtering generally resulting in films with better adhesion to the substrate. As sputtering is a plasma based process, ions also impinge on the deposited film, with the ion flux to atom flux ratio playing a decisive role in the microstructure and morphology of sputtered films.

Sputtering was conducted in a Kurt J. Lesker PVD 75 (figure 3.12a) equipped with three magnetron sputtering sources (figure 3.12b) which can be interchanged between 13.56 MHz RF and DC. This allows multiple materials to be deposited without having to expose the chamber to atmosphere. Following sample and target loading, the chamber was pumped to a base pressure of around 10^{-6} mbar, then back filled with argon to achieve sputtering at pressures of approximately 10^{-3} mbar. Samples were rotated during deposition in order to achieve uniformity. A crystal monitor calibrated for the specific deposition material was used to monitor film thickness.

(a)

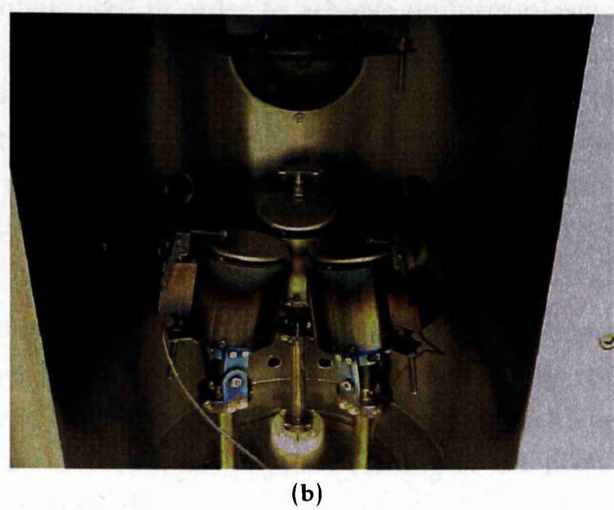

(b)

Figure 3.12: Lesker PVD 75. The deposition chamber is located on the top left of the unit in (**a**). A close up of the deposition chamber with the three magnetron sources is shown in (**b**).

3.2.5.2 Chemical Vapour Deposition

An important class of deposition is chemical vapour deposition (CVD), which is regularly used in the semiconductor industry for silicon dioxide, silicon nitride and polycrystalline silicon depositions. In summary, CVD relies on the reaction of precursors at high temperature to deposit the desired material from the vapour phase. Vapour phase NW growth, as described in section 3.1, is a form of chemical vapour deposition. A plasma can also be used to enhance chemical reaction rates, as in plasma enhanced CVD (PECVD). Due to the increased reaction rates, lower deposition temperatures can be used, allowing process compatibility with a wider range of materials.

Silicon nitride (Si_3N_4) was deposited in an Oxford Instruments PlasmaLab 80 Plus PECVD system. For Si_3N_4 deposition, silane (SiH_4) and ammonia (NH_3) are used as gas precursors; the reaction is as follows:

$$3\,SiH_4 + 4\,NH_3 \longrightarrow Si_3N_4 + 12\,H_2 \tag{3.1}$$

The Oxford Instruments system uses a capacitively coupled parallel plate configuration, similar to the RIE set-up shown in figure 3.11b. Briefly, process gases are injected into the chamber using a shower head gas inlet to achieve deposition uniformity. An RF supply ionises the process gases, inducing a DC self-bias of the wafer electrode due to high electron mobility, which results in ions being attracted towards the sample. The sample plate is heated to 400 °C, helping to increase the reaction (or deposition) rate at the sample surface. Typical settings for a 1 µm/min Si_3N_4 deposition are as follows: 100 sccm of silane and 20 sccm of ammonia to give a chamber pressure of 1 mbar and an RF power of 20 W.

3.2.6 Plasma Cleaning/Ashing

Similar to plasma etching (section 3.2.4), plasma cleaning makes use of reactive species in order to remove contaminants and organics from a sample. As no DC bias is required, instead of a

parallel plate configuration, a barrel reactor is often used in order to achieve uniform plasma densities. Oxygen is typically used for plasma cleaning, and the actual processes that result in removal of contaminants are complex. Oxygen plasmas contain energetic ions, free radicals and short wave UV photons that all contribute to the cleaning process. These ultraviolet photons have sufficient energy to break organic bonds, whilst the oxygen species react with organic contaminants and some hydrocarbons, resulting in volatile reaction products that can be evacuated from the chamber via the vacuum pump. [117]

The use of plasmas to remove photoresist residue following etching is refereed to as plasma ashing. In this work, oxygen plasmas are employed to controllably ash resist films to a desired thickness without causing damage to encapsulated NW arrays. This would be difficult to achieve using for example, RIE, as the DC bias would cause directional physical etching of the NWs, significantly reducing the selectivity of photoresist removal.

Oxygen plasma ashing was conducted in a Quorum K1050X plasma asher. The unit consists of an evacuated barrel reactor powered by a 100 W 13.56 MHz RF supply and matching network. Oxygen flow was controlled via the external flow meter, with a typical flow of 25 sccm resulting in a chamber pressure of 1 mbar.

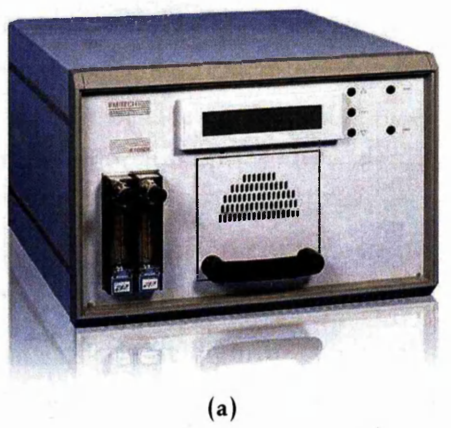

(a)

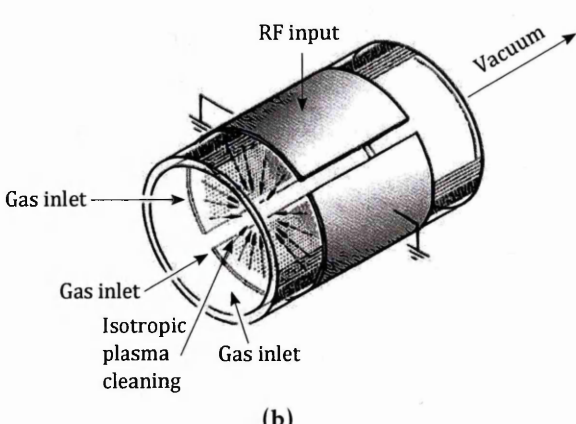

(b)

Figure 3.13: The K1050X plasma cleaner is shown in **(a)**. The the chamber door is visible in the middle of the unit, with a schematic of the barrel reactor contained inside shown in **(b)**.

3.3 Characterisation

The techniques used to characterise devices, NW properties and ZnO surface modification are detailed below. Scanning electron microscopy (SEM) and energy dispersive X-ray analysis (EDX) were used extensively to study NW morphology and the device fabrication process. Atomic force microscopy (AFM) was used in the study of surface topography and to characterise roughness. X-ray photoelectron spectroscopy (XPS) provided information about surface modification and electronic states during the functionalisation process. X-ray diffraction (XRD) and photoluminescence spectroscopy (PL) were used to investigate the structural and optical properties of NW arrays.

3.3.1 Electron Microscopy

An electron microscope is a type of microscope that uses electrons to image a sample with much higher resolution than the restriction imposed on optical microscopy by the diffraction limit. When the electron beam is scanned across the sample, as in scanning electron microscopy (SEM), a detector captures scattered secondary electrons at each point to form an image, with the magnification determined by the raster area of the beam.

Electron microscopes consist of an electron gun located at the top of a column that emits electrons using e.g. thermionic or field emission. The column contains a series of apertures and electrostatic or electromagnetic lenses that act to collimate the electron beam, which then passes through deflection optics allowing the beam spot to be scanned across the sample. An schematic of a typical column layout is shown in figure 3.14. This particular schematic represents a hot cathode field emission column emitter, as situated on the Omicron Nanoprobe system (section 3.3.5).

Hot cathode field emitters typically offer higher currents than cold cathode based SEMs, usually at the expense of image resolution. Hot cathodes are useful for applications such as e-beam lithography, where the increased beam current is desirable in order to reduce write times.

SEM images were acquired using a Hitachi S-4800 ultra high resolution scanning electron microscope (3.15). The system has a cold cathode field emission electron source and an acceleration voltage of 0.5–30 kV, adjustable in 0.1 kV increments. Magnification is variable between 30× up to 800,000×, with an ultimate resolution of 1.0 nm at 15 kV. The SEM is also fitted with an energy-dispersive X-ray detector for elemental analysis (see section 3.3.3).

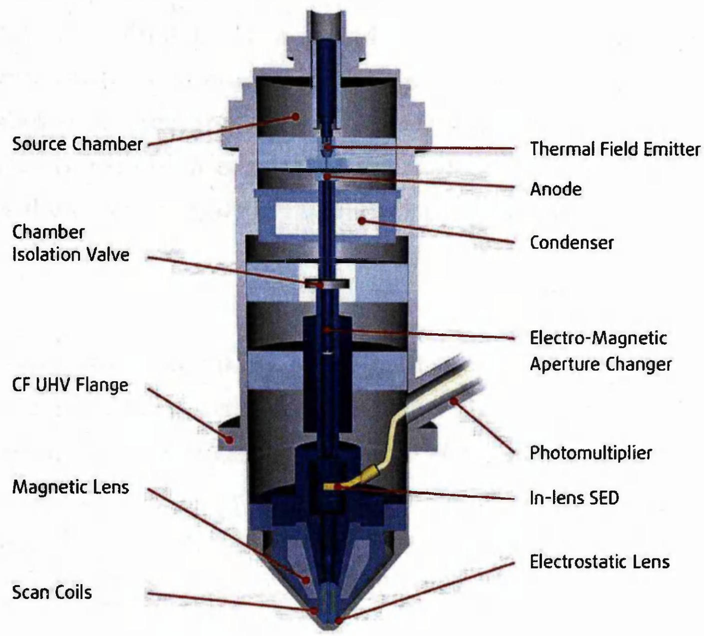

Figure 3.14: Diagram of a hot cathode SEM column showing the photomultiplier for electron detection. The condenser lens, apertures and electrostatic and magnetic lenses all serve to collect, collimate and focus the electron beam. The scan coils defect the beam for raster scanning across the sample surface. Reproduced from [15].

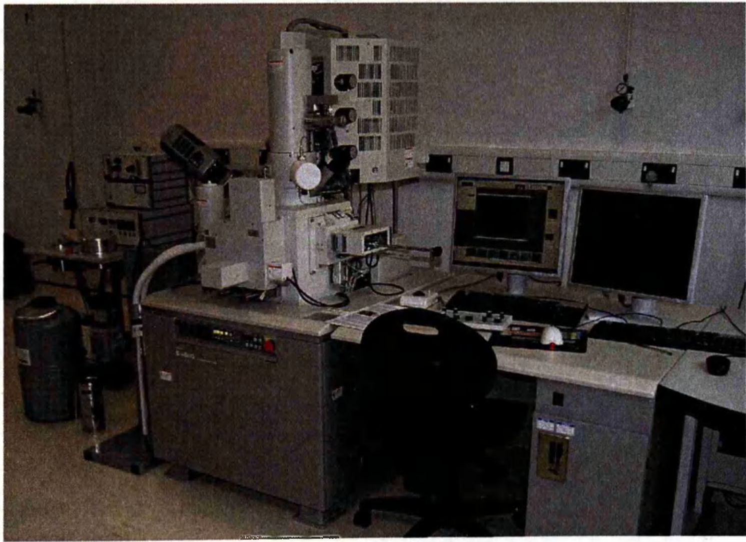

Figure 3.15: Hitachi S-4800 SEM with angled EDX detector visible on the left of the column.

3.3.2 Atomic Force Microscopy

Atomic force microscopy (AFM) is a scanning probe technique in which a sharp tip located at the end of a cantilever is scanned across a sample surface. A feedback loop is used to monitor the effect of the sample on the tip, adjusting the tip-sample separation to maintain a given set point. When scanned over an area, this produces a 3D topographical map of the sample surface. In contact mode, where the tip is in constant contact with the sample surface, the set-point is a given deflection, x, of the cantilever, which is proportional to a force between the tip and sample (Hooke's law):

$$F = -kx, \tag{3.2}$$

where k is the stiffness, or spring constant, of the cantilever. The other most common AFM mode is tapping or intermittent contact mode, in which the cantilever is oscillated above the sample close to its resonant frequency (typically in the 100 kHz range). The set-point can then either be the oscillation amplitude or frequency. As the tip is brought closer to the sample surface, intermolecular forces such as electrostatic and van der Waals (dipole) forces damp the amplitude of oscillation; the tip-sample separation is then adjusted to maintain the set-point. Tapping mode is generally more gentle and leads to less degradation of the tip when imaging hard surfaces.

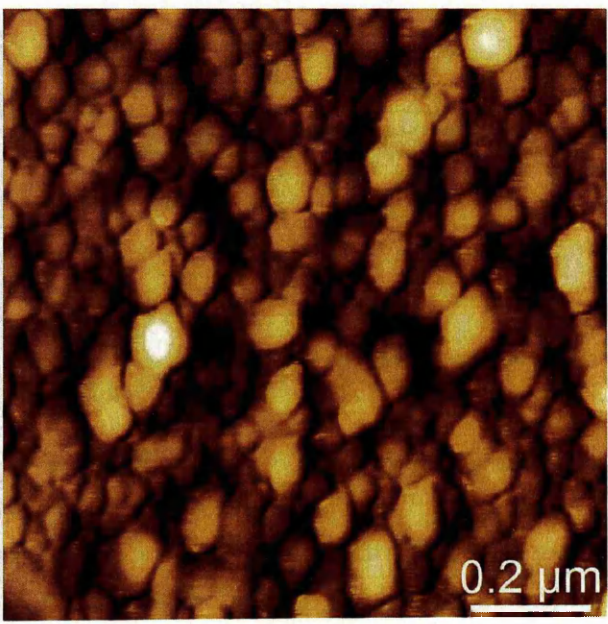

Figure 3.16: 1 µm × 1 µm AFM scan of a ZnO seed layer annealed at 650 °C. The z-range is 10 nm.

The deflection or oscillation of the cantilever is commonly measured using a laser, which must be aligned onto the end of the cantilever. The laser spot reflects off of the back of cantilever onto a photo diode (usually via a mirror). Angular displacement of the cantilever results in a shift of the reflected spot on the photodiode array.

A proportional-integral (PI) or proportional-integral-derivative (PID) controller is used to monitor the difference between the set-point and measured deflection, oscillation amplitude or frequency of the cantilever (the error signal). Feedback gains must be chosen appropriately to minimise artifacts resulting from incorrect tracking of the sample surface. For example, setting

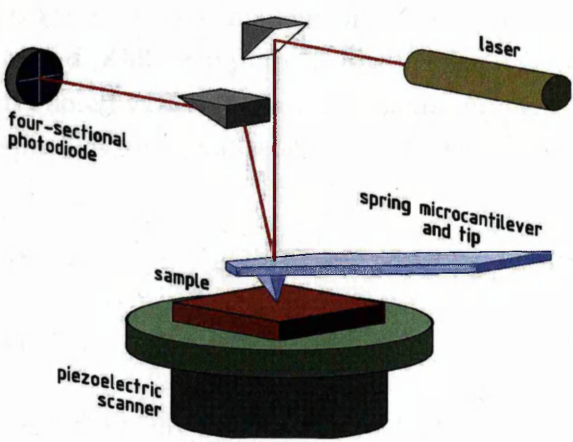

Figure 3.17: Schematic of AFM optics and components. In this set-up, the cantilever and optics are fixed in place and the sample is moved using piezoelectric scanners to form an image and modulate the tip-sample separation.

gains too low will results in sloped features representing abrupt changes in surface topography, as the feedback loop fails to adjust tip-sample separation quickly enough to retain the set-point. High gains will increase noise levels and may lead to overshoot and oscillation of the tip-sample separation around the set-point.

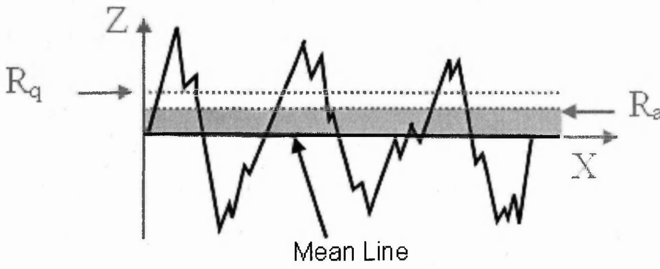

Figure 3.18: Diagram showing average (R_a) and RMS (R_q) roughness for a line profile. Levelling the line profile is equivalent to subtraction of the mean line.

Either the sample stage or cantilever is mounted on a piezoelectric scanner, allowing movement in the x,y and z directions. Resolution is controlled by adjusting the scan area of the tip. A complex interplay exists between the scan speed and feedback loop – reducing the scan speed allows more time for adjustments to be made to the tip-sample separation, potentially offering more accurate tracking of the sample surface, at the cost of increased susceptibility to noise and slower imaging. The direction of the scan may also be important; images are generally built up by tracing and retracing the tip across the sample, before moving the tip perpendicularly to generate the next line in the image. The trace and retrace direction, generally denoted the fast scan axis, has a higher resolution than the slow raster scan direction. Trace and retrace line scans can be useful for adjusting feedback gains and eliminating artifacts by ensuring that the measured topography matches in both scan directions.

Scans from SPM techniques can be analysed by viewing the height (z) values as a function of the distance between between two points drawn on the scan. This is commonly referred to as a line-profile. Figure 3.18 shows an example of a line profile with some common roughness

parameters indicated. R_a is the roughness average or the arithmetic average of absolute values and R_q is the root mean squared (RMS) roughness, which is equivalent to the standard deviation in the z height. Other often quoted values include the maximum peak height (R_p) and minimum valley depth (R_v). For line profiles, these values can be calculated using the following equations:

$$R_a = \frac{1}{n}\sum_{i=1}^{n}|z_i - \bar{z}| \quad (3.3)$$

$$R_q = \sqrt{\frac{1}{n}\sum_{i=1}^{n}(z_i - \bar{z})^2} \quad (3.5)$$

$$R_p = \max_i (z_i) \quad (3.4)$$

$$R_v = \min_i (z_i) \quad (3.6)$$

where $\bar{z}$ is the mean line shown in figure 3.18. These equations can be adapted to give areal roughness parameters which are defined in the ISO 25178 series. The corresponding areal average and RMS roughness parameters are designated S_a and S_q and are calculated by substituting a surface sum ($\sum_x \sum_y$) into equations 3.3 and 3.4.

For this work, a JPK NanoWizard II AFM was operated in AC (tapping) mode. Bruker RTESP (MPP-11100-10) probes were used at their fundamental resonance frequency. The probes have a cantilever length of 125 µm, a width of 35 µm and a thickness of 3.75 µm, resulting in a resonant frequency of around 300 kHz. The cantilevers have a rotated symmetrical tip with a nominal radius of 8 nm. Scans were recorded with sizes varying from 1 µm × 1 µm up to 100 µm × 100 µm, with scan speeds of between 0.5 Hz and 2 Hz. The set-point was kept at 0.6 V, with oscillation in free air normalised to 1 V.

SPIP (Image Metrology) software was used to analyse AFM scans. As in other scanning probe techniques, image processing is required prior to scan analysis. Scans were levelled using a plane fit followed by a line-wise bow removal, with outliers excluded from the levelling to prevent bow artifacts being introduced into the image. This ensure that the mean line shown in figure 3.18 (also refereed to as $\bar{z}$ in equations 3.3 and 3.4) is centered at $z = 0$.

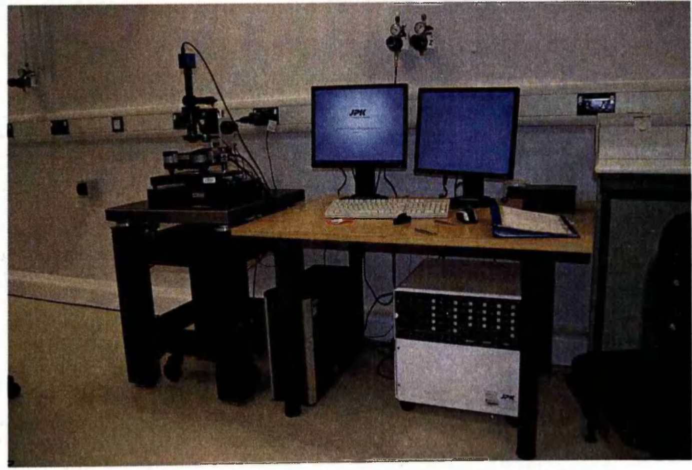

Figure 3.19: JPK NanoWizard II AFM with optical microscope for laser and tip-sample alignment.

3.3.3 Energy-dispersive X-ray Spectroscopy

Energy-dispersive X-ray spectroscopy (EDX or EDS) is a technique used for non-destructive elemental analysis. It relies on the stimulated emission of characteristic X-rays from a sample. High energy particles, typically electrons, are used to eject electrons from the core levels of atoms in the sample. Higher energy, outer shell electrons then relax to fill these previously occupied states. Since the energy differences between shells is characteristic of individual atoms, the detected X-rays can be used to identify specific elements, and also to identify their relative abundance. Characteristic X-rays are only observed if the energy of the transition required for their emission is less than the energy of the incident particles. The notation used for the characteristic X-rays (Siegbahn notation) consists of a letter corresponding to the location of the core level vacancy followed by a Greek letter designating the degree of separation between the core level and the relaxing electron. For example, Fe K_β indicates an iron atom that had its K shell ionised and subsequently filled by an electron in the M shell ($\beta = 2$). If necessary, sub-shells are identified using numerical subscripts.

When used in combination with SEM, it is possible to obtain an EDX spectra at each point in an image, allowing for the elemental mapping of a sample. Bombardment of a sample by electrons results in characteristic X-rays being emitted from a large proportion of the electron interaction volume. The interaction volume is limited by inelastic energy losses and backscattering of incident electrons, and is dependant on the energy of the electrons (acceleration voltage) and the mass and atomic distribution of the sample (figure 3.20). A theoretical expression for the straight line penetration distance, r, in a sample is given by Kanaya and Okayam [118]:

$$r\,(\mu\mathrm{m}) = \frac{2.76 \times 10^{-2} A E_0^{1.67}}{\rho Z^{0.89}}, \tag{3.7}$$

where A is the average atomic weight (g/mol), E_0 is the acceleration voltage (kV), ρ is the density of the sample ($\mathrm{g\,cm^{-3}}$) and Z is the average atomic number.

An alternative to X-ray emission following relaxation is the Auger process. The energy difference from the transition of the electron to the core level vacancy can be coupled to an additional electron (the Auger electron), either in the same or in a higher orbital. If the transferred energy is greater than the orbital binding energy, the Auger electron will be emitted. Consequently, X-ray and Auger emission are in competition, with the relative efficiency of each process dependant on the atomic number of the atoms comprising the sample. This relationship is shown in figure 3.21 for transitions into K shell vacancies. Similar plots may be obtained for L and M shell transitions. Generally, much higher X-ray intensities are attained when studying heavier elements, with $Z > 30$.

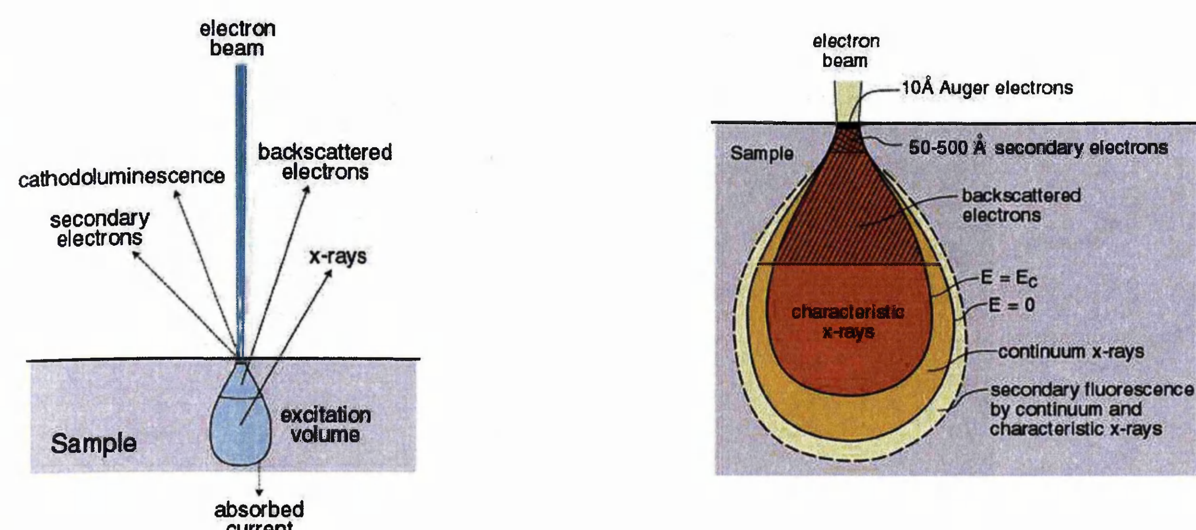

Figure 3.20: Interaction effects due to electron bombardment are shown on the left. A more detailed illustration of the interaction volume is shown on the right. Secondary electron generation and electron induced luminescence occurs close to the sample surface, whereas X-ray generation occurs in a much larger excitation volume. Backscattered electrons are scattered from a penetration distance intermediate between the two.

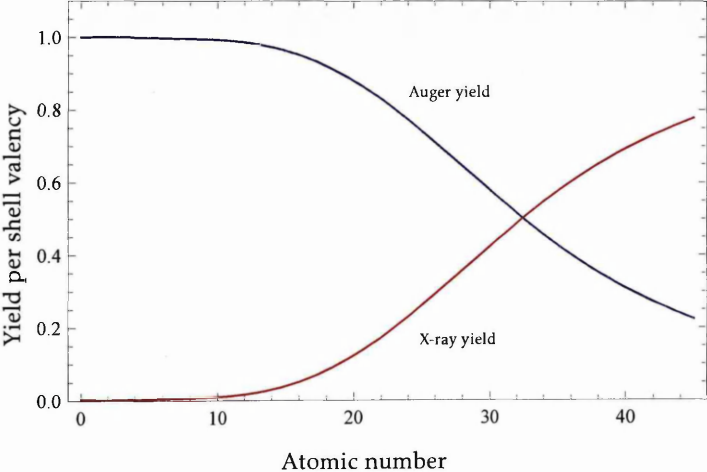

Figure 3.21: Relative efficiency of Auger and X-ray emission for K shell vacancies. A similar graph is also found for L shell transitions.

The EDX detector used was an Oxford Instruments X-Max silicon drift detector integrated into the Hitachi S-4800 SEM (figure 3.22). Typically, acceleration voltages of between 20–30 kV were used, in order to observe the higher order transitions that aid with elemental fingerprinting. If more surface sensitivity was required, this could be dropped to 5 kV while still obtaining sufficient counts. To maximise the count rate, the filament current was set to the upper limit of 20 mA.

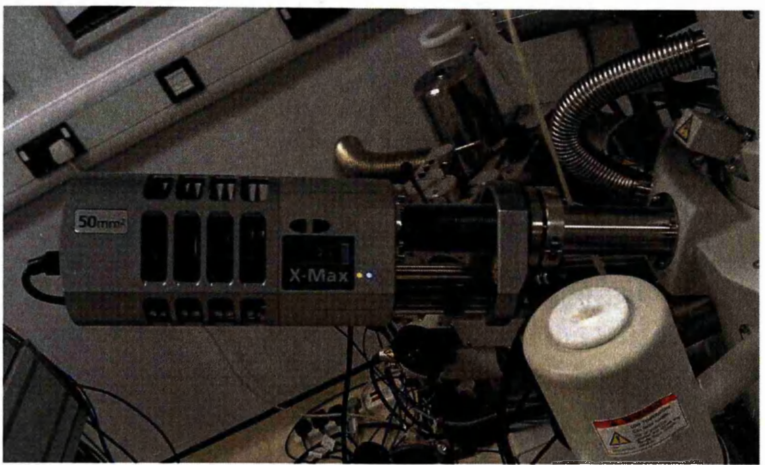

Figure 3.22: Oxford Instruments X-Max silicon drift detector.

The EDX spectra consist of characteristic X-ray peaks at the transition energies imposed on a continuum background of braking X-rays known as bremsstrahlung. These X-rays are emitted by electrons interaction with nuclei in the sample – the strong electromagnetic field close to the nucleus causes the electron to decelerate, emitting a photon with energy up to the incident electron energy. An additional large peak is also observed in the spectrum at very low energies, due to the emitted secondary electrons.

3.3.4 X-ray Photoelectron Spectroscopy

X-ray photoelectron spectroscopy (XPS) is a technique used to study elemental composition and the chemical and electronic states of materials. X-rays of a known energy are used to ionise the core levels of atoms, with the electrons escaping from the sample into vacuum. The electron escape energies are then analysed, providing information on the binding energies of the electrons. As XPS relies on the analysis of electron energies, it is necessary to be conducted under ultra-high vacuum (UHV). A typical laboratory XPS set-up comprises of the following:

- Vacuum system and main analysis chamber, with adjoining chamber for sample preparation.
- An X-ray source, typically Al K_α or Mg K_α.
- Sample stage with manipulators to control position and electron take-off angle.
- Sample heating/cleaning.
- Electron collection lens.
- Electron analyser such as a hemispherical deflection analyser.
- Electron detector/multiplier.

3.3.4.1 Photoemission

Photoemission is the emission of an electron from a solid as a result of the absorption of a photon, and the theoretical underpinnings stem from Einstein's original work on the photoelectric effect [119]. In general, electrons are emitted from a surface if the incident photons have an energy greater than the electron binding energy plus the work function of the solid. This can be

summarised in the following equation:

$$E_k = h\nu - E_I - \phi, \tag{3.8}$$

where E_k is the kinetic energy of the emitted photoelectron, E_I is the energy of the electron in the initial state, ϕ is the work function and $h\nu$ is the photon (X-ray) energy.

From Koopmans' theorem [120], the initial state energy is approximately equal to the binding energy of the electron in the solid. However, this approximation fails to account for the hole left in the solid following electron emission. This hole causes relaxation of the remaining electrons into a lower energy state, with the excess energy being carried away by the photoelectron. The result of this is an increase in the kinetic energy of the photoelectron, or conversely, an apparent decrease in the energy of the initial state (or measured binding energy).

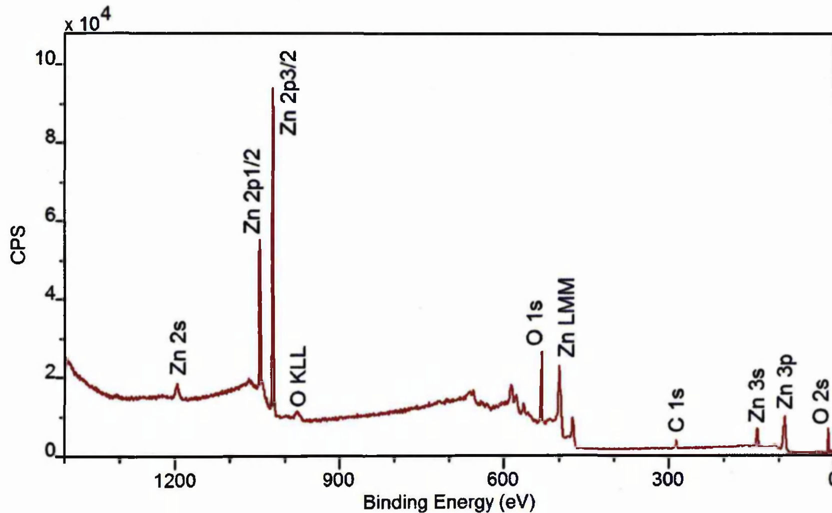

Figure 3.23: Energy distribution curve for a ZnO nanowire sample, with Auger and core level peaks labelled.

The electron analyser measures the kinetic energy of electrons escaping the sample surface, from zero up to a maximum value determined by the incident photons. The result is presented as an XPS spectrum, or energy distribution curve (EDC), as shown in figure 3.23. Although the EDC reflects the density of occupied states in the solid, it is not a direct representation due to the inelastic scattering of electrons as they propagate through the solid. Electrons that have been emitted from narrow core levels without loss of energy produce sharp discrete peaks in the EDC. These core level peaks can be used to identify specific atoms near the surface of the solid, as each element has its own set of discrete core level binding energies. Electrons that have been inelastically scattered or have otherwise had their energy altered contribute to the characteristic stepped background seen in XPS EDCs. The average distance an electron with energy E can travel through a solid without being inelastically scattered is defined as the inelastic mean free path (IMFP), designated $\lambda(E)$. As well as being a function of the electron kinetic energy, the IMFP is also material dependant. Figure 3.24 shows the "universal curve" for the variation of IMFP with electron kinetic energy for a range of materials. The IMFP initially decreases with increasing energy up to a minimum of around 50–100 eV; at low energies the electrons have insufficient

energy to cause plasmon excitation, the dominant scattering mechanism in many materials. In effect, detection of photoelectrons with energies in this range will result in an increased surface sensitivity due to the reduced IMFP. Above 100 eV, the IMFP increases steadily, with the absolute value of the IMFP varying significantly depending on material.

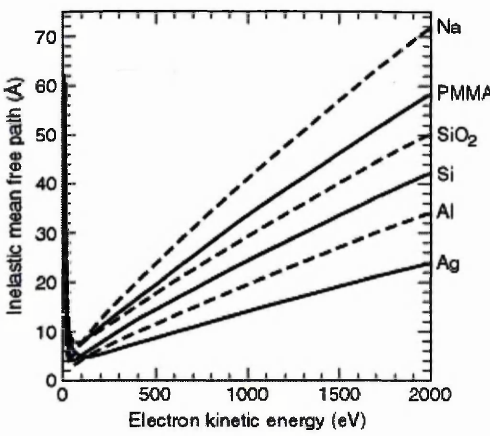

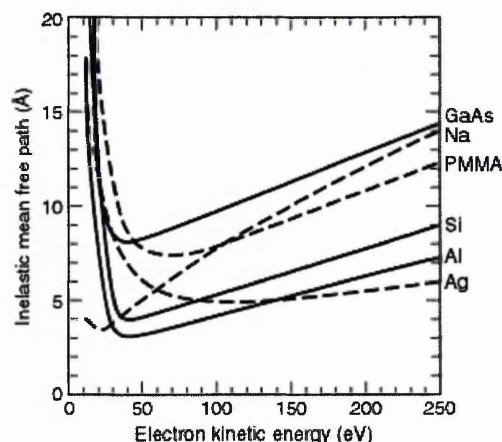

Figure 3.24: The "'universal curve"'. Electron inelastic mean free path up to 2000 eV for a range of materials. Adapted from [16].

3.3.4.2 The Three Step Model

A simple model has been proposed to explain the photoemission process, known as the Three Step Model, which neglects to account for many body effects such as electron-electron interactions and inelastic scattering. While many intricate models describing photoemission as a single quantum mechanical event have been developed, the three step model is sufficient to explain phenomena observed in the photoemission data presented in this work.

The Three Step Model describes the photoemission process in three stages, which all depend on the initial electron energy (E) and the energy of the incident photons ($h\nu$). They are as follows:

1. Photoexcitation of the electron: $P(E,h\nu)$
2. Propagation of the electron through the solid: $T(E,h\nu)$
3. The electron escaping from the surface into vacuum: $D(E,h\nu)$

The intensity of the resulting photocurrent $I(E,h\nu)$ is given by:

$$I(E,h\nu) = P(E,h\nu)\,T(E,h\nu)\,D(E,h\nu). \tag{3.9}$$

Step 1. Photoexcitation

The photoemission process is considered for an individual particle using the independent particle approximation. The unperturbed system is described by the Hamiltonian energy operator:

$$\hat{\mathbf{H}}_0 = \frac{\hat{\mathbf{p}}^2}{2m} + V(r), \tag{3.10}$$

where $\hat{\mathbf{p}}$ is the momentum operator, m is the mass (of the electron in this case) and $V(r)$ is the screening potential energy operator, which accounts for the effects of the other electrons and any surface effects.

If this system is perturbed by the absorption of a photon, the introduction of an electromagnetic wave of vector potential $\mathbf{A}$ will change the momentum operator such that:

$$\hat{\mathbf{p}}' = \hat{\mathbf{p}} + \frac{e}{c}\mathbf{A}, \tag{3.11}$$

where e is the charge on the electron and c is the speed of light. The Hamiltonian can then be written:

$$\hat{\mathbf{H}} = \frac{1}{2m}\left[\hat{\mathbf{p}} + \frac{e}{c}\mathbf{A}\right]^2 + V(r). \tag{3.12}$$

Expanding this Hamiltonian we obtain:

$$\hat{\mathbf{H}} = \frac{\hat{\mathbf{p}}^2}{2m} + V(r) + \frac{e}{2mc}(\hat{\mathbf{p}}\cdot\mathbf{A} + \mathbf{A}\cdot\hat{\mathbf{p}}) + \frac{e^2\mathbf{A}^2}{2mc^2}, \tag{3.13}$$

which can be simplified using equation 3.10 to:

$$\hat{\mathbf{H}} = \hat{\mathbf{H}}_0 + \hat{\mathbf{W}}, \tag{3.14}$$

where $\hat{\mathbf{W}}$ is the electron-radiation interaction Hamiltonian:

$$\hat{\mathbf{W}} = \frac{e}{2mc}(\hat{\mathbf{p}}\cdot\mathbf{A} + \mathbf{A}\cdot\hat{\mathbf{p}}) + \frac{e^2\mathbf{A}^2}{2mc^2}. \tag{3.15}$$

Using the dipole approximation [121], only linear terms in $\mathbf{A}$ apply, hence the interaction Hamiltonian becomes:

$$\hat{\mathbf{W}} = \frac{e}{2mc}(\hat{\mathbf{p}}\cdot\mathbf{A} + \mathbf{A}\cdot\hat{\mathbf{p}}). \tag{3.16}$$

Fermi's golden rule can be used to give the transition probability, or the transition rate, P, which is the transition probability per unit time for an electron-photon reaction from initial state $|\psi_i\rangle$ to final state $|\psi_f\rangle$:

$$P_{i\to f} = \frac{2\pi}{\hbar}\left|\langle\psi_f|\hat{\mathbf{W}}|\psi_i\rangle\right|^2 \delta\left(E_f - E_i - h\nu\right). \tag{3.17}$$

The δ function ensures that energy is conserved between the incident photon energy $h\nu$ and the transition energy $(E_f - E_i)$. The resulting photocurrent from photoexcitation is then:

$$P(E,h\nu) = \frac{2\pi}{\hbar}\sum_i\left|\langle\psi_f|\hat{\mathbf{W}}|\psi_i\rangle\right|^2 \delta\left(E_f - E_i - h\nu\right). \tag{3.18}$$

Step 2. Propagation Through the Solid

Following photoexcitation, the electrons must propagate through the solid to the surface where they will be emitted. The further the electrons travel through the solid, the more likely they are to be inelastically scattered, resulting in a alteration to the photocurrent. The electron propagation

probability, $T(E,h\nu)$, can therefore be expressed in terms of the inelastic mean free path $\lambda(E)$ (see figure 3.24). If N_0 photoexcited electrons at are at a distance x from the surface then the number of electrons, N, that actually reach the surface without being inelastically scattered is given by:

$$N = N_0 \exp\left[\frac{-x}{\lambda(E)}\right]. \tag{3.19}$$

The propagation probability is then simply:

$$T(E,h\nu) = \exp\left[\frac{-x}{\lambda(E)}\right]. \tag{3.20}$$

In effect, the electrons are exponentially attenuated with depth, giving XPS an exponentially surface weighted photocurrent.

Step 3. Escape to Vacuum

Once the electrons have propagated to the surface of the solid, they must possess enough energy to escape into vacuum. This requires sufficient energy to overcome the work function of the solid and also a momentum component normal to the surface. Simplifying this, we may assign a probability of escape from the solid $D(E)$, such that

$$D(E) = \begin{cases} 0 & \text{where } E_{norm} - E_{vac} < \phi \\ 1 & \text{where } E_{norm} - E_{vac} \geq \phi \end{cases}, \tag{3.21}$$

where E_{norm} is the surface normal energy component of the final state and E_{vac} is the vacuum level of the solid.

This leads to a final expression for the photocurrent, written as a product of the three steps described previous:

$$I(E,h\nu) = \frac{2\pi}{\hbar}\sum_i \left|\langle \psi_f | \hat{W} | \psi_i \rangle\right|^2 \delta\left(E_f - E_i - h\nu\right) \exp\left[\frac{-x}{\lambda(E)}\right] D(E). \tag{3.22}$$

3.3.4.3 Interpreting XPS Spectra

In addition to photoelectron peaks, XPS spectra contain several other features. All peaks are imposed on an characteristic stepped background of inelastically scattered secondary electrons, which increases with additional photoelectron peaks. In order to obtain quantitative information, this must be subtracted from peak area measurements using e.g. a Shirley background.

Spin Orbit Splitting and Spectroscopic Notation

Core levels with angular momentum quantum number $\ell > 0$ may exhibit splitting into doublet peaks, due to spin-orbit coupling. The total angular momentum is given by:

$$j = \ell + s, \tag{3.23}$$

where ℓ is the orbital angular moment, and s is the spin quantum number ($\pm 1/2$ for electrons). Electrons with total angular momentum $j = \ell + 1/2$ are shifted to higher binding energies that those with $j = \ell - 1/2$. The resulting difference in energies is known as spin orbit splitting. For levels with $\ell > 0$, the total angular momentum quantum number of the transition is usually given as a subscript in spectroscopic notation e.g. $2p_{3/2}$ corresponds to a core level with principal quantum number $n = 2$, angular momentum quantum number $\ell = 1$ (where $s = 0$, $p = 1$, $d = 2$, $f = 3$, $g = 4$ and so on alphabetically), and total angular momentum quantum number $j = 3/2$. When the subscript is left out, it usually indicates that both doublet states should be considered.

Plasmon Loss Peaks

For certain conductive materials, collective oscillation of the conduction band electrons can increase the probability of photoelectron energy loss at specific energies. This can appear as a series of diminishing peaks on the high binding energy side of the photoelectron peak. Problems with quantification can results from losses to the photoelectron peak and from interference of the plasmon lines with other transitions.

Shake-up and Shake-off Peaks

The photoelectron can interact with other electrons when departing the atom. An example would be excitation of a valence electron into the conduction band, thereby losing an amount of kinetic energy equal to the excitation energy. This is known as a shake-up process, and is responsible for peaks occurring on the high binding energy side of the main photoelectron peak. If the photoelectron transfers enough energy to ionise the atom, this is known as a shake-off process.

Auger Lines

Following creation of a core level hole, the atom relaxes by filling the hole via a transition from an outer level. Excess kinetic energy equivalent to the difference in energy between transition levels becomes available, which can either appear as a characteristic X-ray photon (as in EDX - see section 3.3.3), or be given to another electron, either in the same level or in a more shallow level. This can result in ejection of a second electron (the Auger electron) from the atom. For more information about the Auger process and X-ray notation, see section 3.3.5.

During XPS, Auger electrons are collected together with photoelectrons and give rise to Auger peaks. Auger peaks are generally broader than photoemission peaks, partly due to the availability of multiple final states following the transition. As Auger electron energies are dependant on the transition energy between states in the atom, their kinetic energy is independent of the excitation source. This means that it is possible to distinguish Auger peaks from core level peaks by changing the photon energy, as photoelectron peaks appear at an energy dependant on the excitation wavelength (equation 3.8). This can be achieved, for example, by switching between Al K_α (1486.7 eV) and Mg K_α (1253.6 eV) X-ray sources, which are commonly available on commercial XPS systems. The Mg K_α X-ray source offer slightly reduced ultimate energy resolution, however Al K_α is often used due to the separation between commonly investigated Auger and photoelectron transitions – due to the broad nature of the Auger lines, deconvolution of Auger and photoelectron peaks that reside at the same binding energy can be problematic.

3.3.4.4 XPS at Swansea University

XPS measurements were performed using a Vacuum Generators (VG) electron spectroscopy for chemical analysis laboratory (ESCALab). Samples were clipped onto Mo sample plates, and loaded into the main chamber, which was kept at a pressure of approximately 2×10^{-10} mbar. The samples were illuminated using a Al K_α X-ray source with an energy of 1486.7 eV. Survey scan data was collected in the binding energy range 0 eV to 1200 eV in 0.7 eV steps, at a pass energy of 50 eV. Core level spectra were typically scanned in 0.025 eV steps at a pass energy of 10 eV. All data (including the survey scans) were averaged over 5-15 passes.

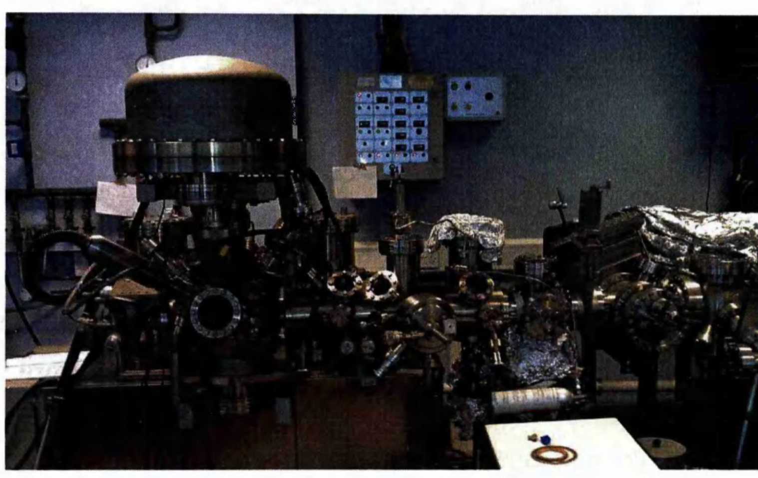

Figure 3.25: VG ESCALab XPS system. The analysis chamber is on the left, with the X-ray source visible and the hemispherical analyser located above the chamber.

3.3.4.5 XPS at the Science City Photoemission Facility

In addition, XPS data were collected at the Science City Photoemission Facility, University of Warwick. The samples were mounted on Omicron sample plates using Ta foil to ensure good electrical contact to the surface, and loaded in to the vacuum chamber. During the experiments the samples were stored in a 12-stage storage carousel, located between the preparation and main analysis chambers, for storage at pressures of less than 2×10^{-10} mbar.

XPS measurements were conducted in the main analysis chamber (base pressure 2×10^{-11} mbar), with the sample being illuminated using an XM1000 monochromatic Al K_α X-ray source (Omicron Nanotechnology), with an energy of 1486.7 eV. The measurements were conducted at room temperature and at a take-off angle of 90° with respect to the surface parallel. The photoelectrons were detected using a Sphera electron analyser (Omicron Nanotechnology), with the core levels and valence band spectra recorded using a pass energy of 10 eV (resolution approximately 0.47 eV). The spectrometer work function, resolution and binding energy scale were calibrated using the Fermi edge and $3d_{5/2}$ peak recorded from a polycrystalline Ag sample immediately prior to the commencement of the experiments. For compositional analysis, the analyser transmission function has been determined using Ag, Au and Cu foils to determine the detection efficiency across the full binding energy range to an accuracy of better than 2%.

Figure 3.26: Science City Photoemission Facility, University of Warwick. The far system is for angle resolved photoemission spectroscopy (ARPES).

3.3.4.6 Analysis of XPS Spectra

Analysis of XPS spectra was done in CasaXPS. Peak regions were given a Shirley background which formed a basis for fitting components to the core level peaks. Peaks were fitted using a mixed line shape comprising of 30% Lorentzian and 70% Gaussian, with suitable limits being imposed on peak position and FWHM to retain the validity of components between spectra. The intrinsic line shape of the photoelectron transitions is Lorentzian, owing to lifetime broadening, however a dominant contribution comes from the X-ray energy width (especially when using a non-monochromatic X-ray source) and spectrometer-induced broadening, which are accounted for by the Gaussian contribution to the line shape. Atomic concentrations were calculated using relative sensitivity factors (RSFs) to account for intensity corrections, with the fractional concentration X given by:

$$X(at\%) = \frac{(A/R)}{\sum_i \left(\frac{A_i}{R_i}\right)}, \tag{3.24}$$

where A is the peak area and R is the RSF for element i. These RSFs are empirically derived, so account for photoionisation cross-sections and other differing photon–electron and electron–electron interactions. Although the kinetic energy dependant escape depths are also naturally taken into account in these RSFs, these escape depths can be largely sample dependant (figure 3.24). A proper treatment of RSFs in order to produce accurate absolute quantification should also take into account sample or matrix dependant corrections.

3.3.5 Auger Electron Spectroscopy

Following ionisation of a core level electron, the atom is left in a metastable state. In order to screen the nuclear potential, an electron in a higher energy level promptly decays into into the core vacancy, typically in under 10^{-15} s. This is accompanied by the release of a photon (X-ray fluorescence), with an energy characteristic of the transition between energy levels (as in EDS – see section 3.3.3). It is also possible for the energy to be transferred to another electron, either in the same or in a higher orbital to the transitioning electron. If this energy is enough to eject

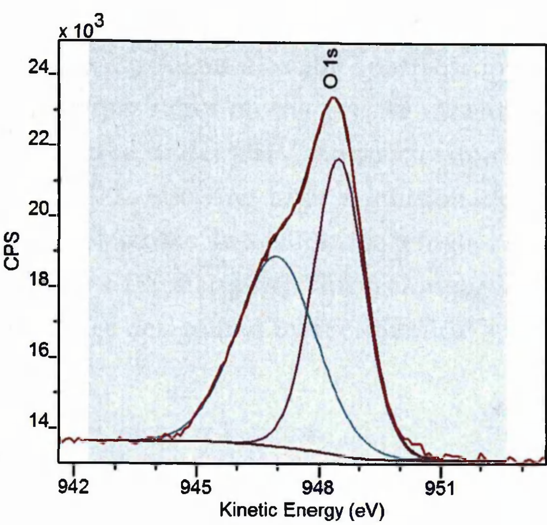

Figure 3.27: An O1s peak fitted with a Shirley background (brown) and two Gaussian/Lorentzian components (pink and blue).

the electron from the atom, this electron is known as an Auger electron, and will have a kinetic energy characteristic of the transition energy, and independent of the excitation energy used to eject the initial core level electron. The relative yield of Auger electrons to X-rays is dependant on the atomic number of the atom, as shown in figure 3.21, with Auger yield much increased at lower atomic number ($Z < 30$). In AES, EDCs are produced similar to XPS (section 3.3.4.1), with

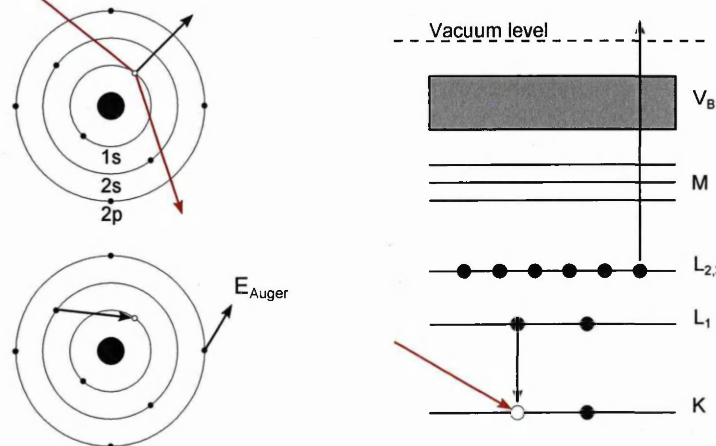

Figure 3.28: A diagram of the Auger process, with the primary electron shown in red. A vacancy is created in the 1s level. An electron from the 2s level then fills the 1s hole, with the transition energy coupled to a 2p electron which is emitted. The same process is shown on the right with an energy level diagram. This particular transition would be labelled $KL_1L_{2,3}$.

energy plotted against the intensity of electrons at the detector. A notable difference between XPS and AES EDCs is that in AES, intensity is usually plotted as a function of electron kinetic energy, as the energy of Auger electrons is independent of the excitation source, whereas in XPS binding energy is usually plotted to maintain the position of core level peaks regardless of excitation, with the location of the Auger peaks determined by the wavelength of the X-rays being used.

As Auger electrons usually have energies ranging from 50–3000 eV, the escape depth for the

electrons is very shallow. For the materials shown in figure 3.24, the IMFP for these electron energies is between 0.5–2 nm, giving Auger electron spectroscopy (AES) an extreme sensitivity to surface species. As the technique relies on the precise measurement of electron energies, it is necessary for AES to be conducted under UHV. Auger electron spectroscopy can be combined with SEM, in a similar way to EDX, allowing high resolution elemental mapping of a sample. Due to the small IMFP of Auger electrons, in addition to a higher surface sensitivity lateral resolution is also much increased over EDX mapping. This technique is referred to as scanning Auger mapping, or SAM. Auger peaks are designated by the chemical symbol followed by three letters in X-ray notation:

- First letter - initial core level vacancy location.
- Second letter - initial location of relaxing electron.
- Third letter - initial location of Auger electron (location of second hole).

For example, $KL_1L_{2,3}$ represents a 1s (K) electron being emitted, leaving behind a hole which is relaxed into by a 2s (L_1) electron, coupled to the 2p ($L_{2,3}$) Auger electron (figure 3.28).

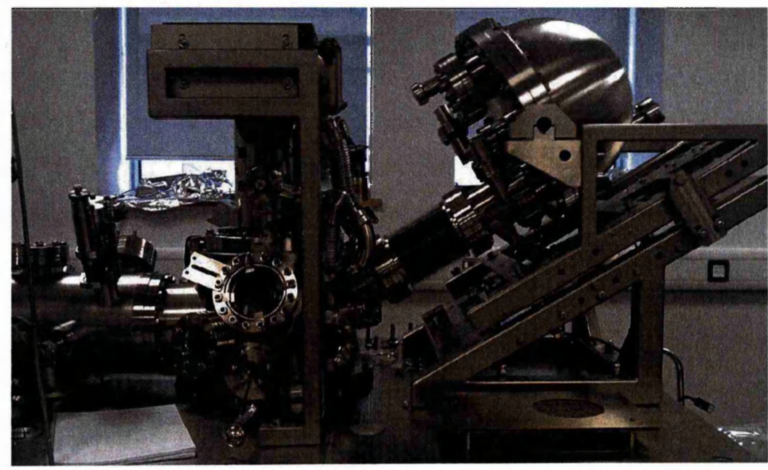

Figure 3.29: Omicron LT Nanoprobe equipped with an NanoSAM Auger electron analyser and a Zeiss GEMINI SEM column. Shown prior to bake-out.

AES was conducted in a Omicron Nanoprobe UHV system equipped with a Zeiss GEMINI SEM column and a NanoSAM electron analyser (figure 3.29). Samples were mounted on Omicron sample plates using Ta strips, then transferred into the main chamber which was maintained at around 2×10^{-10} mbar. The GEMINI column acceleration voltage was set to 5 kV, with a sample current of 1 nA.

With the NanoSAM analyser, kinetic energies can either be measured by holding the analyser pass energy constant (constant analyser energy or CAE mode), as in XPS, or by varying the pass energy whilst holding the retard ratio constant (constant retard ratio or CRR mode). The retard ratio k is defined as:

$$k = \frac{E_k - \phi_a}{E_p} \approx \frac{E_k}{E_p}, \tag{3.25}$$

where E_k is the electron kinetic energy and E_p is the pass energy. The energy resolution ΔE of the

analyser is approximated by:

$$\Delta E = E_p \cdot \left(\frac{d}{2R_0} + \alpha^2 \right), \tag{3.26}$$

where d is the slit width, R_0 is the mean hemisphere radius and α is the half angle of electrons entering the analyser in radians. From equations 3.25 and 3.26 it is clear that in CRR mode, the energy resolution is proportional to electron kinetic energy. This means CRR mode can be useful when studying peaks in the lower ($< 150\,\text{eV}$) energy range, although the sensitivity is also proportional to pass energy, leading to a reduction at lower kinetic energies. In CAE mode, the resolution is constant but the sensitivity is inversely proportional to kinetic energy, offering an improvement over CRR mode at lower kinetic energies. Scans were generally acquired with a retard ratio of 4, an energy step size of 1 eV for the survey scan and 0.2 eV for the Auger peaks.

3.3.5.1 Analysis of Auger Spectra

Auger peaks appear as small broad features on an intense background of inelastically scattered secondary electrons. As the initial ionisation energy is carried by electrons, as opposed to photons in XPS, scattering events cause the kinetic energies of the incident primary electrons to be poorly defined. The kinetic energy is consequently transferred to a core level electron in the first stage of the Auger process, resulting in ejection of core level electrons with a range of kinetic energies. This renders the core level peaks commonly seen in XPS unobservable, due to extreme broadening. As in XPS, Auger electron energy levels are sensitive to atomic binding, resulting in peaks shifts depending on the local chemical environment in the solid. However, Auger peaks are far less well defined than core level photoemission peaks, and can often contain features that span $> 100\,\text{eV}$. This is due to the complexity of the Auger process – multiple final states are available for given transitions, each with independent shifts/loss features. Instead of fitting peaks and measuring chemical shifts directly, spectra are smoothed and differentiated, then compared with "fingerprint" spectra of a known chemical environment. Once differentiated, quantitative analysis of AES spectra can be performed by measuring the peak-to-peak intensities.

Analysis of AES spectra was conducted in CasaXPS. The spectra were smoothed and then differentiated using the Savitzky-Golay quadratic polynomial differentiation method, with a smoothing width of 2 eV, necessary to remove discontinuities prior to differentiation. An example is given in figure 3.30. Peak-to-peak intensities were measured and used in a similar way to XPS peak areas to estimate atomic composition. As in XPS, it is necessary to correct for cross sections and losses using an element specific relative sensitivity factor. Fractional composition X is given by:

$$X(at\%) = \frac{(I/R)}{\sum_i \left(\frac{I_i}{R_i} \right)}, \tag{3.27}$$

where I is the measured peak-to-peak intensity and R is the relative sensitivity factor for element i.

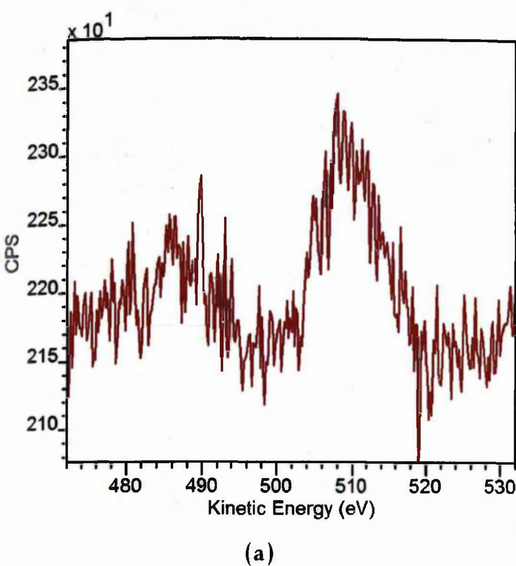

(a)

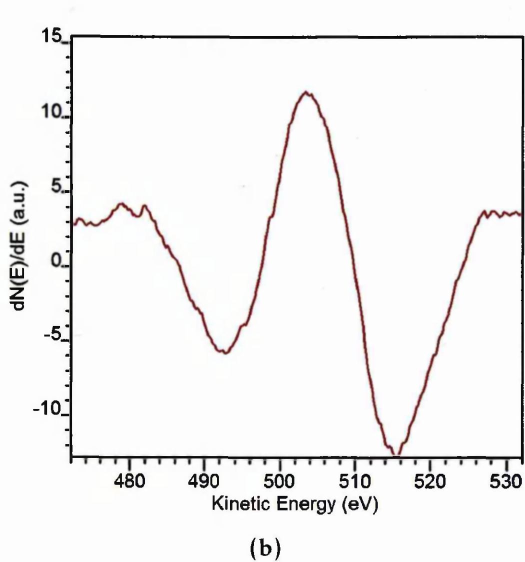

(b)

Figure 3.30: AES of the O KLL transition. In **(a)**, the peak is shown without processing. The smoothed and differentiated data is shown in **(b)**

3.3.6 Photoluminescence Spectroscopy

Photoluminescence spectroscopy (PL) is a an optical technique used to investigate the electronic structure of materials. Luminescence resulting from recombination of an electron-hole pair can be triggered by photoexcitation (photoluminescence), incident electron induced excitation (cathodoluminescence) and through electrical injection (electroluminescence). The later is primarily of interest in device applications e.g. LEDs, whereas photo and cathodoluminescence can be used to study the optical and electronic properties of a range of semiconducting and insulating materials. Luminescence occurs in direct band-gap materials and is a result of the radiative recombination of electron-hole pairs, either across the band gap or between the conduction/valence band and interband states. Two types of luminescence are possible following excitation, distinguished by the duration of emission following the cessation of incident radiation. Fluorescence typically occurs in under 10^{-8} seconds, whereas in phosphorescence re-emission can occur for up to several hours.

In this work, PL is primarily used to measure the band-gap of ZnO nanostructures. The near band edge (NBE) emission resulting from excitonic recombination across the band-gap appears on a PL spectrum as a broad peak centred around the optical band-gap (3.37 eV). This differs slightly from the electronic band-gap by the exciton binding energy (60 meV) [122], hence the designation NBE. In addition, PL is used to qualitatively investigate the interband states associated with defects in ZnO. It is well accepted that the presence of defects in ZnO nanostructures results in their visible emission, particular in the blue-green region. The PL intensity ratio of the NBE emission to the defect-related green emission is widely used to evaluate the concentration of structural and surface defects, and the quality of the ZnO crystal. [123]

Photoluminescence spectra were obtained using a 7 mW 325 nm He–Cd laser at room temperature. The set-up consisted of two optical fibre probes which acted as the source and detector.

Between the laser and the source probe a band pass filter was used to give a well defined incident wavelength and to eliminate higher order harmonics from the laser. A low pass filter at the output attenuated the reflected laser light, with the detector probe located normal to the surface and the source probe tilted at an angle of 45° relative to the detector probe, to aid with minimising laser reflection.

3.3.7 X-ray Diffraction

X-ray diffraction (XRD) is a technique used to study the crystalline and molecular structure of materials, and its discovery and development in the early 1900s essentially gave rise to the field of crystallography. Electromagnetic radiation incident on a material causes electrons to oscillate with the same frequency as the incoming beam. These charges act like Hertzian dipoles, re-radiating elastically at the same frequency (Rayleigh and Thomson scattering). If the material is crystalline, with the atoms arranged in a regular lattice, in certain directions the resulting electromagnetic waves have phase differences that result in constructive interference. This results in well defined electromagnetic waves leaving the sample along directions where path differences constructively interfere. Electromagnetic waves that interfere in this manner in crystalline materials have wavelengths that fall in the X-ray regime. Hence, a diffracted X-ray beam may be described as a beam composed of a large number of scattered X-rays mutually reinforcing one another.

As this model is hard to track mathematically, it is simpler to speak of X-rays reflecting from a series of parallel planes inside the crystal. Bragg's law describes the conditions necessary for constructive interference to occur due to reflections off of the various planes, and can be expressed as:

$$n\lambda = 2d\sin\theta, \tag{3.28}$$

where n is an integer denoting the reflection order, λ is the incident wavelength, d is the spacing between planes and θ is the acute angle between the the incident wave and the planes. If the intensity of scattered X-rays is plotted as a function of the angle θ (commonly 2θ), then very sharp intensities known as Bragg peaks are measured for certain angles where the Bragg condition is satisfied. Bragg's law can be derived heuristically, as in figure 3.31, but can also be recovered from the Laue equations [124]. For a cubic lattice of known lattice spacing a, the Bragg plane separation may be calculated using:

$$d = \frac{a}{\sqrt{h^2 + k^2 + l^2}}, \tag{3.29}$$

where h, k and l are the Miller indices of the Bragg plane in the unit cell. This can be combined with equation 3.28 to index the angle at which a Bragg peak appears to a given lattice reflection:

$$\sqrt{h^2 + k^2 + l^2} = \frac{2a\sin\theta}{n\lambda}. \tag{3.30}$$

An often-used set-up for measuring Bragg peaks for thin films is the $\theta/2\theta$ diffractometer. The

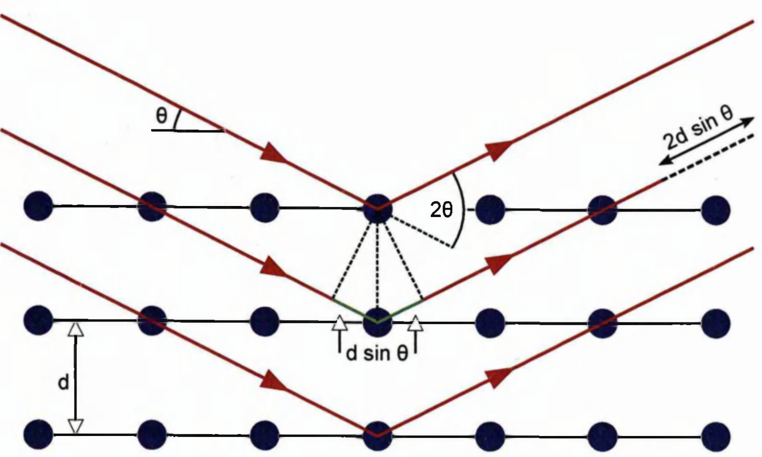

Figure 3.31: Constructive interference between lattice planes is describes by Bragg's law. Lattice sites and planes are shown in blue and black, respectively. The incident and scattered X-rays are shown in red.

sample is placed at the centre of a circle of constant radius swept out by the X-ray source and detector. The obtained 2θ plot gives information on the location of Bragg peaks, corresponding to the lattice parameters, and also on the relative intensities of different peaks, which can indicate a preferred orientation or texture. If the lattice parameters are know, then peak shifts can give precise information on lattice strain.

Crystallographic information was gathered using a Panalytical X'Pert Pro MRD X-ray diffractometer equipped with a Cu K_α hybrid monochromator and a solid state PIXcel detector. 2θ scans were conducted in the coupled scan configuration, with the X-ray source fixed and ω (the angle of the sample in the same plane as θ) moving at half the angular velocity of the detector. The sample angle ω is set almost equal to θ, although a small offset is usually necessary to ensure that when $\theta = 0$, the X-ray beam is parallel to the sample surface.

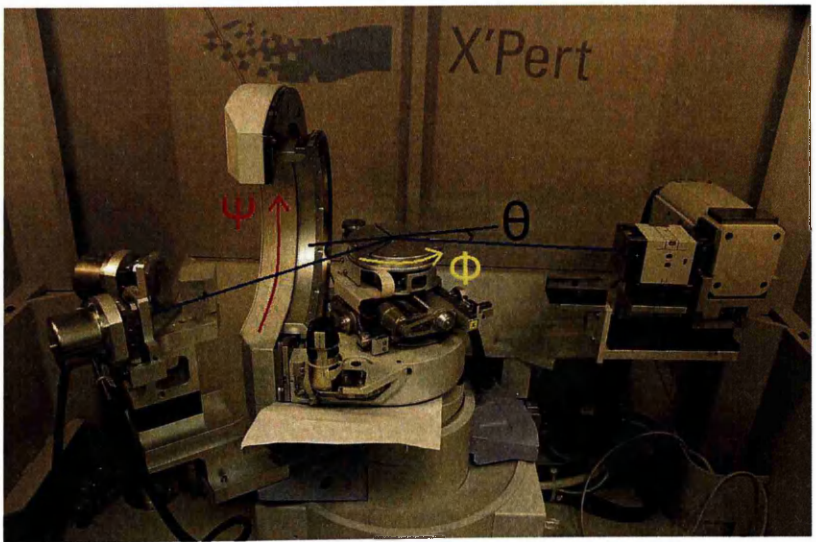

Figure 3.32: Goniometer showing the axis of rotation. In the current position, the sample stage is at $\psi = \pm 90°$, with the ϕ angle (the rotation of the stage) being arbitrary, depending on how the sample is mounted.

3.3.7.1 Determination of Size and Strain

Diffraction peaks are commonly fitted using a variety of line shapes. Although Gaussian and Lorentzian line shapes are sometimes used, diffraction peaks are usually approximated using Voigt profiles and Pearson VII functions. The Voigt profile is a convolution of a Gaussian and Lorentzian distribution and the Pearson VII function is essentially a Lorentzian distribution raised to the power m. When $m = 1$ the standard Lorentzian distribution is recovered, whereas as $m \rightarrow \infty$, the function approximates a Gaussian distribution (in practice $m > 10$). Similarly for the Voigt profile, limiting cases give full Lorentzian and Gaussian distributions.

Peak height indicates total amount of constructive interference, with the peak position indicating the lattice plane spacing. If the lattice spacing is not constant in the material due to e.g. non uniform internal stresses, essentially a range of lattice spacings are present to fulfil the Bragg diffraction criteria. This results in observed peak broadening. In practice, there are several other peak broadening contributions that are generally divided into instrumental and samples contributions. Instrumental broadening arises from factors such as the X-ray energy width, the finite size of the X-ray source, the active diffraction volume in the sample and axial diverge and other alignment issues with the diffractometer. Sample effects include inhomogeneous strain as mentioned, other lattice distortions such as dislocations and stacking faults, concentration gradients in non-stoichiometric compounds and, importantly, crystallite/diffraction domain size. The way in which these broadening contributions are combined depends on the line shape of the diffraction peaks. For example, for Lorentzian line shapes, broadening contributions may simply be summed.

The coherent diffraction domain size results in peak broadening as the order of lattice plane reflections n essentially becomes finite. At a minimum, $n = 2$ is required for first order interference. As the number of lattice planes is increased, the interference becomes increasingly precise, leading to a reduced peak width. The Scherrer equation captures this behaviour and allows a mean lower bound to be set on the size of the crystallites comprising a sample:

$$D = \frac{K\lambda}{\beta \cos\theta}, \tag{3.31}$$

where D is the mean size of the crystallites, K is a dimensionless shape factor with a value close to unity, λ is the X-ray wavelength, β is the FWHM following corrections for instrumental broadening (in radians) and θ is the Bragg angle. The Scherrer equation is limited to grain sizes smaller than around 100 nm, above which n becomes essentially infinite, although the practical size limit depends on the inherent instrumental broadening.

The Scherrer equation assumes all broadening present in the sample is due to the diffraction domain size. Given several assumptions, it is possible to separate the size and inhomogeneous strain broadening contributions. A method for doing this is known as a Williamson-Hall plot. Strain broadening is related to the Bragg angle θ and average sample strain ε by the following equation [125]:

$$\beta = 4\varepsilon \tan\theta\,. \tag{3.32}$$

Assuming the peak shape is Lorentzian, the broadening contributions can be summed to give:

$$\beta = \frac{k\lambda}{D\cos\theta} + 4\varepsilon\tan\theta\,. \tag{3.33}$$

By rearranging the above equation the Williamson-Hall equations are obtained:

$$\beta\cos\theta = \frac{k\lambda}{D} + 4\varepsilon\sin\theta\,. \tag{3.34}$$

If the diffraction angle for several Bragg peaks is plotted with $4\sin\theta$ along the x-axis and $\beta\cos\theta$ on the y-axis, a linear fit allows the strain, ε, to be estimated from the gradient and the crystalline size, D, to be extracted from the y-intercept (figure 3.33). The Williamson-Hall equations derived

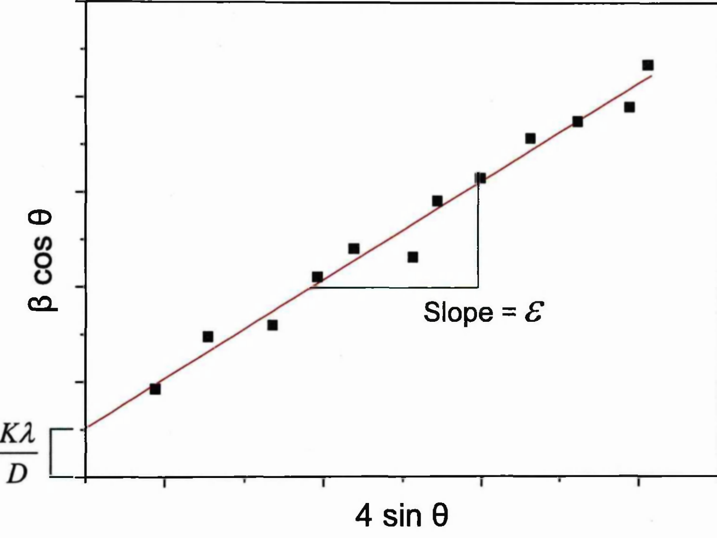

Figure 3.33: Williamson-Hall plot showing how the strain (ε) and size (D) components are obtained from the peak position (θ) and FWHM (β).

above are only valid for Lorentzian diffraction peaks as the broadening contribution are summed. Several other assumption are inherent in the Williamson-Hall approach, such as uniform strain distribution and isotropic crystallite size. These must be carefully considered if accurate absolute values are to be obtained.

3.3.7.2 Texture Analysis

The degree of preferred orientation of crystallites in a polycrystalline films is known as the texture. In thin-films, there are two distinct kinds of texturing: fiber (or monoaxial) texture and biaxial texture. In the case of fiber texture, the majority of crystallites are preferentially orientated with respect to a certain direction in the sample, most commonly the substrate normal. This leaves a degree of rotational freedom, which is usually the twist or rotation of the crystallites in-plane with respect to the substrate. In biaxial texturing the crystallite rotation is also preferred. Strong biaxial texturing can be considered a prelude to epitaxy, and the transition between a biaxially textured film and an epitaxial film is a continuous one. The degree of texturing usually evolves during the growth of thin-films.

Texture analysis of thin films can be conducted using HRXRD. In this work, the two methods used to determine preferred orientation are as follows:

- **Rocking Curve**: Keep 2θ angle fixed, perform ω scan. FWHM of peak decreases with stronger texture.
- **Pole figure**: Keep 2θ angle fixed, rotate sample to perform ϕ scans at various tilt angles, ψ. Texture distribution for a fixed Bragg reflection.

In both cases, the orientation is being measured for a given 2θ angle (or Bragg plane), so in multi-layered samples of differing materials, several pole figures or rocking curves may be required to give information on how texturing is transferred through layers.

Chapter 4

Nanowire Growth

This chapter outlines the work done on the growth and optimisation of vertical zinc oxide nanowire (ZnO NW) arrays for device incorporation. In the following sections, three methods for seeding and patterning the growth are presented, with an emphasis on the ability to electrically contact the underside of the NW arrays, either directly through the substrate or through deposition of a conductive thin film.

4.1 Introduction

All three methods utilise high temperature vapour phase growth, as detailed in section 3.1. Briefly, graphite is used to thermally reduce zinc oxide in a tube furnace, under low pressure argon flow. The argon carries the zinc vapour downstream, where it condenses in a cooler part of the furnace. Along with the argon carrier, a low concentration of oxygen is also introduced to reoxidise the zinc. A brief description of the differing growth methods follows:

- **Seed layer growth:** A thin seed layer of zinc oxide is magnetron sputtered onto the silicon surface to aid with Zn/ZnO nucleation. The array may then be contacted through the conductive silicon substrate.
- **Roughness assisted growth:** The silicon is roughened using wet and dry etching in order to promote nucleation, which occurs directly on the silicon surface with no need for any interfacial layers. The conductive silicon substrate acts as a contact to the base of the NW array.
- **Growth on conductive thin films:** A thin (100 nm) layer of conductive material is sputtered onto the substrate. The conductive layer nucleates vapour and also allows a direct metal-semiconductor contact to be made to the base of the NW array.

In addition to the contact methods proposed above, direct probing of at ZnO layer formed at the base of the array prior to growth of NWs could also be a viable contacting method for all three growth techniques. This base layer growth contacting has been investigated on α-Al_2O_3 with favourable results [82]. As both seed layer and conductive thin film approaches rely on deposition processes, etch back or lift-off processes may be employed to pattern and restrict NW growth. In the case of roughness assisted growth, masking of the substrate prior to etching is used to achieve a similar result.

4.2 Seed Layer Assisted Growth

Previous work conducted at Swansea University on the growth of vapour phase ZnO NWs using sputtered seed layers on Si found this approach to be largely ineffectual [126–128]. Lord reported difficulties in obtaining a *c*-axis orientated seed layer due to the large lattice mismatch with Si. The resulting growth was found to be of poor quality when compared with lattice matched substrates and solution seed layers. A significant improvement in the quality and alignment of hydrothermal NW/film growth has been reported by annealing of Zn/ZnO seed layers, either during deposition or postdeposition before NW growth [7,85,129]. This has been found to drastically improve the *c*-axis alignment and crystalline properties of the seed layers. However, this annealing is commonly conducted at relatively low temperatures when compared to vapour-phase NW growth.

An alternative approach, investigated here, relies on the postdeposition annealing of radio frequency magnetron sputtered ZnO films at temperatures above those reached during the vapour phase NW growth process. The main aim of this approach is to increase the crystalline quality of the ZnO seed, resulting in improvements in NW quality and alignment. However, with device applications in mind, the effect of the annealing on charge transport through the seed layer and across the ZnO/Si and polycrystalline/single crystal ZnO interfaces will also be of significance. Improved growth is expected to be accomplished by achieving strong *c*-axis orientation of crystallites in the seed layer. Generally, thinner seed layers are favoured due to their ability to retain *c*-axis aligned texturing from the flat Si substrate [7, 130]. However, if the seed layers become too thin, this is expected to greatly increase strain and lessen the buffering effect on the Si substrate lattice mismatch.

This work was conducted in collaboration. Detailed results can be found in the PhD thesis of Nathan Smith and in a joint publication entitled "Improving the conduction path through the ZnO nanowire/Si interface for vertical device integration" currently under consideration at ACS Applied Materials and Interfaces. The key results are summarised below.

4.2.1 Experimental

Diced pieces of Si (1 0 0) measuring 10 mm×7 mm were used as the base substrate for NW growth. The wafer properties are as follows:

- Thickness: 610–640 µm
- Dopant: Boron (p-type)
- Doping concentration: $2\times10^{14}\,cm^{-3}$
- Resistivity: 50–70 Ω cm

Following cleaning with acetone and IPA, ZnO seed layers were deposited on the substrates using room temperature RF magnetron sputtering (Lesker PVD 75; section 3.2.5.1) to the desired thickness, as measured by a quartz crystal microbalance. An Ar/O_2 gas mix (10:1) was used in order to retain stoichiometry prior to annealing, giving a chamber pressure of 10^{-3} mbar and a deposition rate of approximately 0.3 Å/s at a target power density of 3.25 W/cm^2.

4.2.2 Summary

- XRD: (0 0 2) peak intensity remains more or less constant in the range 600–775 °C, indicating that c-axis optimisation occurs at temperatures lower than the growth temperature. (0 0 2) peak shift to a higher 2θ angle with annealing temperature was confirmed, corresponding to a reduction in lattice spacing at higher annealing temperatures. No correlation with FWHM was found.
- AFM scans showed the morphology of the films and roughness values to remain consistent through the range of annealing temperatures.
- The PL data showed out of phase oscillation of the NBE peak and defect band intensity with increased annealing temperature. A tentative explanation for the defect quenching is offered, however further work is required to investigate the mechanisms responsible for the NBE and defect intensity variations.
- Electrical measurements taken through the substrate using an STM tip showed Ohmic behaviour, in contrast to what was observed in the preliminary findings. They also indicated a relationship between the relative defect band intensity and the resistance of the junction, however this was the opposite to what was measured using probe station I–V measurements.
- Nanowire growth on annealed seed layers was found to be substantially different to that conducted on the as-deposited films. However, NW growth remained consistent across the range of annealing temperatures, and all resulting growth was found to be of a poor quality and unsuitable for vertical device integration. Growth on the as-deposited sample seemed to occur at the apex of grains, whereas growth on the annealed seeds seemed to be confined to grain boundaries.
- Nanoprobe electrical measurements on individual NWs conducted through the substrate showed significant variation, and in some cases a decrease, from the values measured on the bare seed layers. Although the annealed samples showed a slightly lower resistance, this indicates postdeposition annealing has limited effect on charge transport properties through the substrate. More work would be required to quantify the relative contributions from Si/ZnO interface, ZnO NW and any interface could exist between seed layer and NW.

In summary, postdeposition annealing was found to have an effect on, but not substantially improve, the growth of NWs on ZnO seed layers. A relationship between the ambiguous deep level emission band and charge transport through the seed layer was demonstrated, which could have important implications for contacts and heterojunctions formed at the base of NW arrays.

4.3 Roughness Assisted Growth

It has been shown that topographical alterations to the substrate surface can be used in order to promote NW growth during thermal evaporation. A proposed mechanism for increased nucleation involves surface irregularities present on the substrate acting to limit the free movement of adsorbed Zn atoms, due to the increased energy barrier associated with migration across the surface. [80,131]

Previous studies have focused on substrate roughening using mechanical methods and wet chemical etching. The degree of process control using the above methods is limited, with little work carried out on the optimization of etching parameters to obtain high quality NWs. The resulting growth on Si exhibits poor alignment compared to seed layer grown NWs. The degree of residual contamination present on the substrate following mechanical and wet etching techniques, and the effect of this on subsequent NW growth, is also unclear. [5,80]

In this study, catalyst-free ZnO NW growth is investigated through topographical alterations to the substrate surfaces, by both wet chemical and dry plasma etching. Using this approach, single crystal ZnO NWs are grown directly on a Si substrate without the use of seed layers, allowing direct nucleation of ZnO vapour onto the substrate, potentially avoiding boundaries present at the seed layer interface. The use of mature dry etching technology allows a high degree of process control and the ability to rapidly and uniformly etch large scale substrate with a high degree of reproducibility. Also, as a subtractive process, the need for subsequent fabrication steps associated with additive seed layer patterning is avoided. Systematic optimisation of dry etch parameters allows for an improvement in NW growth for vertical integration.

This work was conducted in collaboration with Nathan Smith and has been published in the Elsevier journal Materials Science and Engineering B under the title "Growth of ZnO nanowire arrays directly onto Si via substrate topographical adjustments using both wet chemical and dry etching methods" [132].

4.3.1 Experimental

Both wet and dry (plasma) etching recipes were studied systematically, with the viability of each etch recipe determined from SEM analysis of the resulting NW growth. Wet chemical etching of Si was conducted using potassium hydroxide (KOH) solution with concentrations of 20% and 50% w/w. The Si substrates were suspended in the KOH solution which was stirred constantly at temperatures from 50 °C to 80 °C. Etching was performed for durations ranging from 30 seconds to 20 minutes.

Dry anisotropic etching of Si was performed using fluorine based chemistry in an Oxford Instruments Plasma Lab 80+ reactive ion etching system (RIE; section 3.2.4.1). Specifically, etching plasmas containing SF_6 and CHF_3 were employed, which have been shown to proportionally increase and decrease resulting surface roughness respectively [133,134]. It has also been demonstrated that the addition of O_2 drastically increases the number of fluorine radicals, and consequently the etch rate, by preventing recombination of reaction products to form SF_6. As

the concentration of oxygen atoms is increased, the etch rate begins to decrease due to increased competition from chemisorbed oxygen on the Si surface. Increasing RF power results in a higher etchant ion flux on the substrate surface, therefore increasing the etch rate [135]. However, the surface roughness reaches a maximum and is decreased at high etch rates. Reaction chamber pressure also has an effect on the scale of the surface roughness, although the relationship is less well understood [136]. In summary, the parameters considered were SF_6, CHF_3 and O_2 flow rates, chamber pressure, RF power and etch duration.

Following etching, selected substrates were analysed using AFM. Scans were conducted in intermittent contact mode, using a tip with a radius of curvature of 20 nm in ambient conditions. Several 10 µm × 10 µm scans were performed on each substrate, with surface roughness values (average, RMS and peak-valley) being averaged over five 1 µm × 1 µm areas.

Zinc oxide NWs were grown on the etched substrates using the standard double tube furnace procedure, as described at the start of the chapter. The NW dimensions were measured using SEM, with crystallographic and optical information being provided by XRD and PL, respectively. For more information on equipment and techniques, see chapter 3.

4.3.2 Results

As mentioned, a systematic approach was taken to optimise each etch recipe, with undeveloped etches frequently leading to uncontrolled growth of nanostructures, or NWs exhibiting poor alignment, non-hexagonal termination and large variations in dimension (4.1). Conversely, etches resulting in vertically aligned NWs that appeared to be crystallized in the wurtzite phase (hexagonal termination) were considered viable. In this work, one sample from each of these successfully developed etch recipes was analysed. A sample of unprocessed Si is used as a basis for comparison. Details of the sample processing can be seen in Table 4.1.

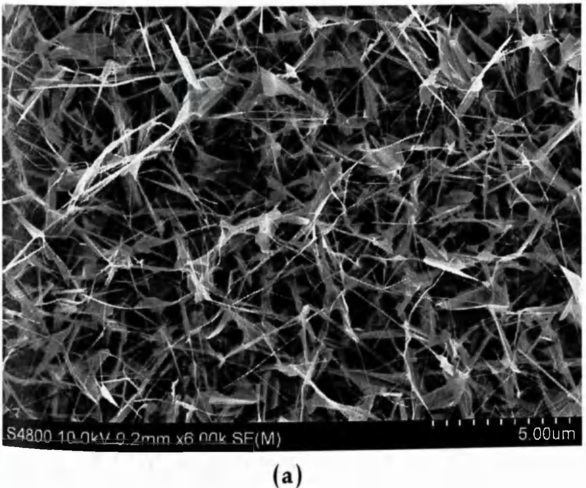

(a)

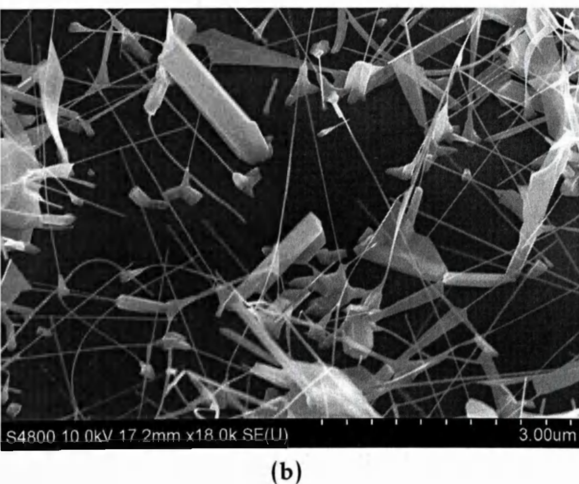

(b)

Figure 4.1: SEM images of poor quality ZnO NW growth obtained during optimisation experiments.It is interesting to note that in (b), not base growth ZnO layer is observed, indicating island type nucleation.

Table 4.1: Summary of samples and their processing conditions.

Sample	Process	Etch conditions
A	Unprocessed	Unprocessed silicon.
B	RI etching	SF_6: 40 sccm, O_2: 5 sccm, 75 mTorr, 150 W, 10 mins.
C	RI etching	SF_6: 30 sccm, CHF_3: 10 sccm, O_2: 5 sccm, 95 mTorr, 100 W, 10 mins.
D	KOH etching	50% concentration, 70 °C, 7 mins.
E	KOH etching	20% concentration, 70 °C, 6 mins.

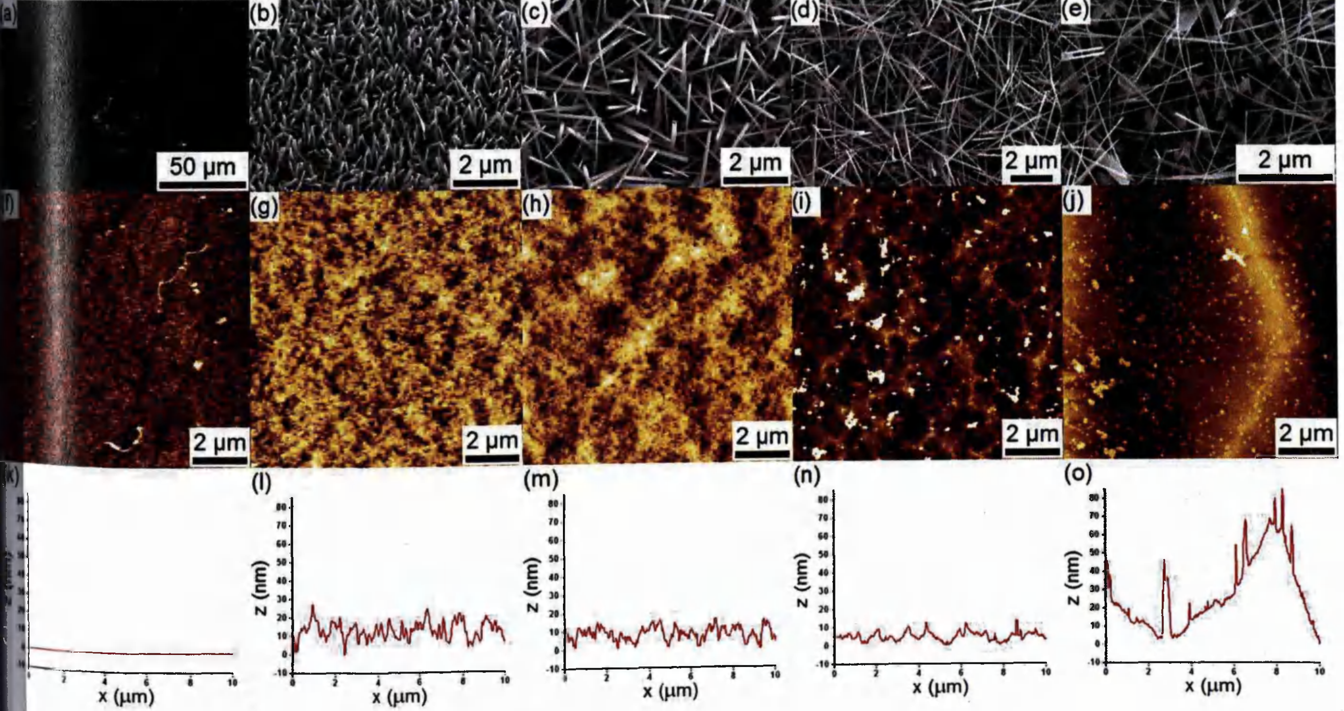

Figure 4.2: (a-e) SEM images of samples A-E respectively (f-j) 10 μm × 10 μm AFM scans of samples A-E respectively. Z-range of AFM scans are shown in table 4.2. (k-o) Typical line scans from AFM scans f-j respectively.

4.3.2.1 Electron microscopy and atomic force microscopy

Figure 4.2 shows SEM images of the NW growth, with corresponding AFM scans of the substrate surface. It is apparent that the surface topography is inherently different for each etch recipe used, and that each etch recipe yields NWs with differing morphology and orientation. Surface roughness values taken from AFM scans are shown in table 4.2, along with characteristics of the NW growth. Nanowire measurements for unprocessed Si were not made due to limited ZnO nucleation (figure 4.2a).

Atomic force microscopy analysis of the KOH etched substrates showed greatly increased z-range and roughness values as indicated in table 4.2. The large peak-valley roughness (S_t) is attributed to the evident surface debris caused by re-deposition of etched material or impurities present in the etch solution. A lateral gradient is visible in figure 4.2j, despite identical plane correction across all scans. Cross-sectional profiling, shown in figure 4.2o, reveals considerable preferential etching and removal of substrate material, as expected from the increased etch rate at lower KOH concentrations (20% w/w) [110]. The early formation of these features is detailed by cross-sectional analysis (figure 4.2n), with similar small scale pyramidal features present. These sloped features are caused by the preferential etching of Si (1 0 0) planes in KOH, leading to the formation of pyramidal structures [111] due to anisotropic etching along the ⟨1 1 1⟩ (and higher order) facets. This preferential etching leads to significant exposure of lattice planes other than the Si (1 0 0) surface, resulting in the growth of nanostructures with differing morphologies, which are randomly oriented with respect to the Si substrate (figure 4.2d-e) [137, 138]. Lower RMS and peak-valley roughness values are given for the plasma etched substrates compared with KOH etching, with the higher power SF_6 based recipe (sample B) resulting in a reduced roughness when compared with the SF_6/CHF_3 plasma mix (sample C). This could be explained by the higher chamber pressure limiting the ion flux over neutral flux ratio [135]. The NW density is significantly higher for sample B, suggesting increased nucleation. AFM line profiles shown in figure 4.2l-m reveal the highly corrugated surface resulting from plasma etching, which could assist with localised vapour trapping and consequent nucleation. Although average NW diameters remain similar across samples, a large increase in the standard deviation of widths is seen with the decrease in NW quality evident in figure 4.2a-e. As mentioned, differences in local crystallographic orientation on the scale of the NW diameters would lead to the observed variation in morphology. In addition, the degree of NW growth coverage and uniformity across the substrate was observed to be much improved for growths employing the plasma etched substrates.

Sample D exhibits NW growth with poor orientation, comparable to that reported previously by S. Ho et al. on KOH etched Si substrates [5]. Significant improvements in NW orientation, density and diameter variation were achieved through optimisation of plasma etching parameters (sample B). Further analysis of the substrate surfaces shown in figure 4.2g-j is achieved using power spectral density plots, with each etch compared in figure 4.3. This analysis technique looks at the intensity of particular frequencies in reciprocal space, providing an understanding of the composition of the surface topography in terms of component size [139]. The KOH etched samples have a PSD approximately an order of magnitude larger than the plasma etched samples

Table 4.2: Roughness and NW morphology measurements.

Sample	AFM z-range (nm)	Average roughness S_a (nm)	RMS roughness S_q (nm)	Peak-valley roughness S_t (nm)	Nanowire density (µm^{-2})	Avg. NW diameter (nm)	St. Dev. of NW diameter (nm)
A	12.66	0.24	0.34	19.02	–	–	–
B	58.42	2.89	3.66	23.90	16.57	61.7	6.7
C	38.24	2.96	3.71	24.82	5.93	79.6	7.9
D	115.1	3.84	7.88	68.75	6.04	75.0	17.7
E	161.6	4.69	7.15	43.03	2.97	59.3	40.1

in the 100 nm to 1 µm component range (indicated by the vertical dashed lines in figure 4.3). In addition, sample E shows a much higher prevalence of low frequency components corresponding to the pyramidal formation visible in figure 4.2j.

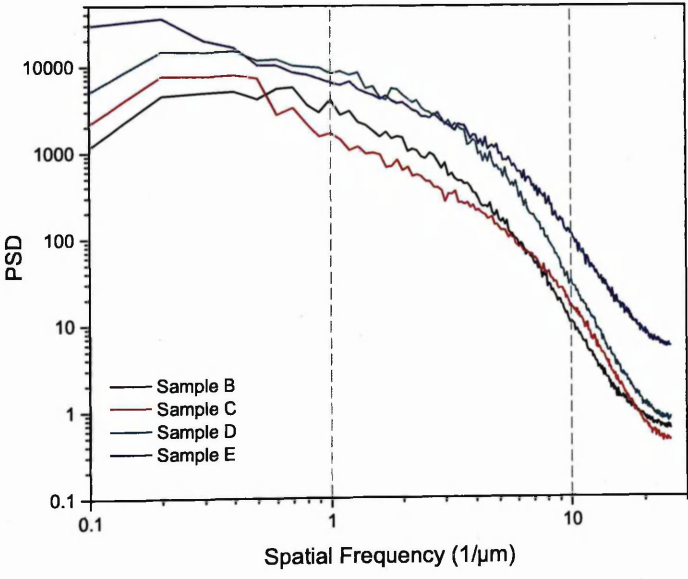

Figure 4.3: Power spectral density plot comparing etched samples.

Both surface debris and varying NW morphologies would be undesirable when constructing ensemble vertical NW devices. Furthermore, devices likely require a high NW density with a uniform NW diameter. These characteristics can be achieved using SF_6/O_2 plasma etched substrates. Consequently, for the remainder of this study, only further analysis of sample B will be presented. Larger SEM images of the growth on sample B are shown in figure 4.4. In order for successful device incorporation, the NWs grown from this surface enhanced method must exhibit typical ZnO NW characteristics, such as crystalline *c*-axis growth with expected optical

response. Furthermore, it is important to verify the growth is not related to surface residue or chemical modification resulting from the dry etching process. Also, due to the direct nucleation of vapour onto the Si substrate, the growth of ZnO NWs could be considerably different for surface enhanced growth, with island (Volmer-Weber) formation replacing the Stranski-Krastanov type growth typically seen on seeded substrates [140, 141].

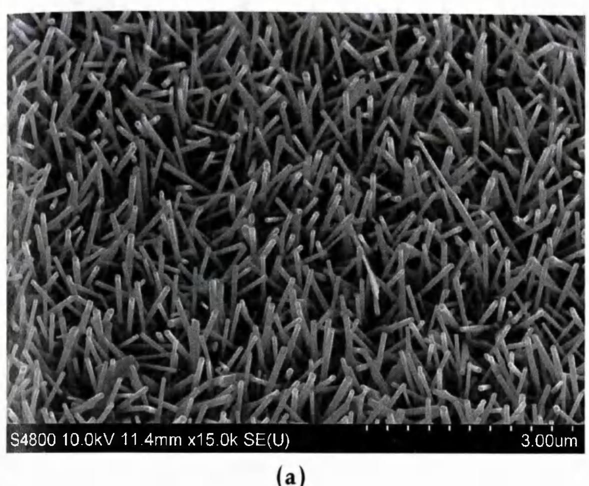

(a)

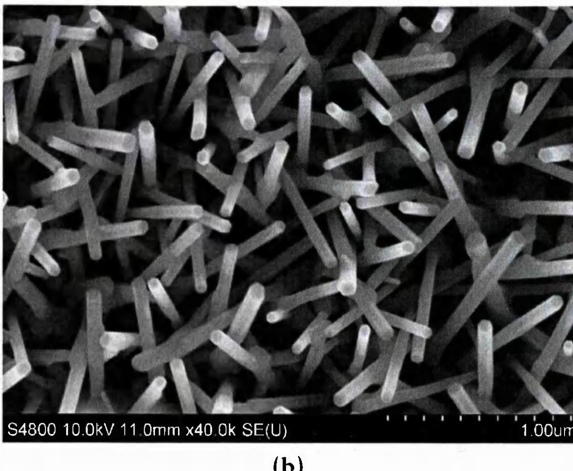

(b)

Figure 4.4: SEM images of resulting NW growth on sample B, which was dry etched using a SF_6/O_2 plasma.

4.3.2.2 X-ray diffraction

X-ray diffraction was employed to assess the crystalline quality and orientation of the NWs. A 2θ scan of sample B is displayed in figure 4.5a, showings diffraction peaks other than the *c*-axis aligned (0 0 2) reflection, which can also be indexed to wurtzite ZnO with lattice parameters $a = 0.3244$nm and $c = 0.5197$nm. It is possible that these peaks relate to NW growth occurring at an angle with respect to the surface normal, although the (1 0 0) peak would only be observed for NWs running parallel with the substrate, which would seem unlikely due to the high density of growth observed in figure SEM. The (1 0 1) reflection would be measured for NWs growing along the [0 0 1] direction tilted at an angle of 31.97° with respect to the substrate, calculated using the lattice parameters given above. Powder diffraction scans show the (1 0 0) reflection to have a similar intensity to the (0 0 2) peak, with approximately a two fold increase in intensity observed for the (1 0 1) peak [125, 142], presumably due to the lattice plane structure factor. The much lower relative intensity measured for the (1 0 0) peak would be consistent with a thin polycrystalline base growth layer occurring at the Si surface. Note that the Si (0 0 2) reflection should be absent by symmetry, but has been found to occur in Si (1 0 0) due to multiple diffraction events [143].

A Williamson-Hall plot for the three wurtzite ZnO diffraction peaks is shown in figure 4.5b. From the linear fit to the data, the crystalline size, D, can be calculated from the y-intercept, and the strain, ε, is given by the slope of the fit. The parameter β is the line broadening due to size and strain effects. This must be extracted from the observed broadening, β_{obs}, which is actually a combination of instrumental and sample broadening contributions. In this case, the observed broadening was taken to be equal to the FWHM of the peaks fitted using a Pearson VII distribution. The shape parameter for the Pearson VII model, denoted m, was close to unity for

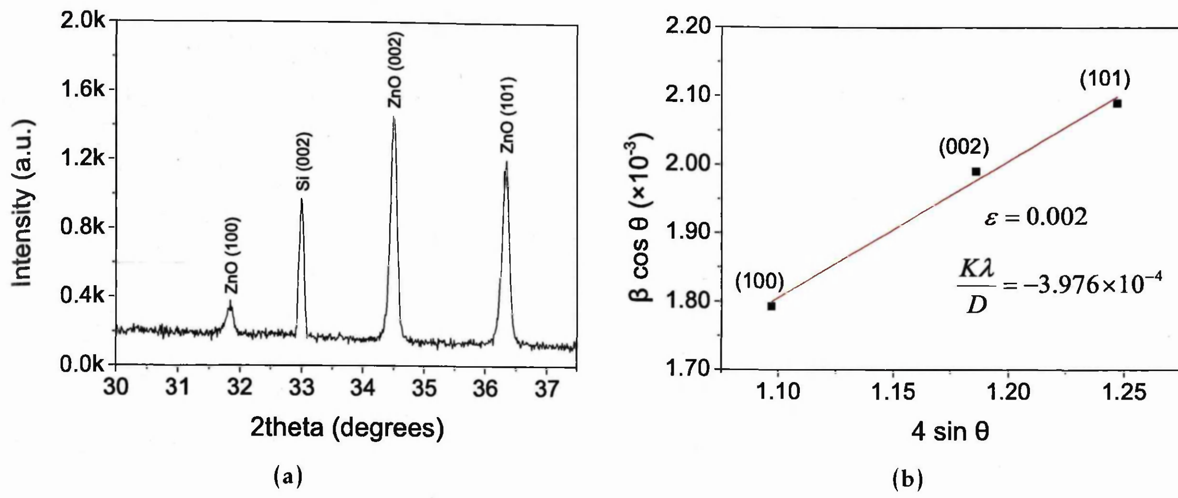

Figure 4.5: **(a)** XRD 2θ scan of surface enhanced NW growth. **(b)** Williamson-Hall plot of the ZnO diffraction peaks.

all three fitted peaks. $m = 1$ is a special case of the function which gives an exact Lorentzian distribution. For Lorentzian peaks, the instrumental and sample broadening contributions can be added linearly [144, 145]:

$$\beta_{obs} = \beta_{size} + \beta_{strain} + \beta_{inst} \tag{4.1}$$

$$\beta = (\beta_{obs} - \beta_{inst}) = \beta_{size} + \beta_{strain}. \tag{4.2}$$

In this case, instrumental broadening was neglected, an assumption which is further examined below, giving a strain value of $\varepsilon = 2.0 \times 10^{-3}$. Previous studies on ZnO nanoparticles have used the Williamson-Hall approach to measure absolute strain values of 1.20×10^{-3}, 0.93×10^{-3} [146] and 1.31×10^{-7} [125], following corrections for instrumental broadening. To discount the effect of instrumental broadening on the additional strain measured here, equation 4.3 can be used to calculate the broadening that would be observed for the strain value of 1.20×10^{-3} reported by Khorsand et al. [146].

$$\beta = \frac{k\lambda}{D\cos\theta} + 4\varepsilon\tan\theta. \tag{4.3}$$

This can be subtracted from β_{obs} to show the instrumental broadening that would be required for the measured strain to be equal to the value previously reported for nanoparticle powders. This instrumental broadening is calculated to be approximately 0.05°, which is greater than the total observed broadening measured for certain Si (0 0 2) and (0 0 4) peaks in section 4.4 (values shown in appendix A). Consequently, the measured increased strain over the nanoparticle powder diffraction values can not be ascribed to instrumental effects alone. In fact, the measured value is similar to the largest reported by Shakti following annealing of polycrystalline ZnO thin films deposited on quartz using the sol-gel method [147]. This suggests that large stresses are present in the CVD grown nanostructures and/or base growth layer, likely due to mismatch and roughness induced dislocations at the Si/ZnO interface. It is worth nothing that the value for the y-intercept, $k\lambda/D$, comes out as negative, which is unphysical, possibly suggesting that the Williamson-Hall analysis overestimates the strain. Inclusion of higher angle peaks in the Williamson-Hall plot could potentially give a positive value for $k\lambda/D$ by reducing the gradient of

the linear fit, leading to a smaller value of ε.

An X-ray pole figure of the c-axis (0 0 2) reflection was measured to study the alignment of NWs grown using the surface enhanced method (4.6) and to highlight any inherited orientation from the Si substrate. The noticeable high intensity horizontal symmetry in the pole figure can be attributed to the gas flow direction in the tube furnace, with the Ar/O_2 mixture flowing from 90° to 270°, as indicated in the figure. A large angular dispersion of the c-axis lattice plane reflections indicates poor vertical alignment of the NW arrays, as expected if Volmer-Weber type growth was occurring on exposed facets of varying orientation. Also, each crystallographic plane usually has a different growth rate because of the difference in sticking probability and surface diffusion rate of each plane [148]. No relation to the Si {1 0 0} (ϕ = 0° and 90°) or {1 1 0} (ϕ = 45° and 135°) lattice planes is discernible in the figure.

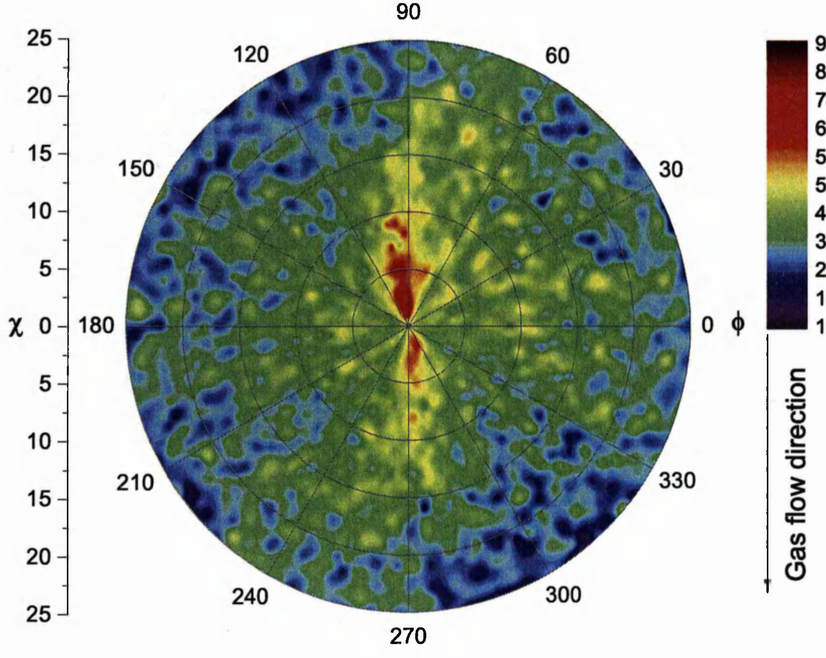

Figure 4.6: XRD pole figure of the (0 0 2) reflection for surface enhanced NW growth.

4.3.2.3 Transmission electron microscopy

High resolution transmission electron microscopy (TEM) was used to examine the Si/ZnO interface, in order to study the consequence of the lattice mismatch and also to look for evidence of oxidation of the Si interface layer. Nanowire array/substrate cross sections were prepared by focused ion beam (FIB), using a FEI Nova 200 NanoLab dual beam SEM/FIB fitted with a Kleindiek micromanipulator to allow the in-situ removal of the section. A Philips CM200 FEGTEM Field emission gun TEM/STEM with Supertwin objective lens operated at 200 kV was used to image the cross sections, which measured several micrometres in length with a width of approximately 100 nm.

A cleaved cross-sectional SEM image of sample B is shown in figure 4.7a, imaged prior to TEM analysis. It is clear that not all ZnO nucleation sites result in the growth of NWs, with a discon-

tinuous base growth layer comprising of a large number of randomly orientated grains visible at the Si surface. Figure 4.7b shows a bright field TEM image of the FIB prepared section, displaying ZnO structures that appear to correspond with the gains at the base of the NW array in figure 4.7a. Figure 4.8 contains TEM data from this area (excluding 4.8d), with the two labelled squares representing the areas imaged in figure 4.8a and 4.8b. The selected area electron diffraction (SAED) pattern shown in figure 4.8c was collected from the area indicated by the circle. The lack of regularly spaced sharp diffraction spots indicates poor ordering in the ZnO crystal structure close to the interface.

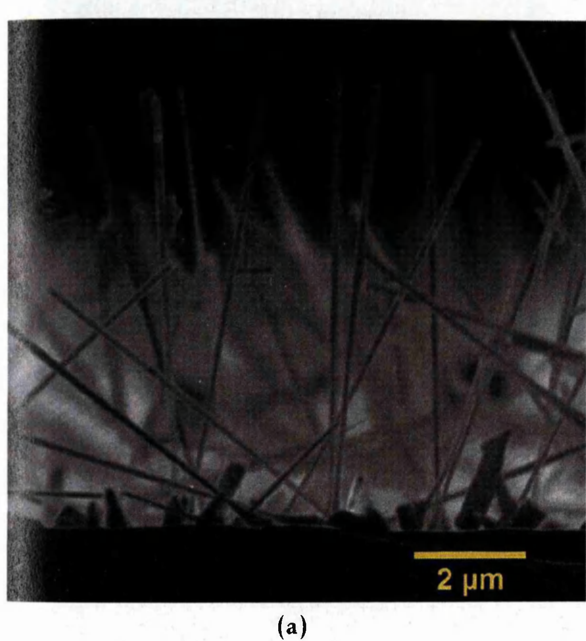

(a)

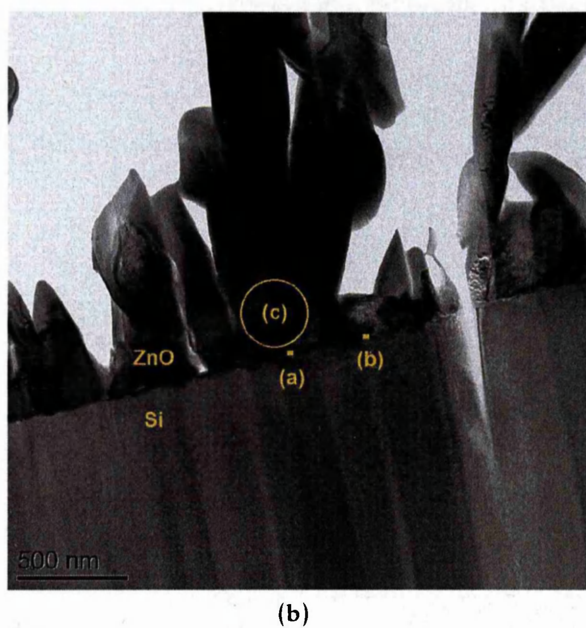

(b)

Figure 4.7: **(a)** Cross sectional SEM image of cleaved substrate. **(b)**Wide bright-field TEM image of the Si/ZnO NW interface with the locations of figure 4.8a, 4.8b and 4.8c indicated.

The ZnO *c*-axis (0 0 2) planes are clearly visible in all three HRTEM sub-figures (highlighted in **(b)**), and appear to be randomly orientated with the respect to the Si (1 0 0) lattice planes. The angle θ indicated in the figures is approximately 19° for **(a)**, 30° for **(b)** and 83° for **(d)**. This agrees with the lack of *c*-axis orientation observed in the SEM and pole figure measurements (figures 4.7a and 4.6) and with the (1 0 0) and (1 0 1) peaks observed in the XRD 2θ scan (figure 4.5). The ZnO lattice parameters were measured as $a = 0.317$ nm and $c = 0.502$ nm. This discrepancy from accepted bulk ZnO lattice parameters ($a = 0.325$ nm and $c = 0.521$ nm [29, 33]) is likely due to lattice strain and poor ordering at the Si/ZnO interface, as indicated by the XRD results and SAED pattern shown in figure 4.8c. In previous work, expected values for the lattice parameters were measured on ZnO NWs far from the substrate interface [149], however these were grown on lattice matched sapphire.

The HRTEM shows localised amorphous regions at the Si/ZnO interface. These regions could be responsible for the non-epitaxial transition and the observed lack of preferred orientation in the growth direction of the NWs. A possible cause for these localised amorphous regions is oxidation of the Si surface, either via direct chemisorption of oxygen or diffusion of oxygen

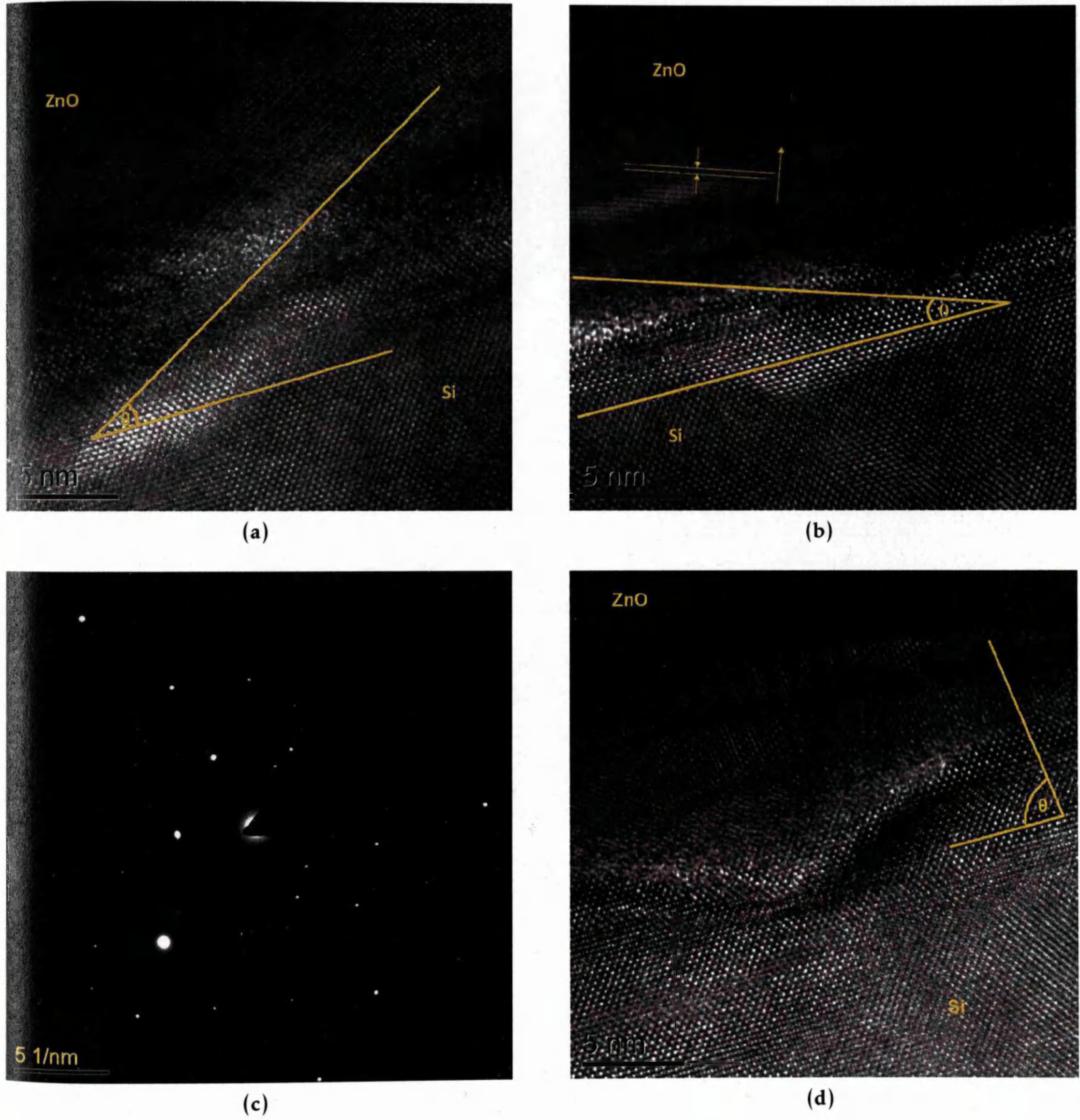

Figure 4.8: HRTEM of the Si/ZnO interface. The angle θ is formed between the Si (0 0 1) substrate lattice planes and c-axis (0 0 2) ZnO planes. Amorphous regions are present at the Si/ZnO interface. The SAED pattern in (c) shows poor ZnO crystallinity close to the interface.

during nanowire growth. Oxygen interstitials have been calculated to be fast diffusers in n-type ZnO [150]. In addition, SiO_x layers have been previously observed at the Si/ZnO interface even following low temperature CVD growth methods [151]. Alternatively, residue films from the etching process could also result in contamination of the interface and may be a factor in the initial nucleation of ZnO.

4.3.2.4 X-ray photoelectron spectroscopy of etched Si

X-ray photoelectron spectroscopy (XPS) was used to investigate residual chemical contamination of the Si surface. Following plasma etching, the sample was loaded in an ESCALAB XPS system (section 3.3.4.4) and scanned using Al K_α radiation with a pass energy of 50 eV. The survey spectra is shown in figure 4.9, with visible peaks for the F1s and S2s transitions indicated on the etched sample. Surface coverage was estimated using peak areas at approximately 0.7% and 5.7% respectively (table 4.3). An unprocessed silicon sample was also scanned to investigate if the etching process resulted in a considerable change to either the C1s or O1s peaks. No significant difference was found between the Si : O : C ratios before and after etching, with the ratios calculated as 72 : 20 : 8 and 74 : 21 : 5 respectively, following peak area corrections using the RSFs show in table 4.3.

Table 4.3: Estimated surface coverage, with peak contribution and atomic % calculated using equation 3.24.

Transition	RSF	Area	Contribution	Atomic %
Si2p	0.82	83444	102134	69.94
S2p	1.43	11861	8294	5.68
C1s	1.00	7926	7926	5.43
O1s	2.93	78095	26654	18.25
F1s	4.43	4533	1023	0.70

The S2s transition had to be used to quantify the sulphur coverage as the S2p doublet, which occurs at around 164 eV, was obscured by the fundamental Si2s plasmon peak, known to be separated from the Si2s photoelectron peak by $\hbar\omega \approx 17$ eV [152]. The sample was subsequently removed from UHV and annealed at 400 °C for 10 minutes under vacuum (1.5×10^{-2} mbar), then immediately rescanned, with no sulphur or fluorine peaks observed (figure 4.9). This suggests that the residual reaction products were weakly adsorbed to the sample surface, indicating that removal would occur during NW growth before the onset of carbothermal reduction. It is therefore unlikely that surface residue films would be a factor in the initial nucleation of Zn/ZnO vapour, or in the formation of the amorphous regions present at the Si/ZnO interface following NW growth.

4.3.2.5 Photoluminescence spectroscopy

Photoluminescence was used to investigate the optical properties of NWs grown using the surface enhanced method. Figure 4.10 shows the PL spectrum of NWs grown on a surface enhanced substrate, and represents the average of 5 normalised spectra collected at different points on the sample. The sample exhibits the standard near band edge emission at 3.29 eV [153, 154] along with the visible blue-green emission centered at around 2.49 eV, commonly attributed to point defects such as oxygen vacancies [155, 156]. Intensity variation in the defect region is common across samples, with a high degree of variability being reported in this region between similarly grown NWs [156, 157]. The figure also contains the maximum and minimum integrated intensity for the NBE peak and defect band, which is often expressed as a ratio to give an indication of

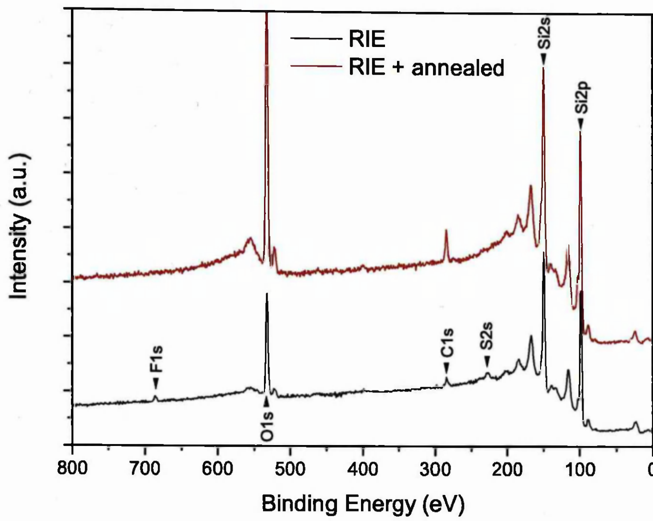

Figure 4.9: XPS survey scan showing removal of weakly bound RIE reaction products following annealing under vacuum at 400 °C.

defect density. The ratio $A_{\mathrm{NBE}}/A_{\mathrm{Defect}}$ is between 0.31 to 1.03, which is comparable to previous values reported using vapour transport NW growth [158,159].

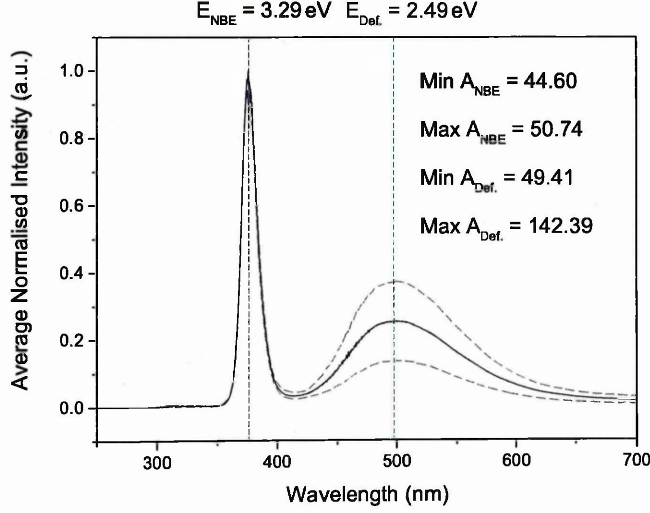

Figure 4.10: Normalised PL spectrum averaged over 5 points on the sample. The dashed grey lines show the standard deviation.

4.3.3 Selective Area Growth

This surface treatment technique can be easily implemented to achieve selective growth, which it crucial for vertical device incorporation. Using a chemically enhanced negative photoresist (Micro-Chem AZ nLOF 2070), diluted with thinner (MicroChem AZ EBR Solvent) for compatibility with electron beam lithography, substrates were patterned using e-beam lithography (Raith eLine). The exposed substrates are then developed and plasma etched using the process detailed previously. Once etched the remaining resist is removed and the substrates are cleaned via sonicating in acetone/IPA/DI. This resist is ideal for the RIE process, due to its high selectivity and thermal stability. A schematic of the processing steps is shown in figure 4.11.

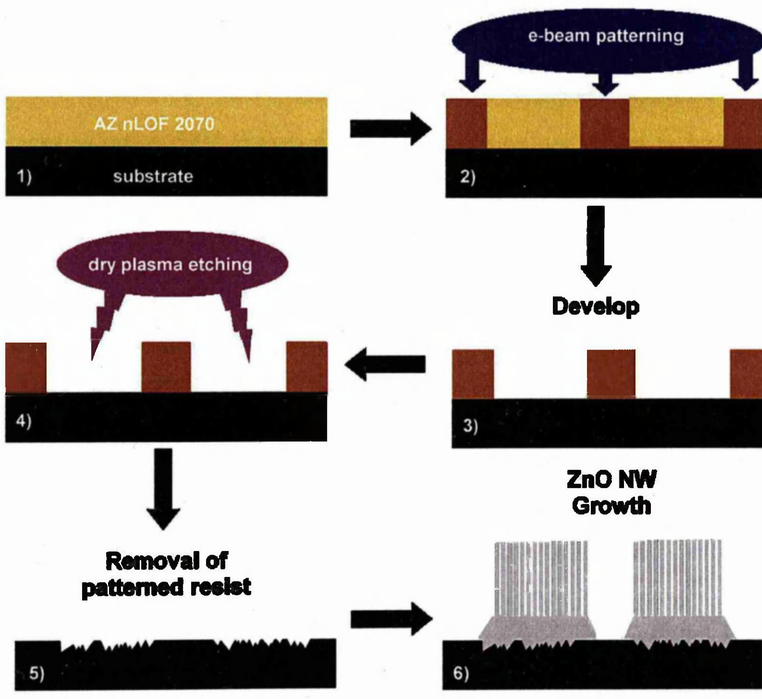

Figure 4.11: Schematic diagram showing the lithography processing steps. (1) Spin coated AZ nLOF 2070 resist, (2) patterned with electron beam (3) developed unexposed area (4) plasma etching (5) removal of patterned resist (6) selectively growth of NWs.

Figure 4.12a exhibits an example of NW growth following this patterning/etching procedure. The selective growth is shown in Figure 4.12b, with the Swansea University logo masked from the etching process. The areas which have been etched yields an array of NWs, whereas the masked written areas remain unprocessed, resulting in minimal ZnO nucleation, as seen in figure 4.2a. Due to the variation in NW orientation with respect to the substrate, some degree of overlap may exist between NW arrays in close proximity. Therefore, for typical vertical integration applications, the feature size of the patterned area must be sufficiently large to avoid short circuits between patterned areas that require electrical isolation. For applications in which such shorting between NW arrays is desirable [156], surface enhanced growth offers an attractive option for NW array patterning, with minimal processing.

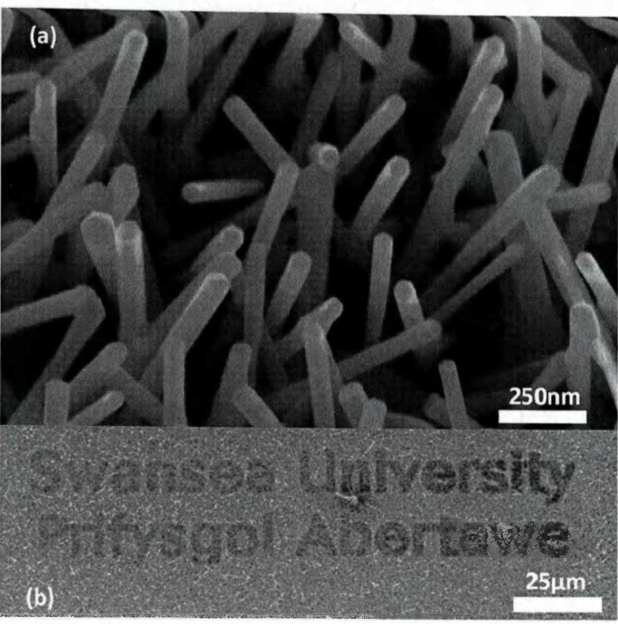

Figure 4.12: **(a)** High magnification SEM image of NWs grown using patterning technique. **(b)** SEM showing an example of patterning with 'Swansea University, Prifysgol Abertawe' excluded from NW growth.

4.3.4 Summary

- The optimum dry etching recipe was found to be an 8 : 1 ratio of SF_6 to O_2 resulting in a chamber pressure of 75 mTorr at an RF power of 150 W. A etch duration of 10 minutes was found to be sufficient to result in growth.
- Atomic force microscopy gave surface average and RMS roughness on the order of a few nm following the optimised etch process.
- X-ray diffraction, HRTEM and PL show that the NWs are crystalline, grow in the (0 0 2) direction and exhibit typical NBE emission under UV excitation. However, close to the interface the ZnO was found to be highly disordered, and XRD analysis suggested a high degree of stress present at the interface. This is likely due to the large lattice mismatch between Si and ZnO, and also due to roughness effects.
- Analysis of XPS data shows that the ZnO nucleation is not a result of any chemical alteration of the substrate surface, but is instead due to a direct alteration to surface topography.
- The ability to pattern arrays using conventional lithography processes has also been demonstrated.

In conclusion, vertically aligned catalyst-free NWs have been grown on Si substrates modified using refined dry and wet etching methods to assist in ZnO nucleation. Selective growth of catalyst-free NWs has been achieved using a novel plasma etching technique combined with a high resolution electron beam lithography process. Nanowires grown on plasma etched substrates exhibit a smaller spread of diameters with much improved orientation and significantly higher densities when compared to those grown on wet etched substrates. In addition, NWs grown on plasma etched substrates exhibit a higher degree of uniformity across the substrate. However, problems with crystallinity and oxidation could exist at the interface, and more work is required to investigate charge transport through the array.

4.4 Growth on Conductive Thin Films

An alternative approach to contacting the NW arrays through the substrate is to deposit conductive thin films that serve both to nucleate the ZnO vapour and act as a bottom contact to allow charge transport through the NW array. Also, the conductive layer could act as a buffer to compensate for the large lattice mismatch between Si and ZnO [160], reducing the stress present in the ZnO and leading to better alignment for vertical device applications.

Previous work on the growth of NWs on ITO buffed Si concluded that In atom difffusion resulted in n-type doping of the base layer growth and lower portion of the array, which the authors reasoned could give good Ohmic contacts at the interface between NWs and ITO film [161].

4.4.1 Experimental

The thin films were deposited on n-type Si (1 0 0) (section 3.2.1) to a thickness of 100 nm using DC magnetron sputtering, with the exception of indium tin oxide (ITO), which was deposited using RF to prevent charging. Also, following Kurdesau et al. pure Ar was used to improve the conductivity of the film, at the expense of the transparency, by making the film slightly oxygen deficient [162]. For each deposition, the target power density was altered to keep the deposition rate constant between materials (1.2 Å/s), as measured by a quartz crystal microbalance. A summary of deposition parameters is shown in table 4.4. Sputtered films were subjected to a

Table 4.4: Deposition parameters for conductive thin films.

Thin-film	Pressure (mTorr)	Ar flow (sccm)	Power (W)
Al	1.69	30	60
Cr	1.66	30	55
Ti	1.70	30	100
Cu	1.66	30	25
ITO	2.79	50	80
Mo	1.70	30	55
W	1.71	30	75

45 minutes growth process, as outlined at the start of the chapter and the resulting NW growth was inspected using SEM. X-ray diffraction was used to characterise the vertically aligned arrays using two methods:

- Standard coupled 2θ scans were used to study the crystallographic properties of the NWs and to look for evidence of metal and metal oxide compounds formed during the high temperature growth process.
- Pole figures of the ZnO (0 0 2) reflection were measured to gain information about the alignment of the NWs and to study texture inheritance from the underlying thin films and Si

substrate.

Finally, PL spectroscopy was employed to measure the optical band-gap and to gain information about the defect density and possible incorporation of dopant atoms from the thin films during NW growth.

4.4.2 Results

4.4.2.1 Electron microscopy

Top down SEM images of the resulting NWs are shown in figure 4.13. Several of these images were used to calculate the density of NW growth on each sample, with the results shown in table 4.5 and in figure 4.15a. The wire tips were examined under high magnification to look for evidence of metal catalyst particles. To aid this, backscatter electron (BSE) imaging was also employed to highlight heavy elements. This technique has been used to great effect when imaging Au catalyst particles located at the tips of catalytically grown NWs and also embedded in the base growth layer [82]. All NWs displayed hexagonal termination without any evidence of metal catalyst droplets at their ends, indicating that the NWs grow via the vapour-solid mechanism [163]. There are also clear differences in degree of alignment and widths of the NWs between samples – this is further discussed below.

The samples were also cleaved to study in cross section under SEM (figure 4.14). All samples show growth of high quality dense arrays aligned, on average, perpendicular to the substrate, with the exception of the W sample where there appears to noticeable preferential tilting. Nanowire diameter measurements were conducted in cross section to avoid errors due to imperfect alignment when measured normal to the substrate, along with array height and buffer layer thickness measurements. The results are shown in table 4.5. Some interesting differences are immediately apparent at the Si surface between samples:

- Cu: The NW array grown on the Cu layer has become detached from the substrate, with contact between array and substrate only bridged by intermittent deposits. These deposits were confirmed to be Cu rich using EDX, and were observed along the length of the cross section, along with detachment of the array from the substrate. Copper has the second lowest melting point (1085 °C) of the thin films following Al, which also shows sign of decomposition (see below). In addition, Cu has a much higher co-efficient of linear thermal expansion when compared with Si and the other materials (excluding Al). It therefore seems likely that detachment and subsequent melting of the Cu thin film occurs during the growth process. This confirms that Cu is unsuitable for use as a buffer or contact layer for the growth of vertical ZnO NW arrays on Si. However, there may be other applications related to the transfer of NW arrays from the growth substrate that could utilise this detachment.
- Al: Pitting of the Si substrate and no visible ZnO base growth layer or Al thin film is observed following NW growth. Again, EDX was used to locate discrete Al rich deposits at the base of the NWs. Due to decomposition of the Al thin film and the occurrence of island type NW growth, this method of nucleating ZnO NWs would also be unsuitable for

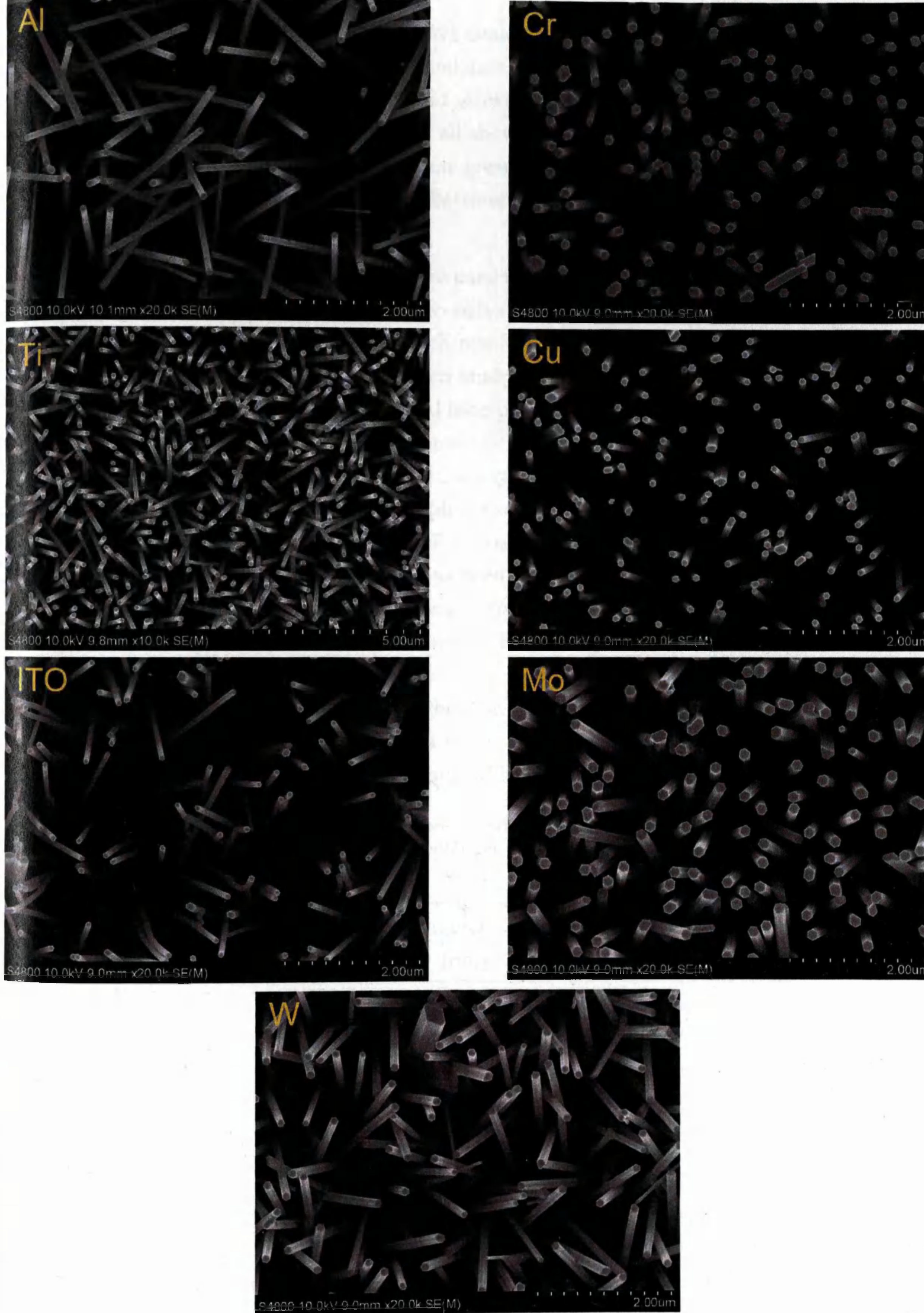

Figure 4.13: SEM images of ZnO NWs grown on 100 nm sputtered conductive layers viewed normal to the substrate. A noticeable difference in alignment, density and diameter of the NWs can be seen between samples. Molybdenum appears to result in wide dense growth in contrast to the arrays grown on ITO. Catalyst particles are conspicuously absent on the NW tips (confirmed using the BSE and EDX detectors). Note the lower magnification for the Ti sample.

device incorporation. Although the NWs could potentially be contacted through the Si, Al is known to be a p-type dopant in Si and an n-type dopant in ZnO and diffusion of the Al is likely to have occurred at the elevated growth temperatures [164].

- Cr, Ti, ITO, Mo and W: These samples all show the accumulation of a base growth layer at the Si surface. The thickness of this base growth layer is shown in table 4.5. In the case of Cr, a poor quality interface is visible between the Si substrate and the Cr layer, although this could be an result of cleaving.

Energy dispersive X-ray spectroscopy was also used to look for evidence of metal incorporation in the NW arrays. However, the results were inconclusive – large acceleration voltages were needed to study some of the metal transitions which resulted in a large interactions volume, meaning that spatial resolution become an issue when studying the base growth, as the sputtered layer was in close proximity. No evidence of metal incorporation was found along the length or at the tips of NWs, although it's plausible that dopant densities are below the threshold of detection. Figure 4.15 shows plots of base layer thickness against NW density and NW diameter against array height. For the metal thin-film samples, there appears to be a correlation between the density of NW growth and the thickness of the base layer. The growth of this base layer has been studied on α-Al_2O_3 substrates, and has been shown to follow a Stranski-Krastanov type growth process, with islands of ZnO merging to form a polycrystalline film, from which NWs emerge later in the growth process. Studied under TEM, the grains in the film appear to coalesce with increased thickness of the base layer, forming what appears to be a single crystal with few defects or dislocations [82]. If this is also the case on the sputtered thin films, then increased thickness of the base growth could lead to a higher degree of monoaxial texturing, with denser arrays observed on thicker, more highly orientated base growth layers.

Table 4.5: Table of mean NW densities and dimensions for NWs grown on conductive thin films. The height refers to the average length of the array above the base growth layer (BGL), not the average length of individual NWs. The uncertainty is the standard deviation.

Thin-film	Density (μm^{-2})	Diameter (nm)	Height (μm)	BGL thickness (μm)
Al	2.33 ± 0.59	97 ± 15	7.47 ± 0.46	–
Cr	4.11 ± 0.23	135 ± 14	7.83 ± 0.19	1.0
Ti	3.64 ± 0.21	144 ± 32	6.16 ± 0.05	0.9
Cu	4.57 ± 0.54	123 ± 24	8.31 ± 0.14	1.1
ITO	2.52 ± 0.34	89 ± 8	10.75 ± 1.22	1.9
Mo	5.81 ± 0.52	170 ± 26	6.38 ± 0.04	1.3
W	2.23 ± 0.32	142 ± 14	5.61 ± 0.39	0.7

4.4.2.2 X-ray diffraction measurements

Couple 2θ XRD scans of the NW arrays are shown in figure 4.16. The legend in the top right hand corner of each figure gives information on phases to which the peaks may be attributed. For a full list of the peaks and their indexed reflections, see appendix A. The large peak at around 69°

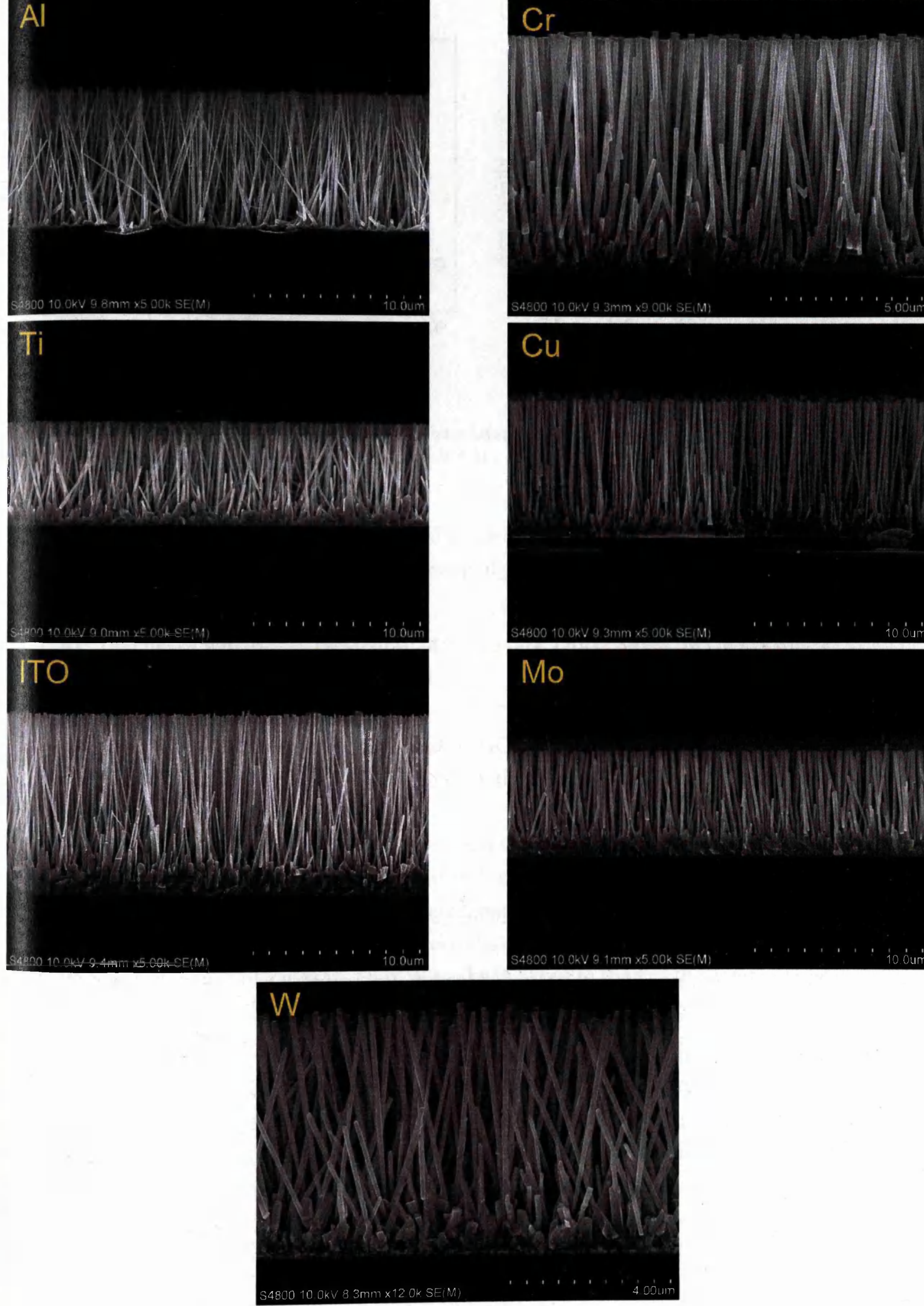

Figure 4.14: Cross-sectional SEM images of ZnO NWs arrays. The 100 nm sputtered conductive layer and base growth ZnO is visible is some of the images. Evidence of diffusion of aluminium layer into the silicon substrate is visible. It is also apparent that the copper layer has become detached from the silicon substrate. Clear differences in the morphology and density of the NW arrays are visible between samples.

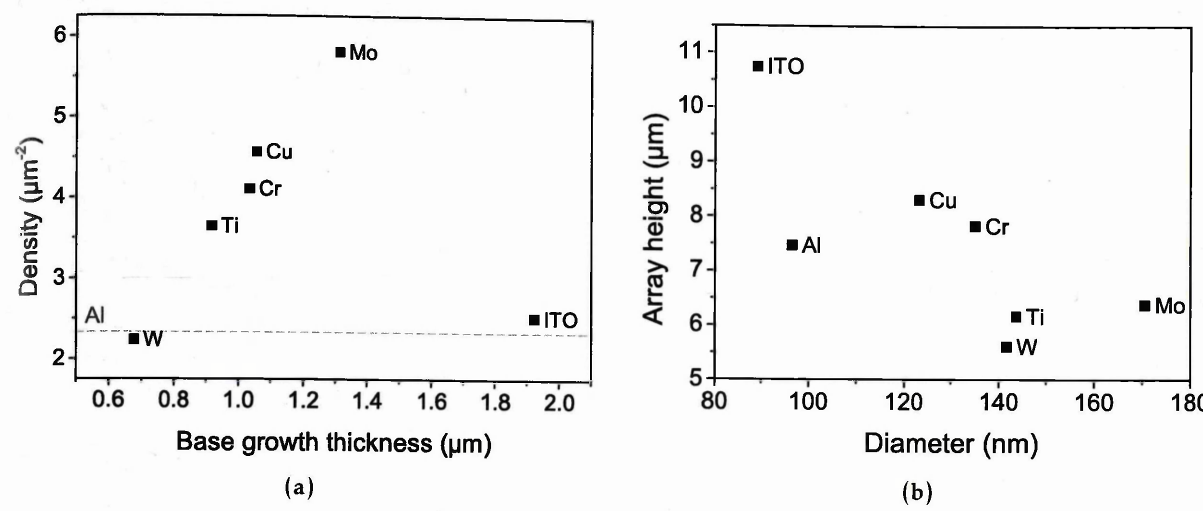

Figure 4.15: Plots showing relationship between (a) base layer growth thickness and NW density (b) NW diameter and array height. Error bars left out for clarity (see table 4.5).

can be indexed to the Si (0 0 4) reflection, and there is also a weaker narrow Si (0 0 2) peak visible around 33°. Presented below is a brief summary of peaks corresponding to metal or metal oxide phases, excluding Si and ZnO.

- **Al:** Two peaks which may be attributed to the rare $ZnAl_2$ phase. No oxide phases.
- **Cr:** Small intensity Cr (1 1 0) peak (BCC lattice structure). No evidence of CrO or CrZn phases.
- **Ti:** Several peaks that can be attributed to TiO_2 in the rutile phase (tetragonal crystal system). Isolated rutile peak at 27.533° is for the (1 1 0) reflection. Also some evidence of $TiZn_3$.
- **Cu:** Evidence of Cu and possibly CuZn phases. In the case of Cu, peaks are indexed to the (1 1 1) and (2 0 0) reflections (FCC lattice structure).
- **ITO:** ITO (2 2 2) peak. Small peak for tetragonal SnO_2 (2 1 1) reflection.
- **Mo:** Peaks for Mo (1 1 0) and (2 1 1) reflections (BCC lattice structure). No oxide phases.
- **W:** Some evidence of $ZnWO_4$. Four W peaks indexed to the (1 1 0) (dominant peak), (2 1 1), (2 2 0) and (3 1 0) reflections (BCC lattice structure).

Unsurprisingly, no diffraction peaks for elemental Al were found in the first sample, indicating that the Al rich deposits seen with cross sectional EDX were likely $ZnAl_2$ alloys. The Cr, Cu, Mo and W films appear to have retained their elemental metal phase through the growth process and show no evidence of metal oxide phases, although Cu and W do show signs of alloying with Zn. The Ti sample exhibits no elemental metal diffraction peaks, indicating that it has fully oxidised during the growth process into the rutile phase. Titanium is known to oxidise readily – oxidation of Ti deposited on ZnO at room temperature has previously been invoked to explain the Ohmic behaviour of the contact [165]. On the ITO sample, only one peak was observed corresponding with ITO, which was indexed to the (2 2 2) reflection, indicating strong monoaxial texturing of the film. Combined with the SEM analysis, this suggests that Cr, Mo, ITO and W are all suitable materials to use for direct contacting to the underside of the NW arrays, and that

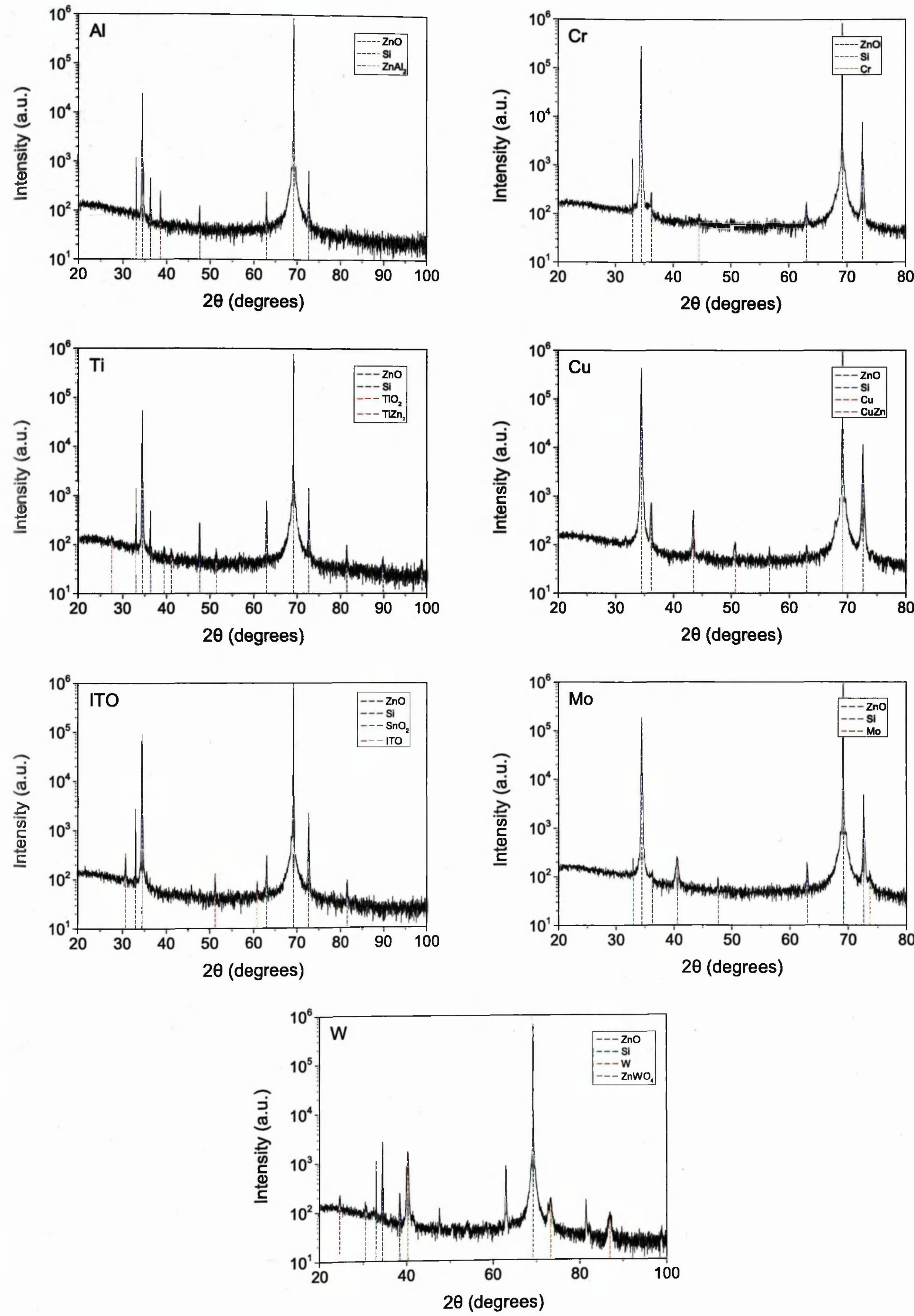

Figure 4.16: XRD 2θ scans of NW growth on the metal layers. A table listing the peaks shown in each figure is found in appendix A.

they are compatible with the vapour-phase growth temperatures. Although the Ti film appears to have oxidised, it still has demonstrable worth as a buffer layer in order to promote nucleation and growth of ZnO NW arrays on Si.

Multiple wurtzite ZnO peaks were observed in all scans. The lattice parameters a and c can be calculated by combining Bragg's law with the formula for the interplanar spacing in a hexagonal unit cell:

$$\frac{1}{d_{hkl}^2} = \left(\frac{2\sin\theta}{\lambda}\right)^2 = \left[\frac{4}{3}\left(h^2+k^2+hk\right)+l^2\left(\frac{a}{c}\right)^2\right]\frac{1}{a^2}, \tag{4.4}$$

where d_{hkl} is the interplanar spacing between the $(h\,k\,l)$ lattice planes. For the simple case of the wurtzite ZnO c-axis $(0\,0\,2)$ reflection, this can be solved to give:

$$c = \frac{\lambda}{\sin\theta}. \tag{4.5}$$

The c lattice parameter can then be used to calculate a using the other ZnO reflections where h or $k \neq 0$. These values can be compared to the standard bulk lattice parameters of $a = 0.32495$ nm and $c = 0.52069$ nm [29, 33]. A table of the lattice parameters is given below with the difference between the bulk and measured lattice parameters given as Δa and Δc. This shows that devi-

Table 4.6: Lattice parameters for wurtzite ZnO NWs grown on different thin films. The c-axis parameter was obtained using the $(0\,0\,2)$ peak and the a-axis parameter was subsequently obtained using the $(1\,0\,1)$ peak, except for those marked with an asterix, in which case the $(1\,0\,3)$ was used.

Thin film	ZnO lattice parameters			
	a (nm)	Δa (pm)	c (nm)	Δc (pm)
Al	0.32460	0.35	0.52010	0.59
Cr	0.32538	0.43	0.52003	0.66
Ti	0.32411	0.84	0.51995	0.74
Cu	0.32607	1.12	0.52000	0.69
ITO	0.32380*	1.15	0.51997	0.72
Mo	0.32458	0.37	0.51996	0.73
W	0.32458*	0.37	0.52001	0.68
Bulk ZnO	0.32495		0.52069	

ation from the bulk ZnO lattice parameters is small for NW growth on all films, indicating the growth of NWs of high crystalline quality.

To investigate the alignment of the NW and any texture inheritance from the underlying thin-film or substrate, pole figure measurements were conducted by keeping the 2θ angle fixed at the ZnO $(0\,0\,2)$ reflection, whilst tilting the sample in χ at various increments of the sample stage rotation ϕ. For more information on this technique, see section 3.3.7. This gives a polar plot of ZnO $(0\,0\,2)$ intensity over the sample. The results are shown in figure 4.19.

Generally, $(0\,0\,2)$ intensity increases closer to the centre of the pole figure, as expected for NW arrays aligned, on average, normal to the substrate, although interestingly, this isn't the case for

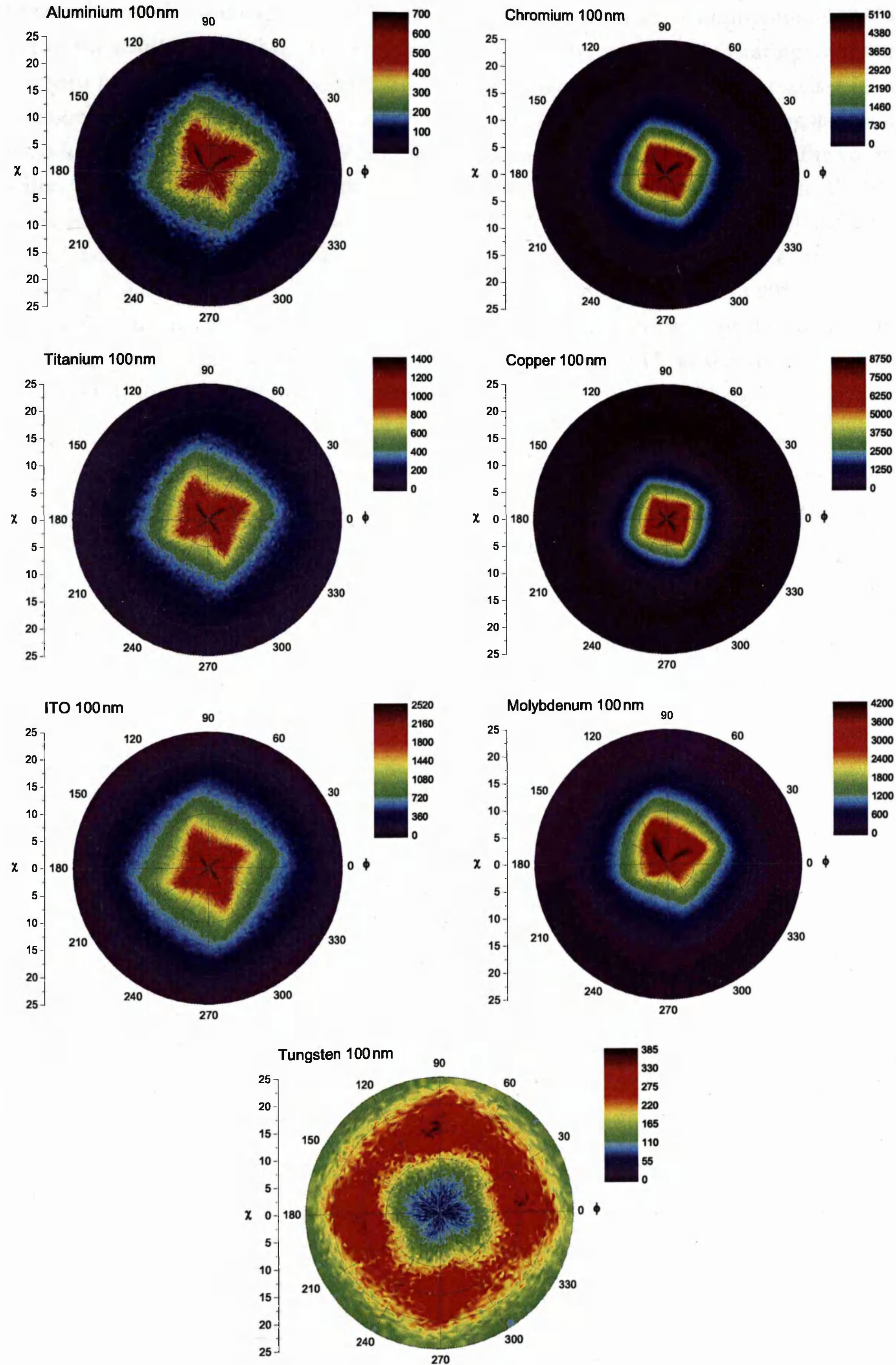

Figure 4.17: XRD pole figures of the ZnO (0 0 2) reflection. The linear intensity colour scale is shown in the top right of each figure and allows for a direct comparison between samples. Gas flow direction was from $\phi = 90°$ to $\phi = 270°$ i.e. down the page.

the W sample, which exhibits four peak intensity regions at a tilt angle of approximately 15° with respect to the substrate normal. These are spaced at 90° intervals in ϕ, indicating an inherited relationship from the underlying cubic Si substrate. In fact, all samples show c-axis alignment that is dependant on ϕ, with greater intensity for a given value of χ observed along ϕ directions corresponding to the Si (011) lattice planes. The Si surface must cause texturing of the sputtered thin-film, which is then passed on to the nucleating ZnO. In the case of the W sample, the unique texturing is unlikely to be due to W alone, as W forms the BCC crystal structure, along with Mo, and both have very similar lattice parameters. However, $ZnWO_4$ crystallises in the more complex monoclinic crystal system [166], which has an angle between lattice vectors $\beta \neq 90°$. The resulting preferential texturing caused by this crystal system could be responsible for the equally spaced areas of high intensity in the pole figure. This high intensity at $\chi \approx 15°$ also corresponds with the preferential tilting of the NW noted previously in the SEM image shown in figure 4.14.

Symmetric inheritance from the cubic structure of Si has been reported for ZnO films grown using MBE [30]. This led to growth of the ZnO zinc blende phase on Si (1 0 0). To encourage the growth of the wurtzite phase, this symmetric inheritance was blocked by nitridaition pretreatment of the Si surface. To investigate this effect and confirm that the symmetry in the pole figures was related to inheritance from the cubic Si substrate, a 100 nm amorphous layer of Si_3N_4 was deposited on Si (1 0 0) using chemical vapour deposition (CVD; section 3.2.5.2). A 100 nm layer of ITO was subsequently sputtered onto the film and the sample was subjected to the standard growth process. The resulting pole figure is shown in figure 4.18. The amorphous Si_3N_4 layer

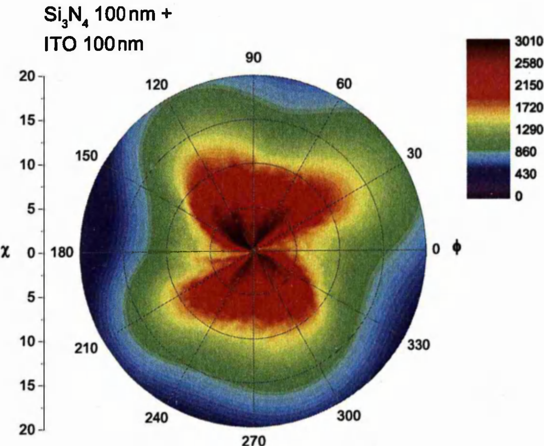

Figure 4.18: ZnO (0 0 2) X-ray pole figure of ITO on Si_3N_4 showing no symmetric inheritance from the Si substrate.

appears to have blocked the cubic inheritance from the substrate. The noticeable horizontal symmetry is ascribed to the gas flow direction in the tube furnace – the gasses were injected upstream (towards $\phi = 90°$), causing some preferential nucleation and growth of NWs in the plane of gas flow. This was also observed on the growths without the Si_3N_4 layer shown figure 4.17, with a slightly higher c-axis intensity observed for upstream tilt angles (towards $\phi = 90°$).

Rocking curves along this plane were extracted from the pole figures by plotting χ against intensity. The results are shown in 4.19, with the FWHM giving an indication of NW alignment. The FWHM varied from approximately 10° for the Cu thin-film up to around 22° for Al. As

expected, a decrease in the FWHM corresponds with an increase in c-axis intensity normal to the substrate, as shown in figure 4.21b. However, a much larger order of magnitude increase is seen in peak intensity with an approximate two-fold decrease in FWHM. This indicates that the total peak area, or the total amount of untextured c-axis ZnO is correlated with peak intensity. Physically, this means that the larger the degree of monoaxial texturing in the ZnO base growth and NW arrays, the larger the total amount of nucleation. This supports the idea put forward in the previous section that base growth thickness and texturing play a large role in the degree of subsequent nucleation and ultimately in the density of the NW arrays.

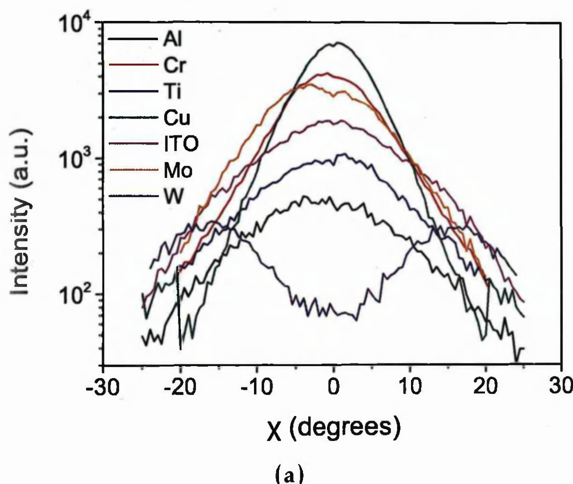

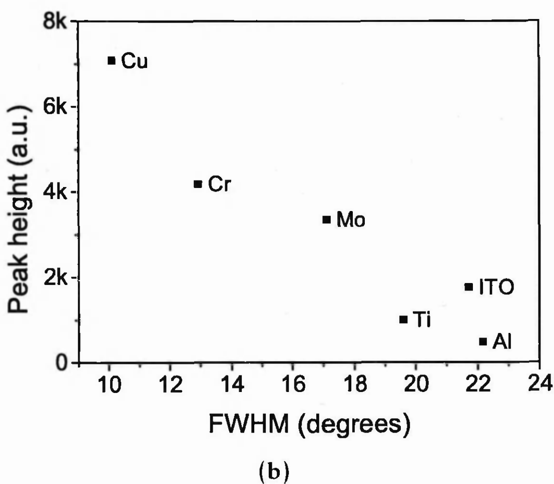

Figure 4.19: (a) Rocking curves conducted along the furnace gas flow direction ($\phi = 270°$) for the ZnO (0 0 2) reflection. Positive values of χ represent the downstream direction and negative values the upstream direction. This leads to a slight asymmetry in the curves, with a higher degree of texturing observed in the upstream direction, as previously reported in section 4.3.2.2. **(b)** Plot of rocking curve FWHM against maximum peak intensity. The order of magnitude increase in peak intensity with a two-fold decrease in FWHM indicates that peak area, or total quantity of c-axis aligned ZnO, is roughly correlated with peak height.

4.4.2.3 Photoluminescence spectroscopy

The optical properties of the samples were studied using PL spectroscopy, with the results shown in figure 4.20. All samples exhibited the signature ZnO luminescence, displaying the NBE emission peak positioned at around 375 nm, originating from excitonic transitions between valence and conduction bands, and a deep level broad emission band over visible wavelengths, related to intrinsic or extrinsic defects [45]. All samples, with the exception of Al, showed large undistinguishable visible emission, much larger than commonly observed using conventional seed layers [7, 45, 167] and catalyst particles [168–170]. This can be attributed to metal, zinc-metal or metal oxide incorporation into the NWs during the growth process. Similar large defect emission has been observed by Eustis et al. on CVD NWs grown on a Cu TEM grid. Subsequent TEM and EDX characterisation confirmed the presence of Cu impurities along the length of the NWs [171]. The Al sample showed deep level emission more similar to that reported in previous work, which could could indicate that the majority of the Al alloyed with Zn into the $ZnAl_2$ phase detected using XRD, preventing further incorporation into the lattice during growth.

Due to the broadness and intensity of the deep level emission, no individual components could be resolved. An estimate of the relative defect density between samples can be gleaned by looking at the relative integrated intensity between the NBE emission and the defect band. This is shown in figure 4.21a along with the absolute NBE peak intensity, which follows a similar trend. With the exception of the Al sample, which shows an order of magnitude increase in the integrated intensity ratio and NBE peak intensity compared with the other samples, the samples all show similar integrated defect intensity related to dopant incorporation, with the Mo sample exhibiting the largest relative integrated defect intensity and Ti and ITO the smallest.

Interestingly, a variation in NBE peak position was also observed between samples, indicating changes in the ZnO band-gap dependant on the growth film. This is shown in figure 4.21b. Sernelius et al. found that the optical band-gap of Al doped ZnO was widened in proportion to the Al doping [172] and this was fully explained using a effective-mass model, possibly suggesting the large red shift measured in this work is a result of doping involving alloys or oxide phases. The same is true for Ti doping of ZnO NWs investigated by Lee et al. [173]. For the two metals that retained their element phase with no evidence of alloying or oxidation (Cr and Mo), the blue shift in the optical band-gap agrees with work previously published [174, 175]. This suggests that the electrical properties of the NWs containing alloys, oxides and mixed phases may be significantly different to those reported for elementally doped ZnO.

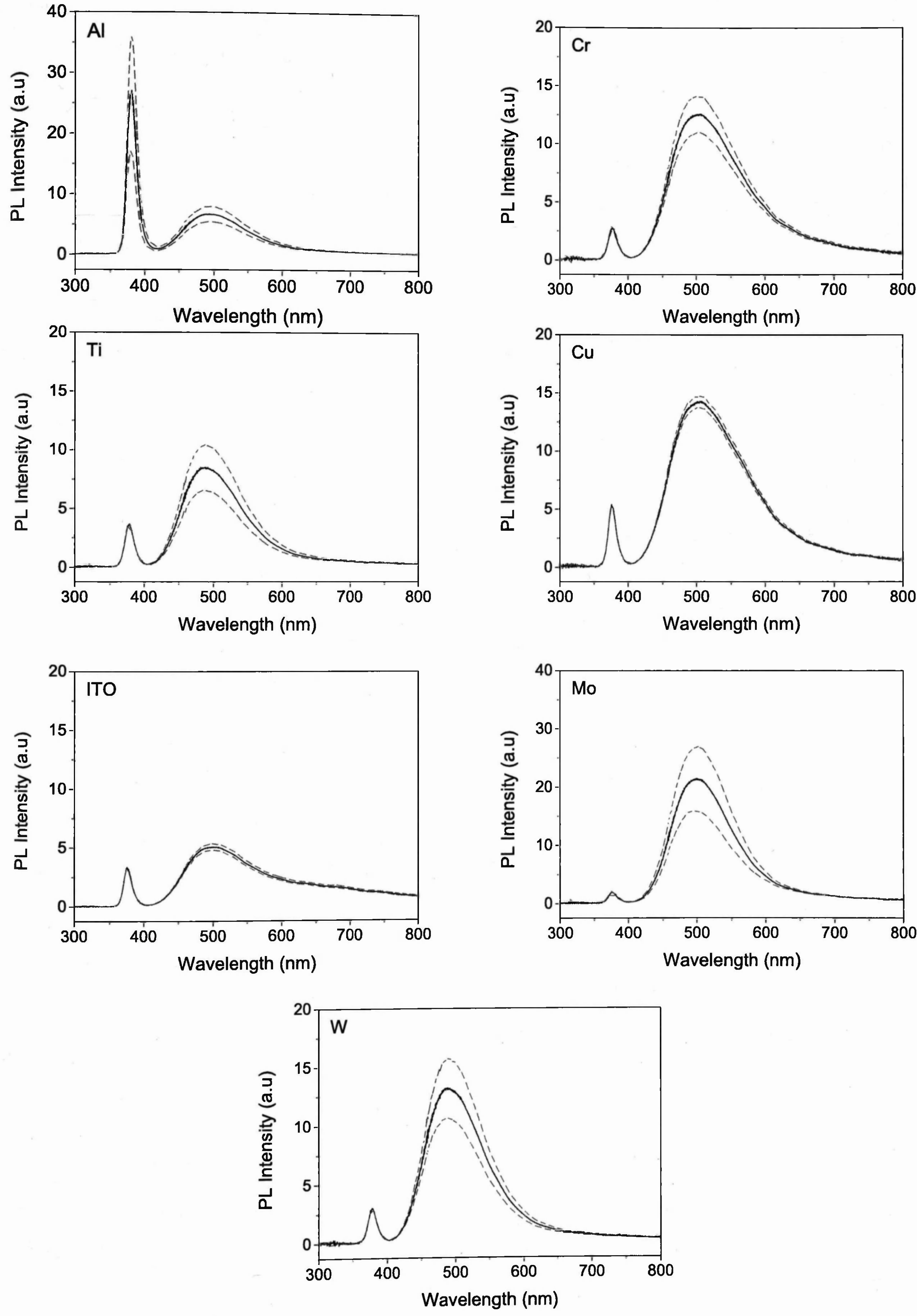

Figure 4.20: PL spectra of NW arrays grown on metal thin-films, normalised to the NBE excitonic peak and averaged over 5 areas on the sample. The dashed lines show the standard deviation. Notice the different intensity scale for the Al and Mo samples.

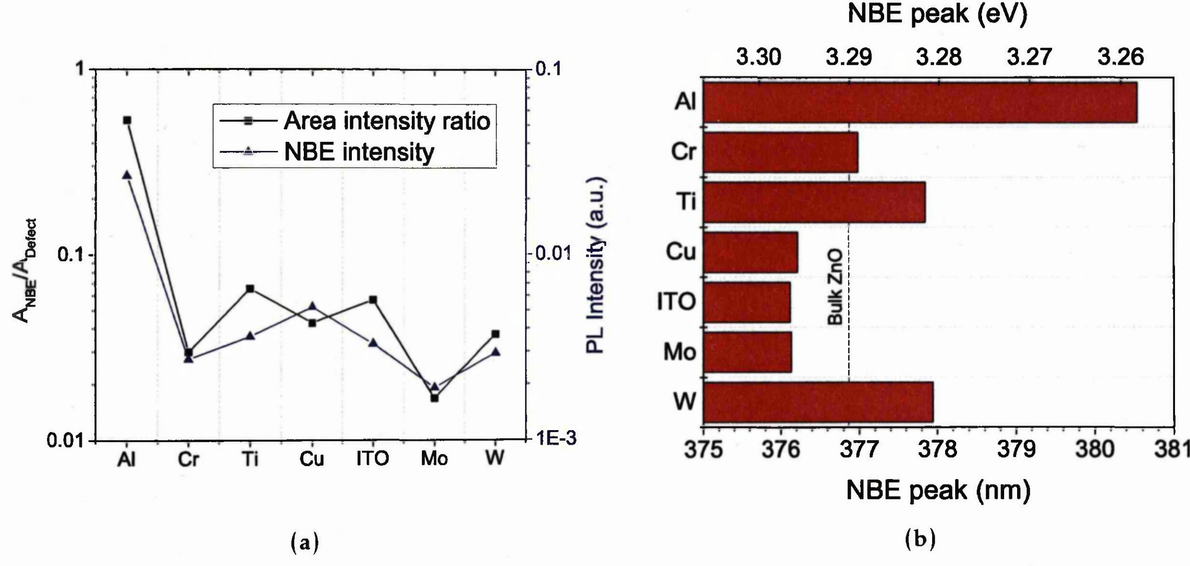

(a) (b)

Figure 4.21: (a) Integrated intensity ratio and NBE peak intensity. Fractional integrated intensity ratios indicated that the ZnO is highly defective. This could be attributed to dopants from the sputtered conductive layers used to encourage ZnO nucleation and *c*-axis aligned growth. (b) Position of NBE peak, as compared with intrinsic (undoped) bulk ZnO. The effect of dopants from the sputtered conductive layers on the width of the band-gap is complex, due to the presence of mixed zinc-metal and metal oxide phases identified using XRD.

4.4.2.4 Summary

The growth of highly aligned ZnO NW arrays on conductive thin-films deposited using magnetron sputtering onto Si substrates has been demonstrated, without the use of metal catalyst particles. Previous work done on the growth of ZnO NWs on metals suggests that in the results presented here, the Si substrate is acting to texture the sputtered metal films, which buffers the lattice mismatch between the single crystal Si and ZnO, resulting in the growth of highly aligned arrays of ZnO NWs ideal for vertical device integration. Further work is required to characterise both the electrical properties of the doped ZnO NWs and the quality of the contact created between the conductive layer and the array.

- SEM showed densely aligned arrays with no catalyst particles found using SE/BSE detectors. With the Cu sample, the buffer layer became detached from the substrate, whilst the Al film had decomposed and growth appears to have occurred on the Si surface without accumulation of a buffer layer. The thickness of the base growth layer is found to be related to the density of growth for the metal films. All samples showed an inverse correlation between NW diameter and average array height.
- XRD measurements showed NWs of high crystalline quality. Evidence of zinc alloys was found in the Al, Cu and W samples. The Cr, Cu, Mo and W films appear to have retained at least some of their elemental metal phases, whilst the Ti sample shows evidence of complete oxidation. Pole figure measurements show highly aligned c-axis orientation of the ZnO with biaxial inherited texture from the underlying Si which indicates the Si textures the metal films and is responsible for the high degree of alignment seen in the NW growth.
- PL measurements show strong evidence of metal, metal alloy or metal oxide incorporation into the growth. Also, a shift in ZnO band-gap is seen depending on buffer layer. More work would be needed to establish the extent, type and uniformity of the doping present in the NWs, which likely has large implications for the incorporation of these NWs into devices.

4.5 Summary and Comparison of Vapour-Phase Growth Methods

Despite attempts at optimisation, the seed layer grown NWs remained of a poor quality in terms of morphology and density. However, correlation of deep level luminescence with electrical conduction through the ZnO/Si interface is of interest and has implication for the other two growth methods, especially for the quality of the metal-semiconductor contacts created to the bottom of the NW arrays grown on conductive films, which exhibit large integrated defect to NBE intensity ratios.

The surface enhanced method shows promise for direct growth of ZnO NWs on Si, however the lack of a base growth layer means that alignment is inherently problematic, as island type growth will invariably lead to varying orientations depending on the exposed facets. This could also create problems for conduction through the substrate, which would be the required contacting method due to the lack of a base growth layer. The XRD analysis seems to suggest large strain present in the NWs, with FWHM values for the (0 0 2) and (1 0 1) of 0.119 41° and 0.126 04° respectively, which can be compared to the smaller FWHM values for growth on metal layers shown in appendix A. This is supported by the TEM, which shows a poor quality defective interface, highlighted by the lack of ordering in the SAED pattern. Amorphous areas also seem to exist at the interface, which could be regions of SiO_x formed during the NW growth process. Further work would be required to analyse the feasibility of using the Si substrate as an electrical contact to the NWs. This approach, however, does offer advantages over the other methods on offer, mainly the simple manner in which patterned growth may be attained on a substrate using basic photolithography, without the lift-off or etch back steps required by additive processes.

Sputtered conductive films showed great promise for use in vertical NW devices. Growth of high aspect ratio highly aligned dense NW array was achieved using all sputtered films, demonstrating the superiority of this technique over those previously investigated in this work. Cr, ITO and Mo in particular, seem to offer great promise as bottom contacts to arrays, and more work is required to investigate the electrical properties of this interface. A draw-back to this method is that doping seems to be inherent in growth on sputtered films – this would create problems for integration of these NWs into UV optical devices. Again, further work is required to characterise the type and heterogeneity of the dopants and their effect on the electrical properties of the NWs.

Chapter 5

Surface Modification and Attachment of Biomolecules to Zinc Oxide Nanowires

This chapter deals with modifications to the surface of zinc oxide nanowires (ZnO NWs) for the conductometric detection of proteins. Antibodies are immobilised on the surface of the nanowires to allow selective binding of the target antigen.

Surface modification and protein binding to nanowire arrays was investigated using electron microscopy (SEM), in order to study the effect of the biofunctionalisation process on the NW surface, X-ray photoelectron spectroscopy (XPS), to provide chemical analysis of the surface modification and the attachment of biomolecules, and photoluminescence spectroscopy (PL), to give an indication of optical properties and extrinsic surface state modification. Nanoscale electrical measurements were performed on individual nanowire field effect transistors (FETs) to determine the impact of the biofunctionalisation on their electrical properties, and importantly to relate these to surface changes measured using XPS and PL. The implications of these measurements on the detection of proteins using the functionalisation methods outlined here, and on the design of ZnO nanowire immunosensors is then discussed.

5.1 Introduction

Two approaches are taken to antibody immobilisation; the first uses a linking molecule to attach the antibody to the ZnO NW surface, whilst the second relies on activation of carboxylic groups on the antibody for direct binding to the modified ZnO surface. For both methods, silanization of the hydroxyl terminating zinc oxide is required to modify the surface terminating species into amino groups. The functionalisation of ZnO to allow detection of proteins can be broken down into the following processes:

- Surface modification – preparation of the ZnO surface for subsequent attachment of the antibody.
- Antibody immobilisation – covalent attachment of the antibody to the surface, including preparation of the antibody and activation of necessary functional groups.
- Blocking of non-specific binding sites – for antigen specific detection, functional groups that act as non-specific binding sites for proteins must be blocked.
- Antigen sensing – binding of the target antigen with the antibody.

In this study, human chorionic gonadotropin (hCG) was used as a model protein biomarker. Human chorionic gonadotropin is glycoprotein hormone with a molecular mass of around 37 kDa [176], secreted by the trophoblastic cells of the placenta chorionic vesicle to promote the devel-

opment of the sexual gland [177]. In healthy human serum and urine, the concentration of hCG is extremely low, usually less than 5 mIU/ml. Levels increase markedly during the first 20 weeks of pregnancy and elevated levels can be detected six to twelve days after fertilisation [178]. Most chemical pregnancy tests rely on these early elevated levels to diagnose pregnancy. However, increased level of hCG in serum and urine can be indicative of trophoblastic cancer, germ cell tumours, choriocarcinoma and many diseases related to pregnancy [179].

It is well know that the surfaces of metal oxides, such as ZnO, are covered in a layer of hydroxyl (–OH) groups, with hydroxyl coverage measured using XPS to be 8–15 nm^{-2} for a range of common metals [180]. This intrinsic hydroxyl coverage makes ZnO amenable to silanization through the use of a organofunctional alkoxysilane. In this work, (3-aminopropyl)triethoxysilane (APTES) is used to modify the –OH groups present on the ZnO surface into amino (NH_2) groups suitable for antibody attachment. An example of the silinization reaction is shown in figure 5.1. In an aqueous solution, the ethoxy (CH_3CH_2O) groups on the APTES are hydrolysed, releasing ethanol. Hydrogen bonding occurs between the ZnO surface hydroxyls and the –OH groups present on the APTES molecule, which then bonds to the surface through a condensation reaction, accompanied by the release of H_2O.

Figure 5.1: APTES hydrolysis followed by condensation reaction at hydroxylated ZnO surface.

With the presence of surface NH_2 groups, the antibody can be attached using one of the two following methods:

- Use of glutaraldehyde as a cross-linker: glutaraldehyde (GA) is an organic molecule consisting of two aldehyde (–CHO) groups separated by a carbon chain. This can be used as a link between the amine terminated ZnO surface and amine groups present on the antibody.
- Use of EDC/NHS as a zero-length cross-linker: EDC dehydrates the carboxylate groups present on the antibody into active o-acylisourea intermediates. The NHS then reacts with O-acylisourea intermediates to form a semi-stable NHS-ester which favours conjugation with amines. As the EDC/NHS results in conjugation of the activated carboxyl group with the amines on the NW surface without forming a linkage between molecules (peptide bond), the method is referred to as zero-length cross-linking [181].

5.1.1 The hCG antibody

Antibodies (abbreviated Ab), also known as immunoglobulin (Ig), are proteins produced by the immune system to provide a response against foreign substances, such as bacteria and viruses. Anti-hCG belongs to the IgG antibody isotype, consisting of two "heavy" and two "light" polypeptide chains forming the characteristic Y shape, which can also be subdivided into the fragment antigen-binding (Fab) and the fragment crystallizable region (Fc) regions, as shown in figure 5.2.

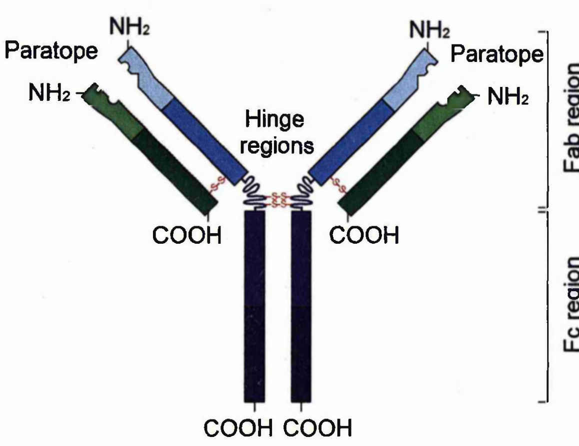

Figure 5.2: Diagram of the hCG antibody. The heavy and light chains are shown in blue and green, respectively, and are shown linked by disulfide bonds (red).

The Fab region contains the paratopes, or antigen binding sites, which are located at the N-terminus (or NH_2 terminating region) of the polypeptide chains. Primary amine groups are also distributed over the antibody due to their occurrence on lysine residues. The C-terminus (COOH terminating region) is located at the opposite end of the light and heavy chains, as shown in figure 5.2. [182]

5.1.2 Glutaraldehyde cross-linking method

The GA cross-linking method is depicted in figure 5.3. Glutaraldehyde reacts with the APTES modified ZnO surface, forming an imine bond at one end of the glutaraldehyde. This leaves the aldehyde group at the opposite terminus to react with amine groups on the antibody, which may be applied to the surface directly without the need for activation of functional groups. The imine bond is formed through a carbinolamine intermediate which undergoes dehydration to give the imine product [183].

Although figure 5.3 depicts bonding at the C-terminus of the Ab heavy chain, as mentioned the amine groups are distributed over the whole Ab and the N-terminus of the polypeptide chains is actually situated at the paratopes. Due to this, the orientation of the Ab on the surface is essentially random, which could result in uncontrollable antigen binding efficiencies and potential blocking of the antigen binding sites [182,184].

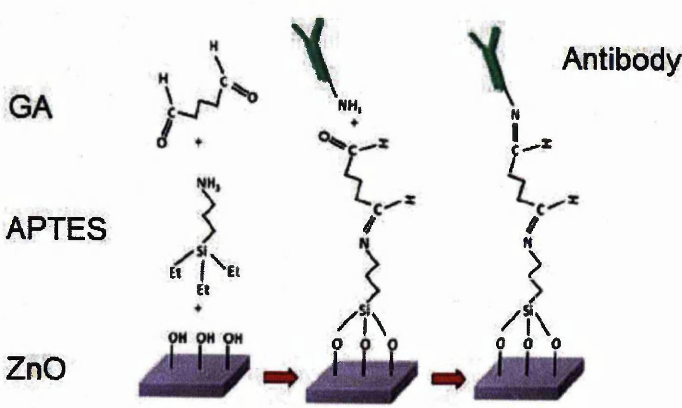

Figure 5.3: Schematic of antibody attachment using GA. Adapted from [17].

5.1.3 EDC/NHS zero-length cross-linking method

This method involves activation of the carboxyl groups prior to application of the Ab to the amine terminating surface. This is achieved using 1-Ethyl-3-[3-dimethylaminopropyl]carbodiimide hydrochloride (EDC or EDAC), which is a zero-length cross-linking agent. EDC reacts with a carboxyl group to form an amine-reactive *O*-acylisourea intermediate. If this intermediate does not encounter an amine (top pathway in figure 5.5), it will hydrolyse and regenerate the carboxyl group (middle pathway in figure 5.5) [18]. To prevent hydrolysis, *N*-hydroxysuccinimide (NHS) may be used to convert the carboxyl group into a stable amine-reactive NHS ester, which subsequently reacts with the primary (surface) amine to give an amide bond. This reaction is shown in the bottom pathway in figure 5.5. Note that in the figure, the sulfonate sodium salt of NHS, Sulfo-NHS, is depicted. However, the reaction and final conjugate product resulting from NHS and Sulfo-NHS are identical.

EDC
1-Ethyl-3-(3-dimethylaminopropyl)carbodiimide • HCl

NHS
N-Hydroxysuccinimide

Figure 5.4: Chemical structure of EDC and NHS. Adapted from [12, 18].

As the Ab –COOH groups are generally less distributed than the amine groups and are located at the opposite ends of the polypeptide chains to the paratopes, in contrast to the GA cross-linking method this could result in a preferred orientation of the conjugated Ab on the ZnO Surface. The ideal Ab orientation is achieved when the Fc fragment binds to the amine terminating surface, avoiding inhibition of the paratopes and exposing the Fab region to the analyte solution [184].

A disadvantage of the EDC/NHS method when compared to GA cross-linking is the issue of agglomeration and multilayer attachment of anti-hCG. Following carboxyl activation, the amine-

Figure 5.5: Sulfo-NHS plus EDC (carbodiimide) cross-linking reaction scheme. Adapted from [12].

reactive NHS ester will potentially bind to amine groups present on neighbouring antibodies. This could occur in solution, resulting in agglomeration, or at the ZnO surface, resulting in multilayer formation which could severely decrease sensitivity by diminishing the effect of protein-antibody conjugation on the surface properties of the NWs.

5.1.4 Bovine serum albumin

The purpose of bovine serum albumin (BSA) in this application is to act as a blocking reagent. In a practical sensing application involving bodily fluids, it would be critical to block any potential protein binding sites to prevent non-specific binding of the target protein and other proteins present in the analyte. This is achieved using BSA, a cheap stable protein which interacts minimally with biological reactions. BSA is applied prior to sensing to prevent non-specific protein-surface and protein-protein interactions. In this application, where a solution of the target protein is applied directly, non-specific protein interactions are irrelevant. However, even in the absence of additional proteins, binding of the target protein to e.g. surface functional groups is still an issue that could effect repeatable sensing. The molecular weight of BSA is approximately 66.5 kDa [185] – significantly larger than the molecular weight of 37 kDa given for the hCG protein [176].

5.2 Experimental

Nanowires were grown on 10 mm × 10 mm silicon (1 0 0) samples sputtered with a 100 nm layer of Ti, as described in section 4.4. Sputtered thin-films were found to act as a buffer between the lattice mismatch of ZnO and Si, and symmetric inheritance from the underlying Si results in strong texturing of the deposited layer, which leads to the growth of highly aligned vertical arrays of ZnO NWs. In addition, the sputtered film shows promise for use as a bottom contact to the array for vertical device integration and, combined with conventional photolithographic patterning of thin-films, offers a convenient method for selective area growth. The NW arrays were subsequently treated with APTES then functionalised using the activated carboxyl EDC/NHS method and the glutaraldehyde cross-linking method in parallel. The APTES, GA, EDC, NHS, BSA and phosphate buffer saline (PBS) were all purchased from Sigma-Aldrich. The anti-hCG and hCG protein were purchased from Abcam plc.

5.2.1 Surface Modification

The as-grown NWs were treated with (3-aminopropyl)triethoxysilane (APTES) in order to modify the hydroxylated ZnO surface to terminate in amino groups for subsequent antibody immobilisation. The NW arrays were immersed in a 0.5% solution of APTES in DI water for 10 minutes, then rinsed in DI water and dried under N_2 flow.

5.2.2 Antibody immobilisation via glutaraldehyde - Pathway A

Following silanization, glutaraldehyde was employed as a linking group between the amino terminating ZnO surface and the amine groups present on the antibody. Glutaraldehyde consists of two aldehyde (COH) groups linked by aliphatic carbon. Nanowire arrays were immersed in a 2.5% solution of glutaraldehyde in DI water for 1 hour, then rinsed and dried using N_2.

A 200 µg/ml solution of anti-hCG in PBS was prepared and applied directly to the NW arrays for a duration of 2 hours. Samples were subsequently rinsed in PBS, then DI water and dried using N_2.

5.2.3 Antibody immobilisation via EDC/NHS - Pathway B

The EDC/NHS solution was prepared using the following method: 800 µl of a 50 mM NHS solution in PBS was added to 200 µl of the antibody at a concentration of $2\,\mathrm{mg\,ml^{-1}}$. 1 ml of 25 mM EDC solution in PBS was then added. The solution was vortexed and applied to the sample for 2 hours. The sample was then rinsed in PBS and DI water and blow dried in N_2.

5.2.4 Blocking of non-specific binding

Following antibody immobilisation, bovine serum albumin (BSA) was used to prevent non-specific binding of the antigen by blocking exposed amino groups. A 5% solution of BSA in PBS was prepared and applied to the sample for 30 minutes, following which it was rinsed in PBS, then DI

water and dried using N_2.

5.2.5 Antigen binding

The hCG protein was applied directly to the NW arrays at a concentration of 250 ng/ml in PBS. This corresponds to approximately 5.6 mIU/ml, which represents a slight increase above normal levels. The antigen was left on the sample for 15 minutes. The samples were then rinsed in PBS and DI and dried using N_2.

5.2.6 Summary

Both antibody immobilisation methods use the same anti-hCG concentration to allow direct comparisson between samples during conductivity measurements. For clarification, the two antibody immobilisation pathways are shown schematically in figure 5.6.

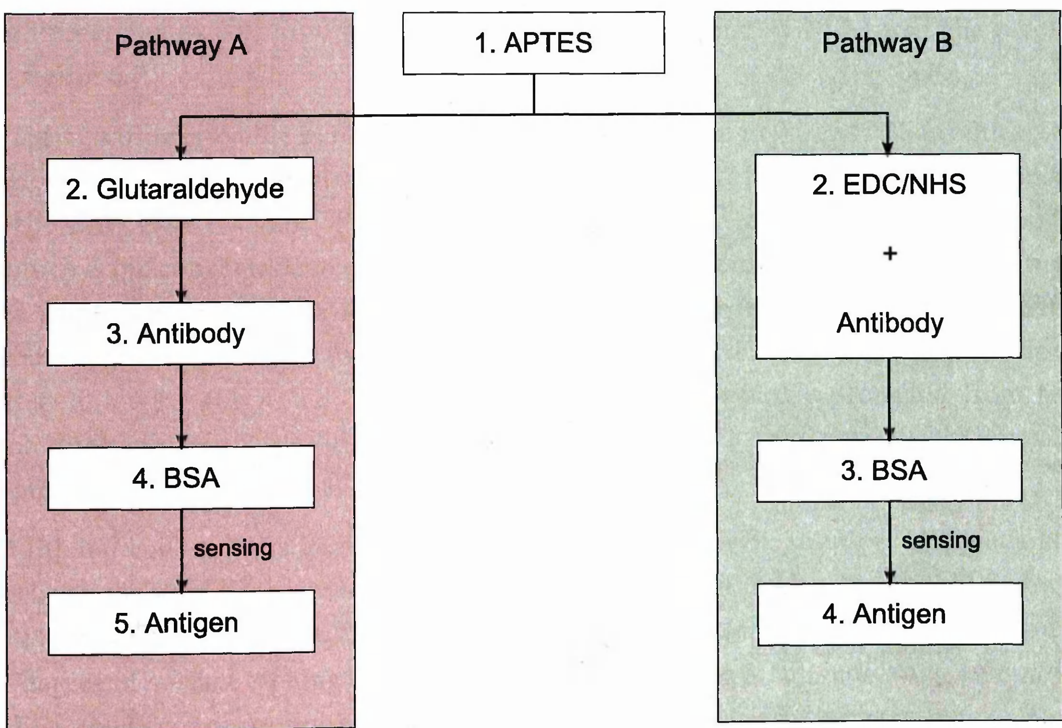

Figure 5.6: The two biofunctionalisation processes. APTES is initially used for amine surface termination. The antibody is then either attached using a linking molecule (pathway A), or by activating groups and directly attaching the antibody to the amine terminating surface (pathway B).

5.3 Electron microscopy

High resolution images of the NWs were obtained at each stage of the functionalisation using scanning electron microscopy (SEM). This allowed direct observation of modifications to the surface of the NWs. In addition to looking for binding and agglomeration of macromolecules, this allowed the surface of the NWs to be monitored for signs of etching or dissociation of the ZnO.

5.3.1 Zinc oxide compatibility tests

Zinc oxide is amphoteric and readily dissolves in both acids and bases. A previous study showed heavy etching of ZnO NWs following immersion in DI water (pH 4.5–5) and ammonia (pH 8.7–9) for 30 minutes and slight etching following immersion in NaOH (pH 7.0–7.1) for 30 minutes. Biocompatibility with horse blood serum was also investigated and showed the wires could survive in the fluid for a few hours, indicating a sufficient "survival time" for incorporation into biosensors [186].

In order to test the compatibility of the ZnO NWs with the phosphate buffered saline (PBS) used for preparation of the biomolecular solutions, SEM images were taken of ZnO NW arrays following immersion in 0.01 M, 0.1 M and 1 M PBS for approximately 24 hours. The results are shown in figure 5.7.

Some light etching is visible in figure 5.7b following immersion in 0.01 M PBS for the extended period. However, higher concentrations show heavy etching (0.1 M) and complete dissociation (1 M) of the ZnO. The standard PBS concentration recommended for storage of antibodies is 0.01 M, which is the concentration used for the remainder of this work. The maximum immersion time for a single step of the process is 2 hours for the antibody immobilisation. These images suggest that negligible etching of the ZnO surface should occur after this duration. It is important to note that following the APTES treatment, the wires may be partly protected from further interaction due to the surface modification. Silanization has been shown to greatly increase the stability of ZnO nanoparticles [187,188].

An additional concern was etching of the ZnO in the EDC/NHS solution. Aqueous NHS is known to be slightly acidic, however, protonation of the EDC/NHS Ab solution will be buffered by the PBS. Immersion of ZnO in 25 mM/50 mM EDC/NHS PBS solution for 24 hours resulted in a similar degree of surface etching caused by the neat PBS (figure 5.7b), indicating compatibility with the EDC/NHS concentrations used for the carbodiimide cross-linking reaction.

(a) 0.01 M PBS

(b) 0.01 M PBS – area indicated in (a)

(c) 0.1 M PBS

(d) 1 M PBS

Figure 5.7: SEM images of NW arrays following 24 hour immersion in different concentrations of PBS. Both (a) and (b) are images for the 0.01 M PBS solution, with (b) providing a magnified high contrast image of the rectangular area indicated in (a). Although large scale structures, such as the NWs, are still visible, light pitting of the ZnO surface is seen in these images, whereas the samples immersed in the 0.1 M (c) and 1 M (d) solutions exhibit complete dissociation.

5.3.2 APTES

The NWs were imaged following immersion in the APTES solution to check the uniformity of coverage and also to ensure that the ZnO surface was absent of any considerable etching or roughening. Following Teixeira et al. [189], initially much high concentrations of APTES were investigated. The effect of immersion of 40% APTES in DI for 10 minutes is shown in 5.8a. Despite rinsing, the image shows considerable retention of APTES resulting in the formation of a multilayer film, although hexagonal facets are still visible in areas, indicating that the ZnO is compatible with high concentrations of APTES. Figure 5.8b shows the effect of immersion in 0.5% APTES solution in DI. For this concentration, no differences were observed before and after APTES treatment using SEM, with no obvious accumulations of APTES found on the sample.

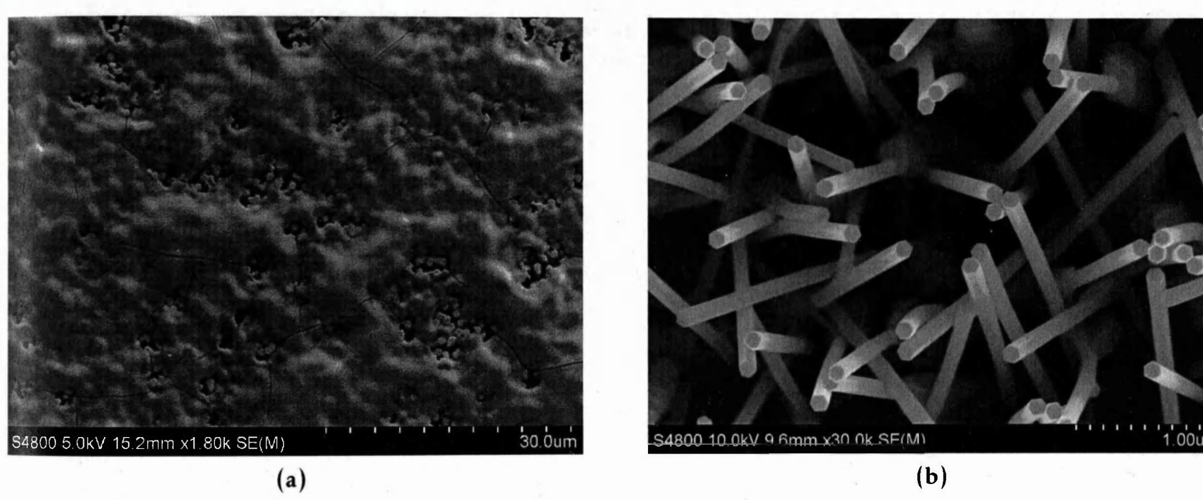

Figure 5.8: Top down SEM images of NWs following treatment with **(a)** 40% and **(b)** 0.5% APTES in DI.

5.3.3 Glutaraldehyde - Pathway A

The GA sample showed significant etching of the ZnO surface following 1 hour immersion. Although aqueous GA is mildly acidic at higher concentrations (> 50%), litmus paper showed the pH of the 2% solution to be indistinguishable from DI water (~pH 6). The etching is therefore likely due to chemical dissociation caused by the DI water:

$$ZnO(s) + 2H^+ \longrightarrow Zn^{2+} + H_2O \quad (5.1)$$

where the Zn^{2+} ions are dissoluble. However the etching was substantially less than that reported by Zhou et al. following immersion in DI water for 30 minutes. From their study, the etch rate of the non-polar m-plane of the NWs is estimated at around 8 nm/min, which would result in full dissociation of the arrays grown on sputtered Ti in around 20 minutes. Figure 5.9 shows an SEM image of the array after 1 hour. Although the m-planes are clearly etched, the NWs have retained their structure and hexagonal termination. This discrepancy from the etching behaviour observed by Zhou et al. could be related to the increased stability resulting from the APTES treated silanized surface, although it could also be explained by the lower pH value of 4.5 for the

DI water used in their work. [186]

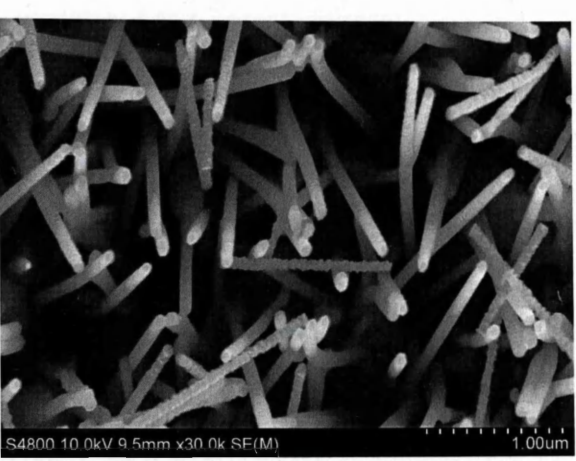

Figure 5.9: SEM image of the NWs following treatment with APTES and glutaraldehyde. Some etching of the ZnO surface is observed which can be attributed to the dissociation of ZnO in DI water.

5.3.4 Anti-hCG, BSA and the hCG protein - Pathway A

Top down SEM images of the NWs following antibody, BSA and antigen treatment are shown in figures 5.10 and 5.11. No further dissociation of the ZnO is evident, and there appears to be considerable softening of the etched *m*-plane surfaces compared with the GA treated sample in figure 5.9, possibly caused by macromolecular attachment. In particular, figure 5.11a shows what appears to be a uniform shell of macromolecules coating the surface of the NWs. No large agglomerations or films were observed on any of the three samples.

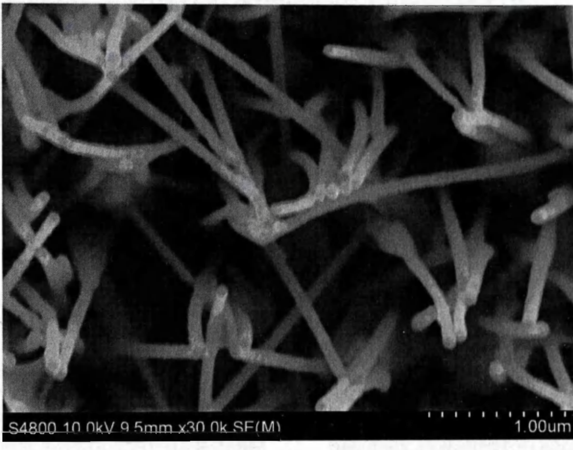

Figure 5.10: SEM image of GA treated sample following attachment of antibody.

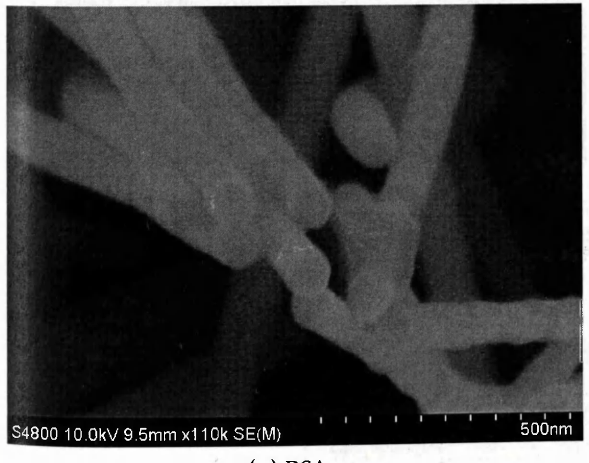

(a) BSA.

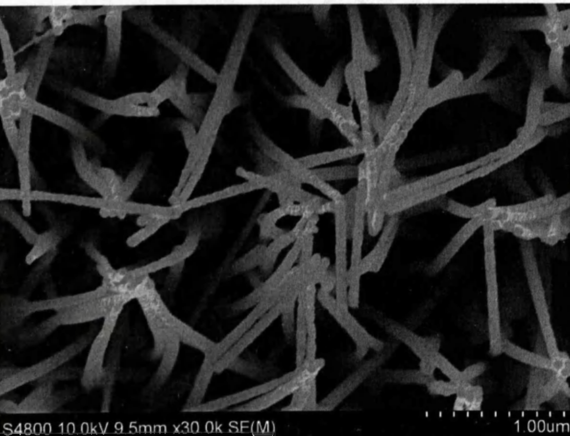

(b) Antigen.

Figure 5.11: SEM images of GA treated samples following attachment of proteins.

5.3.5 EDC/NHS treated anti-hCG - Pathway B

Figure 5.12 shows the NWs following attachment of anti-hCG using EDC/NHS cross-linking. In contrast with the previous method, there is no obvious etching of the NWs, as expected from the EDC/NHS compatibility test. When to compared to the as-grown and APTES treated samples, a clear texture is visible on the surface of the NWs. This texture is especially prominent for the sample subsequently treated with BSA and the hCG protein, shown in figure 5.13, suggesting further addition of material. The coatings appear to be uniform and again, no large agglomerations or films were found on the sample surface. This is an important observation for this attachment method - as mentioned, carboxyl activation could potentially result in severe agglomeration and multilayer formation due to peptide bond formation between neighbouring antibodies. Although multilayer formation can't be ruled out, the SEM analysis suggests a larger change in surface texture following hCG protein attachment when compared with antibody immobilisation, suggesting minimal antibody-antibody conjugation.

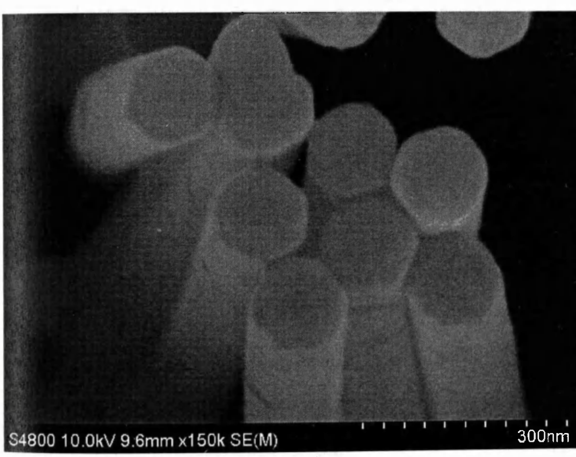

(a) Antibody

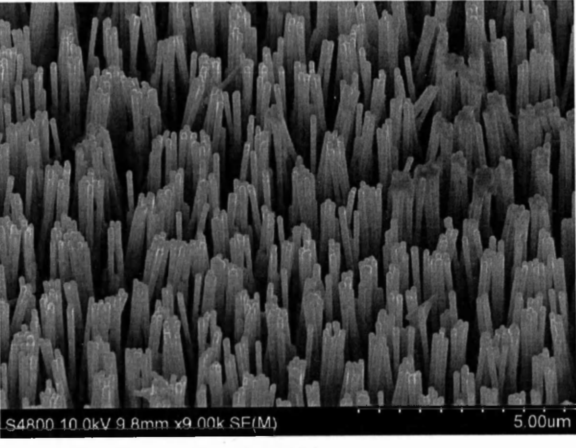

(b) BSA

Figure 5.12: SEM images of EDC/NHS antibody and BSA samples. No etching of the surface is observed, which can be contrasted with the GA samples shown above (figure 5.9).

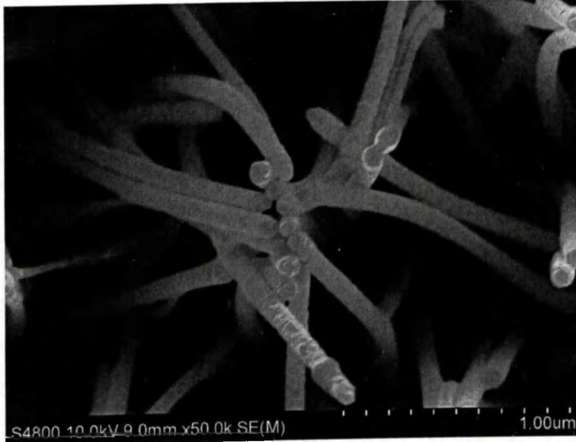

Figure 5.13: Antigen

5.4 X-ray Photoelectron Spectroscopy

Following functionalisation and antibody immobilisation, the samples were scanned using X-ray photoelectron spectroscopy (XPS) to study changes to surface composition and to determine the effect of the surface modification and attachment of biomolecules on the electrical properties of the NWs. The XPS data were collected at the Science City Photoemission Facility, University of Warwick using an XM1000 monochromatic Al K_α X-ray source (see section 3.3.4.5 for details of equipment and data analysis methods). The complete set of samples shown in figure 5.6 up to and including binding of the hCG protein (antigen) from both cross-linking methods were scanned.

Core level spectra were recorded using a pass energy of 10 eV with an energy step size of 0.1 eV. The binding energy windows and elemental sensitivity factors used for quantification are shown in table 5.1. In addition to those listed, the Zn 2s, 3p and 3d photoelectron peaks and also the O, C and Zn Auger peaks were observed on the survey spectra. No evidence of Ti from the sputtered buffer layer was found on any of the samples.

Table 5.1: Binding energy scan range and relative sensitivity factors (RSFs) for core levels.

Core level	Binding energy (eV) initial	Binding energy (eV) final	RSF [190]
P 2p	130	138	0.39
C 1s	282	294	0.25
N 1s	395	405	0.42
O 1s	526	540	0.66
F 1s	684	698	1.00
Zn 2p	1015	1055	4.80*

* given for the Zn $2p_{3/2}$ transition.

5.4.1 Quantification

Following Shirley background subtraction, the peak areas were measured and corrected using the RSFs shown above. These RSFs are empirically determined to account for the differences in scattering cross-sections between transitions and the kinetic energy dependant electron escape depth. It should be noted that full quantitative analysis must take matrix effects into account. Calculation of the matrix correction can be rather complicated and requires an in-depth knowledge of the electron interactions and elemental distribution of the sample [191]. In the case of biofunctionalised samples, this would quickly become intractable. Due to this, in the quantification presented here, matrix dependant electron attenuation is not accounted for. This means that a large variation in the relative abundance of the elements may be expected, depending on the kinetic energy of the transition and the matrix being sampled (see the "universal curve" in section 3.3.4.1). Although the empirical RSFs should account for mean free path correction,

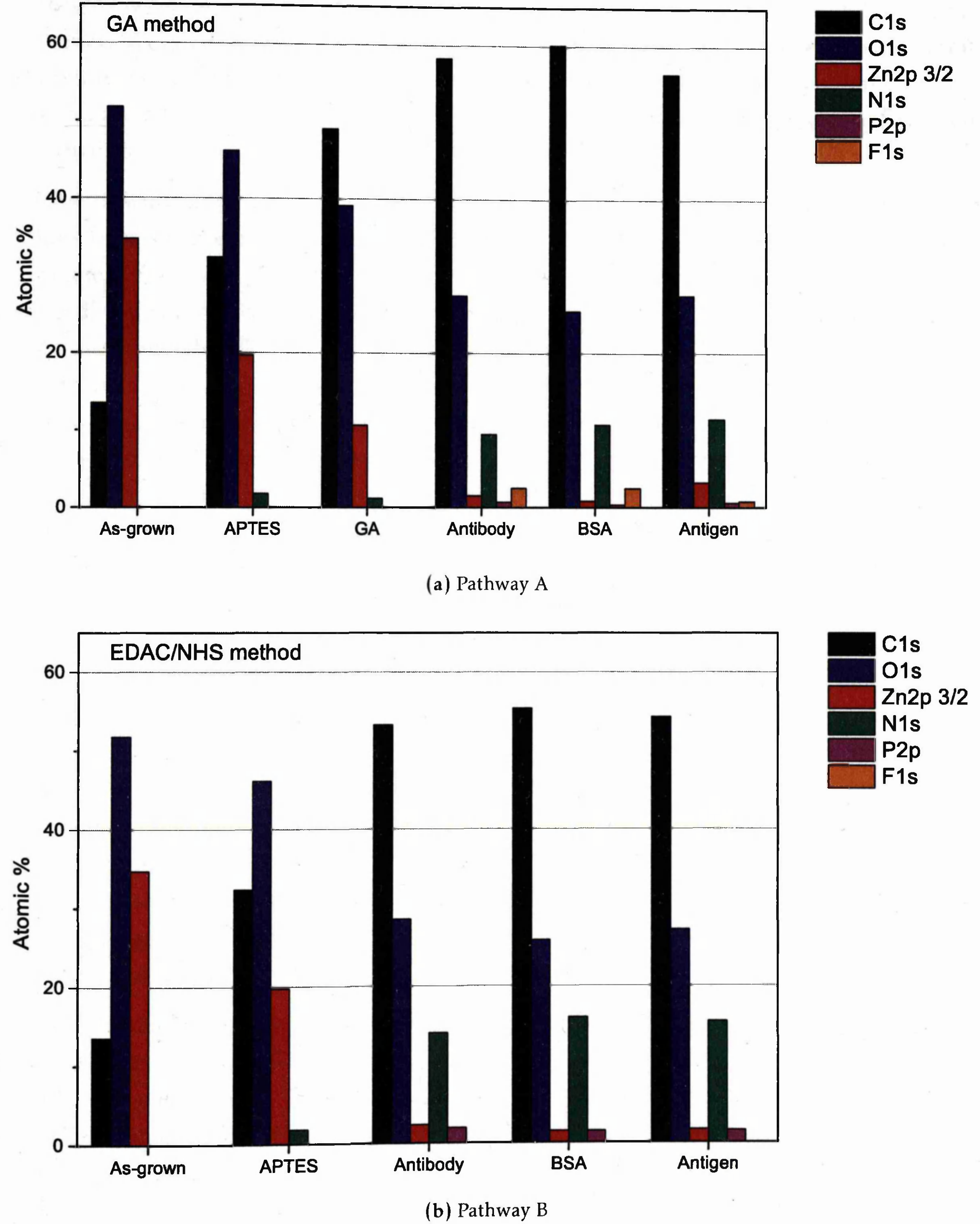

(a) Pathway A

(b) Pathway B

Figure 5.14: Relative composition of each sample, as measured using XPS. (**a**) GA treated samples (**b**) EDC/NHS antibody treated samples.

there is often a large variation in empirically derived RSFs and ideally, quantification should be based on a set of system specific standards. Indeed, the matrix correction factors are known to range from 0.3 to 3 for XPS [192], giving an indication of the importance of matrix correction for accurate elemental quantification. An additional issue with RSF correction is the propagation of uncertainty from low intensity peaks to high intensity peaks when reported as atomic %. Therefore, the quantitative analysis presented previously should not be considered absolute, but instead gives an indication of relative changes between samples following surface treatments. The relative atomic percentages are graphed in figure 5.14

The as-grown sample shows a higher concentration of O relative to Zn, likely due to contributions from surface oxygen species and also possibly from the increased kinetic energy and inelastic mean free path (IMFP) of the O 1s photoelectron compared to the Zn 2p (although, as mentioned, this should be taken into account in the RSF). The as-grown sample exhibits a C : O ratio of approximately 0.26. Following treatment with APTES, the appearance of the N 1s peak, a relative increase in C, and a decrease in measured Zn are all indicative of successful attachment of APTES. No evidence of Si was found, however this is consistent with previous reports on APTES treated metal oxide nanoparticles [193]. APTES has a molecular formula of $C_9H_{23}NO_3Si$, but in solution will lose 3 ethanol groups via hydrolysis of the triethoxy groups into trihydroxyl groups, as shown in figure 5.15. For a completely hydrolysed molecule, this will result in an equal C : O ratio, instead of the ratio of 3 given by the (non-hydrolysed) molecular formula. However, it is unclear if some ethoxy groups are still retained following immersion in DI water for 10 minutes. If all ethoxy groups were present, it would still be possible for the APTES to hydrogen bond to the surface OH through the NH_2 group, as shown in figure 5.15. The fact that the measured C : O ratio is around 0.70 suggests that hydrolysis is taking place, indicating that covalent attachment through silinization is likely. Figure 5.15 shows several possible reaction routes for the APTES molecule, with the surface attachment followed by condensation of the silanol groups (route 1) being the most suitable for subsequent Ab immobilisation. Multilayer formation can also occur due to the amine group of one molecule hydrogen bonding to the silanol group of a molecule covalently attached to the ZnO surface. The ability to form highly branched polycondensed layers at differing stages of hydrolysis makes accurate surface coverage determination from elemental composition problematic.

The GA treated sample shows a further increase in the O : Zn ratio combined with a relative increase in C, as expected. The molecular formula for GA is $C_5H_8O_2$, giving an ideal C : O ratio of 2.5. The measured C : O ratio is approximately 1.25, showing a significant increase from the APTES treated sample, consistent with the addition of GA. SEM imaging of the GA sample revealed significant surface etching of the NWs, indicating removal of the silanized surface. Despite this, only a slight reduction in N is observed following GA treatment. This suggests that some of the silanized surface has been retained, either at the base of the array or on the surface of NWs. Even in the event that the silanized surface is completely removed, GA cross-linking may still function via physical adsorption to the ZnO surface [194].

Both cross-linking methods result in significant compositional changes following application of the antibody. The relative Zn concentration is reduced to a few percent, indicating similar

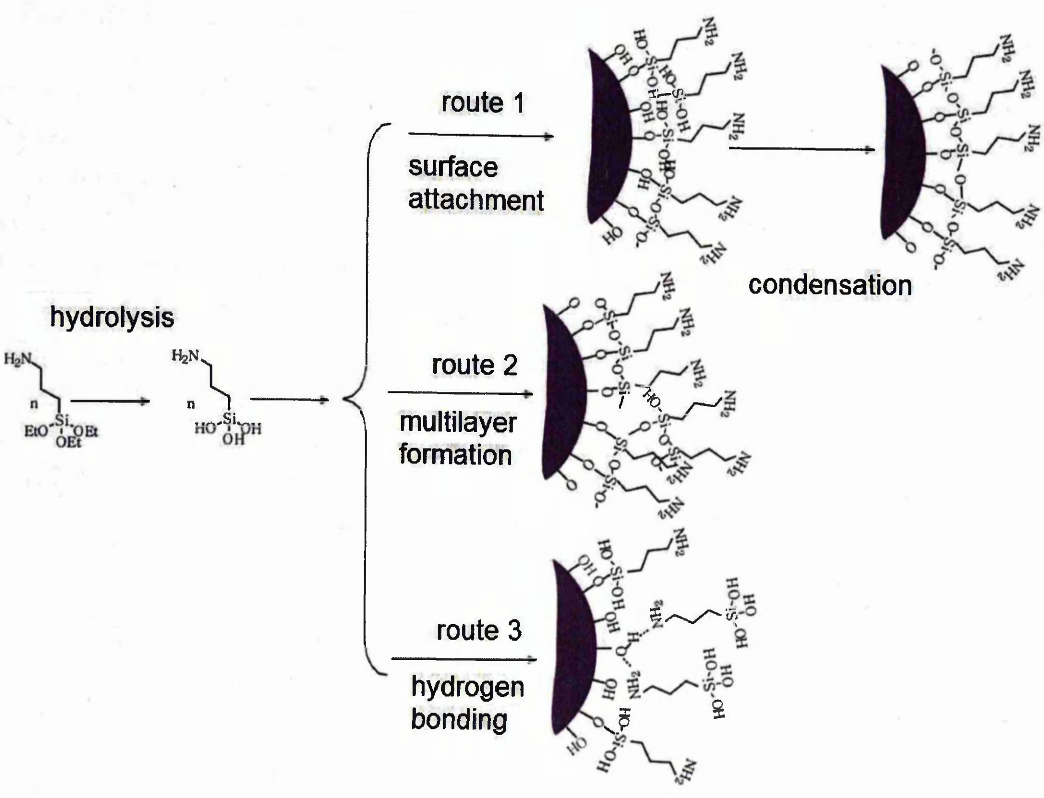

Figure 5.15: APTES silinization of the ZnO surface resulting in different layer formations. Adapted from [19].

levels of surface coverage using both methods. Large increases in the O : Zn ratio, and the relative C and N concentrations are consistent with antibody immobilisation. The P 2p contribution can be attributed to residue from the PBS solution. This could also be the cause of the F 1s peak, however, it is unclear why F was only detected on the GA functionalised samples. A possible explanation is binding between the –CHO terminus of the GA and trace fluorine compounds in the PBS solution. The relative N 1s contribution is larger for the EDC/NHS activated antibody compared with the GA method, and this is also true of comparisons following application of BSA and the hCG protein. This could be indicative of increased Ab coverage or possibly a different binding orientation. Residue from EDC/NHS could also be a factor, however this would seem unlikely, as the molecular formula for EDC ($C_8H_{17}N_3$) indicates that a relative increase in carbon would also be observed, which is not seen when compared with the GA method. In addition, no traces of chlorine were detected following the use of EDC.

Relatively little change is seen in both methods following application of BSA and the hCG protein. Although no significant change is seen in the O : Zn ratio, this may be expected. Due to its size, the anti-hCG would already result in effective attenuation of the NW surface photoelectrons at the point of attachment. Therefore, further grafting of macromolecules to the already immobilised anti-hCG would have relatively little effect on the relative contribution form Zn 2p photoelectrons resulting from incomplete surface coverage. As the composition of the amino acids comprising the proteins is fundamentally similar, consisting of C, N, H and O, the use of elemental analysis is limited when characterising the attachment of further biomolecules to the immobilised antibody.

5.4.2 Peak fitting

The XPS core level peaks were fitted using 30% Lorentzian – 70% Gaussian line shapes following a Shirley background subtraction (section 3.3.4.6). The same initial peak positions were used for all samples with a fitting restriction of ±0.1 eV to account for Fermi shifts and other variations. The resulting fits to the C 1s, O 1s, Zn $2p_{3/2}$ and N 1s peaks are shown for the as-grown, APTES treated and APTES and glutaraldehyde treated samples in figure 5.16. Peak fits following attachment of the antibody, BSA and antigen using the glutaraldehyde and EDC/NHS cross-linking methods are shown in figures 5.17 and 5.18, respectively. These spectra have all been normalised to the trace maxima. This corresponds to the largest intensity fitted component of the as-grown sample (blue component), attributed to lattice zinc and oxygen (Zn^{2+} and O^{2-}) and adventitious carbon [195].

Table 5.2 shows the fitted peak positions with commonly attributed hybridisation states. References [180, 195–199] relate to work conducted on ZnO, nanostructures and other metal oxides, whilst references [200, 201] focus on biofunctionalisation.

Table 5.2: Fitted components for C, O, Zn and N peaks. The legend applies to the components shown in figures 5.16, 5.17 and 5.18 and also to the quantification in figure 5.19.

Core level	B.E (eV)	Legend	Contributions
C 1s	285.7	■	C–C [196]
	287.0	■	C=O [196], C–O [201], C–N [200]
	288.9	■	O–C=O [201], N–C=O [201]
	289.8	■	O–C=O, COOH [196], N–C=O [201]
O 1s	531.0	■	Zn–O [195]
	532.6	■	COOH, $Zn(OH)_2$ [196], ZnO_x [197]
	533.5	■	H_2O [195], CO_2 [197], OH^-, O_2 [198], C–O, O–C=O [180], CHO [202]
	534.3	■	H_2O [180, 199]
Zn $2p_{3/2}$	1022.4	■	Zn–O [196]
	1023.2	■	$Zn(OH)_2$ [196]
	1024.8	■	–
	1020.6	■	–
N 1s	401.0	■	N=C [201], NH_2 [200]
	402.6	■	N–C=O [201]

The contributions are included as a guide and it should be noted that there is much overlap between the assignment of certain chemical states. In addition, shake-up peaks have not been accounted for in this analysis. The shake-up peaks are part of a class of intrinsic loss events due to electron-electron interactions and appear on the high binding energy side of the main photoelectron peaks. This is particularly problematic for the C 1s and O 1s transitions. For the more chemically complex surface treatments, each hybridisation state could give rise to multiple

shake-up peaks, and consequently each fitted component is likely related to multiple hybridisation states and/or loss features. This is not an issue for the elemental quantification given above, however, it can cause the lower binding energy components to be underestimated due to losses which are subsequently included in the higher binding energy components.

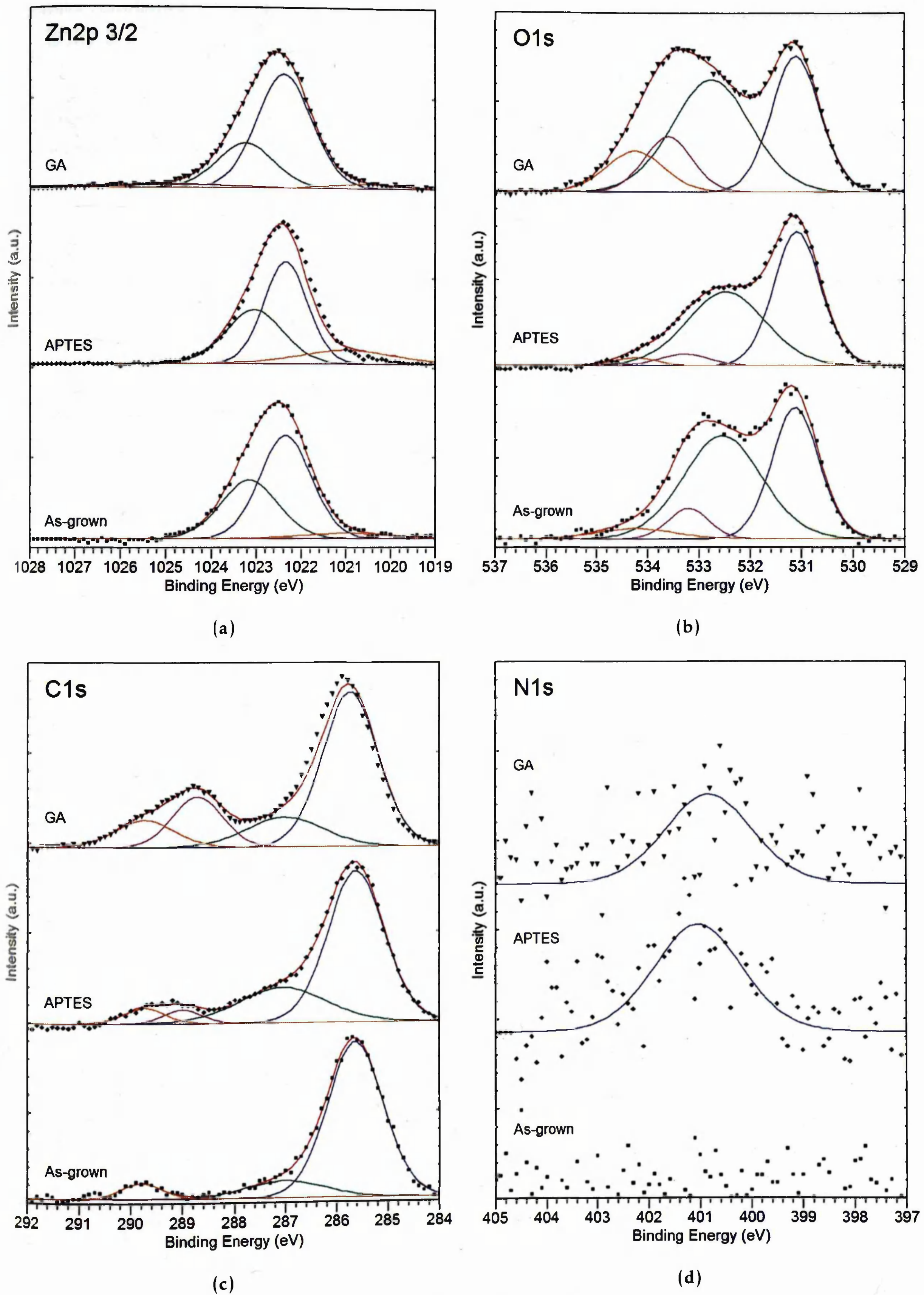

Figure 5.16: Normalised XPS spectra of as grown ZnO NWs, NWs treated with APTES and NWs treated with APTES and glutaraldehyde.

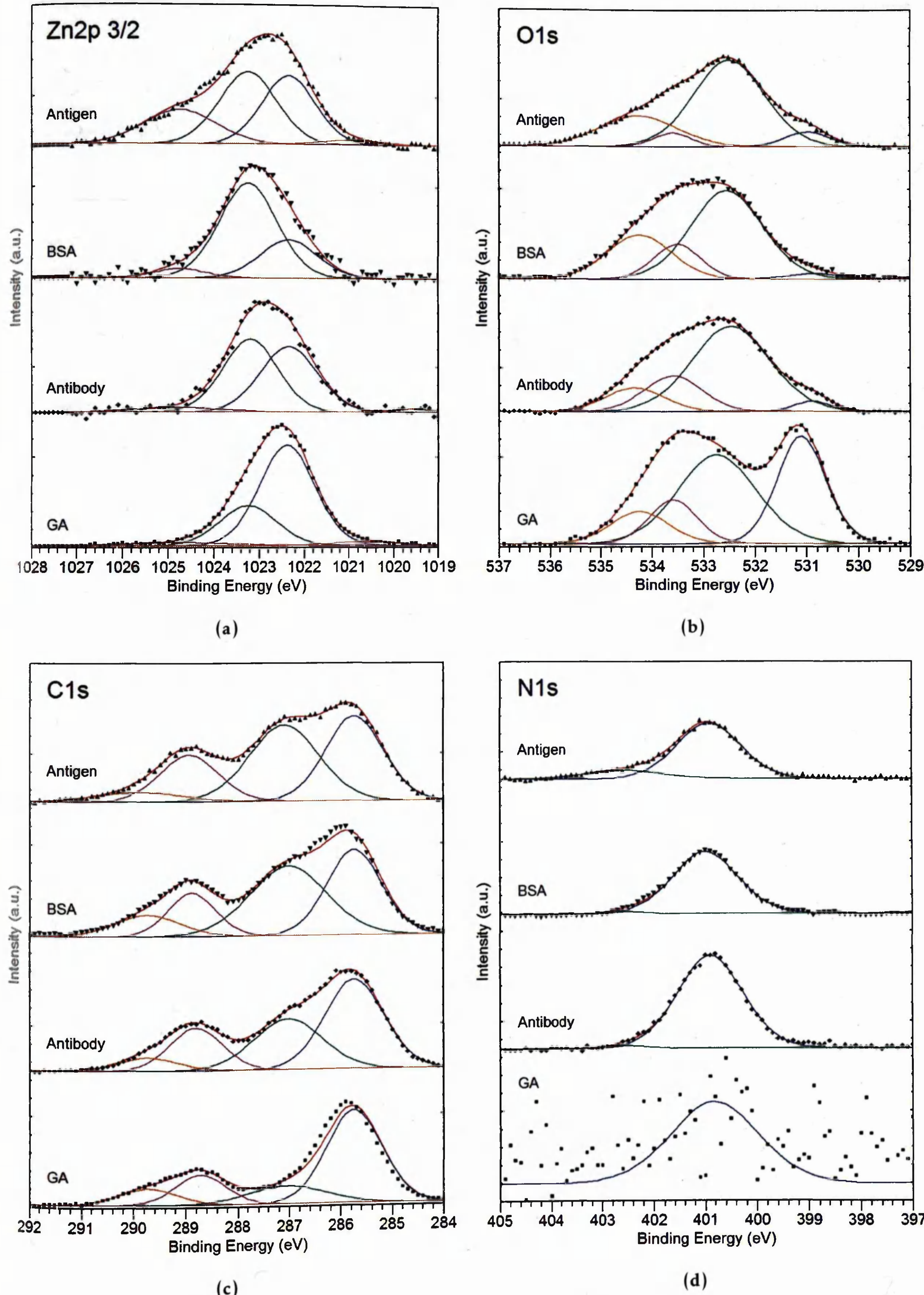

Figure 5.17: Normalised XPS spectra of ZnO NWs progressively treated with glutaraldehyde, the hCG antibody, BSA and the hCG protein.

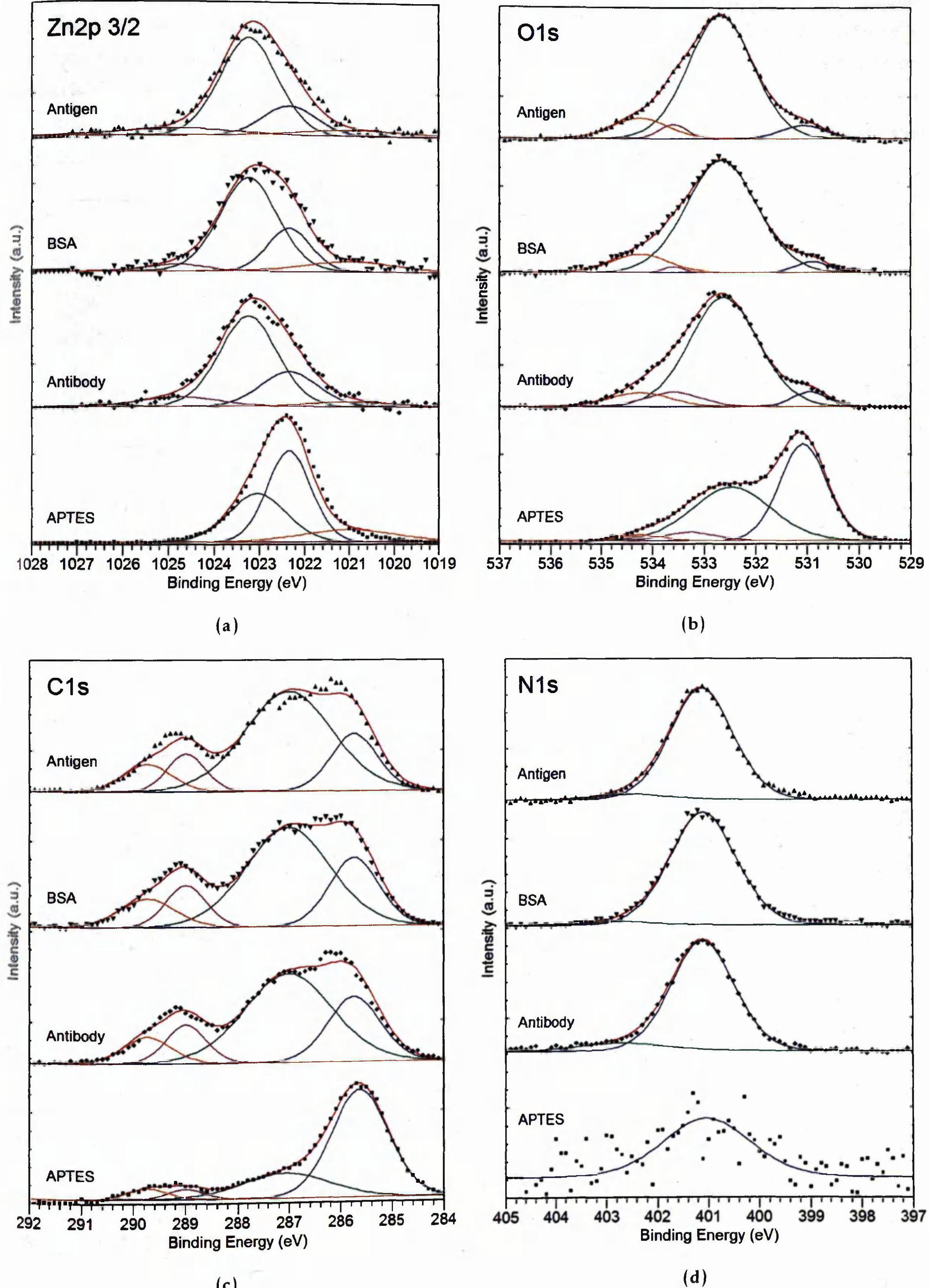

Figure 5.18: Normalised XPS spectra of ZnO NWs progressively treated with APTES, the hCG antibody activated using EDAC/NHS, BSA and the hCG protein.

The relative contribution of each component to the elemental concentration is shown in figure 5.19. To clarify, the preceding spectra showed normalised components, which allows for a relative comparison between components at each stage of the functionalisation. However, for direct comparison of each component between samples, the relative elemental concentrations shown previously in figure 5.14 must be taken into account. This is the information displayed below in figure 5.19.

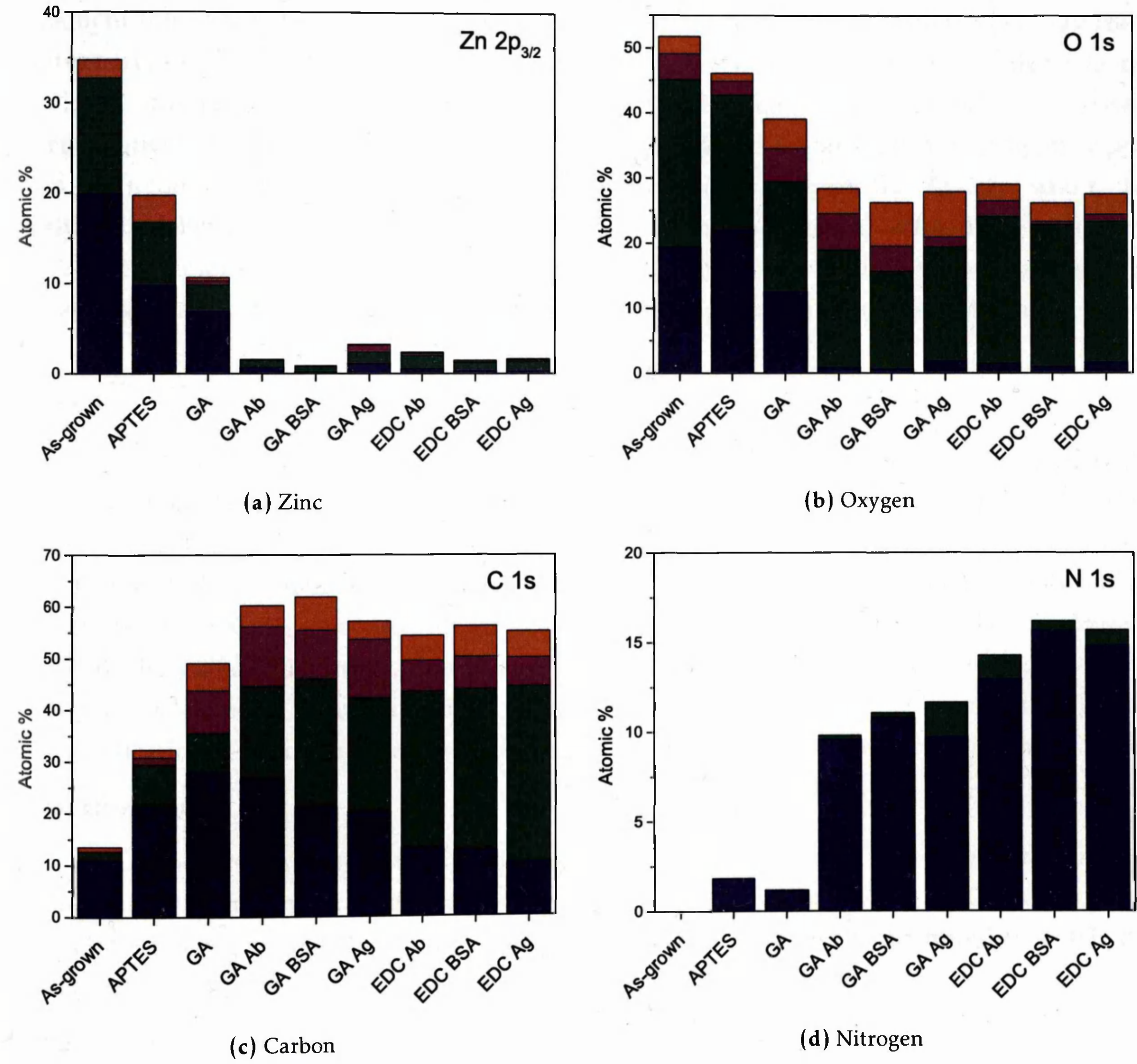

(a) Zinc

(b) Oxygen

(c) Carbon

(d) Nitrogen

Figure 5.19: XPS: Elemental composition of each sample by component. The fitted peaks are shown in figures 5.16, 5.17 and 5.18. Table 5.2 shows the approximate fitted peak positions with colour key and commonly attributed hybridisation states.

It is important to study the component composition of the as-grown NWs for later comparison with functionalised samples. As previously mentioned, the as-grown sample displays high intensity Zn and O peaks (blue components), attributed to lattice atoms. The larger (green) component fitted on the high binding energy side of the lattice O is commonly seen with metal oxide nanostructures and is attributed to hydroxyls and other strongly bound surface oxygen [195,196]. The smaller pink and orange components at even higher binding energies are likely the result of

adsorbed H_2O and oxygen species such as O_2 [195]. In the case of the Zn $2p_{3/2}$ transition, the higher binding energy (green) component can also be attributed to the presence of surface hydroxyls, forming $Zn(OH)_2$ [196], with additional possible contributions from lower co-ordination number (oxygen vacant) ZnO_x, which would result in a shift to higher binding energy from the increased Madelung energy [203]. The origin of the Zn components at 1020.6 eV and 1024.8 eV is less clear, although four components were required to obtain an accurate least squares approximation to the trace for all samples. A possible explanations for the low binding energy (orange) component present on the as-grown sample is a shift due to the decreased Madelung energy contribution from e.g. interstitial oxygen or zinc vacancies. In section 4.4.2.3, PL revealed a large deep level emission for ZnO NWs grown on Ti layers, consistent with interband defect states caused by metal incorporation. Lattice point defects and defect complexes formed by incorporation of Ti could also play a part in the binding energy shifts seen for the Zn $2p_{3/2}$ and O 1s transitions. Polymerised or short chain adventitious carbon is responsible for the large (blue) component seen for the C 1s transition (C–C bonds) with small contributions from singly (green) and doubly (orange) bound oxygen functionality [204], or from shake-up losses from the main C–C peak.

APTES

The APTES sample shows an increase to the (blue) C 1s component which is associated with aliphatic carbon. The increase in the higher binding energy (green and pink) components could be related to C–O and C–O–Si bonds, due to the APTES molecule remaining in its non-hydrolysed state. This may offer a method for determining the degree of covalent attachment, as molecules retaining their $Si(OC_2H_5)_3$ groups would not participate in silanization, and are likely hydrogen bonded to the surface. However, this increase could also be related to the presence of $C–NH_2$ groups. The C–Si bond should appear at a lower binding energy to the C–C component [205], and no indication of shouldering or a shift to lower binding energies is seen for the aliphatic peak.

Glutaraldehyde

An expected increase is seen in the (blue) aliphatic carbon component and also in the higher binding energy (pink and orange) components that can be attributed to the CHO groups. The relative increase in the pink and orange O 1s components can also be attributed to aldehyde groups.

Macromolecules

A substantial decrease is seen in the lattice oxygen component of the O 1s spectra. Although an overall decrease in oxygen is seen relative to the other elements, the remaining oxygen is dominated by the green component which can be attributed to COOH and other organic groups. The pink and orange components associated with aldehyde groups remains larger for the GA cross-linked samples when compared to the EDC/NHS samples. This likely indicates a reduced Ab coverage when using the GA method. This is also corroborated by the larger green organic component when using EDC/NHS cross-linking.

Contributions to the C 1s from aliphatic carbon remain high when using the GA method,

despite an increase seen for the components ascribed to oxygen and nitrogen bonded carbon (green and pink). Despite this, similar carbon concentrations are measured for both cross-linking methods, with the EDC/NHS samples show a much larger relative contribution from the green peak associated with oxygen and nitrogen bonding. This can be used to make a claim about the reduced Ab coverage when using the GA method analogous to the one made above regarding the O 1s contributions.

Interestingly, when using the GA method a large additional component is seen at high binding energy for the Zn $2p_{3/2}$ transition following attachment of the antigen. This coincides with an increase to the high binding energy shoulder of the N 1s peak and could indicate non-specific binding of the antigen to the ZnO surface, possibly due to insufficient rinsing following immersion in the antigen solution.

5.4.3 Valence band scans

Valence band spectra were obtained in the binding energy range -0.5 to 7.5 eV. The spectrometer work function was calibrated using the Fermi edge and $3d_{5/2}$ peak recorded from a polycrystalline Ag sample immediately prior to the commencement of the experiments. When mounting the samples, welded Ta strips were used to ensure a good electrical contact to the surface of the NW arrays. Charge neutralisation was also used to test the quality of the contact to the samples, with no charging observed. A typical VB scan is shown in figure 5.20 for the as-grown sample. To obtain the location of the VB maximum (E_V) relative to the Fermi level ($E_F = 0\,\text{eV}$), a linear fit is extrapolated from the lower binding energy edge of the VB spectrum to a line fitted to the instrument background which provides the exact onset of the VB emission $\zeta = E_V - E_F$.

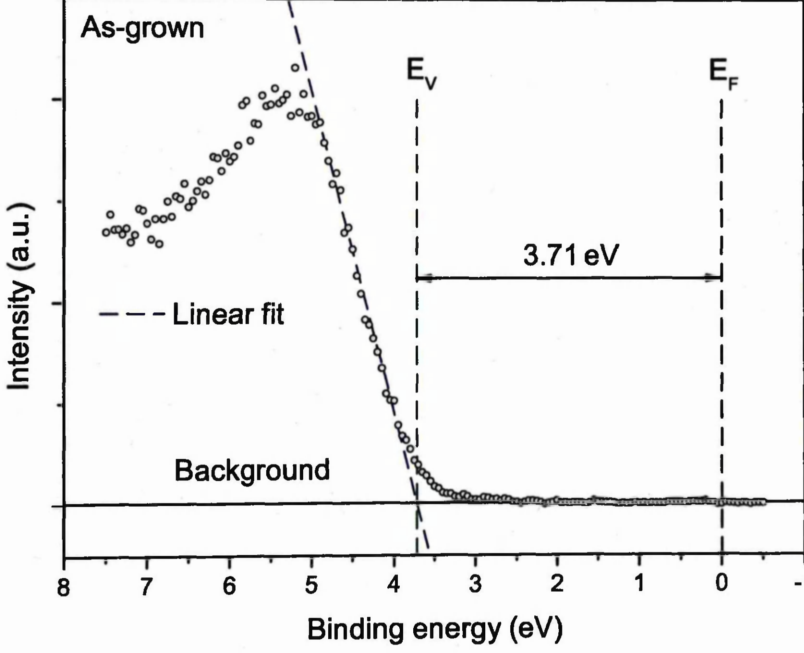

Figure 5.20: XPS spectra of the Fermi level energy and valence band maximum of the as-grown ZnO NWs. A valence band position greater than the ZnO band-gap indicates surface metallisation.

Table 5.3 shows the value of ζ for the set of samples. It is interesting to note that all samples appear to exhibit an energy difference between the VB and the Fermi level greater than the ZnO band-gap ($\zeta > E_g$). Subsequent PL, detailed in section 5.5, revealed the band-gap for all samples to be similar to that given in the previous chapter (3.34 eV following addition of the exciton binding energy), ruling out potential enlargement of the band-gap due to e.g. Ti incorporation.

As previously mentioned, care was taken to ensure that the samples were not charging. If charging were to occur, the emission of photoelectrons results in a net positive charge region at the surface. Consequently, the surface acquires a positive potential, reducing the kinetic energy E_k of the emitted electrons by the amount ΔV_C. The binding energy, E_b for all photoelectrons is therefore shifted to a higher value:

$$E_b = h\nu - (E_k - \Delta V_C). \tag{5.2}$$

Table 5.3: Location of valence band maximum relative to the Fermi level.

Sample	ζ (eV)
As-grown	3.71
APTES	3.65
GA	3.67
GA Antibody	3.58
GA BSA	3.70
GA Antigen	3.65
EDC Antibody	3.66
EDC BSA	3.62
EDC Antigen	3.68

An indication that this may be the case is provided by the C–C adventitious carbon peak, which appears to be located at a high binding energy. When used as a binding energy reference, the spectrum is usually adjusted to locate the carbon peak at around 285 eV, approximately 0.7 eV less than that measured here. If the same correction is applied to the valence band position for the as-grown sample, it would be located at around 3 eV, indicating surface depletion which has been extensively reported for ZnO nanostructures [52, 195, 206, 207]. At the time of writing, this is being verified on a separate XPS system, with direct comparison with NWs grown on sapphire, which have been shown to exhibit surface depletion, resulting in the Fermi level residing a few kT below the conduction band [208].

Due to differences in the growth method or incorporation of Ti dopants, it is possible that these wires are instead exhibiting surface accumulation. Hu et al. have studied surface accumulation in ZnO NWs and suggest the NW is composed of a bulk semiconductor surrounded by a metallic surface accumulation layer, which is essentially a 2D electron gas. They attributed this surface accumulation to an excess of hydroxide – during formation of the hydroxide the adsorbed atomic H donates electrons to the ZnO surface i.e. it acts as an electron donor that increases the carrier concentration in the surface layer. Interestingly, for the as-grown sample, the O 1s surface oxygen component attributed to hydroxide (green component) is substantially larger relative to the lattice oxygen peak when compared to previous XPS studies of ZnO NWs [100, 195]. Figure 5.21 shows the band diagram for surface accumulation at the m-planes of the NWs, as observed by Hu et al. At the side facets of the NW, the Fermi level is within allowed electronic states, hence the NW surface is referred to as "metallised".

As a consequence of the polar symmetry of ZnO crystallised in the wurtzite phase, the $(0\,0\,0\,1)$ and $(0\,0\,0\,\bar{1})$ surfaces exhibit different bulk terminations, with the first being terminated by zinc atoms and the opposite face terminated by oxygen atoms. The electrostatic potential due to the internal dipole moments causes a shift of the bands relative to the Fermi level in opposite directions at the two polar surfaces [20], as showing in figure 5.22. This simplified charge transfer mechanism is associated with a significant energy cost, and other stabilisation mechanisms such as surface reconstructions [209] and adsorption of impurities [20] are commonly used to com-

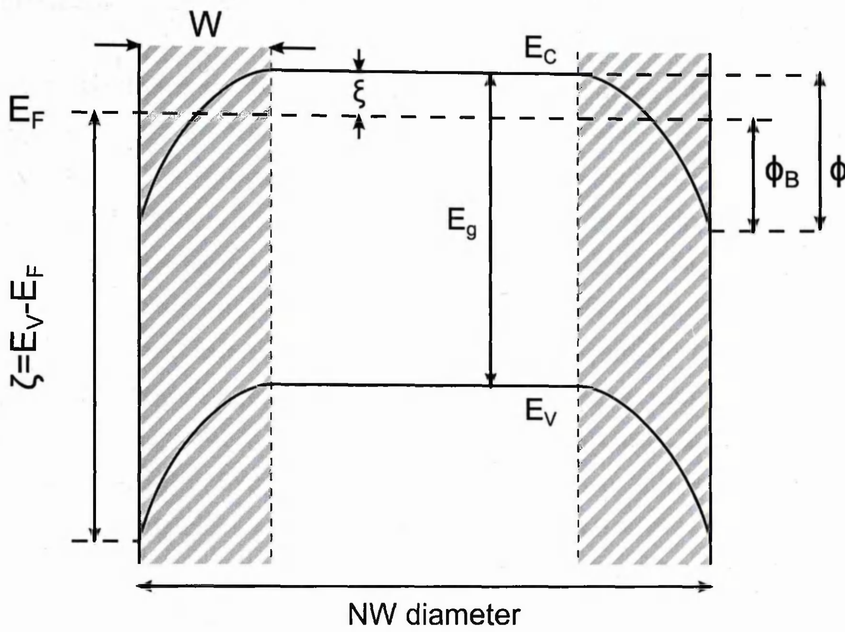

Figure 5.21: Band diagram of surface accumulation with conduction band minimum (E_C), valence band maximum (E_V), Fermi level energy (E_F), surface band bending (ϕ), surface barrier height (ϕ_B), and width of the surface band bending region (W).

pensate for the internal dipole moments. As the electron take-off angle is, on average, normal to the NW tips, it is possible that the accumulation measured in the VB scans is a result of the increased electron contribution from the polar facets of the NWs, instead of from the non-polar m-planes. However, as mentioned, depletion if this is not commonly observed on XPS measurements conducted on NW arrays [208], and is discussed further in combination with the electrical measurements in section 5.6.

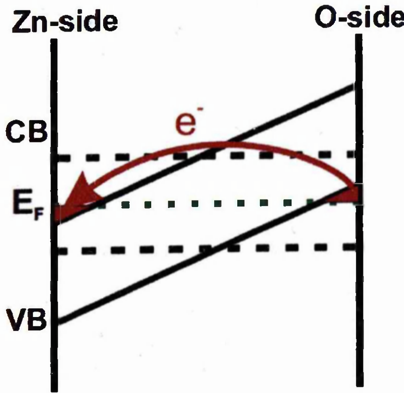

Figure 5.22: Schematic of surface metallisation along length of ZnO NW. Reproduced from [20].

5.5 Photoluminescence Spectroscopy

Photoluminescence spectroscopy was used to optically characterise the samples studied using XPS. The samples were illuminated using a 7 mW 325 nm He–Cd laser at room temperature, as described in section 3.3.6. Of particular interest were changes to the widely reported ZnO deep level visible emission, which is commonly attributed to both extrinsic and intrinsic defects and/or interface states. Due to the large surface to volume ratio of the NWs, modulation of the surface chemistry can have a dominant effect on this deep level emission. If these interband defect states are electrically active, modulation of this emission could be indicative of large surface dominated variations in the NW conductive properties. Figure 5.23 shows the PL spectra for the two antibody attachment methods. The data is the normalised average spectra taken from five locations on each sample. Error bars have been omitted to allow the spectra to be plotted on the same graph, however cross sample NBE to defect variation was found comparable to that measured for the NWs grown on sputtered conductive layers in section 4.4.2.3.

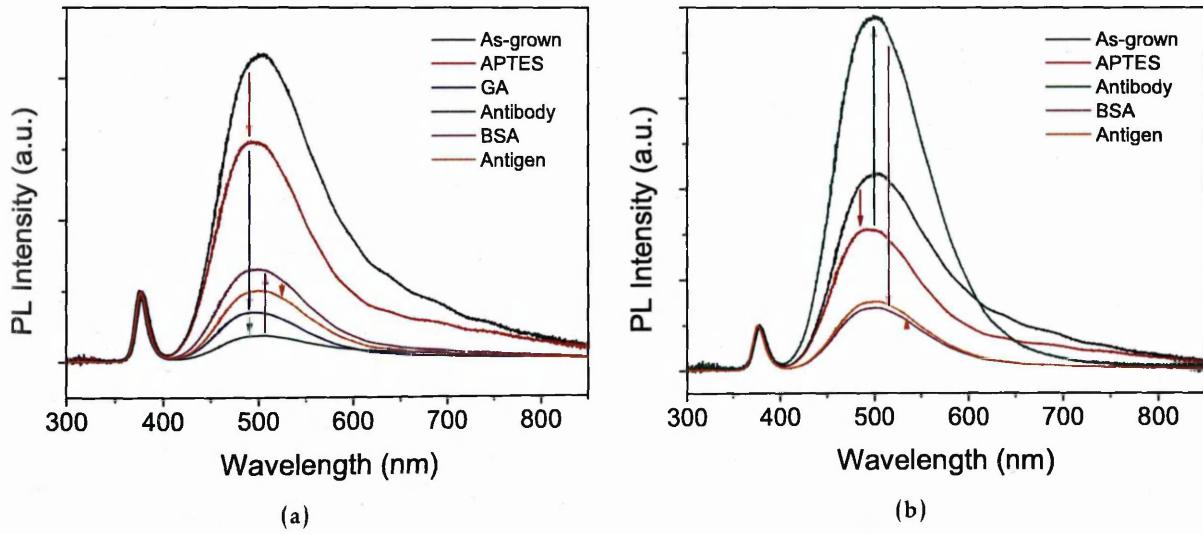

Figure 5.23: PL spectra, normalised to the NBE emission, for **(a)** GA antibody immobilised samples (pathway A) **(b)** EDAC antibody immobilised samples (pathway B). The arrows are a guide between progressive attachment steps.

The location of the NBE emission is shown in table 5.4 and is used to calculate the band-gap through addition of the exciton binding energy (60 meV). As previously mentioned, measurement of the NBE excitonic emission is of particular interest to ensure that the band-gap remains constant across samples. When considering surface band bending, this rules out changes to the band-gap and confirms that the valence band XPS scans are indeed describing surface metallisation. Variation in the band-gap across samples is relatively small with a total range of 34 meV or around 1%.

A large degree of variation is seen in the deep level visible emission caused by intrinsic defects and extrinsic surface states. For the GA cross-linking method, silinization and subsequent functionalisation and attachment of biomolecules results in surface passivation i.e. an increase in the ratio between the NBE emission and defect emission. In the case of the EDC/NHS, attach-

ment of the activated Ab yields a large increase in the visible emission, which is subsequently quenched following application of BSA and hCG. This is in contrast to the lowest level defect intensity measured following attachment of the Ab using the GA method. This reflects the differing surface chemistry and Ab attachment mechanisms for the two methods. Interestingly, the BSA and antigen treatments result in a similar NBE to defect ratio for both cross-linking methods. The integrated intensity ratios are discussed in further detail and compared with individual NW resistivity measurements in section 5.6.1.3.

Table 5.4: Position of the NBE peak as measured using PL. The band-gap, E_g, is obtained following addition of the exciton binding energy (60 meV).

Sample	NBE peak (nm)	E_g (eV)
As-grown	378.93	3.332
APTES	377.76	3.342
GA	375.06	3.366
GA Antibody	375.85	3.359
GA BSA	375.38	3.363
GA Antigen	376.16	3.356
EDC Antibody	377.61	3.343
EDC BSA	376.45	3.353
EDC Antigen	376.42	3.354

5.6 Electrical Measurements

Electrical measurements were conduced on individual ZnO NWs in the lateral NW FET configuration, following transfer from the samples analysed using XPS and PL. To avoid NW alignment processes or patterning of contacts using e.g. E-beam lithography, the measurements were conducted in an Omicron UHV Nanoprobe system. Briefly, the nanoprobe consists of four independent STM tips capable of creating nanoscale non-destructive contacts to individual NWs. An SEM located above the sample stage allows for accurate sample positioning and precise tip approach and contact formation. The tungsten tips, formed using DC etching, were current annealed *in-situ* to > 2200 K in order to remove tip oxide and contaminants [210]. Two tips were used to probe individual NWs, with initial low voltage current-voltage (I-V) characteristics used to establish the quality of the contacts. A noisy or highly non-linear I-V response was indicative of poor quality contacting, which could usually be corrected by increasing the contact pressure (lowering the tip height) or by repositioning the tip, in order to achieve an Ohmic I-V response.

The NWs were shear transferred from the growth substrate to lie laterally on a 100 nm thick layer of silicon dioxide, which was grown thermally using dry oxidation of the n-type Si substrate. Following growth of the SiO_2 layer, the surface of the dielectric was spin coated in a protective layer of photoresist and buffered oxide etch (BOE) solution was used to remove the oxide from the rear portion of the substrate to allow electrical contact for back-gated measurements. Prior to NW transfer, the substrates were cleaned using Piranha solution (section 3.2.1) in order to remove resist solvent residues, which have previously been shown to result in heavy electron beam deposition leading to nanoprobe contacting issues [88]. A schematic of the nanoprobe electrical measurements in the FET configuration is shown in figure 5.24.

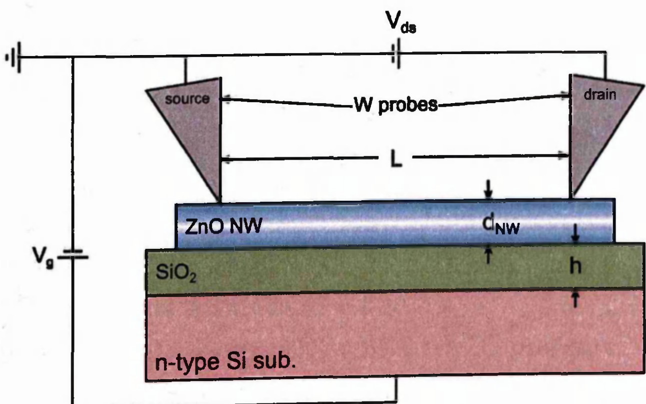

Figure 5.24: Schematic cross-section of measurement set-up in the lateral FET configuration. The diameter of the NW, thickness of the dielectric layer are and length of the channel are labeled d_{NW}, h and L, respectively.

Figure 5.25 shows an SEM image of a NW in contact with the two tungsten tips. The dimensions of individual NWs were measured for subsequent analysis, as shown in the inset cross-sectional line profile. The width was measured at approximately half the maximum grayscale value across the NW, whilst the channel length was measured between tips. As the sample surface is normal to the beam, the tip obscures the full width of the NW, leading to problems deter-

mining the point of contact between tip and NW. Consequently, the uncertainty in channel length is given by measuring the inside and outside separation between tips. For more infromation on measumrement error and uncertainty propagation see appendix B.

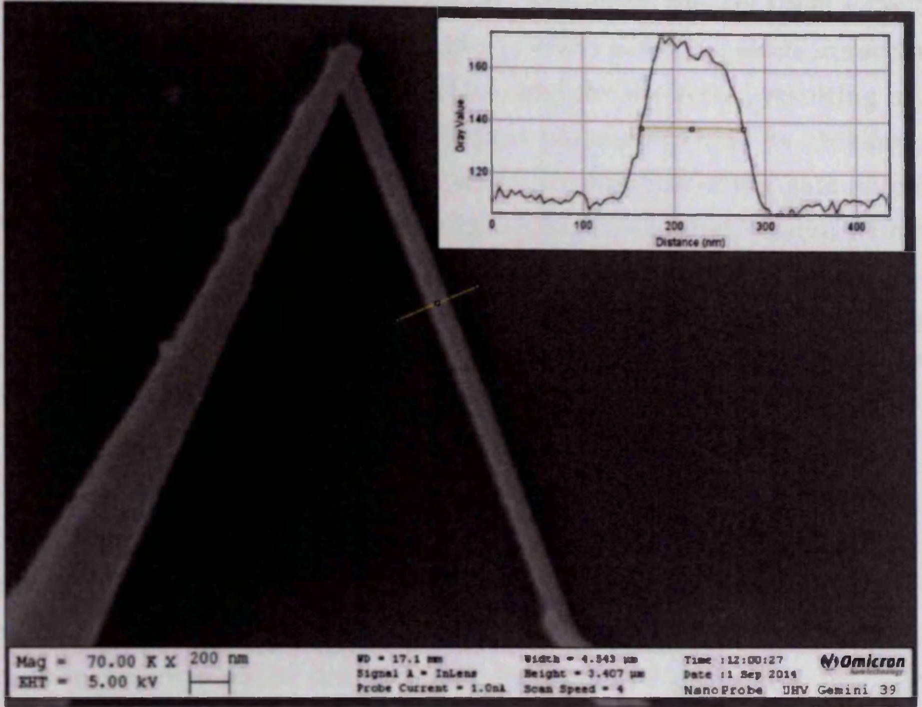

Figure 5.25: Nanoprobe SEM image showing two tungsten probes contacting a silanized NW treated with anti-hCG and BSA. A line profile across the wire is shown inset.

As mentioned, the NWs were transferred from the samples used for XPS and PL analysis, so comprised a full set of progressively treated samples for both antibody cross-linking methods. To summarise, the sample treatments were as follows:

1. As-grown
2. APTES treated (silanized)

Pathway A (glutaraldehyde cross-linking method):

3. APTES + glutaraldehyde
4. APTES + glutaraldehyde + anti-hCG
5. APTES + glutaraldehyde + anti-hCG + BSA
6. APTES + glutaraldehyde + anti-hCG + BSA + hCG protein

Pathway B (zero-length cross-linking method):

7. APTES + EDC/NHS treated anti-hCG
8. APTES + EDC/NHS treated anti-hCG + BSA
9. APTES + EDC/NHS treated anti-hCG + BSA + hCG protein

5.6.1 Back-gated measurements

For ZnO NW FETs, the majority carriers are electrons which result from intrinsic point defects such as oxygen vacancies and zinc interstitials [29]. Therefore, the ZnO NW FETs belong to the n-channel group of devices. This means that under positive gate bias, electrons accumulate at the interface between the active layer (the NW surface) and the dielectric, resulting in an increased conductivity. In this configuration, several physical parameters may be obtained by studying the behaviour of the drain-source current, I_{ds}, under modulation of the gate potential, V_g. The transconductance, g_m, is defined as the differential of the drain-source current with respect to the gate voltage. The point at which the transconductance is maximal can be used to calculate the threshold voltage, V_{th}, which is defined as the gate voltage obtained by extrapolating the linear region of the transfer characteristics from the point of maximum slope to the off-state drain-source current. The threshold voltage characterises the operating mode of the FET. Commonly, ZnO NW FET devices operate in on-type, n-channel depletion mode (D-mode) [211] i.e. non-zero current at zero gate bias and a negative threshold voltage. However, some groups have observed enhanced mode (E-mode) behaviour, characterised by an off-state current at zero gate bias and a positive threshold voltage. Generally, this has been attributed to surface defects acting as traps and scattering centres, reducing the carrier density at the NW surface [212]. Consequently, formation of a channel requires additional localised charge, necessitating a positive gate threshold.

In the linear regime, with the FET acting as a voltage controlled resistor, the transconductance is expressed as [213]:

$$g_m = \mu \frac{C_g \left(V_g - V_{th}\right)}{L^2}, \tag{5.3}$$

where μ is the majority carrier mobility, C_g is the gate-NW capacitance and L is the channel length. This can be used to calculate μ, the total charge (Q_{tot}) and the carrier concentration (n) in the NW, provided the gate capacitance is known. Typically, in back-gate NW FET geometries, an analytical formula derived from a metallic cylinder on an infinite plane of dielectric is used for calculating the gate-NW capacitance [214]. The model and assumptions are detailed below.

For the back-gated measurements, a set of 5×100 point IV curves were collected over the range -1 V to 1 V for each gate voltage, at a rate of 0.02 seconds per point. The back-gate voltage was stepped from -20 V to 20 V in 1 V increments. These IV curves were averaged to give an I_{ds} value for each value of V_{ds} and V_g. Measurements were conducted on a NW FET for each of the nine stages of surface treatment detailed above.

5.6.1.1 Analysis

Analysis of the transfer characteristics of each FET device was conducted in *Mathematica*. The general approach is to calculate the transconductance and threshold voltage from the transfer characteristics (I_{ds}–V_g curves). The threshold voltage and the gate capacitance, which is a function of the material properties and NW dimensions, can then be used to calculate the carrier concentration.

Transconductance and threshold voltage

In order to extract the transconductance and threshold voltage, I_{ds}–V_g curves were plotted for a given V_{ds}, and fitted with Boltzmann-Sigmoid functions, which are of the form:

$$y(x) = A_2 + \frac{A_1 - A_2}{1 + \exp\left(\frac{x - x_0}{\mathrm{dx}}\right)}, \tag{5.4}$$

where A_1 and A_2 are the initial and final values such that

$$\lim_{x \to -\infty} y(x) = A_1 \qquad \text{and} \qquad \lim_{x \to \infty} y(x) = A_2, \tag{5.5}$$

x_0 is the centre of the linear region, dx is the time constant determining the gradient of the linear region of the Boltzmann-Sigmoid function and x is the dependant variable, which in this case is the gate voltage, V_g. Assuming n-channel behaviour, A_1 and A_2 correspond to the off-state and on-state values of the drain-source current I_{ds}. The gradient of the I_{ds}–V_g curve gives the transconductance, which is defined as:

$$g_m = \left(\frac{\partial I_{ds}}{\partial V_g}\right)_{V_{ds}}. \tag{5.6}$$

For the Boltzmann-Sigmoid function, the gradient at the centre of the linear region is calculated by taking the differential of equation 5.4 when $V_g = x_0$. This simplifies to:

$$g_{m(V_g = x_0)} = \frac{-A_1 + A_2}{4\mathrm{dx}}. \tag{5.7}$$

If a straight line is fitted at point x_0 with gradient g_m, the intersection of this line with $I_{ds} = A_1$ gives the threshold voltage, V_{th}, which is simply:

$$V_{th} = -2\mathrm{dx} + x_0. \tag{5.8}$$

In other words, V_{th} is defined as the gate voltage obtained by extrapolating the linear region of the I_{ds}–V_g characteristics from the point of maximum slope to the off-state source-drain current. An example is shown in figure 5.26.

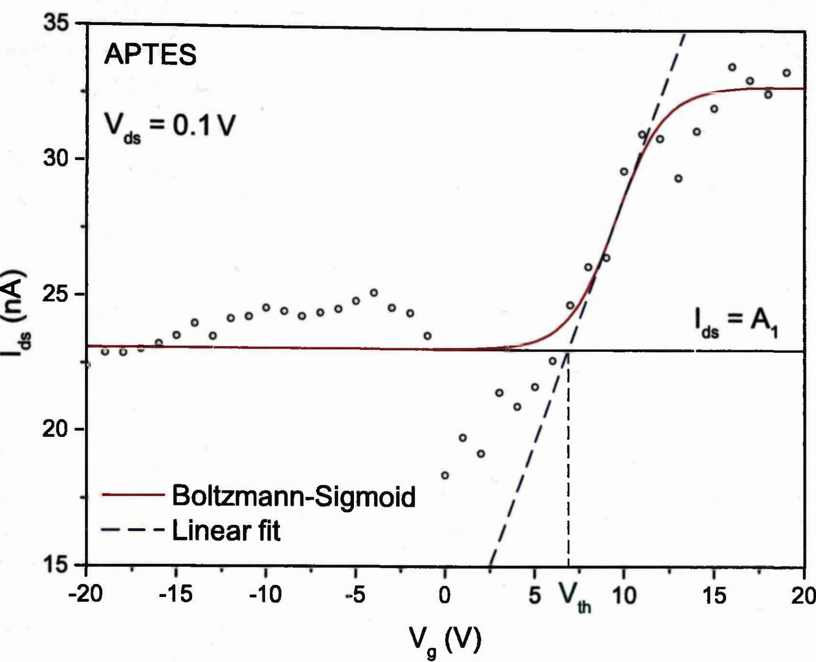

Figure 5.26: I_{ds}–V_g plot for APTES treated NW with V_{ds} = 0.1 V. The transconductance, g_m, is given by the gradient of the linear fit (blue).

Table 5.5 shows a summary of the maximum transconductance and threshold voltages. The method for calculating the total charge using the gate capacitance relies on the assumption that the entire channel is essentially at the same potential as the source. In practical terms, this means that the channel potential between source and drain must be small compared to the gate potential i.e. $V_{ds} << V_g$ [215]. Consequently, the transfer characteristics at V_{ds} = 0.1 V were used to obtain the values for g_m and V_{th} used in subsequent calculations. The transfer characteristics and the associated Sigmoid fits are shown in appendix B, along with information on how the transconductance and threshold voltage uncertainties were calculated from the 1σ confidence interval of the fitted Sigmoid functions. As mentioned, the transfer characteristics for certain NWs show a high degree of variation across small changes in V_g. An indication of the the stability of the threshold voltage across the full range of V_{ds} can be gleaned by looking at the standard deviation in V_{th} over all 100 source-drain voltage values. Plots of V_{th} as a function of V_{ds} are shown in appendix B figure B.2.

The antibody sample is distinct in possessing a negative maximum transconductance value, indicative of p-type behaviour, with an associated large uncertainty due to the poor quality of fit. The values are included for completeness, however the transfer characteristics show no correlation between I_{ds} and V_g for the antibody sample, with large uncertainties in the fitted parameters for the Sigmoid function (figure B.1). The reason for the poor gate coupling is unclear, with a possible explanation being contact issues between the sample and biased stage or NW and dielectric layer. Due to this, the antibody sample will not be included in subsequent calculations of the carrier concentration. Note a large uncertainty is also seen in the maximum transconductance value for the glutaraldehyde treated sample.

Table 5.5: Maximum transconductance and threshold values.

Sample V_{ds}	Max g_m (nS) 0.1 V	V_{th} (V) 0.1 V	Mean V_{th} (V) −1 to 1 V	St. Dev. V_{th} (V) −1 to 1 V
As-grown	2.53 ± 0.13	-18.83 ± 0.28	-13.87	4.29
APTES	21.8 ± 2.10	7.13 ± 0.35	6.21	1.41
GA	2050 ± 2800	-0.04 ± 0.48	-0.07	0.03
Antibody	-4690 ± 19200	-0.24 ± 0.26	-1.35	4.01
BSA	3.82 ± 1.39	-58.45 ± 5.52	-52.34	41.84
Antigen	13.8 ± 2.44	-2.07 ± 0.70	0.92	3.51
EDAC Antibody	26.4 ± 6.47	-14.12 ± 0.70	0.53	17.60
EDAC BSA	6.98 ± 0.24	-6.42 ± 0.08	-6.35	0.55
EDAC Antigen	33.3 ± 5.20	-7.65 ± 0.58	-6.29	4.59

Aside from the APTES treated NW, all NWs exhibit a negative threshold voltage which correspond to depletion mode operation i.e. I_{ds} is greater than the off-state drain-source current at $V_g = 0\,\text{V}$. This is consistent with the surface accumulation measured using valence band XPS – a conductive channel exists at the surface and the device is close to the fully on state at $V_g = 0\,\text{V}$. In order to place the device in the off state the channel must be depleted by pulling the gate voltage negative.

Carrier Concentration

Under the assumptions of a metallic NW embedded in an infinite sheet of dielectric, the gate capacitance can be calculated using:

$$C_g = \frac{2\pi\varepsilon_{\text{SiO}_2}\varepsilon_0 L}{\text{Log}\left[\frac{h+r}{r} + \sqrt{\left(\frac{h+r}{r}\right)^2 - 1}\right]}, \tag{5.9}$$

where r is the NW radius, h is the thickness of the dielectric layer, L is the channel length and $\varepsilon_{\text{SiO}_2}$ is the dielectric constant of SiO_2. This may be used in combination with the threshold voltage, V_{th}, to calculate the carrier concentration, n at gate voltage V_g:

$$n = \frac{C_g\left|V_g - V_{th}\right|}{\pi e r^2 L}. \tag{5.10}$$

where $C_g\left|V_g - V_{th}\right|$ corresponds to the total charge Q_{tot} in the NW. The charge is divided by the elementary charge multiplied by the volume of the NW, hence the carrier concentration is calculated assuming uniform charge distribution inside the NW. From the valence band XPS measurements this assumption is known to be false; in fact the carrier concentration at the surface should be much higher than that in the bulk. Nonetheless, the carrier concentrations calculated here give an indication of the effect of the surface treatments on the number of free carriers and provide a basis for comparison with existing NW FET devices.

The carrier concentrations for pathways A and B are shown below in tables 5.6 and 5.7 respectively, calculated at $V_g = 0\,\text{V}$ using $V_{ds} = 0.1\,\text{V}$. Due to the small threshold voltage for the glutaraldehyde treated sample shown in table 5.5, the calculated carrier concentration is significantly lower, with a much larger fractional uncertainty when compared with the remaining samples. The transfer characteristics shown in figure B.1 suggest a valid Sigmoid fit with a well defined on and off-state drain-source current. In addition, the threshold voltage shows a high degree of stability across the range of V_{ds} (figure B.2), which is also seen in the low standard deviation in V_{th} shown in table 5.5 (0.03 V).

Table 5.6: Carrier concentrations for pathway A.

Sample	n (cm^{-3})
As-grown	$2.1(\pm0.1)\times10^{18}$
APTES	$3.9(\pm0.2)\times10^{17}$
GA	$4.9(\pm37)\times10^{15}$
Antibody	–
BSA	$6.3(\pm0.7)\times10^{18}$
Antigen	$2.6(\pm0.9)\times10^{17}$

Table 5.7: Carrier concentrations for pathway B.

Sample	n (cm^{-3})
As-grown	$2.1(\pm0.1)\times10^{18}$
APTES	$3.9(\pm0.2)\times10^{17}$
EDC Antibody	$7.9(\pm0.8)\times10^{17}$
EDC BSA	$4.9(\pm0.4)\times10^{17}$
EDC Antigen	$4.4(\pm0.5)\times10^{17}$

These carrier densities are similar to those measured by Hong et al. for ZnO NWs in the back-gate geometry exhibiting surface depletion, grown using both catalytic and non-catalytic methods. At $V_g = 10\,\text{V}$, the reported carrier concentrations range from $1.62\times10^{17}\,\text{cm}^{-3}$ to $1.26\times10^{18}\,\text{cm}^{-3}$ [216]. Using equation 5.10, the carrier concentrations at $V_g = 10\,\text{V}$ for the samples measured here range from $1.56\times10^{17}\,\text{cm}^{-3}$ (APTES) to $7.38\times10^{18}\,\text{cm}^{-3}$ (BSA). The intrinsic carrier concentrations at $V_g = 0\,\text{V}$ are also, on average, slightly higher than those previously reported [211, 217, 218]. This could also be suggestive of surface accumulation, especially for the NWs with higher carrier densities (as-grown, BSA), as additional carriers at the surface would result in a net increase to the calculated carrier concentration when uniform charge distribution is assumed. Conversely, for surface depletion the calculated carrier concentration under the assumption of uniform charge would result in the channel carrier density being underestimated.

5.6.1.2 Comparison with XPS valence band scans

As discussed in section 5.4.3, the XPS valence band scans showed the Fermi level at the NW surface to be situation inside the conduction band for all samples, consistent with downward band bending due to the presence of surface donors such as hydroxyls. The different band bending conditions are shown schematically in figure 5.27. Surface depletion would result in a reduced conductivity prior to the application of a gate voltage. This would mean at $V_g = 0\,\mathrm{V}$, the device would not be in the fully on state and consequently the gate would need to be pulled positive in order to extend the channel towards the surface, giving a positive threshold voltage. As mentioned, this was only observed for the APTES treated sample. The XPS results comprise of a sample average measured over a large number of NWs. The surface state density of NWs is known to vary substantially from wire to wire on the same sample, and this surface state variation has previously been used to explain the high degree of variation also seen in resistivity measurements conducted on individual NWs [88]. It is conceivable that variation in the surface state density between NWs grown on the same sample could result in NWs exhibiting both surface charge accumulation and depletion, depending on the relative abundance of donor and acceptor states at the surface. This wire-to-wire variation could also explain the anomalous result obtained for the carrier concentration in the glutaraldehyde treated sample. The XPS valence band scans showed the valence band for the glutaraldehyde sample to be in a similar position to the EDC antibody and EDC antigen samples from pathway B (table 5.3), despite the carrier concentrations for these samples being two orders of magnitude higher. For these reasons, the APTES and GA samples will not be included in subsequent comparisons between the FET measurements and the XPS VB data.

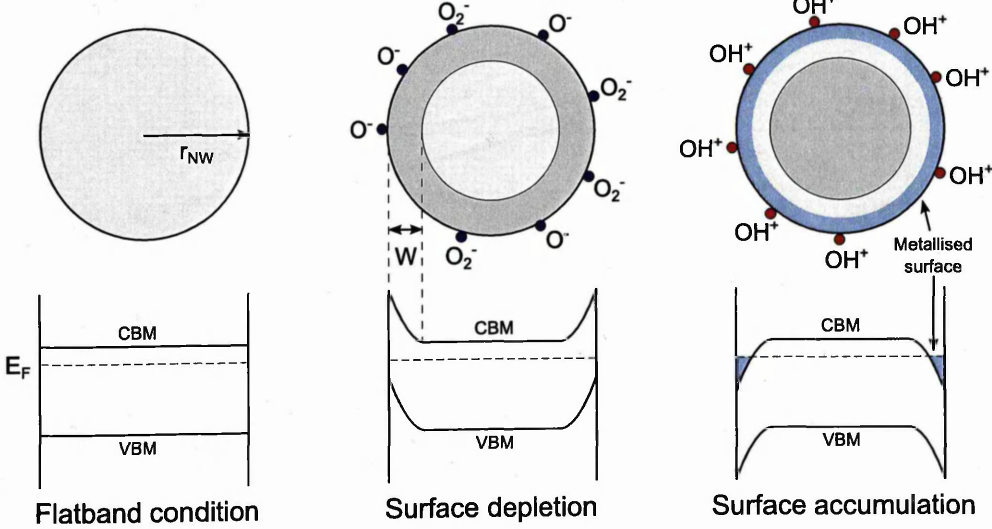

Figure 5.27: Schematic cross-section of a nanowire with corresponding energy band diagram for n-type flatband condition, surface depletion, and surface accumulation.

For non-degenerate semiconductors, the Fermi level, E_F, is located at least $3kT$ below the conduction band. In this case, the location of the Fermi level relative to the conduction band may

be calculated using Boltzmann statistics:

$$\xi = E_F - E_C = kT \ln(n/N_C), \tag{5.11}$$

where N_C is the density of states at the conduction band. For weakly degenerate semiconductors, where the Fermi level is situated near to the conduction band (within $3kT$), the relative location is given by the Joyce-Dixon approximation [219]:

$$\xi = E_F - E_C \approx kT \left[\ln\left(\frac{n}{N_C}\right) + \frac{1}{\sqrt{8}}\left(\frac{n}{N_C}\right) - \left(\frac{3}{16} - \frac{\sqrt{3}}{9}\right)\left(\frac{n}{N_C}\right)^2 + \ldots \right]. \tag{5.12}$$

In the case of more extreme degeneracy ($E_F - E_C > 10kT$), the position of the Fermi level is much more sensitive to changes in the carrier concentration, and an approximation for the relative location of the Fermi level is given by:

$$\xi = E_F - E_C \approx kT \left(\frac{3}{4}\sqrt{\pi}\frac{n}{N_C} \right)^{\frac{2}{3}}. \tag{5.13}$$

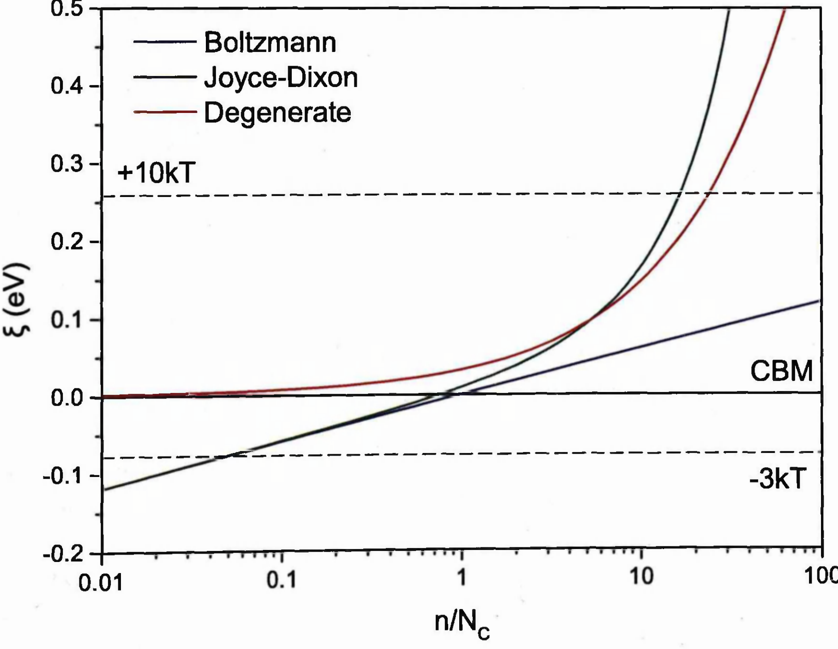

Figure 5.28: The three Fermi level approximations for different degeneracy conditions.

In all three cases, an increase of the Fermi level away from the valence band results in an increase in carrier concentration, with a large increase in the Fermi level position associated with a small increase in carrier density under degenerate conditions. To evaluate the relationship between the back-gate measurements and the XPS valence band results, the calculated carrier concentrations may be plotted as a function of the Fermi level position relative to the valence band. The result is shown in figure 5.29. Note that the GA and antibody samples from pathway

A and the APTES samples have been excluded for reasons previously mentioned. In brief, the APTES sample showed a positive threshold voltage indicating surface depletion, which was in contrast to the sample average measured using VB XPS. The carrier concentration calculated for the GA sample was significantly lower than expected given the VB data, and the Ab sample exhibited poor transfer characteristics with no influence from the gate bias on the source-drain current.

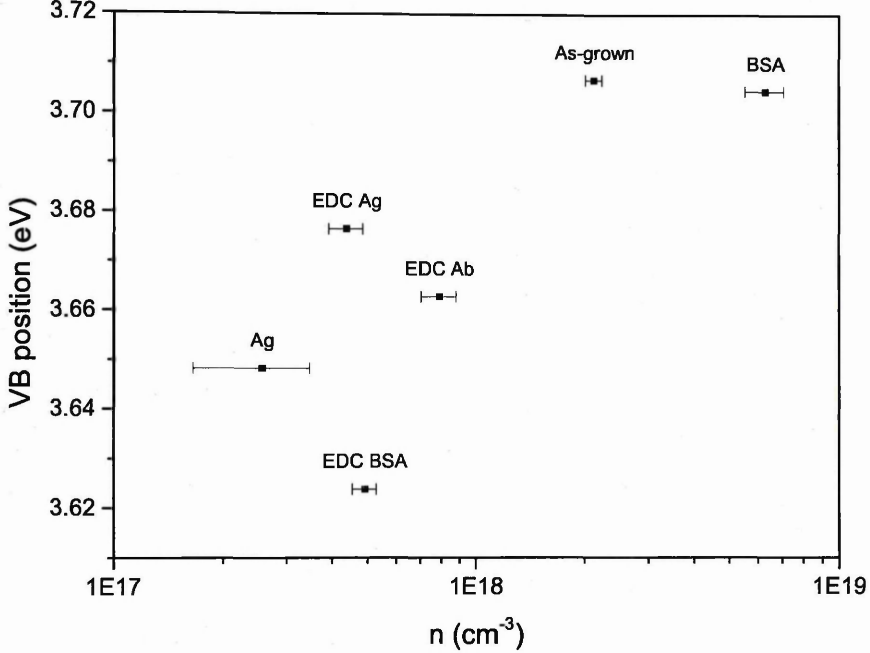

Figure 5.29: Plot of the valence band position relative to the Fermi level as a function of the the carrier concentration (n).

A correlation between the Fermi level position and carrier concentration is seen as expected, with the carrier concentration changing by a factor of approximately 25 between the antigen and BSA samples. The range of variation in the Fermi level position is approximately 0.08 eV.

From figure 5.21 it is clear that the position of the Fermi level relative to the conduction band at the NW surface $\xi = \zeta - E_g$, where $\xi = E_F - E_C$. In order to examine the relationship between the carrier concentration and relative Fermi level position, the PL band-gap measurements (E_g) given in section 5.5 may be subtracted from the position of the Fermi level relative to the valence band maximum (ζ), measured using XPS, to obtain a value for ξ. The values for the relative Fermi level position are given below in table 5.8.

As $10kT \approx 0.26$eV, all relevant samples appear to be exhibiting extreme degeneracy at the surface, indicating that equation 5.13 should apply. In order to further explore the relationship between carrier density and Fermi level position, the change in carrier concentration predicted by the variation in ξ can be calculated. Assuming degeneracy, the ratio of the carrier concentration to the conduction band effective density of states N_C can be obtained by solving equation 5.13 for n/N_C:

$$\frac{n}{N_C} = \frac{4}{3\sqrt{\pi}} \left(\frac{e\xi}{kT} \right)^{\frac{3}{2}}. \tag{5.14}$$

Table 5.8: Position of the Fermi level relative to the conduction band ($\xi = E_F - E_C$).

Sample	ξ (eV)
As-grown	0.375
APTES	0.303
GA	0.301
GA Antibody	0.226
GA BSA	0.342
GA Antigen	0.292
EDC Antibody	0.320
EDC BSA	0.271
EDC Antigen	0.323

A graph of the expected variation in carrier concentration, obtained by substituting the values of ξ in table 5.8 into equation 5.14 is shown below in figure 5.30. Assuming the effective density of states at the conduction band remains constant across samples, the ratio of n/N_C for the BSA and antigen samples gives a relative increase in carrier concentration of approximately 36.1/28.6 = 1.26, which compares with the increase of 25 given in figure 5.29.

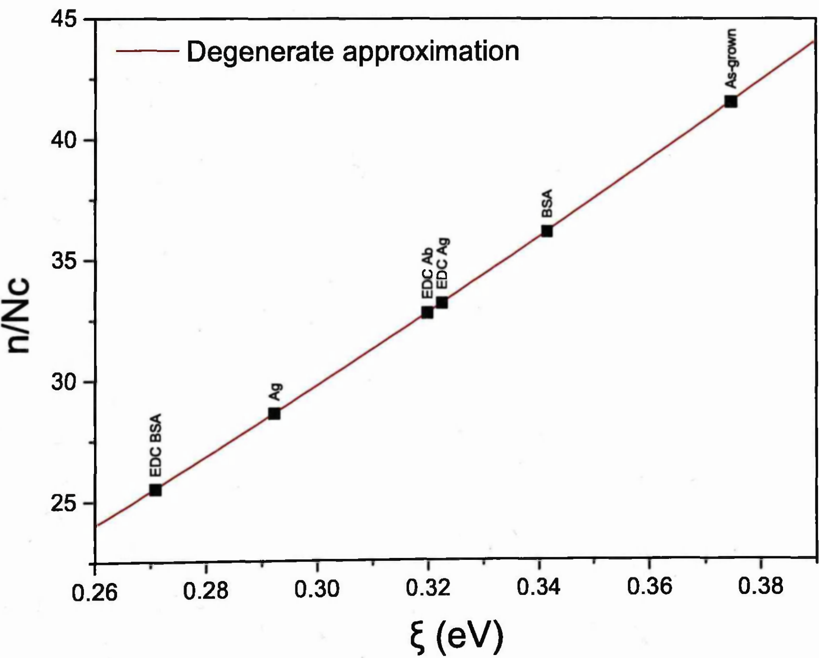

Figure 5.30: Graph of expected carrier concentration calculated using equation 5.13 based on XPS and PL data (table 5.8).

Clearly the carrier concentration varies significantly more than expected for the range of ξ. As can be seen in figure 5.28, under less degenerate conditions described by the Joyce-Dixon approximation, a large change in carrier density can be accommodated by a relatively small change in Fermi level position. This is possibly an indication that, as discussed in section 5.4.3, charging

may indeed be leading to the large downwards band bending and extreme degeneracy reported using valence band XPS. Assuming that the charging is systematic i.e. the binding energy shift in valence band position is constant between samples, the additional band bending induced due to charging may be quantified by fitting a modified version of the Joyce-Dixon approximation to ξ as a function of n. With the addition of an extra charging term, ΔV_C, the approximation becomes:

$$\xi = kT\left[\ln\left(\frac{n}{N_C}\right) + \frac{1}{\sqrt{8}}\left(\frac{n}{N_C}\right) - \left(\frac{3}{16} - \frac{\sqrt{3}}{9}\right)\left(\frac{n}{N_C}\right)^2\right] + \Delta V_C, \tag{5.15}$$

where ΔV_C is simply the measured increase in binding energy due to the surface acquiring a positive potential. If the conduction band effective density of states N_C is assumed to take the value of $2.94 \times 10^{18}\,\text{cm}^{-3}$ [208], the resulting fit of equation 5.15 to the data is shown in figure 5.31, following subtraction of ΔV_C.

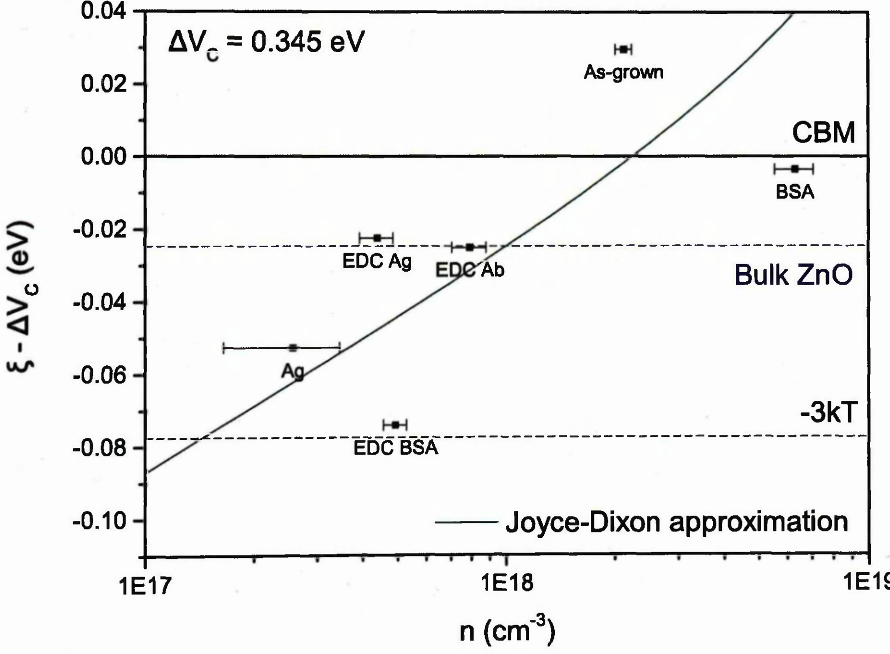

Figure 5.31: Fit of Joyce-Dixon approximation (equation 5.15) to data. Note that ΔV_C has subsequently been subtracted from the data and fit.

The fit suggests a binding energy increase of approximately 0.345 eV due to X-ray photoemission induced surface charging. Correcting the Fermi level position by the same amount places all points within $3kT$ of the conduction band, indicating weak degeneracy. For the purposes of calculating depletion widths, the carrier concentration in the bulk of ZnO NWs is usually estimated to be $1 \times 10^{18}\,\text{cm}^{-3}$ [208]. Using the Joyce-Dixon approximation, this can be combined with the conduction band effective density of states to estimate the Fermi level position in the bulk of the NW. The position is calculated to be -0.025 eV relative to the conduction band minimum, as indicated in figure 5.31. If this is the case, it would suggest that both upward and downward surface band bending is occurring depending on the NW surface modification, although the actual position of the bulk Fermi level relative to the conduction band minimum may be largely differ-

ent to the calculated value, due to the metal incorporation during the growth process leading to changes in n and N_C.

It is important to remember that the carrier concentration values given here are calculated assuming uniform charge distribution, whilst the XPS valence band photoelectrons are gathered from the NW surface. The initial strategy for explaining the discrepancy between the Fermi level position and carrier concentration was to assume an error in the carrier density or conduction band density of states.

In the case of the carrier concentration, under strong downward band bending as measured using valence band XPS, charge transport would be dominated by surface conduction and the assumption of uniform charge distribution would not hold. Instead, the carrier concentration would need to be corrected by assuming the charge was localised at the surface with negligible conduction in the NW bulk. This could be done by substituting the volume of the NW ($\pi r^2 L$) in equation 5.10 for the volume of the accumulation region. The width of the accumulation region W can be calculated from the surface band bending ϕ using the following equation [220]:

$$W = \sqrt{\frac{2\varepsilon_{ZnO}\varepsilon_0\phi}{en}}, \tag{5.16}$$

where ε_{ZnO} is the relative permittivity of ZnO and n is the carrier concentration in the bulk. As the values of ϕ are similar between samples, the mean value of W is calculated to be 25.5 nm with a range of 2.8 nm. The correction to the carrier concentration is then given by:

$$\frac{n_{acc}}{n} = \frac{r^2}{r^2 - (r-W)^2}, \tag{5.17}$$

where n_{acc} is the carrier concentration in the accumulation region. Figure 5.32 shows a graph of the relative correction to the carrier concentration as a function of the fractional accumulation width. For such large fractional accumulation widths, the correction factors are calculated to be between 1.17 and 1.72 using the appropriate NW dimensions, as measured using SEM. As conduction would still be present in the NW bulk, this actually overestimates the average carrier concentration correction factor in the accumulation region. Although uniform charge distribution inside the accumulation region is again assumed, the photoelectron escape depth at the valence band kinetic energies is likely a significant fraction of the accumulation width. As the carrier concentrations range over an order of magnitude, this correction can be assumed to be essentially systematic across samples.

The effective density of states at the conduction band minimum for ZnO is 2.94×10^{18} cm^{-3} [208, 221]. However, section 4.4 presented evidence of metal incorporation in NWs grown on sputtered thin-films, which could result in changes to the electron density of states. As mentioned the initial strategy in explaining the discrepancy between carrier concentration and XPS valence band position was to assume an error in the conduction band density of states and attempt to fit a value for N_C using the degenerate carrier and Joyce-Dixon approximations (equations 5.13 and 5.12). Any error in the carrier concentration due to localised surface accumulation could also be

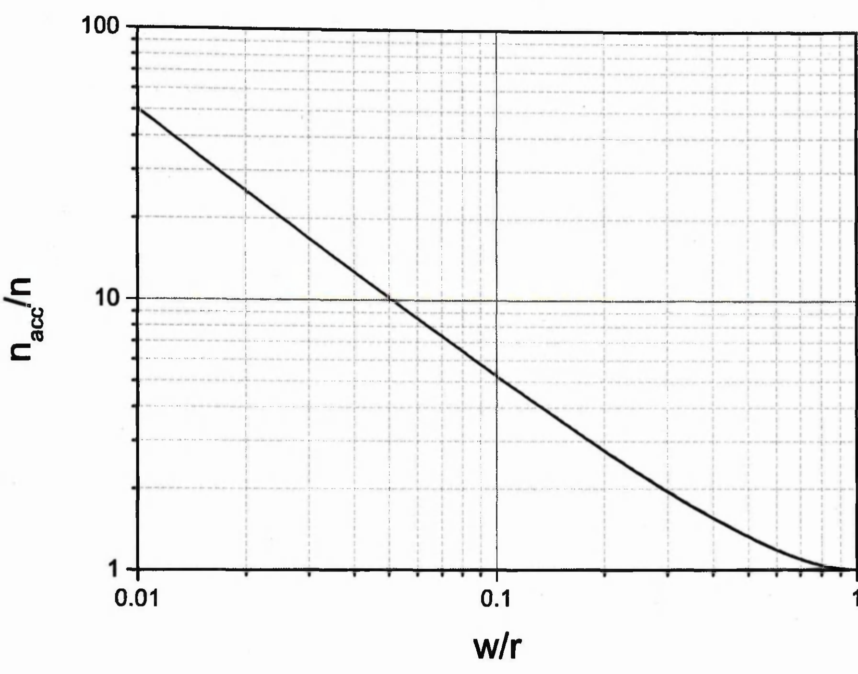

Figure 5.32: Graph showing the local increase in carrier concentration with reduced accumulation width.

assumed to be systematic, and therefore would be included in the fitted value of N_C. However due to the range of variation in the carrier concentrations previously discussed, this strategy failed to fit the Fermi level approximations accurately.

If instead both the conduction band density of states N_C and the additional charging term ΔV_C in equation 5.15 are chosen as fitted parameters, many solutions exists to fits of the Joyce-Dixon approximation, depending on the initial values of N_C and ΔV_C. As N_C is reduced below around $10 \times 10^{17}\,\text{cm}^{-3}$, the fit fails to converge due to the high degree of degeneracy. As N_C is increased the value of ΔV_C also increases. At a large value of $N_C = 10 \times 10^{20}\,\text{cm}^{-3}$ the value for ΔV_C becomes approximately 0.39 eV, which is only an additional 0.045 eV correction from that calculated using the accepted value of the effective conduction band density of states for ZnO. This constitutes strong evidence that the valence band position binding energy reported using XPS is incorrect due to photoemission induced surface charging. Following corrections, the samples exhibit much weaker surface degeneracy, indicating that both surface accumulation and surface depletion could be occurring, depending on the NW surface treatment and position of the Fermi level in the NW bulk.

5.6.1.3 Comparison with PL integrated intensity ratio

No correlation was found between the carrier concentration, XPS valence band position and the PL integrated intensity ratio $A_{\mathrm{NBE}}/A_{\mathrm{Defect}}$. However, when the resistivity of each NW is calculated at $V_g = 0\,\mathrm{V}$ by extracting the gradient of a linear fit to the I_{ds}-V_{ds} curves and correcting for cross sectional area and channel length (equation 5.18), an inverse correlation is seen between the integrated intensity ratio and the NW resistivity. This relationship is shown in figure 5.33, and indicates that a greater surface state density is associated with an increase in NW resistivity.

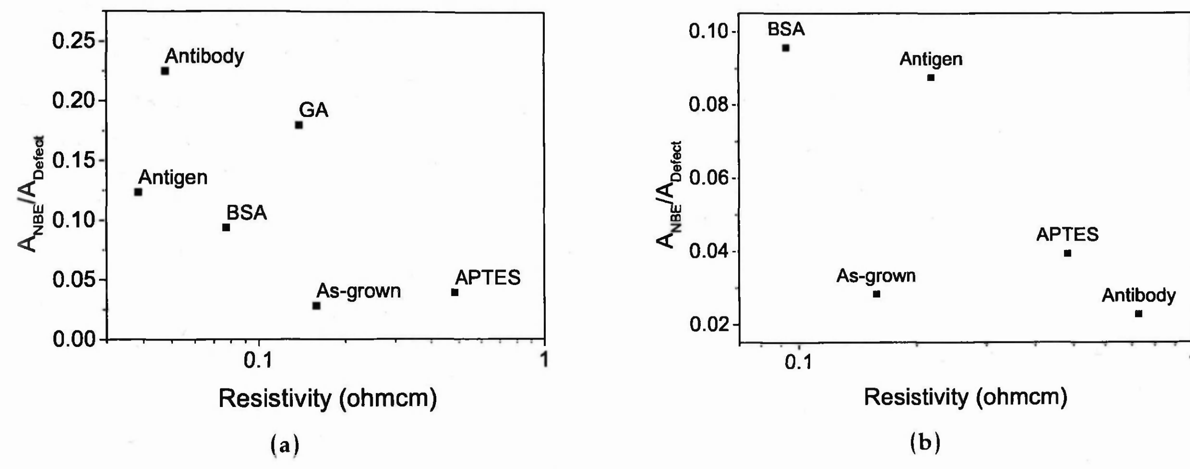

Figure 5.33: NW resistivity against integrated intensity ratio between the NBE peak and defect band for **(a)** Pathway A (GA antibody immobilised samples) **(b)** Pathway B (EDAC antibody immobilised samples).

As the calculated carrier concentration and valence band measurements showed no correlation with NW resistivity, this suggests that modulation of channel conductance due to surface modification and the attachment of biomolecules is dominated by extrinsic surface state related mechanisms which do not directly relate to chemical field-effect gating of the NWs. In addition to electrostatic gating of the NW surface, several other mechanisms including local changes to workfunction and band alignment has been used to explain changes in the NW conductance resulting from the attachment of biomolecules [93].

5.6.2 Resistivity Measurements

In addition to the NWs measured under application of a gate potential, several other NWs were contacted in the planar configuration for each surface treatment and two-point resistance measurements were recorded using a tip-to-tip potential of 1 V. The nanoprobe SEM was used to measure the NW dimensions and channel length *in-situ* following tip approach, allowing the NW resistivity ρ to be calculated:

$$\rho = \frac{RA}{L}, \tag{5.18}$$

where R is the resistance, L is the channel length and A is the assumed circular cross sectional area of the NW. A total of 262 IV measurements were recorded on 46 individual NWs. Measuring the resistivity of the NW channel provides a clear indication of the viability of the NWs and biofunctionalisation process for use in conductometric sensing.

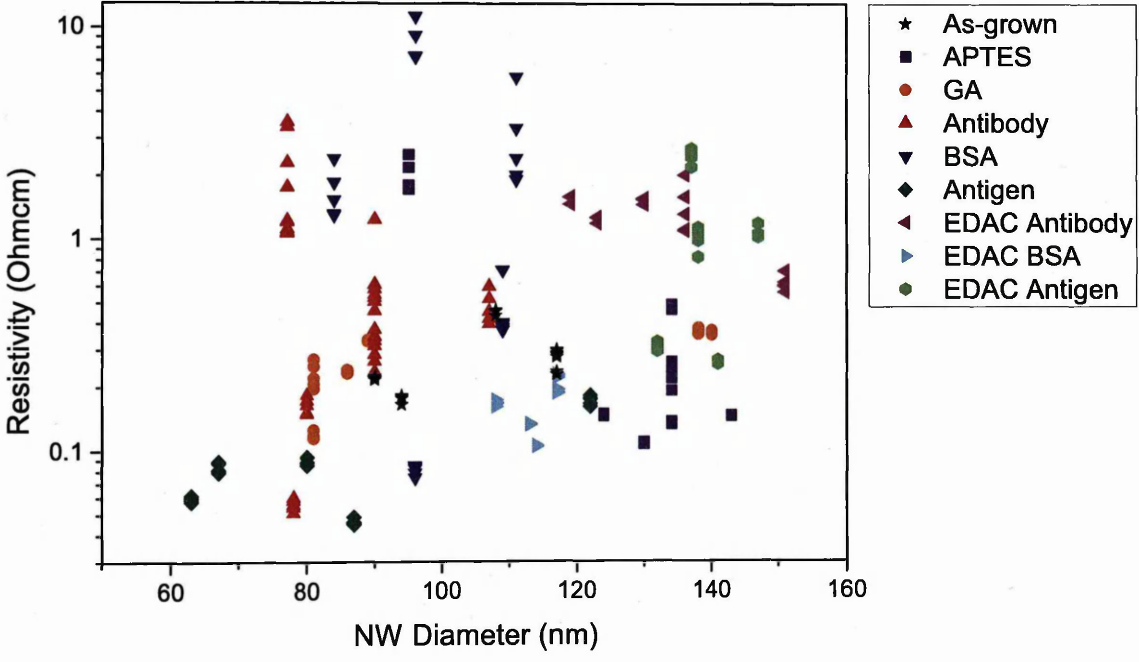

Figure 5.34: Resistivity-NW diameter plot comprising of 262 IV measurements performed on 46 individual NWs.

For non-flatband conditions i.e. upward or downward surface band bending, the enhancement or depletion of a conductive channel at the NW surface should lead to a dependence of the resistivity on the cross sectional area or diameter of the NWs. This has previously been seen before for NWs exhibiting surface depletion, where the resistivity increases rapidly as the NW dimensions are reduced and the surface begins to dominate the conduction properties [88, 216]. In the case of surface accumulation, the opposite behaviour would be expected, with the resistivity decreasing sharply with decreased diameter as the accumulated charge as the surface begins to dominate conduction. This should be especially apparent in the case of surface metallisation, as carrier concentration in the degenerate region of the semiconductor is much larger when compared with the bulk. Figure 5.34 shows a scatter plot of all 262 resistivity measurements plotted as a function of NW diameter. It is apparent that the NWs exhibit a large degree of resistivity

variation, both when comparing between samples and between different wires in a given sample, which are identifiable by a series of points with the same NW diameter. The resistivity values are spread over two orders of magnitude, which is consistent with intrinsic measurements previous conducted on NWs using a four-probe STM technique [88, 222]. However, the values range from between 0.05 Ω cm to 10 Ω cm which is almost an order of magnitude higher than the spread measured by Lord et al. on NWs grown using catalysed, non-catalysed and hydrothermal methods measured with a four-probe technique [88]. This average increased resistivity could be a result of the surface treatments but also could indicate contributions from the contact resistance, as these measurements were conducted using a two rather than four probe configuration. The fact that the as-grown sample shows a resistivity and spread in agreement with previous results is a good indication that the contact resistance does not form a dominant contribution to the conduction path.

Importantly, no obvious correlation is seen between resistivity and NW diameter. This is perhaps unsurprising given the NW dimensions under study. Lord et al. found that an increase in resistivity was only observed for NWs exhibiting surface depletion once the NW diameter was reduced below around 60 nm [88], which is the lower bound on NW diameter measured here. Any weak correlation at these dimensions would likely be hidden by the larger changes induced by the surface treatments. In addition, in the case that both surface accumulation and depletion are occurring depending on surface treatment, as shown in figure 5.31, the trend direction would depend on the value of ξ at the surface relative to the bulk.

Figure 5.35 shows the spread in resistivity for each surface treatment. The bars represent the average resistivity per NW, obtained by summing the individual NW resistivities and dividing by the number of measurements for each sample, shown in table 5.9.

Table 5.9: Number of NWs and I-V measumrents for each sample.

Sample	No. of NWs	No. of measurements (N)
As-grown	5	30
APTES	6	37
GA	5	30
GA Antibody	5	40
GA BSA	5	25
GA Antigen	5	25
EDC Antibody	5	25
EDC BSA	5	25
EDC Antigen	5	25

Although only a small number of NWs were measured for each sample or surface treatment, it is apparent that both the variation between samples and the variation between repeated measurements on the same NW are not consistent between samples. The BSA sample from pathway A shows a large change in resistivity between NWs and also between repeat measurements on the

same NW. The sample subsequently treated with the hCG antigen shows a much reduced spread, both between NWs and between repeated I-V measurements. This indicates that the resistivity spread is not simply explainable in terms of unrepeatable contacting due to the presence of layered biomolecules at the NW surface. If this was the case, the resistivity spread would be expected to increase progressively for each pathway with the additional attachment of biomolecules. Instead, the result suggests that particular surface treatments lead to large unstable variations in NW resistivity, and this instability and resistivity spread may be reduced by the subsequent binding and immobilisation of further biomolecules. This is in agreement with the intrinsic measurements conducted by Lord et al. on ZnO NWs [88]. They concluded that the resistivity spread mentioned previously could be attributed to small variations in the occupancy of surface states associated with the adsorption of environmental species. This result was confirmed using ethanol as a surface pacifier to neutralise the effect of the surface states, which resulted in a significant decrease in resistivity spread. The result shown in figure 5.35 indicates that the addition of extrinsic surface states through surface modification and functionalisation can also lead to a decrease in both the temporal and wire-to-wire resistivity spread, similar to that previously induced by the removal of environmental adsorbates. This has significant implications for the design of NW biosensors and suggests that sensors integrating small numbers of surface reactive metal oxide NWs may be prone to large temporal and inter-device variations.

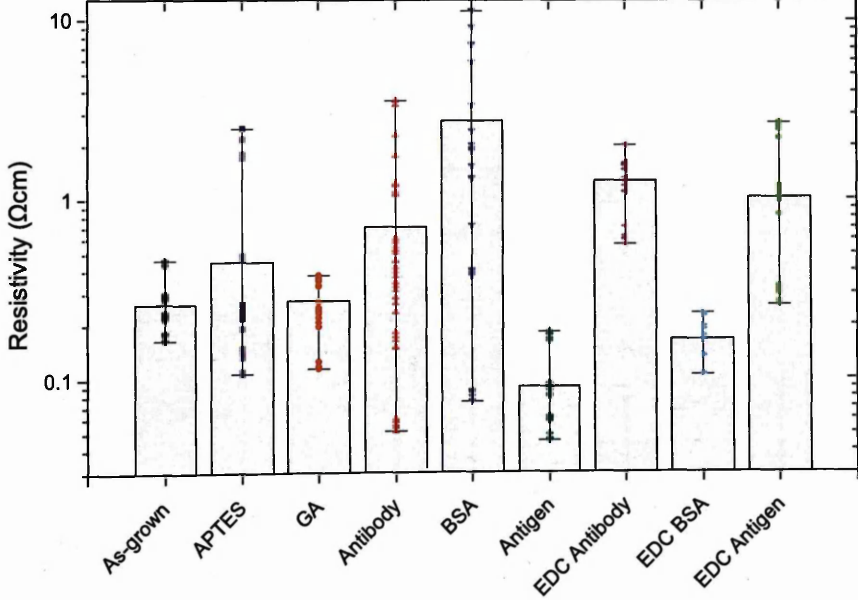

Figure 5.35: Average resistivity of each sample set overlayed with the spread in resistivity. The points show the resistivity values from individual NW measurements.

Crucially, in the case of both pathways, the addition of the hCG antigen appears to have a large effect on the average resistivity. For the low number of NWs measured here, little overlap is seen between measurements on the BSA and Ag samples from pathway B (EDC method), which could indicate that for this functionalisation method, devices consisting of low numbers of NWs may capable of detecting attachment of the hCG protein at the concentration used here (250 ng/ml).

Instead, a more effective strategy would appear to be integration a large number of NWs in order to average out the wire-to-wire variability. Pathway A offers an example of how ensemble devices may offer a solution to the issue of resistivity spread in biosensing applications. Although there is significant overlap in the resistivity values between samples, on average the resistivity drops by over an order of magnitude following attachment of the hCG antigen. The reverse is seen for pathway B, with a slightly smaller increase in the resistivity seen following attachment of the antigen. Along with the PL result shown previously, this could be suggestive of the different antibody attachment orientations, which could conceivably lead to a difference in charge transfer or surface state modification.

It is important to consider how these variation in resistivity would impact the measured resistance of a practical ensemble device. For example, the BSA sample from pathway A in figure 5.35 exhibits the largest spread in resistivity, however it is unclear how much the higher resistivity NWs would contribute to the measured current when considered in the aggregate. To investigate this, the resistivity values can be used to calculate a resistance for each data point, assuming a standard NW length of 6 µm. The parallel resistance R_p for each sample can be calculated using:

$$\frac{1}{R_p} = \sum_{i=1}^{N} \frac{A_i}{\rho_i L_i^{'}}, \tag{5.19}$$

where R_p is the parallel resistance, N is the number of measurements (shown in table 5.9), A is the NW cross-sectional area, as measured using SEM, and $L^{'}$ is the standard NW length of 6 µm. The result is shown in figure 5.36, with the bars giving the average resistance value per NW ($R_P \times N$).

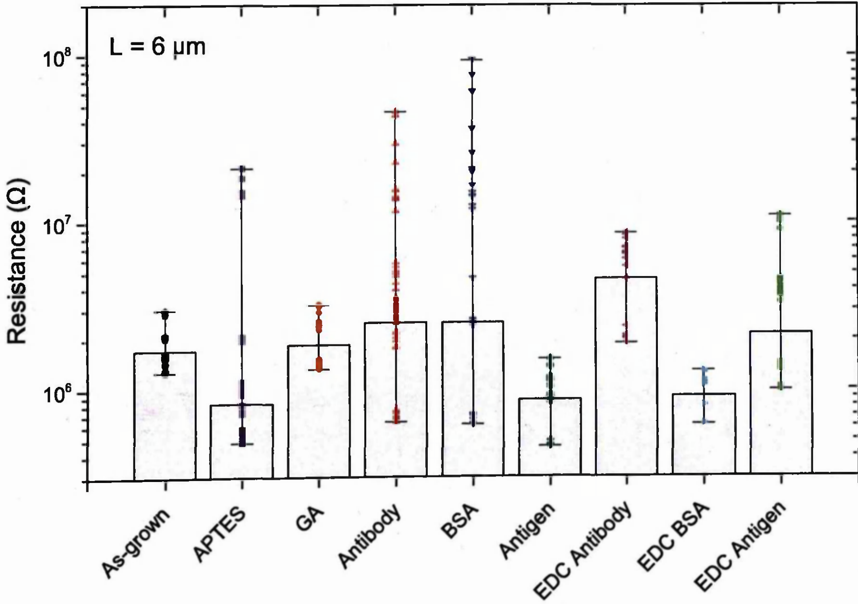

Figure 5.36: Average resistance per NW assuming a channel length of 6 µm.

Despite the average resistance per NW being weighed towards the lower resistance values, the change in resistance between the BSA and hCG antigen samples for both pathways mirrors

that seen in the average resistivity. In the case of pathway A, the change is less pronounced for reasons mentioned above. As there is considerable variation in average NW diameter between samples (figure 5.34), this indicates that some sample-to-sample variation in NW growth can be tolerated without impacting the changes seen during the antigen attachment. To investigative this further and to ensure that this effect is not an artefact caused by variation in the NW diameters, the resistance values were again calculated as above, but under the assumption of constant NW diameter $d' = 144\,\text{nm}$. The resulting plot is shown in figure 5.37.

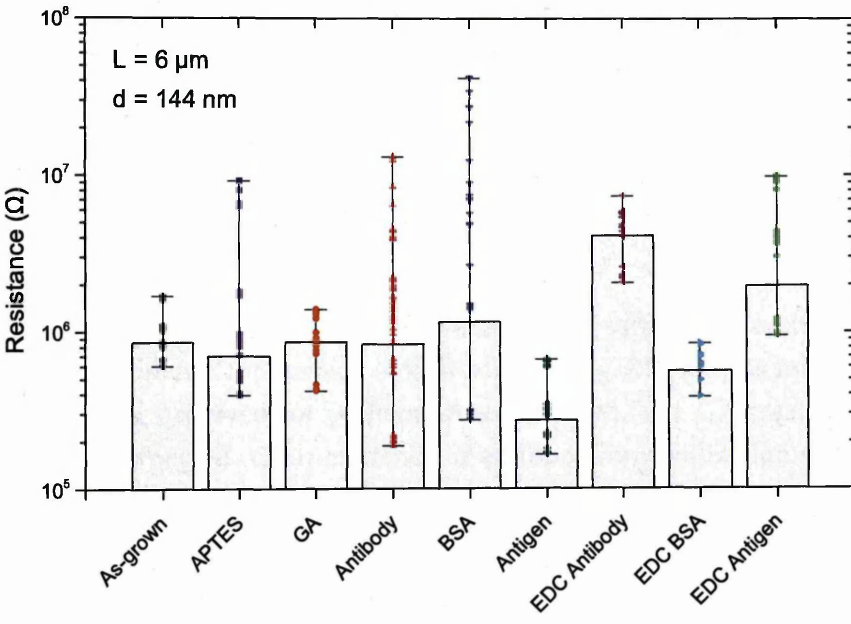

Figure 5.37: Average resistance per NW assuming a channel length of 6 μm and a NW diameter of 144 nm.

There is a notable increase in the average resistance per NW for the APTES sample as a result of the large average NW diameter (figure 5.34). However, the same trend is seen as before between the BSA and Ag samples for both pathways, with a remarkably similar response exhibited using both antibody attachment methods, indicating that practical integration of an ensemble conductometric sensor would be feasible using the functionalisation processes outline here.

5.7 Chapter Summary

Zinc oxide NWs grown on sputtered Ti thin-films were functionalised to allow the conductometric detection of a typical clinical concentration of the hCG protein (250 ng/ml). This was achieved using two parallel pathways – pathway A utilised GA as a cross-linker between the silanized ZnO surface and the antibody, and pathway B used EDC/NHS to activate the antibody carboxyl groups, resulting in zero-length cross-linking between the antibody and silanized ZnO surface.

Electron microscopy was used to analyse the NWs following functionalisation, and evidence of molecular attachment to the ZnO surface was found, particularly following the antigen attachment step for both pathways. In addition, it was found that the GA solution caused significant etching of the ZnO surface, likely as a result of the long duration immersion in DI water. In retrospect, this problem could be avoided by using PBS to prevent the dissociation of ZnO, as the accompany SEM results demonstrated the compatibility of ZnO with low concentration PBS.

X-ray Photoelectron Spectroscopy was used to analyse the samples as each stage of the functionalisation process. Evidence for surface modification using APTES was found for both pathways, despite the etching observed for pathway A under SEM. The GA treatment also gave an increase in C and O, as expected. Clear evidence of antibody immobilisation was found for both attachment methods, although relatively little difference was seen in the elemental composition between pathways. Subsequent treatment with BSA to block non-specific binding and attachment of the hCG protein gave minor differences in elemental composition overall, although some changes were seen in the fitted components and relative N composition.

Valence band XPS was also conducted to study the surface band bending resulting from attachment of the biomolecules. Large values for the valence band maximum were measured, indicating severe downward band bending resulting in surface metallisation. It was suggested this could be explained due to localised photoelectron induced surface charging, which would result in an increased binding energy shift.

Photoluminescence spectroscopy was used to give an indication of extrinsic surface state density. Large variations were observed in the deep level visible emission depending on surface treatment, suggesting that surface modification and attachment of biomolecules results in effective modulation of the surface state density. Interestingly, significant differences were found between the two Ab attachment methods, which could possibly be indicative of the differing average Ab attachment orientations. In addition, PL allowed direct measurement of the optical band-gap, which allowed band-gap enlargement to be ruled out as a source of the large valence band binding energy measured using XPS.

Electrical measurements were conducted in the lateral FET geometry using a nanoprobe consisting of two STM tips situated below an SEM column. Back-gated measurements allowed determination of the transfer characteristics and threshold voltages for each sample, which were indicative of surface accumulation, as suggested by the XPS valence band scans. The carrier concentrations was determined from the threshold voltages, and were found to be comparable to, if

slightly higher, than those reported for similarly grown NWs.

A positive correlation was found between the valence band binding energy measured using XPS and the carrier concentration, as expected. Following subtraction of the band-gap measured using PL, an attempt was made to fit the relationship using an approximation for the relative Fermi level position inside a degenerate semiconductor. This was found to be ineffective, due to the large changes in Fermi level position predicted by the variation in carrier concentration between samples. Instead, the relationship was fitted allowing for a correction to the valence band binding energy due to photoelectron induced charging. The result suggested weak degeneracy, with the samples exhibiting surface accumulation or a combination of accumulation and depletion, depending on the location of the Fermi level inside the NW bulk. No correlation was found between the carrier concentration, valence band position and resistivity measurements, however a correlation between PL deep level visible emission and resistivity was found, indicating that surface band bending may not correlate directly with measurable changes in conduction, and that other surface state related mechanisms may be responsible for resistivity variations between NWs.

Resistivity measurements were subsequently conducted on a 46 NWs with significant variations found both between similarly treated NWs and in repeated measurements conducted on the same NW. This temporal and wire-to-wire variation in conductivity has significant implications for the design of NW biosensors and demonstrates the need for ensemble integration in order to reduce the statistical spread seen for certain surface treatments. The average resistance per NW of an ensemble devices was calculated for each sample, and indicates that both functionalisation methods could be used for conductometric detection of clinical levels of the model hCG protein, assuming parallel incorporation of NWs into a sensing device.

Chapter 6

Device Fabrication

This chapter outlines a strategy for creating an ensemble zinc oxide nanowire (ZnO NW) device for use in sensing applications. In the previous chapters, it has been demonstrated that selective growth of high quality vertically aligned ZnO NW arrays is possible on industry standard silicon substrates, and that ZnO NW based immunosensors are feasible, though likely require a high degree of parallelism in order to average out the surface state modulated wire-to-wire variability.

The proposed design consists of vertically aligned NW arrays grown in silicon microchannels, through which an analyte may be flown and hence detected. In order for a potential to be applied across the wires, the NW tips must be contacted by means of a floating metal top contact. This challenging device structure was implemented using conventional microfabrication techniques.

6.1 Vertical Device Fabrication

Despite extensive research interest and the development of several novel approaches, fabrication of ensemble nanowire (NW) devices remains a challenge. Generally, the approaches fall into one of two categories – integration of as-grown NWs on the growth substrate, and assembly of parallel devices following transfer and alignment. Many strategies involving self-assembly and directed assembly of transferred NWs have been investigated [90,223], however these approaches are complex, requiring the NWs to be harvested and aligned *en masse*, with additional top down processing required for contact formation. Perhaps more importantly, the transfer and assembly approach usually results in planar devices, effectively reducing the number of NWs available to be contacted for a given device size. As explored in chapter 4, an attractive alternative is the integration of vertically grown arrays, which can be grown either onto conductive layer or directly onto the conductive substrate. In particular, conductive layers have been shown to provide an elegant solution to the problem of NW growth on commercially viable substrates, with the conductive layer also serving as a bottom electrode, providing a means for contacting the array.

Comparatively little work has been done on vertical sensing devices, likely due to the difficulty in fabricating repeatable top contacts to NW arrays. Contacting of vertically grown NWs has previously either been achieved using electrodes placed in mechanical contact with the arrays [224], or by embedding the wires in a insulating scaffold onto which metal contacts may be deposited [225] using e.g. spin coating or sputtering/evaporation. This scaffold is commonly referred to as an encapsulation layer [226,227]. Mechanical contacting is an inherently simple but limited approach with little scope for repeatable optimisation and reliable formation of contacts. In addition, biosensing applications require the contact to either be submerged into an analyte or to form a microfluidic channel, which in either case would likely result in stability problems

for mechanical contacts. In applications in which deposited top contacts have previously been used, such as piezoelectric energy harvesting [228], piezotronic pressure sensing [227] and UV photodiodes [229], the matrix or encapsulation material is typically a polymer, spin on glass or deposited SiO_2 which forms part of the permanent device structure. Obviously, this is not a viable integration strategy for FET sensors, as the surface of the NWs is rendered inaccessible.

The integration method presented here uses cross-linked negative photoresist as an encapsulation layer, which forms a stable platform for further photolithography and metallisation processes to be conducted on top of the embedded NW array. Following metal deposition, photolithography and wet etching to create the desired contacts, the encapsulation layer is removed, leaving behind a floating metal contact and exposing the NW surface for sensing.

This method was used to fabricate floating contacts on NW arrays in order to validate the processing and integrity of sputtered metal contacts. Following fabrication of these preliminary devices, a sensing structure was fabricated consisting of top and bottom contacts forming a microchannel, through which an analyte may be passed and hence detected.

6.2 Floating Metal Contacts

A strategy for creating top contacts using conventional microfabrication techniques is shown in figure 6.1. The processing steps are as follows:

1. Encapsulation of NW array in negative photoresist – this can be achieve using spin coating (section 3.2.2.2). The photoresist must be cross-linked to ensure its stability during the subsequent photolithography and metal etching processes.
2. Plasma ashing – an O_2 plasma is used to controllably ash the photoresist layer to the required height. This must be done at relatively low power to prevent heating and cracking of the photoresist. A desktop ashing system was found to be suitable (section 3.2.6).
3. Once the encapsulation layer is ashed to the required height, the sample is sonicated in DI water for a short period to planarise the NW array. This cleaves the portion of any NWs protruding above the encapsulation layer.
4. Another brief period of ashing ensures that the tips of the NWs are properly exposed for contacting.
5. Metal deposition – a contact material such as Ti or ITO is sputtered onto the encapsulation layer.
6. Conventional photolithography and metal etching – positive photoresist is spin coated, exposed and developed to mask the contact areas. The exposed metal is then wet etched.
7. Removal of encapsulation layer – the structure is soaked in a powerful photoresist stripper to ensure removal of all cross-linked photoresist. This could potentially be aided through the use of oxygen plasma ashing (see section 3.2.6).

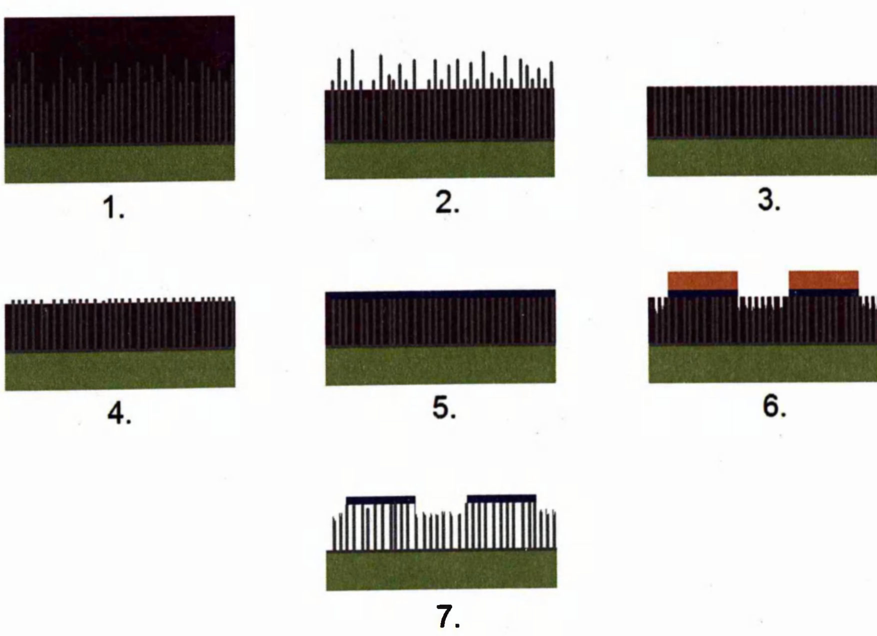

Figure 6.1: Cross sectional schematic of the floating contact fabrication process. The colours correspond to the following: green - Si substrate, purple - negative photoresist encapsulation layer, blue - metal top contact, orange - positive photoresist etch mask.

6.2.1 Encapsulation of nanowire arrays

To investigate the viability of creating floating metal contacts using this method, NWs were grown on 10 mm × 10 mm silicon (1 0 0) samples. The substrates were cleaved then cleaned using a standard procedure consisting of solvent and acid cleaning processes. For more information see section 3.2. A 100 nm Ti thin-film was sputtered deposited and the NWs were grown as described in section 4.4. The NWs were grown for a duration of 45 minutes, with subsequent cross-sectional scanning electron microscopy (SEM) revealing the array height to be around 7 µm. Following growth, the NW arrays were encapsulated in a layer of AZ nLOF 2070 (Microchemicals GmbH; section 3.2.2.1). Encapsulation in nLOF 2070 was achieved using spin coating. Due to the viscous nature of nLOF 2070, the sample was allowed to sit for 1 minute following application of the photoresist, in order to prevent voids forming in the encapsulation layer [230], and left to settle on the chuck for 10 minutes following spin coating. The spin speed curve shown in figure 3.6b was found to be of little assistance in estimating the resulting film thickness, as the NWs inhibited movement of the viscous fluid across the sample, resulting in layers much thicker than the array height. It was initially hoped that the film could be spun to a thickness equal to, or even slightly less than that of the array height, meaning that minimal plasma ashing would be required, leading to a quicker, more controlled process. However, this approach proved problematic. Figure 6.2 shows the result of spin coating the NW arrays with a speed of 4000 rpm and acceleration of 1000 rpm s^{-1} for a duration of 45 seconds.

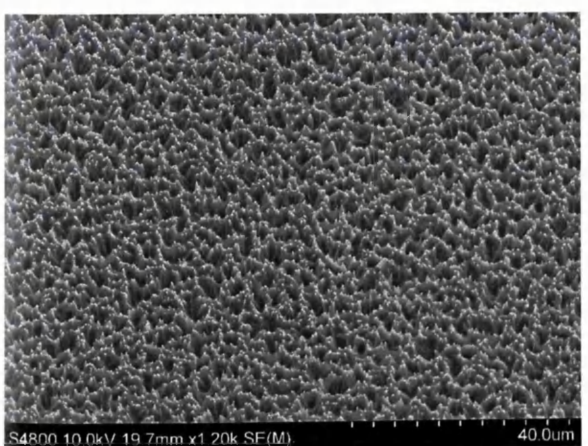

(a) Non-uniform photoresist encapsulation layer.

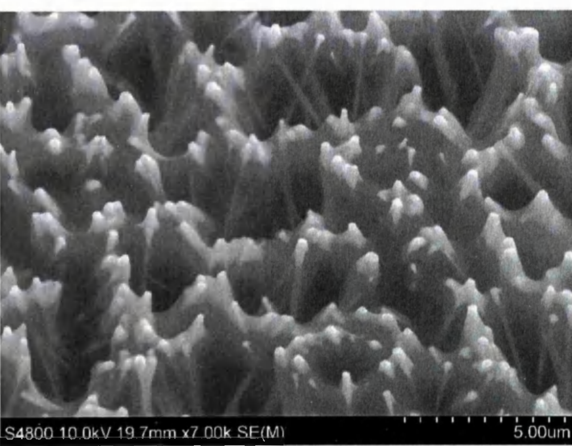

(b) NWs inhibit flow of photoresist across sample.

Figure 6.2: SEM images of photoresist forming dome shaped deposits around NW bundles following high speed spin coating. A lower spin speed is necessary to improve film uniformity.

The rapid spin speed resulted in accumulation of the resist around NW bundles, which would prevent uniform ashing and planarisation and likely result in issues during metal deposition and support removal. An improved strategy was found to be to encase the NWs in a film much thicker than the height of the array to prevent drag caused by the NWs from influencing the uniformity of the film. Several microns of the film could then be removed via plasma ashing to arrive at the required height. A spin speed of 2500 rpm and acceleration of 1000 rpm s^{-1} for a duration of 30 seconds was found to result in a film approximately 12 µm thick, measured from the substrate

(including the base growth layer), as seen in figure 6.3. No voids or cracks were visible in the resist film following spin coating.

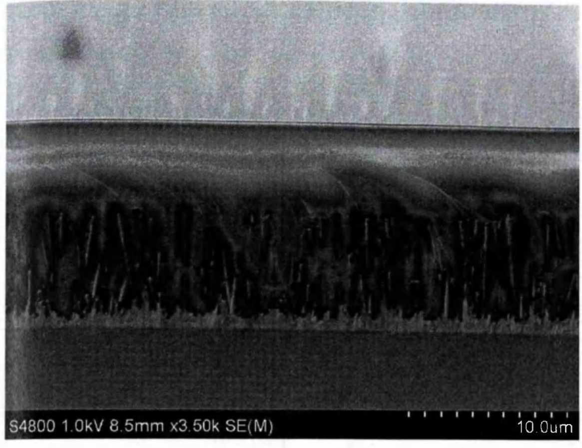
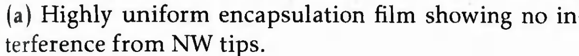

(a) Highly uniform encapsulation film showing no interference from NW tips.

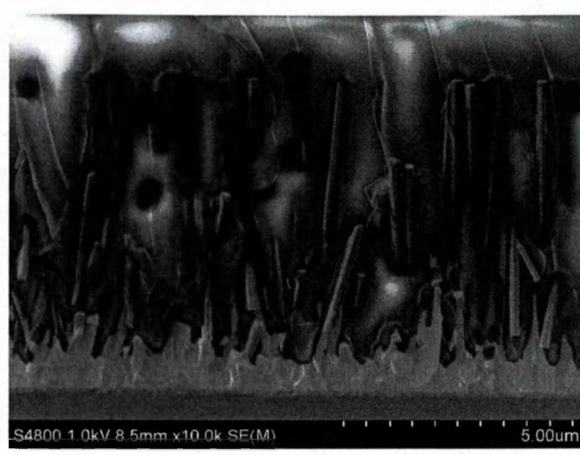

(b) Intimate encapsulation of NW array.

Figure 6.3: Cross-sectional SEM images of NWs encapsulated in a thick AZ nLOF 2070 photoresist layer. (a) demonstrates a high degree of uniformity across the top of the encapsulation layer. No voids or defects are seen in the film, as shown in (b).

6.2.2 Controlled ashing of resist films

Samples were ashed using an O_2 plasma (section 3.2.6) at a relatively high flow rate to ensure the fast removal of reaction products. The ashing rate was found to be non-linear, likely due to heating of the sample during extended periods in the plasma. An RF power of 100 W was initially used, but this was found to result in excessive heating of the substrate, resulting in cracks forming in the resist film (figure 6.4).

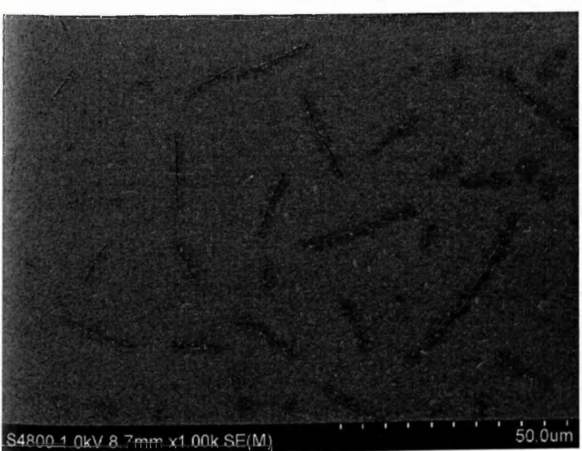

(a) High density of large voids observed across sample.

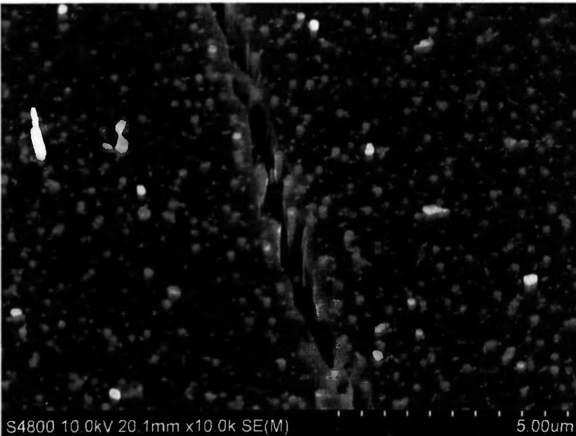

(b) Voids appear to extend significant distance into NW array.

Figure 6.4: SEM images of cracks formed in photoresist encapsulation layer due to unequal thermal expansion of the substrate/polymer film following O_2 plasma ashing at an RF power of 100 W. These voids would cause problems for top-contact deposition and uniform NW contacting and could, in extreme cases, result in shorts between bottom and top contacts.

Instead, a lower RF power of 50 W was used to prevented overheating and cracking of the resist film. A calibration curve for the 50 W process is shown in figure 6.5, with each point representing a freshly coated sample. It is likely that some degree of cross-linking or other chemical alterations occur at the film surface due to the glow discharge, which would invalidate this curve for multiply ashed samples.

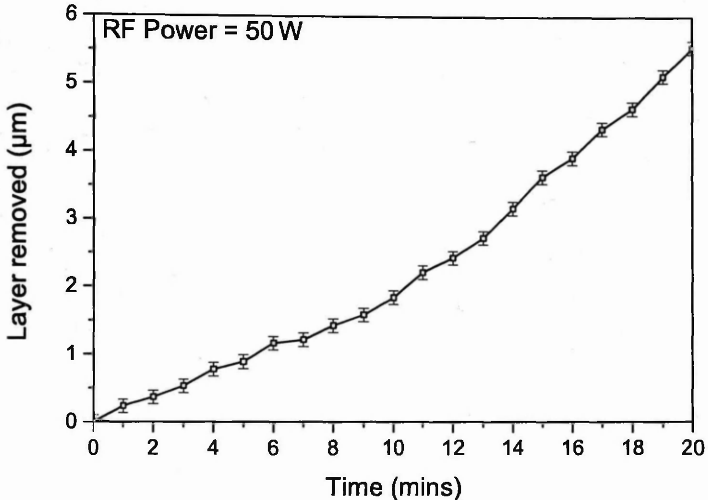

Figure 6.5: Calibration curve for controlled encapsulation layer (AZ nLOF 2070 photoresist) removal as a function of ashing duration conducted in an O_2 plasma at an RF power of 50 W. A slight non-linearity is seen in the ashing rate likely due to sample heating.

Figure 6.6 shows the result of controlled ashing. The sample was cleaved following encapsulation and the excess thickness was measured using SEM, allowing an ashing time to be estimated using the calibration curve shown above. Figure 6.6a shows NWs with their full length exposed, which is a result of the isotropic ashing at the cleaved edge of the sample.

6.2.3 Planarisation of nanowire array

Due to the distribution in the length of the NW arrays, following ashing the protrusion of the NW tips through the encapsulation layer is highly variable, with the percentage of NW tips exposed and the average amount of protrusion being related to the length distribution and the thickness of the encapsulation layer. Uniform NW length is desirable for a number of reasons, mainly to improve the structural properties of the deposited metal electrode and to homogenise the contact resistance at each NW. Due to the NW length distribution, ashing further into the encapsulation layer increases the number of NWs available to be contacted at the expense of a decreased encapsulation layer thickness and ultimately NW length. Figure 6.7a shows heavy ashing of the encapsulation layer which results in a large number of exposed tips. Metal deposition onto such an irregular surface could easily result in a fragile, discontinuous contact.

Following ashing, the sample was placed in deionised (DI) water and sonicated for 5 minutes, then rinsed and dried under N_2 flow. This was found to remove the NW tips, which tend to cleave quite cleanly at the encapsulation layer interface, as shown in figure 6.7b. This method is routinely used for harvesting NWs from the growth substrate for transfer and directed assembly

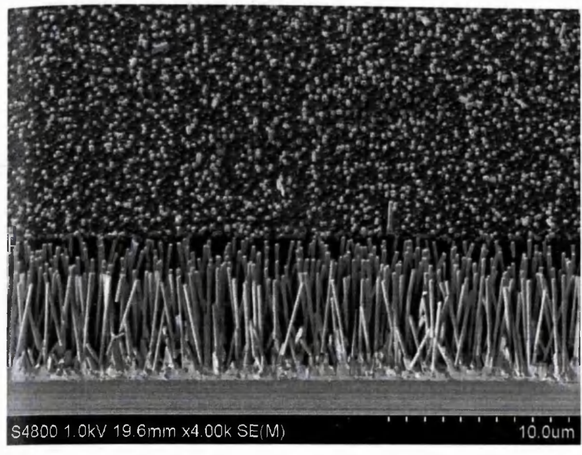

(a) Isotropic ashing exposing NW tips and NW array at edge of sample.

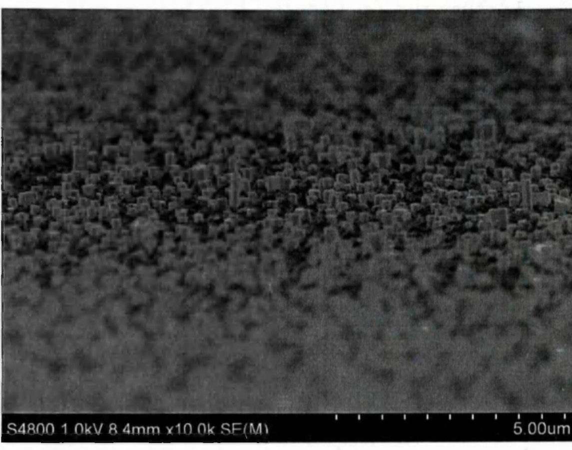

(b) Uneven protrusion of NW tips through encapsulation layer.

Figure 6.6: Tilted SEM images showing NW array in encapsulation layer following controlled resist ashing. (a) 35° tilted SEM image of cleaved edge of sample following ashing – NWs are seen on the exposed edge of the sample due to the isotropic ashing. The exposed NW tips can be seen in the background. (b) 60° tilted SEM image of exposed NW tips showing variation in NW length and tip protrusion. A subsequent planarisation step is required in order to level NW tips.

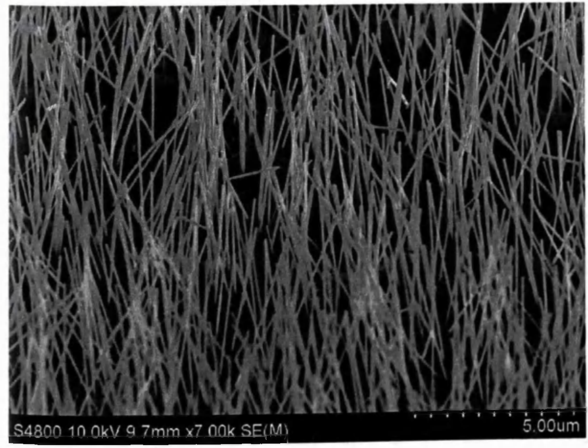

(a) Before sonicating.

(b) After 5 minutes of sonicating.

Figure 6.7: SEM images of ultrasonic planarisation of NW arrays. This step will likely been required to increase the density of contacted NWs and more importantly to ensure contact uniformity between individual NWs in the array.

[89,231,232].

The sample was then further ashed for 30 seconds at 50 W to remove an additional 100 nm of the encapsulation layer, exposing the planarised NW tips for contact formation. This additional step may provide a straight forward yet powerful method of controlling the contact properties. The electron transport properties at nanoscale metal-semiconductor interfaces have been shown to transition from thermionic emission dominated (Schottky contacts) to tunnelling dominated (Ohmic contacts) depending on contact size [233]. Further ashing and expose of the m-planes also decreases the relative contact area of the polar facet. This demonstrates the need for accurate control of NW growth and processing parameters if reproducible devices are to be achieved.

6.2.4 Top contact deposition and patterning

The choice of contact material is obviously crucial to device performance, especially when creating nanoscale contacts, which are known to suffer from increased contact resistances due to carrier injection effects [234]. It is interesting to note that low resistance Ohmic contacts are not necessarily desirable for sensing applications, and it has been shown the Schottky contacted FET devices can actually result in a increased sensitivity due to the attachment of biomolecules changing the Schottky barrier height [93]. For inital device fabrication, Ti and Al were chosen, which have both been shown to give good quality Ohmic contacts to ZnO, partly due to their high affinity for oxygen, which results in vacancy formation and doping of the ZnO interface [234]. In addition, the NWs grown on Ti appear to be exhibiting surface charge accumulation (chapter 5), which would aid with the formation of Ohmic contacts.

The top contacts were sputtered using a Lesker PVD 75 system (section 3.2.5.1). Both the titanium and aluminium contacts were deposited at a chamber pressure of 1.7 mTorr and RF power of 100 W, giving deposition rates of 1.2 Å/s and 1.8 Å/s, respectively. The top contacts were deposited to a thickness of 200 nm, as measured using a quartz crystal microbalance.

Following deposition, the metals were spin coated in AZ 6612 positive photoresist (section 3.2.2.1), as described in section 3.2.2.2. The photoresist was exposed through a mask consisting of 50 µm × 50 µm squares at a dose of 350 mJ/cm^2, then developed as described in section 3.2.2.4. The metals were etched, using the corresponding recipes in section 3.2.3, before the samples were washed in DI water and blown dry using N_2. The resulting titanium top contacts with the photoresist masks still in place are shown in figure 6.8.

6.2.5 Removal of encapsulation layer

In the case of the aluminium contacts, O_2 plasma was used to remove the etching mask and NW encapsulation layer. Ashing lasted a total of 1 hour, and the results are shown in figure 6.9. Due to masking from the metal contact, photoresist still remained trapped despite the long ashing duration, as can be seen in 6.9a. Also visible in the same figure are spherical deposits located on top of the contacts. These deposits were examined using EDX and were found to be rich in phosphorous, which can be attributed to the phosphoric acid present in the etching solution. Figure 6.9b reveals that despite attempts to keep the encapsulation layer level, some texturing

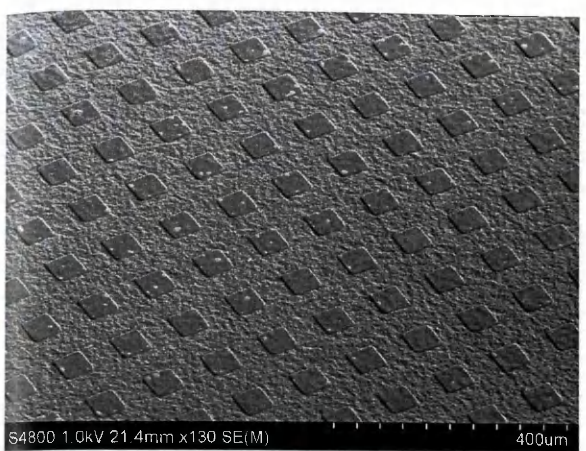

(a) Array of Ti top contacts following wet chemical etching.

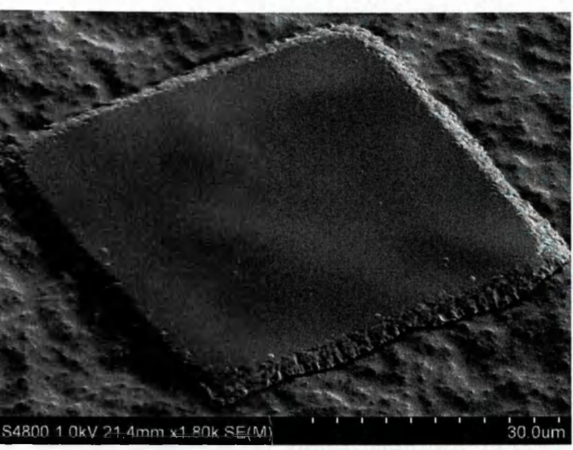

(b) Close-up of Ti top contact prior to removal of positive photoresist etch mask and encapsulation layer.

Figure 6.8: SEM images of Ti top contacts coated with photoresist mask following metal deposition and etching. No NW protrusions are seen from the encapsulation layer as the ZnO has been etched away by the BOE solution.

and variations in the height of the contact are still visible. However, figure 6.9c shows that despite these height variations, the planarisation step resulted in equal tip protrusion. Considerable residue is visible in the etched uncontacted wires shown in figure 6.9d. Further EDX analysis showed the absence of phosphorous, indicating that the deposits are likely residues left over from the encapsulation layer.

With the titanium contacts, removal of the encapsulation layer and etch mask was accomplished using Technistrip P1316 photoresist stripper (purchased from MicroChemicals GmbH). P1316 is a TMAH based stripper compatible with metals and capable of stripping both positive and negative AZ series photoresists. Prior to use on the contacts, the compatibility of P1316 with ZnO was investigated, with SEM analysis of NW arrays showing no discernible difference before and after immersion in P1316 at 75 °C for a 24 hour period. In order to remove the encapsulation layer fully, the Ti contact samples were left immersed in P1316 at 75 °C for approximately 18 hours. The resulting SEM images are shown in figure 6.10.

In contrast to the O_2 ashed samples, the cross-sectional image in figure 6.10c demonstrates complete removal of the encapsulation layer with relatively little residual contamination, although some residue is still visible on the uncontacted wires shown in figure 6.10f. Due to the absence of the planarisation step, a high degree of variation in contact area is visible in figure 6.10d between wires. Figure 6.10e shows a defect in the contact, with the presence of tapered NWs in the void likely an indication that the defect is due to a pinhole in the photoresist mask.

Electrical measurements were attempted on the floating contact pads using an I-V probe station, but were found to be problematic. Prior to contact measurements, both probe station tips were landed on the uncontacted NWs and I-V measurements were conducted to confirm an Ohmic conduction path between tips through the NWs and base growth layer. Precise approach of the tips on the scale of the contact pads was found to be unreliable, and considerable variation in the I-V characteristics were found by simply altering the tip height, suggesting that

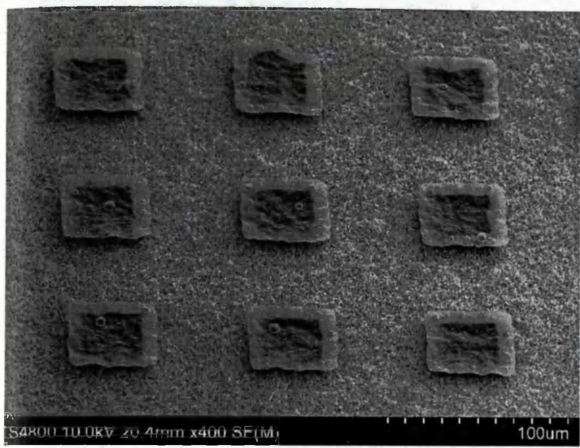

(a) Floating Al contacts showing phosphorous rich spheres.

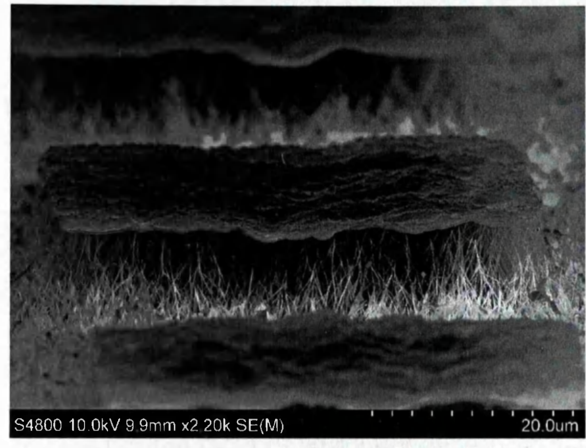

(b) Tilted view of contact.

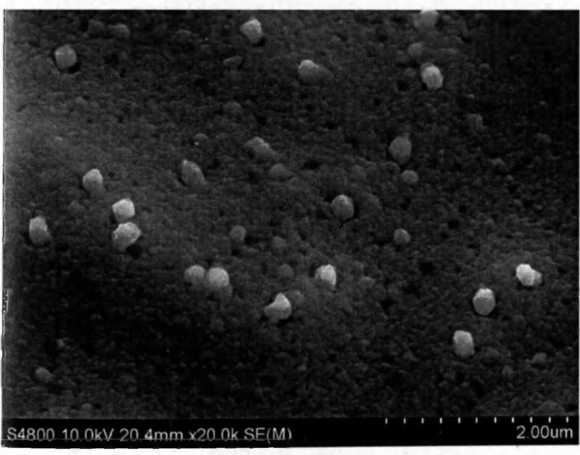

(c) Polycrystalline contact with NW tips.

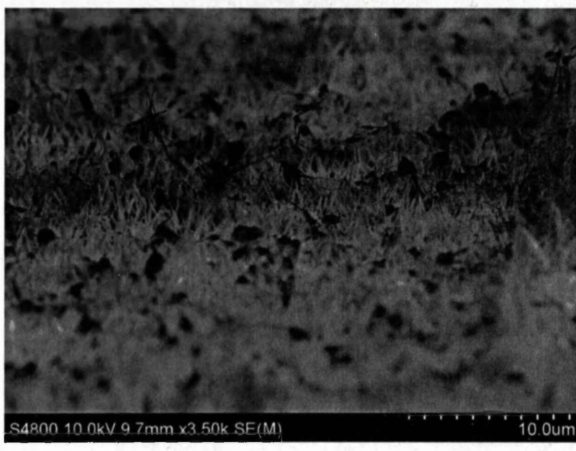

(d) Etching or resist residue attached to exposed NWs.

Figure 6.9: SEM images of floating Al contacts following removal of the encapsulation layer using plasma ashing. In (a), a lighter boarder is observed around the edge of the contact. This could suggest possible retention of resist in the centre of the contact, although it could also be indicative of etching of the NWs at the extremity of the capped array due to percolation of the etchant solution through the uncapped NW growth. This is supported by the lower density of NW growth at the contact edges observed in (b). (c) demonstrates the uniform contacting to the NW tips resulting from planarisation of the NW arrays. Deposits and residues identified as phosphorous rich using EDX were present on the contacts following removal of the encapsulation layer. These can be observed in (a) and also on the uncontacted etched NWs shown in (d) and indicate the need for an alternative etchant solution.

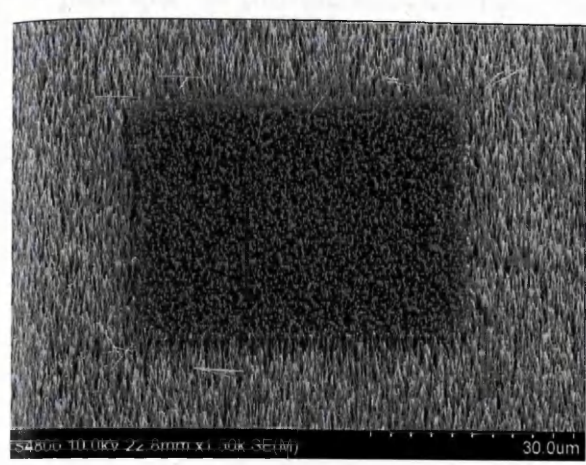

(a) Ti contact pad measuring approximately 40 µm × 40 µm.

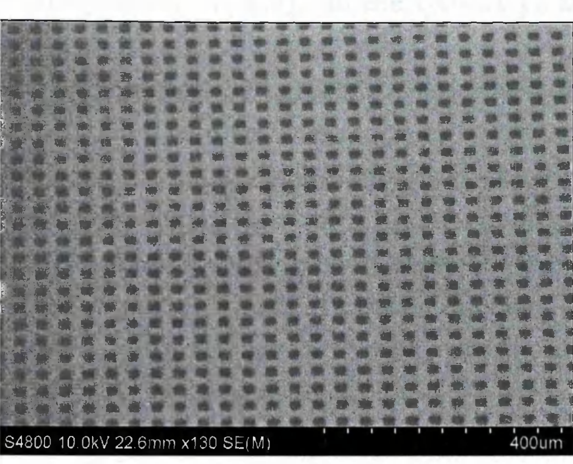

(b) Array of floating Ti contacts.

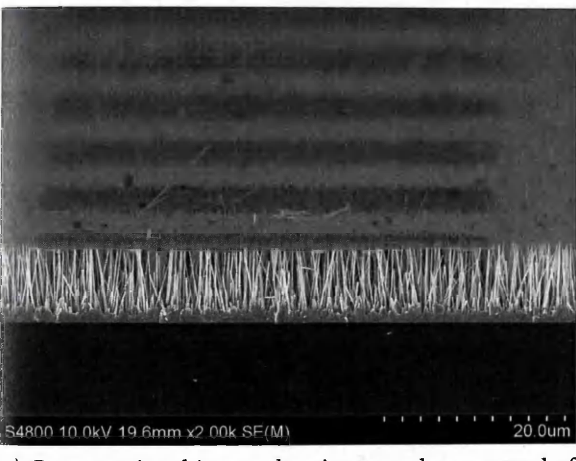

(c) Cross sectional image showing complete removal of encapsulation layer.

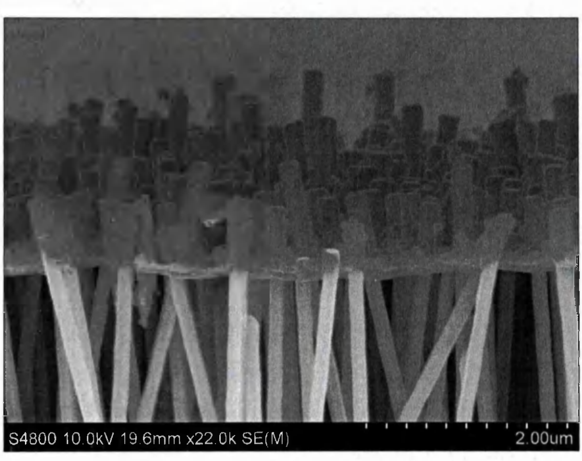

(d) Close up of tips coated in Ti.

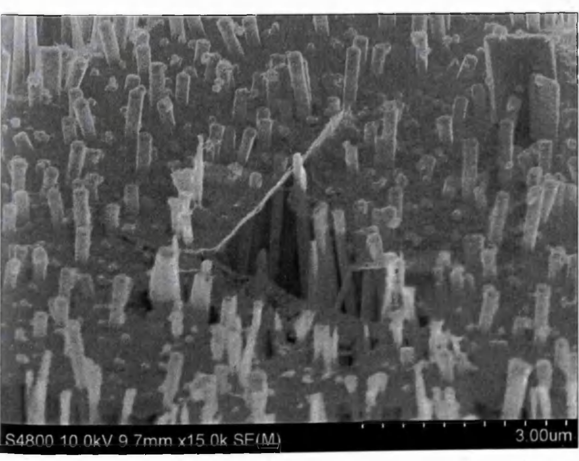

(e) Defect in contact.

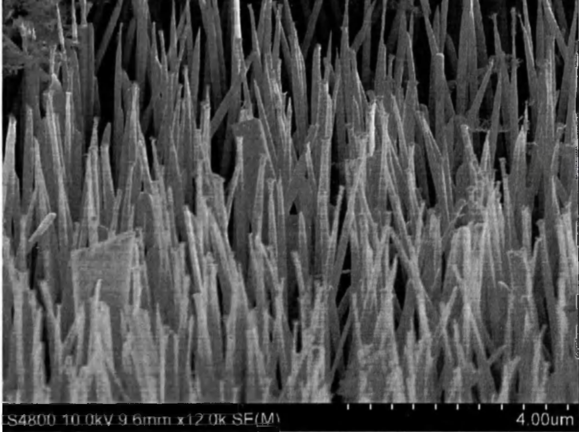

(f) Etched wire tips following expose to BOE.

Figure 6.10: SEM images of floating Ti contacts following removal of encapsulation layer using P1316 resist stripper. In contrast to the images shown in 6.9, a planarisation step has not been conducted in order to level the NWs following encapsulation and NW tip exposure. This is apparent in (d) and (e), where unequal protrusion of the NWs through the top contact is clearly visible. This will likely create issues with variable contact resistance and quality between individual NWs. (f) shows tapered NW tips damaged due to exposure to the BOE solution used to pattern the Ti top contact.

the pads did not provide sufficient rigidity for contact probing. Damage to the contact pads could also be observed following tip retraction using the probe station optical microscope. Measurements were recorded following tip approach onto the uncontacted etched NWs (shown in figure 6.10f) and the I-V characteristics were found to be similar in variation to those recorded for the contact pads, suggesting conduction may have been occurring through the NWs directly contacted by the probe station tip, rather than through the contact pad. For the Al contacts, there is a possibility that extended O_2 plasma ashing resulted in oxide growth of the Al film, rendering it non-conductive. At the time of writing, additional methods of contacting such as wire bonding and conductive AFM (c-AFM) are currently under investigation. These preliminary results demonstrate that free-floating NW contacts suitable for use in sensing applications can be implemented using standard semiconductor fabrication techniques.

6.3 Fabrication of a Vertical Nanowire Sensing Device

The previous section demonstrated the viability of using a removable encapsulation layer as a means for fabricating metal contacts to the top of NW arrays for sensing applications. However, several challenges related to contacting the arrays still require addressing:

- **Selective area nanowire growth:** The sputtered conductive layer requires patterning in order to selectively grow the NW arrays.
- **Contacting the bottom electrode:** Although the sputtered conductive layer can be used to form an intimate contact with the base growth of the NW arrays, following growth an additional ZnO etching step is required in order to expose the conductive layer for direct probing or bonding.
- **Top contact support:** As demonstrated in the previous section, the floating top contacts are delicate and direct probing or bonding to the unsupported contacts is undesirable for a number of reasons. Instead, a raised growth-free area of the substrate could provide a rigid support over which the contact may be extended and probed.
- **Microchannel formation:** Related to the previous issue. Microfluidics provide a means for delivering the analyte directly to the sensing elements. In realistic sensing applications involving low detection thresholds, flow of the analyte is desirable in order to avoid accurate volume measurement. If the top electrode is used to bridge the gap between supporting raised areas of the substrate, a microchannel containing the sensing elements is formed, with the raised areas of the substrate additionally providing the necessary support for contacting the top electrode.
- **Prevention of short circuit paths between the electrodes:** When using a conductive substrate such as Si, either one or both of the contacts require electrical isolation from the substrate to prevent short circuit paths between the electrodes.

Shown in the following section is the fabrication process for a model device aimed at solving the issues raised during the fabrication of the floating contact devices and identified above. The model device, shown schematically in figure 6.11, is aimed to provide fabrication solutions that can later be adapted to optimise the electrical, microfluidic and ultimately sensing performance of the vertical NW devices. The model device is not intended as an optimised biosensor, and many possible configurations for vertical devices are available using these vertical integration strategies.

6.3.1 Overview of fabrication process

The fabrication process uses the previous photoresist encapsulation strategy to form a top contact to the NW arrays. The principle difference between the floating contact approach and the process outline here is the photolithographic patterning of the encapsulation layer to act as an etch mask for the ZnO NWs. The main reason for this is to allow exposure of the bottom contact for direct probing or contacting. In addition, it also ensures that NW growth is restricted to the desired area. This is important for isolating multiple devices fabricated on the same substrate – uniform

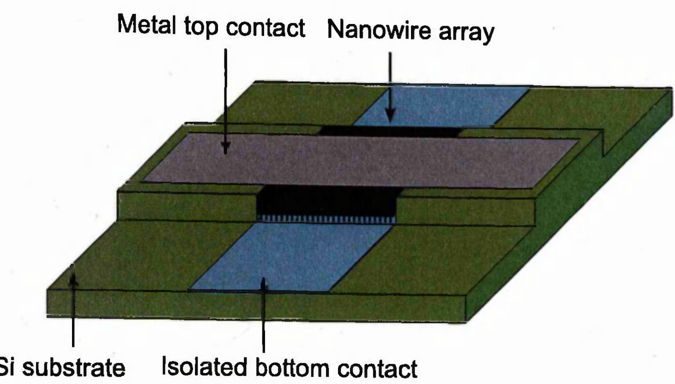

Figure 6.11: Model device consisting of a top (grey) and bottom (blue) electrode which form a microfluidic channel containing the NW sensing elements. The bottom contact must be electrically isolated from the Si substrate to prevent a short circuit path between contacts. This may be achieved by pre-sputtering a thin insulating SiO_2 layer prior to contact deposition.

growth coverage would put all devices in electrical contact through the base growth layer. Excess growth would also have a detrimental effect on the sensitivity and detection threshold of the sensor, due to binding of the target protein to ZnO surfaces not involved in the sensing circuit.

A diagram of the fabrication process is shown in figure 6.12. The process is divided into three distinct modules, indicated by the coloured regions in the diagram. These three modules provide the basis for structuring the experimental details and results, which are shown together in sections 6.3.2, 6.3.3 and 6.3.4, respectively.

- **Microchannel formation (1-2):** Formation of a channel or trench through which an analyte may be passed. The channel is etched to the same depth as the NW arrays and the top contact is extended over the masked region of the substrate, which acts as a top contact support.
- **Bottom contact deposition and NW growth (3-6):** Prior to NW growth, the conductive layer or bottom contact is sputter deposited and patterned using a lift-off process.
- **Top contact deposition (7-16):** The NWs are encased in negative photoresist, which is then patterned to expose areas of unwanted growth. The ZnO is etched back to leave the encapsulated sensing array. Two further photolithographic processes are then necessary to pattern the top contact.

All process was conducted on 15 mm × 15 mm n-type silicon (1 0 0) substrates. The substrates were cleaved then cleaned using a standard procedure consisting of solvent and acid cleaning processes. For more information see section 3.2.

6.3.2 Etching of microchannels

The substrates were spin coated in positive AZ 6612 photoresist (section 3.2.2.1) at 3000 rpm for 45 seconds, with an initial acceleration of 1000 rpm/s (section 3.2.2.2), then soft-baked at 110 °C for approximately 1 minute 30 seconds (section 3.2.2.1). An MA8 mask aligner was used for UV exposure, with an exposure dose of 350 mJ/cm^2, as measured at the Hg h-line (405 nm) (section 3.2.2.3). Following resist hydration, the samples were developed as described in section 3.2.2.4.

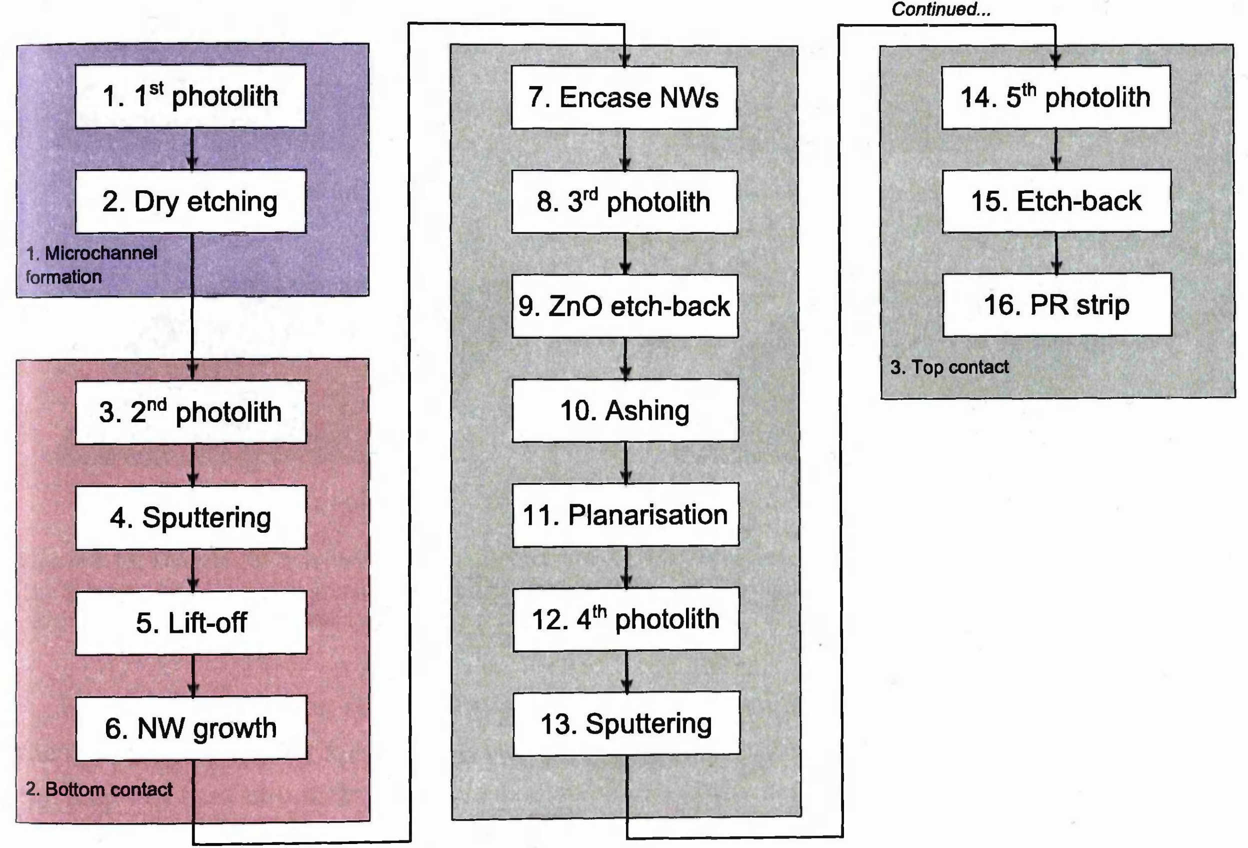

Figure 6.12: Flow diagram of fabrication process for vertical NW sensing devices. The processes are split into three distinct sections - (1) Formation of microchannels using dry etching. (2) Bottom contact deposition and NW growth. (3) Top contact deposition.

Dry etching was conducted in an Oxford Instruments PlasmaLab 80 Plus RIE system, using the process detailed in section 3.2.4.1. In brief, SF_6, CHF_3 and O_2 were introduced to the reaction chamber at flow rates of 30, 10 and 5 sccm, respectively. Chamber pressure was maintained at 0.1 mbar during the process, and the samples were etched at an RF power of 100 W for 7 minutes. The residual resist was stripped using acetone prior to rinsing in IPA and DI water. Following the solvent clean, some residual photoresist still remained visible under SEM (figure 6.14c), necessitating an additional 15 minute O_2 plasma clean at 100 W (section 3.2.6).

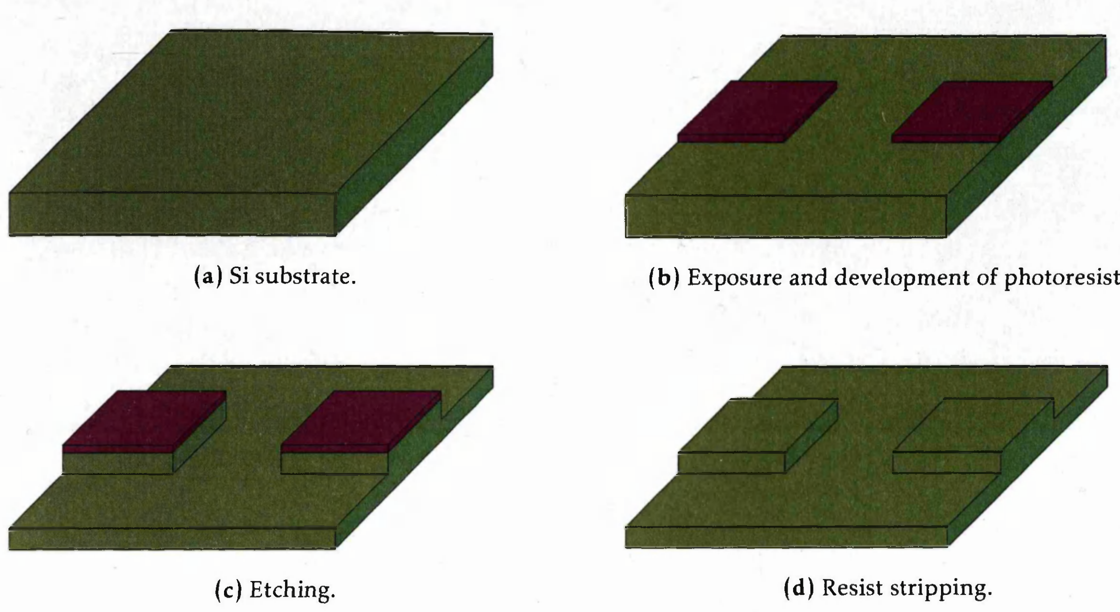

(a) Si substrate.

(b) Exposure and development of photoresist.

(c) Etching.

(d) Resist stripping.

Figure 6.13: Diagram of first photolithography and etching process to create a trench support structure for the device. The Si substrate is shown in green and the photoresist mask in pink. This process is a typical example of semiconductor etching employing a photoresist mask.

The process is shown schematically in figure 6.13. Scanning electron microscope images of the resulting structures are displayed in figure 6.14. Significant undercut of the resist is visible at the edges of the features in figure 6.14a. The width of the near feature in the image is measured to narrow to approximately 132 µm close to the resist film, compared with the 140 µm width of the feature on the mask, indicating an undercut of approximately 4 µm per side, assuming accurate development of the photoresist film. A close up of the residual resist in figure 6.14b reveals a pitted surface. Due to thinning of the resist mask during the etch process, these pits were found to have transferred through onto the underlying masked areas of the substrate. This has implications for undesired ZnO nucleation and for the ZnO etch back process, which will be discussed further in section 6.3.3.

The cross-sectional SEM image in figure 6.14c reveals an isotropic etch profile. Photoresist residue is still visible on the masked Si, despite the sample having undergone a solvent clean. As mentioned above, this was removed using plasma cleaning. Indicated on the figure is the 4 µm undercut, with the vertical line demonstrating the location of where a completely anisotropic sidewall would be expected. The channel depth was found to be approximately 6.25 µm, giving an etch rate of 0.9 $\mu m\,min^{-1}$.

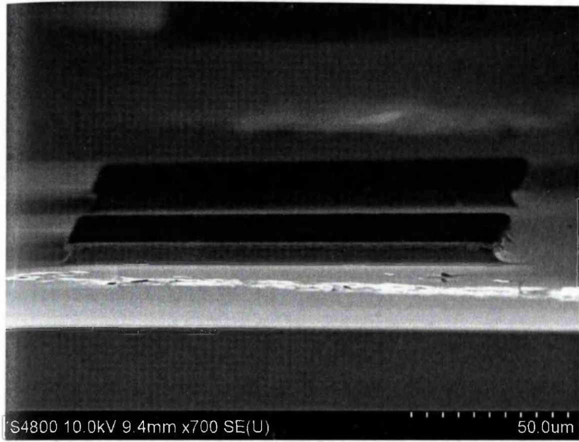

(a) Raised Si features following etching with PR mask still in place.

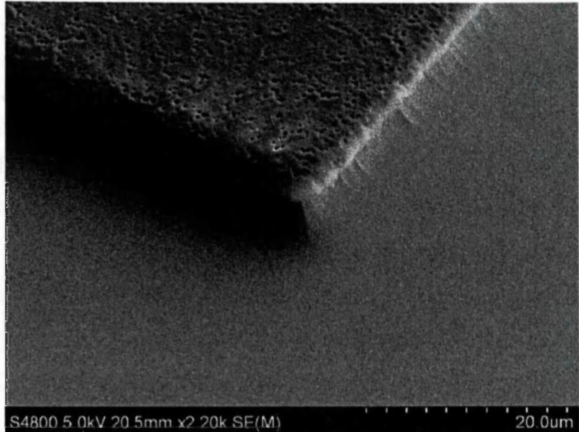

(b) Pitted surface of PR mask following etching.

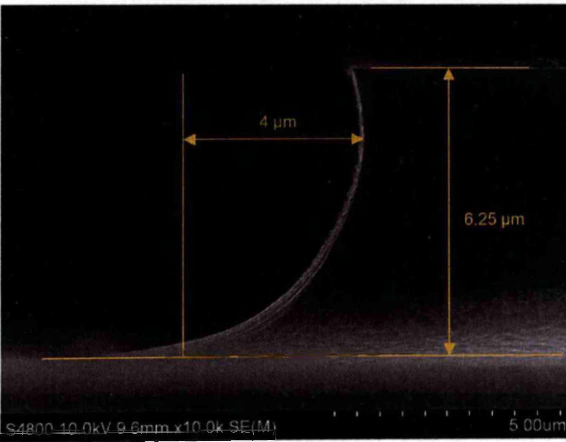

(c) Cross-section of etching profile following solvent resist strip.

Figure 6.14: SEM images of etched silicon with the photoresist etch mask still in place. In (a), the undercut of the etch mask is clearly visible. (b) shows surface pitting of the etch mask due to the high etching bias used in RIE. (c) shows a cross-sectional SEM image following photoresist stripping. An undercut of approximately 4 µm is visible.

6.3.3 Deposition of conductive layer and nanowire growth

The 2nd photolithography process was required to pattern the conductive layer or bottom electrode. This was necessary to isolate individual devices, but it was also hoped that it would restrict NW growth to the surface of the sputtered layer. Unfortunately, likely due to the surface roughness of the etched substrate following RIE, NW growth was found to occur across the substrate. The 2nd photolithography process used AZ 6612 photoresist (section 3.2.2.1) spin coated at a lower speed of 2000 rpm for 45 seconds, with an initial acceleration of 1000 rpm/s (section 3.2.2.2). The lower speed was used to achieve a thicker resist film in order to aid with the subsequent lift-off process. The soft-baking, exposure and development processes were as described above in section 6.3.2.

As mentioned previously, in this design the bottom and top electrodes are both in direct contact with the conductive Si substrate. In order to avoid short circuit paths through the substrate between contacts, a thin insulating layer of SiO_2 was used to isolate the bottom contact. Initially, both CVD Si_3N_4 (section 3.2.5.2) and sputtered SiO_2 layers were deposited following RIE and prior to the start of the 2nd photolithography process. This resulted in coverage of the substrate with an insulating layer, meaning both contacts were electrically isolated. However, this strategy resulted in two problems. Firstly, the hydrophilic SiO_2 and Si_3N_4 surfaces resulted in poor photoresist adhesion, due to residual moisture, leading to features lifting off of the substrate during development. Secondly, the SiO_2 and Si_3N_4 were found to promote nucleation of the ZnO, resulting in a high degree of unwanted growth coverage. The growth was comparable to that described in section 4.4 on sputtered conductive layers in terms of length, diameter and base-growth layer thickness, however the alignment was found to be poor, likely as a result of the amorphous nature of the insulating layers. The fact that the base-growth layer was found to be similar in thickness to the growth on the bottom electrode is problematic during the ZnO etch back for reasons discussed in section 6.3.4. Due to these issues with complete insulating coverage, the alternative approach was to sputter the SiO_2 prior to deposition of the bottom electrode, resulting in isolation of the conductive layer from the substrate.

The SiO_2 was sputtered to a thickness of 50 nm in a Lesker PVD 75 system (section 3.2.5.1), as measured using a quartz crystal micro-balance. Both Ar and O_2 were used with flow rates of 50 and 5 sccm, respectively, resulting in a chamber pressure of 3.3×10^{-3} mTorr. The RF supply was ramped slowly and maintained at 200 W during the process.

The bottom electrode was also sputtered in the same system to a thickness of 100 nm, as described previously (sections 6.2.1 and 4.4). It should be noted that due to the use of an amorphous insulating layer, symmetric texture inheritance of the sputtered conductive layer from the Si substrate is slightly diminished. This was shown to be the case with ITO deposited on a 100 nm CVD Si_3N_4 layer in section 4.4.2.2, where the alignment and preferential tilt of the NWs was found to be reduced when compared to those grown on conductive layers sputtered directly onto crystalline Si. Although this slight reduced alignment is not anticipated to be problematic for vertical device integration, modulation of the texture inheritance may be possible by altering the thickness of the insulating layer [235].

The lift-off process was accomplished using dimethyl sulfoxide (DMSO), as detailed in section 3.2.2.5. The samples were sonicated in DMSO for 5 minutes, then rinsed and sonicated in fresh DMSO for another 5 minutes to minimise redeposition. Following the lift-off, the samples were rinsed in DI water and dried under N_2 flow. Figure 6.15a shows a diagram of the resulting pattern following the lift-off process.

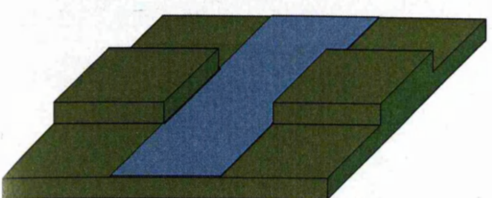
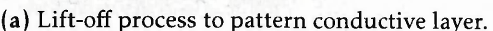

(a) Lift-off process to pattern conductive layer.

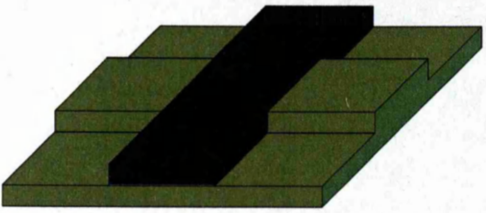

(b) Growth of ZnO NWs.

Figure 6.15: Diagram showing (a) simultaneous lift-off patterning of bottom contact and insulating SiO_2 layer (blue) and (b) subsequent selective area NW growth.

Nanowire growth was conducted using the method described in section 4.4 for a duration of 45 minutes, resulting in NWs with an array height of around 7 μm, as measured using SEM. Figure 6.16 shows an SEM image of the resulting growth alongside a cross-sectional image of the substrate interface.

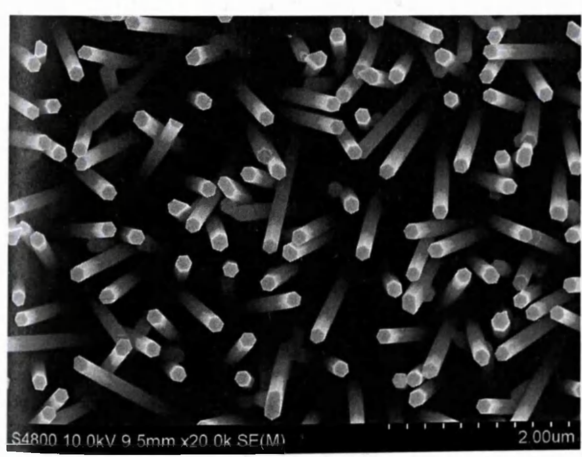

(a) Top down SEM view of NW growth on Ti/SiO_2 layers.

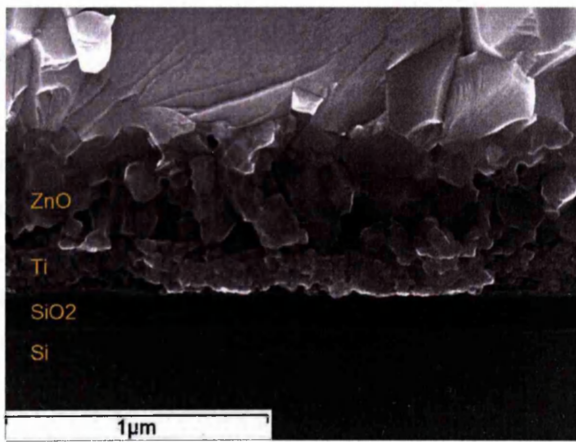

(b) Cross-section SEM image of interface.

Figure 6.16: SEM images of ZnO NWs growth on sputtered SiO_2/Ti layers. (a) demonstrates that despite the presence of an amorphous oxide layer, the NWs still appear highly aligned. This suggests that the oxide layer is still thin enough (50 nm) to allow for symmetric inheritance from the Si substrate (see sections 4.4.2.2). (b) shows a cross-sectional SEM image of the ZnO/Ti/SiO_2/Si interface. The polycrystalline nature of the Ti layer and initial ZnO nucleation is clearly visible.

Figure 6.17a demonstrates the additional growth promoted by depositing an insulating layer of Si_3N_4 across the sample. This can be contrasted with figure 6.17b, where an SiO_2 layer has been deposited prior to the lift-off, isolating only the bottom electrode and leaving the etched Si surface exposed during NW growth. Preferential growth on the masked area of the of the Si is seen in figure 6.17b, likely due to the surface pitting resulting from the etch process previously

discussed in section 6.3.2.

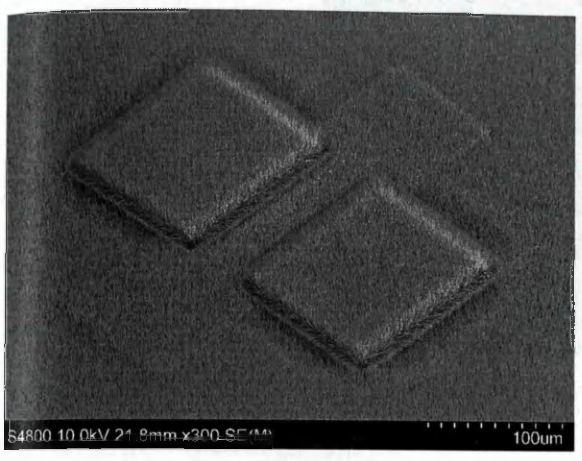

(a) Uniform coverage of Si_3N_4.

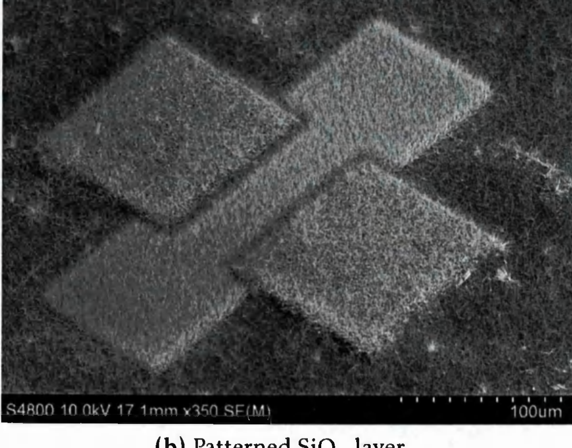

(b) Patterned SiO_2 layer.

Figure 6.17: SEM images of NW growth on device structure showing the difference between unwanted growth on (a) deposited Si_3N_4 and (b) etched Si substrate. In (b), the bottom contact is electrically isolated from the substrate by a thin pre-sputtered SiO_2 layer deposited prior to bottom contact deposition and patterned simultaneously using the lift-off process. This method results in less non-specific ZnO nucleation over the substrate surface.

Figure 6.18 shows a top-down SEM image demonstrating the unwanted growth on the masked Si area and Si sidewalls. The separation between the masked Si area and the bottom contact is approximately 8.27 µm, as indicated on the figure. The reason this is considerably larger than the 4 µm that would be expected from the sidewall undercut is due to the mask design. During development of the lift-off photoresist mask, over expose or development will result in a slightly enlarged contact area. This has the potential to result in metal deposition on the sidewalls, which could create shorts between the top and bottom contacts. With this in mind, the lift-off pattern on the photomask was designed with three different widths for the bottom contact. The first design has a contact width the same as the separation between channels, which in this case is 50 µm. The second design is inset by 3 µm either side (44 µm width) and the third is inset by 6 µm either side (38 µm width). For the devices in this section, the third design with the largest inset was used in order to avoid shorts. This has the effect of creating a larger span between the highly aligned growth on the contact and the raised Si support, which could compromise the integrity of the top contact. The separation between bottom contact and Si sidewall shown here indicates an enlargement of 1.73 µm over what would be expected by considering the undercut and lift-off mask inset.

Large areas of unwanted growth were found to be located at the corners of the raised Si areas, as indicated by the red circle in figure 6.18. Figure 6.19 shows a top down SEM image of the lifted-off contact prior to growth. The red circles in the figure indicate areas of metal retention on the corners of the Si supports. This indicates insufficient resist coverage for the lift-off process – thinning can occur at sharp edges during spin coating, which results in metal deposition and ultimately large areas of unwanted ZnO nucleation. Spin coating and lithography conducted on etched features can be problematic due to variations in resist thickness. This is also evidenced by the non-equal separation between the contact and the sidewall along the length of the channel,

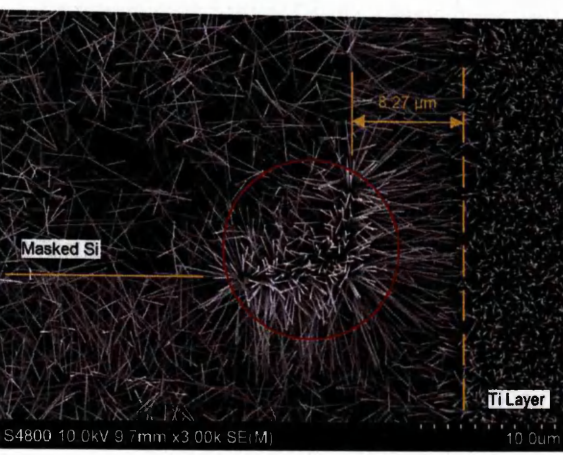

Figure 6.18: Top-down SEM image of unwanted ZnO deposits and NW growth on Si and Si sidewalls of etched support structure. This unwanted nucleation is problematic for subsequent processing steps such as encapsulation layer spin coating and top contact deposition.

due to non-uniform resist coverage following spin coating.

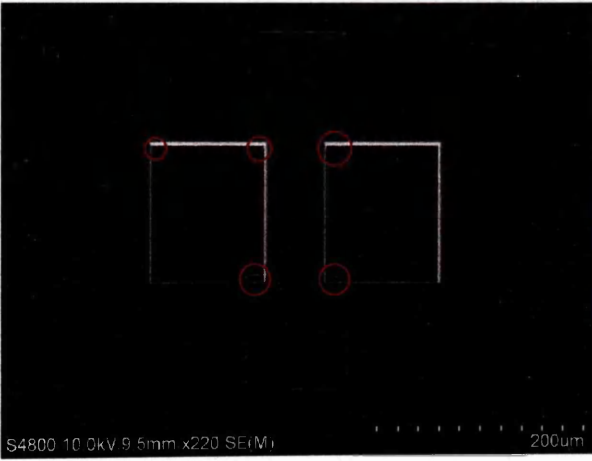

Figure 6.19: Top down SEM image of etched structure following bottom contact lift-off. The red circles indicate areas of metal retention due to non-uniform resist coverage on step edges following spin coating. Although these deposits do not interfere directly with the fabrication steps, they result in unwanted nucleation during NW growth that will interfere with subsequent encapsulation layer and top contact deposition (see figure 6.18).

6.3.4 Deposition of top contact

The top contact deposition process is shown schematically in figure 6.20. Essentially, the NWs are encapsulated in a negative resist film, as described for floating contacts in section 6.2.1, then the encapsulation layer is patterned to serve as an etch mask for removing unwanted ZnO nucleation from the raised Si support areas (figure 6.20a). A positive resist is used to protect the device from the top contact deposition (figure 6.20b). The contact is then sputtered (figure 6.20c) and patterned using an additional photolithography and etch back step (figure 6.20e). The remaining resist is then removed using P1316 photoresist stripper, as described in section 6.2.5 (figure 6.20e).

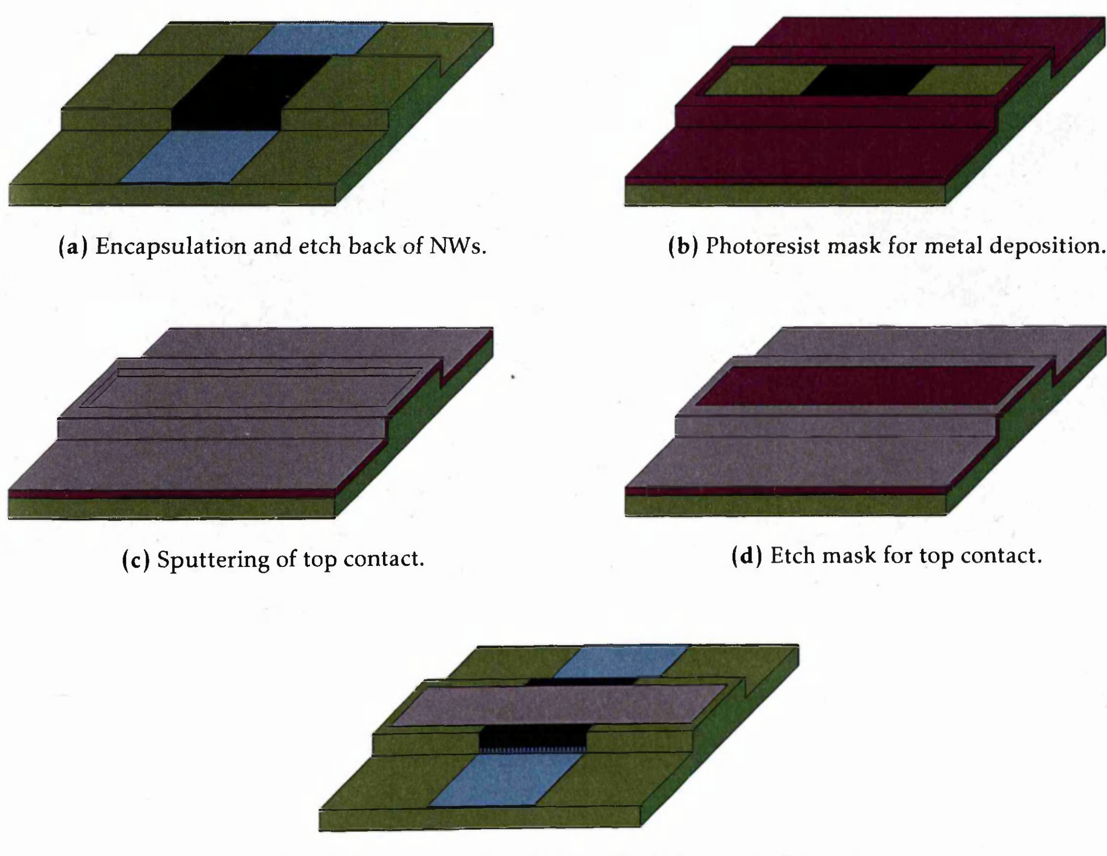

(a) Encapsulation and etch back of NWs.

(b) Photoresist mask for metal deposition.

(c) Sputtering of top contact.

(d) Etch mask for top contact.

(e) Etching of metal and removal of photoresist/encapsulation layer.

Figure 6.20: Diagram of top contact deposition and patterning. The Si substrate is shown in green, the bottom contact in light blue, the encapsulated NW array in dark blue, the positive photoresist etch mask in pink and the metal top contact in grey. (b) an initial lift-off layer of positive resist is use to mask the sample from contact deposition. (c) the metal contact is sputtered over the sample. (d) a photoresist etch mask is patterned on top of the metal contact. (e) the metal is etched using wet chemistry and the photoresist and encapsulation layers are removed.

The encapsulation layer was formed using AZ nLOF 2070 negative photoresist, as described in section 6.2.1. The portion of the array in the channel was then exposed using an MA8 mask aligner with an exposure dose of $1000\,mJ/cm^2$, as measured at the Hg i-line (365nm) (section 3.2.2.3). Following exposure, a post-exposure bake is necessary to cross-link the resist (section 3.2.2.1). This was done on a hotplate at $110\,°C$ for 1 minute 30 seconds. Following resist hydra-

tion, the samples were developed as described in section 3.2.2.4.

The ZnO was etched using 10 mmol HCl and 1 mol NH_4Cl, which have both been shown to etch ZnO thin films at a rate or approximately 300 nm/min [114]. Following Zhang et al. NH_4Cl was used in order to try and prevent undercutting and create a more anisotropic etch profile [114]. The etch-back of the ZnO was found to be difficult to control and is one of the principle challenges remaining in the fabrication process. The main issue is the thickness of the base-growth layer – severe undercutting of the base-growth results in damage to the encapsulated NWs. This is shown in figure 6.21. Figure 6.21b demonstrates how, once the encapsulation layer has been removed, etching of unwanted growth and surface debris also results in over-etching and undercutting of the NWs in the channel. Etching with HCl was found to be more problematic, likely due to the high dilution causing an instability in the concentration of H^+ during the etch process, which results in a highly variable and inconsistent etch rate [114].

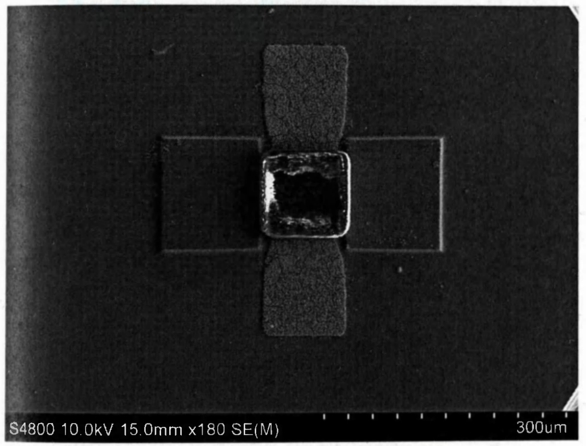

(a) Encapsulation layer following etch-back.

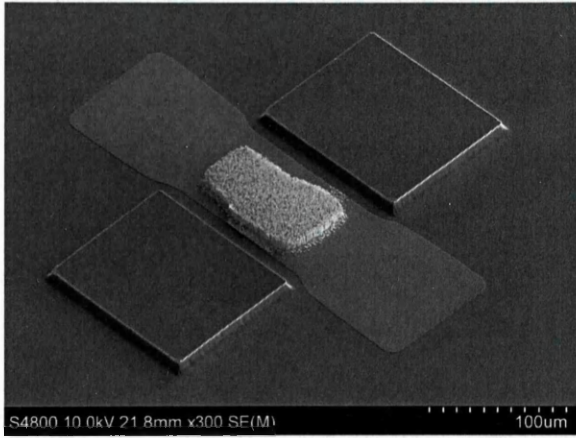

(b) Damage to encapsulated NWs due to undercut during etching.

Figure 6.21: SEM images of NW array and device structure following etching of the ZnO in dilute HCl. The base growth layer allows for a large undercut into the array leading to. (a) shows the bare Si surface and encapsulation layer following etch back. The NW array is just visible inside the encapsulation layer. (b) shows the same device following removal of the encapsulation layer to reveal the damaged NW array.

Ashing and planarisation were carried out as described in sections 6.2.2 and 6.2.3, respectively. Due to the cross-linking of the resist film following expose and baking, the ashing rate of the encapsulation layer was found to be around 25% slower than that stated in section 6.2.2, with an ashing duration of 25 minutes required to remove approximately 5 µm of resist.

The 4th photolithography process was required to mask the substrate and bottom electrodes from the top contact deposition. This was accomplished using AZ 6612 using the same recipe as for the bottom contact lift-off process (section 6.3.3). Titanium was used as the top contact material, due to the favourable etching results demonstrated on the floating contacts when using BOE. The Ti was sputtered to a thickness of 200 nm, as described in section 6.2.4. The 5th photolithography process also employed AZ6612 to act as an etch mask, using the standard spin coating and baking parameters, as described elsewhere (section 3.2.2.2). The contacts were etched in BOE for between 2-3 minutes, then rinsed in DI water and dried under N_2. Removal of the the photore-

sists and the cross-linked encapsulation layer was accomplished by immersing the substrates in P1316 photoresist stripper at 75 °C for approximately 18 hours. The samples were then rinsed in DI water and IPA and allowed to dry naturally. Scanning electron microscope images of the resulting structures are shown in figure

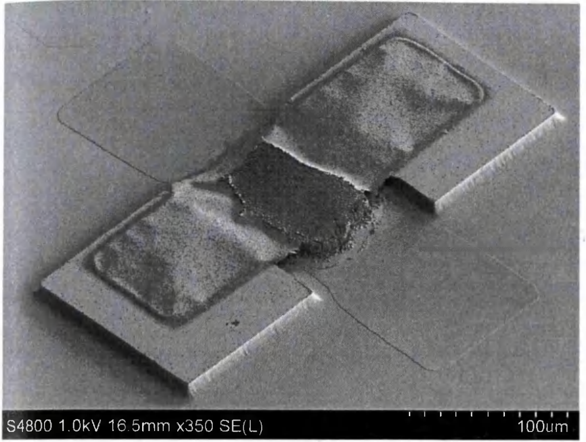

(a) 100 µm wide top contact with 100 µm NW array.

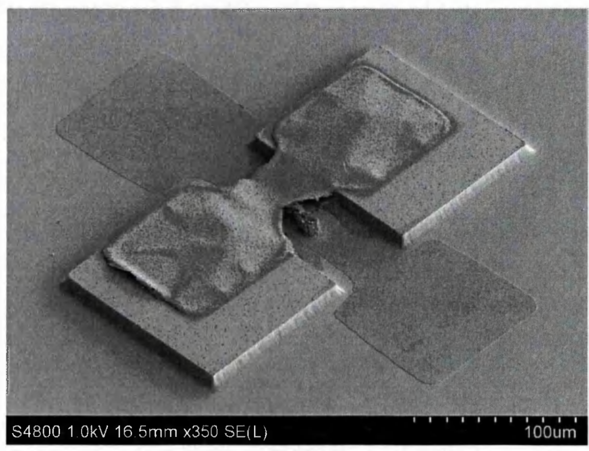

(b) 50 µm wide top contact with 50 µm NW array.

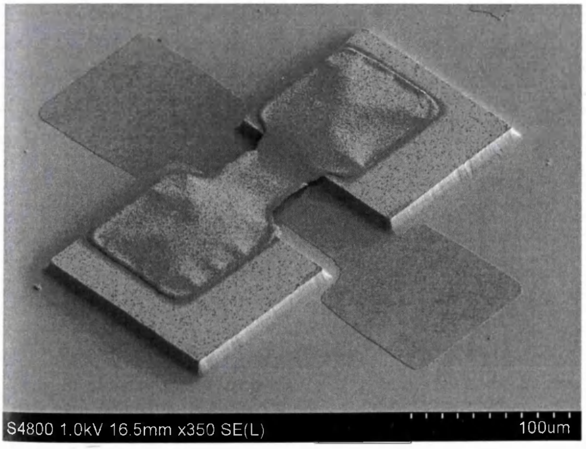

(c) 50 µm wide top contact with 50 µm NW array.

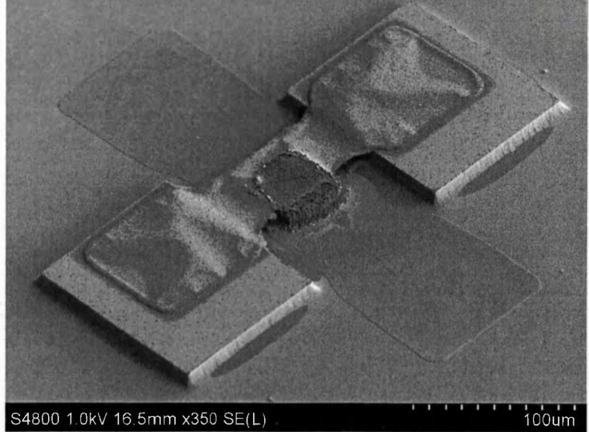

(d) 50 µm wide top contact with 100 µm NW array.

Figure 6.22: SEM images of devices following removal of encapsulation layer.The top and bottom contact dimensions vary between images. A slight misalignment is apparent in the top contact etch mask, and consequently the top contact, in all four images. In (a), etching of the array has led to collapse of the top contact and shorting between the bottom and top contacts, which has been exacerbated by the top contact misalignment. Due to the small array size in (b), severe etching has removed most of the nucleated ZnO. In (c), complete removal of the NW array is observed. The top contacts appear fragile in all four images, with some bowing of the contact visible around the array in (d).

Significant over-etching resulted in poor quality arrays, with only figures 6.22a and 6.22d showing contact between the NWs and top electrode. Despite this, the top contact appears resilient enough to span unsupported between the two raised Si regions, despite agitation of the samples in liquid during the rinsing process. Cross-sectional SEM revealed complete removal of the encapsulation layer from the channel, with only minimal organic residues appearing in the NW arrays, as shown previously in figure 6.10f. Due to over-ashing, the device shown in figure 6.22a appears to exhibit a short between the top and bottom contacts.

Again, electrical measurements proved problematic, although probing was more straight for-

ward due to the large contact pads available for the top and bottom electrodes. Probing between the two bottom contact pads revealed a highly resistive film, likely caused by severe oxidation of the Ti bottom contact during the growth process, which prevented I-V measurements being taken through the device. X-ray diffraction measurements in section 4.4.2.2 revealed peaks which could be indexed to rutile TiO_2, with no peaks being detected for elemental Ti. The electrical measurements corroborate this and indicate that Ti is of limited use as a buffer layer due to its inability to be used as a bottom electrode.

6.4 Chapter Summary

A method for depositing suspended metal contacts on vertical NW arrays has been developed and refined to allow the photolithographic patterning of floating top contacts for device applications. A suitable photoresist (AZ nLOF 2070) for the smooth encapsulation of NW arrays was identified and a spin coating process was developed in order to form a uniform encapsulation film free of voids and fissures. This required that the resist be spun coated to a thickness greatly exceeding that of the NW array to avoid problems with the NW morphology inhibited flow of the viscous fluid across the sample surface, leading to dome shaped deposited forming around NW bundles. Oxygen plasma ashing was used to controllably remove a layer of resist in order to expose the NW tips for contacting. Planarisation of the NW arrays was achieved by sonicating the samples in DI water in order to remove the portion of the NW tips protruding above the encapsulation layer. This will be an important step in ensuring uniform contact properties between individual NWs. After a further brief ashing to expose the NW tips, the metal contact is sputtered deposited over the encapsulation layer. Patterning of the contact layer is achieved using an additional photolithography and wet chemical etch step. Finally, the remaining photoresist and encapsulation layer are removed using either oxygen plasma or wet chemical techniques. The major outcomes from the optimisation of this process are as follows:

- A negative resist is suitable for the encapsulation layer as it forms a stable base for subsequent photolithographic processes. This resist layer must be spin coated to a film thickness considerably in excess of the NW array height to prevent the NW morphology for interfering with the film uniformity.
- Oxygen plasma ashing provides a suitable means for controllably removing the encapsulation layer to exposure the desired portion of the NW array. Excessive RF power causes heating of the sample resulting in cracking of the encapsulation film, likely as a result of uneven thermal expansion.
- Cleavage of NW tips protruding from the encapsulation layer in order to planarise the array height may be achieved using brief sonication of the same in DI water.
- Some etchants may be unsuitable for etching the top contact following sputter deposition and photolithography. A phosphoric acid based aluminium etchant resulted in phosphorous rich deposits on the top electrode and uncontacted NW arrays following encapsulation layer removal. Buffered oxide etchant appears to be suitable for use with titanium.
- Some combination of wet chemical stripping and oxygen plasma cleaning/annealing may be optimal in order to remove resist deposits and surface contaminants.

Significant electrical characterisation of the top contacts and vertical NW devices is still required. Initial I-V measurements between contacts as well as detailed nanoscale characterisation of the bottom contact/NW and NW/top contact interfaces is necessary in order to understand charge transport through the NW sensing elements and respective interfaces. This contact and interface characterisation would ideally be suited to a nanoprobe system, as previously used for the individual NW FET measurements described in chapter 5.

Using this approach to top contact fabrication, a design for a simple sensing device was developed, consisting of channels etched in silicon through which an analyte may be flown and hence detected. However, fabrication of this device structure proved problematic, with several challenges remaining related to unwanted nucleation leading to non-specific growth of NWs. One of the main issues is etching of the Si substrate results in roughness assisted NW growth, as detailed in chapter 4.3. Removal of this unwanted growth results in severe undercut of the base growth ZnO layer nucleated on the bottom contact, leading to etching of the NW sensing array. Several solutions to this problem are currently under consideration, including alternative etching techniques and etch chemistry, a de-roughening process such as oxide growth and removal using BOE and deposition of a material to inhibit ZnO nucleation.

Chapter 7

Conclusions

In this thesis, the growth and functionalisation of vertical arrays of zinc oxide nanowires (ZnO NWs) was investigated for applications in conductometric immunosensing. Using high temperature chemical vapour deposition (CVD), three methods of substrate preparation to initiate the growth of ZnO NW arrays were explored, namely sputtered ZnO seed layers, roughness assisted growth and sputtered conductive thin-films. The aim was establish a method for growing uniform arrays of high aspect ratio NWs on silicon substrates, suitable for use in an ensemble biosensor device.

Despite efforts to optimise the crystalline quality of sputtered ZnO seed layer through post-deposition annealing, the seed layers were found to result in poor quality NW growth unsuitable for integration into vertical NW devices. In particular, the morphology, aspect ratio and density of the NWs were found to be less desirable when compared with the literature and the other two techniques investigated here. Despite this, further investigation of electrical conduction through the ZnO/Si interface revealed a correlation between conductivity and deep level visible photoluminescent emission, commonly attributed to the native defects in ZnO. These results have implications for the creation of electrical contacts to the base of NW arrays required for vertical device integration.

Growth of NWs directly onto the silicon substrate was achieved using a surface enhanced method. Both wet and dry etching techniques were employed to alter the substrate surface topography, resulting in increased nucleation of ZnO vapour, leading to island type growth of ZnO NWs. This technique has two distinct advantages, firstly the NWs are grown directly onto the substrate, which avoids deposition steps which could potentially lead to problematic interfaces when using the substrate as an electrical contact to the base of the NW array. Secondly, patterning of NW growth is easily achieved using conventional lithographic techniques which may combined with both wet and dry etching methods, as demonstrated using e-beam lithography. Although the morphology was much improved over the NWs obtained using seed layers, as a consequence of the etching the roughened surface consists of multiply exposed crystalline facets of varying orientations. This leads to difficulties in obtaining coherently orientated growth ideal for use in vertical NW devices. X-ray diffraction (XRD) revealed large strain present in the NW arrays, likely as a result of the large lattice mismatch between wurtzite ZnO and silicon. This was supported by transmission electron microscopy (TEM) conducted on a cross-section of the array and substrate, which shows a poor quality defective interface. Amorphous regions also appear to exist at the interface, which could be explained by oxidation of the silicon substrate during NW growth. The poor quality of this interface could result in reduced conduction and high interfacial resistances when using the silicon substrate as an electrical bottom contact.

The most promising method for achieving NW arrays suitable for vertical device integration was the use of sputtered conductive thin-films, a method which has previously received little research interest. It is of particular interest in vertical device integration as the conductive films could potentially be used as intimate contacts to the base growth layer of the NW arrays. Growth of high aspect ratio highly aligned dense NW arrays was achieved on all sputtered films. In particular, chromium and molybdenum show great promise for use in vertical devices as XRD failed to identify any metal-oxide phases, indicating that the metal contact layers could survive exposure to the growth conditions. Indium tin oxide (ITO) also shows promise for use as issues with oxidation are avoided. A large deep level visible photoluminescent emission was observed for all samples, which is likely indicative of diffusion of the metal into the array during growth.

Two methods for the attachment of antibodies to the ZnO surface were investigated. Both methods relied on the use of (3-Aminopropyl)triethoxysil (APTES) to modify the hydroxyl terminated ZnO surface to amine termination. The first immobilisation method then relied on the use of glutaraldehyde as a linker between the amine terminating NW surface and amine groups present on the N-terminus of the antibody polypeptide chains. The second method relied on activation of the carboxylic groups present on the heavy chain of the antibody using 1-Ethyl-3-(3-dimethylaminopropyl)carbodiimide (EDC) and N-hydroxysuccinimide (NHS) which allowed zero-length cross-linking to occur between the antibody and amine terminated NW surface. Human chorionic gonadotropin (hCG) was used as a model protein. This hormone is commonly used as a indicator in pregnancy tests and has been identified as a excellent tumour marker for monitoring the growth of germ cell tumours. A typical clinical concentration of the protein concentration of (250 ng/ml) was used for the sensing step of the biofunctionalisation process.

X-ray photoelectron spectroscopy (XPS) was used to confirm successful surface modification and functionalisation. Relatively little difference was seen between both attachment methods, although a slightly larger nitrogen contribution was observed for the EDC/NHS method, which could be indicative of greater antibody coverage or a different binding orientation. Valence band (VB) XPS was also used to obtain information on the surface band-bending induced by the biofunctionalisation process.

Electrical measurements were conducted on individual NWs using a nanoprobe system. The NWs were transferred from the growth substrates to lie horizontally on a thermally grown silicon dioxide layer. Resistance measurements were conducted in the lateral field effect transistor (FET) geometry, with a back-gate potential used to obtain the carrier concentration for each sample. A correlation was found between the carrier concentration and the valence band position, as measured using XPS. No correlation between the valence band position and NW resistivity was found. A relationship was however found between NW resistivity and photoluminescence visible emission attributed to intrinsic and extrinsic surface defects. This seems to suggest that surface band-bending does not correlate directly with measurable changes in conduction, and that other surface state related mechanisms may be responsible for resistivity variations between NWs.

Resistivity measurements conducted on a large number of NWs gave some indication of the statistical spread in resistivity of the NWs at each step of the biofunctionalisation process. The

temporal and wire-to-wire variation in conductivity has significant implications for the design of NW biosensors and demonstrates the need for ensemble integration in order to reduce the statistical spread seen for certain surface treatments. The average resistance per NW of an ensemble devices was calculated for each sample, and indicates that both functionalisation methods could be used for conductometric detection of clinical levels of the model hCG protein, assuming parallel incorporation of NWs into a sensing device.

With this in mind, a strategy for integrating a large number of NW in parallel was developed using standard semiconductor fabrication techniques. This consisted of using a temporary polymer encapsulation layer to support deposition of a top contact to the NW tips. The polymer layer could then be removed to leave a free floating metal contact, allowing a potential to be applied across the NW array. Using this strategy, an ensemble vertical NW sensing device was designed.

7.1 Future Work

- Characterise the extent, type and heterogeneity of the dopants present in NWs grown on conductive layers and their effect on the electrical and optical properties of the NWs.
- Investigate the quality of the electrical contact between the sputtered conductive layers and NW arrays.
- Quantify the surface coverage and degree of attachment of biomolecules.
- Study the change in resistivity of NWs treated with varying amounts of the hCG protein (calibration curve).
- Further develop and refine the design suggested for an ensemble vertical NW sensing device.

7.2 Publications

- Richard A. Brown, Jonathan E. Evans, Nathan A. Smith, Afshin Tarat, Daniel R. Jones, Chris J. Barnett, Thierry G. G. Maffeis. **The effect of metal layers on the morphology and optical properties of hydrothermally grown zinc oxide nanowires**. *Journal of Materials Science*, March 2013.
- Alex M. Lord, Michael B. Ward, Jonathan E. Evans, Philip R. Davies, Nathan A. Smith, Thierry G. Maffeis, Steve P. Wilks. **Enhanced Long-Path Electrical Conduction in ZnO Nanowire Array Devices Grown via Defect-Driven Nucleation**. *The Journal of Physical Chemistry C*, September 2014.
- Alex M. Lord, Thierry G. Maffeis, Martin W. Allen, David Morgan, Daniel R. Jones, Jonathan E. Evans, Nathan A. Smith, Steve P. Wilks. **Surface state modulation through wet chemical treatment as a route to controlling the electrical properties of ZnO nanowire arrays investigated with XPS**. *Applied Surface Science*, September 2014.
- Nathan A. Smith, Jonathan E. Evans, Daniel R. Jones, Alex M. Lord, Steve P. Wilks. **Growth of ZnO nanowire arrays directly onto Si via substrate topographical adjustments using both wet chemical and dry etching methods**. *Materials Science and Engineering B*, June 2014.
- Nathan A. Smith, Jon E. Evans, Daniel R. Jones, Alex M. Lord, Kenith E. Meissner, S. P. Wilks. **Improving the conduction path through the ZnO nanowire/Si interface for vertical device integration**. *Submitted to ACS Applied Materials and Interfaces.*

Appendices

Appendix A

List of X-ray Diffraction Peaks

Shown below is a summary of all measured XRD peaks from the 2θ scans presented in section 4.4, sorted by peak position.

Table A.1: XRD peaks for NWs grown on 100 nm sputtered thin films. Peak position indicates the 2θ value.

Thin Film	Index	Peak Position (°)	Intensity (a.u.)	FWHM (°)
Aluminium	Si (0 0 2)	33.014	1220	0.045
	ZnO (0 0 2)	34.460	22963	0.084
	ZnO (1 0 1)	36.296	381	0.109
	$ZnAl_2$	38.547	193	0.096
	ZnO (1 0 2)	47.574	87	0.116
	ZnO (1 0 3)	62.911	199	0.124
	Si (4 0 0)	69.183	840000	0.044
	ZnO (0 0 4)	72.615	613	0.097
Chromium	Si (0 0 2)	33.015	1471	0.042
	ZnO (0 0 2)	34.465	284947	0.072
	ZnO (1 0 1)	36.228	183	0.103
	Cr (1 1 0)	44.491	98	0.135
	ZnO (1 0 3)	63.001	106	0.288
	Si (4 0 0)	69.182	917371	0.053
	ZnO (0 0 4)	72.617	8516	0.060
Titanium	TiO2 (1 1 0)	27.533	50	1.643
	Si (0 0 2)	33.013	1364	0.040
	ZnO (0 0 2)	34.470	52150	0.086
	ZnO (1 0 1)	36.343	453	0.098
	TiO_2 (2 0 0)	39.450	40	0.322
	TiO_2 (1 1 1)/$TiZn_3$	41.139	29	0.322
	ZnO (1 0 2)	47.640	251	0.156
	$TiZn_3$	51.380	35	0.295
	ZnO (1 0 3)	62.962	727	0.161
	Si (4 0 0)	69.185	830437	0.053

Thin Film	Index	Peak Position (°)	Intensity (a.u.)	FWHM (°)
Titanium	ZnO (0 0 4)	72.622	1384	0.086
(continued...)	ZnO (1 0 4)/TiO_2	81.477	66	0.206
	ZnO (2 0 3)	89.793	29	0.254
	ZnO (1 1 4)/$TiZn_3$	98.835	25	0.523
Copper	ZnO (1 0 0)	31.750	54	0.351
	ZnO (0 0 2)	34.467	418191	0.084
	ZnO (1 0 1)	36.167	636	0.082
	Cu (1 1 1)/CuZn	43.398	420	0.190
	Cu (2 0 0)	50.620	69	0.361
	ZnO (1 1 0)	56.563	42	0.187
	CuZn/ZnO (1 0 3)	62.973	51	0.238
	Si (4 0 0)	69.182	1307050	0.054
	ZnO (0 0 4)	72.617	10537	0.097
ITO	ITO (2 2 2)	30.673	235	0.163
	Si (0 0 2)	33.011	3084	0.050
	ZnO (0 0 2)	34.468	86232	0.093
	SnO_2 (2 1 1)	51.163	85	0.162
	SnO_2	60.818	52	0.204
	ZnO (1 0 3)	62.994	263	0.204
	ZnO (0 0 4)	72.621	2268	0.077
	ZnO (1 0 4)	81.553	49	0.238
Molybdenum	Si (0 0 2)	33.008	146	0.056
	ZnO (0 0 2)	34.469	174792	0.083
	ZnO (1 0 1)	36.300	62	0.086
	Mo (1 1 0)	40.536	189	0.499
	ZnO (1 0 2)	47.616	49	0.172
	ZnO (1 0 3)	62.973	146	0.236
	Si (4 0 0)	69.184	1064670	0.054
	ZnO (0 0 4)	72.619	4598	0.087
	Mo (2 1 1)	73.768	62	0.534
Tungsten	$ZnWO_4$ (1 1 0)	24.580	212	0.513
	$ZnWO_4$ (1 1 1)	30.651	130	1.015
	Si (0 0 2)	33.010	1156	0.043
	ZnO (0 0 2)	34.466	2510	0.103
	–	38.405	220	0.288
	W (1 1 0)	40.260	1690	0.379
	–	47.606	115	0.167

Thin Film	Index	Peak Position (°)	Intensity (a.u.)	FWHM (°)
Tungsten	ZnO (1 0 3)	62.944	847	0.181
(continued...)	Si	69.183	727606	0.050
	W (2 1 1)	73.250	172	0.729
	–	81.457	148	0.228
	W (2 2 0)	87.008	76	1.168
	–	98.758	34	0.780
	W (3 1 0)	100.823	31	1.444
		104.265	382	0.349
		115.212	33	1.646

Appendix B

Gated Measurements

B.1 *Mathematica* Code and Transistor Characteristics

Mathematica was used to import the raw I–V plots and process the data into transfer characteristics that could then be fitted using Boltzmann-Sigmoid sigmoid functions. The fitted function could then be used to extract the threshold voltage and carrier concentration, as detailed in section 5.6.1. The annotated *Mathematica* code is given below:

```
Constants and variables

In[1]:= k = 1.3806488*10^-23;

In[2]:= T = 300;

In[3]:= \[Epsilon]0 = 8.854187817*10^-12;

In[4]:= \[Epsilon]SiO2 = 3.9;

In[5]:= \[Epsilon]ZnO = 8.6;

In[6]:= e = 1.602176565*10^-19;

In[7]:= Nc = 2.94*10^24;

In[8]:= nbulk = 10^24;

(*d = NW diameter in nm*)
In[9]:= dvalues = ({
    {144.97, 147.08, 142.85, 144.97, 142.85},
    {84.5, 83.43, 87.71, 82.36, 82.36},
    {78.8, 79.34, 78.26, 76.63, 77.71},
    {95.24, 91.61, 93.42, 95.69, 94.33},
    {85.02, 86.13, 86.68, 85.58, 88.89},
    {140.7, 143.48, 142.12, 141.44, 142.12},
    {114.36, 119.29, 115.35, 115.35, 118.31},
    {134.57, 137.34, 142.17, 142.17, 144.24},
    {172.4, 172.91, 194.06, 221.06, 237.11},
    {91.04, 92.75, 91.04, 91.47, 91.47}
   });

In[10]:= d = Mean[Transpose[dvalues]]*10^-9.;

In[11]:= \[CapitalDelta]d =
  Table[Max[dvalues[[i]]] - Min[dvalues[[i ]]], {i, 1, 10}]*10^-9.;

(*L = NW channel length in nm*)
```

```
In[13]:= Lvalues = ({
    {1727, 1667, 1688},
    {1723, 1654, 1590},
    {1760, 1612, 1497},
    {2647, 2546, 2410},
    {1597, 1526, 1401},
    {936, 874, 816},
    {2587, 2474, 2374},
    {3526, 3323, 3423},
    {2312, 2217, 2105},
    {3668, 3895, 3821}
   });

In[14]:= L = Mean[Transpose[Lvalues]]*10^-9.;

In[15]:= \[CapitalDelta]L =
  Table[Max[Lvalues[[i]]] - Min[Lvalues[[i ]]], {i, 1, 10}]*10^-9.;

(*h = dielectric thickenss*)
In[16]:= h = 100*10^-9;

In[17]:= \[CapitalDelta]h = 5*10^-9;

(*band gap and valence band position*)
In[19]:= Eg = {3.342, 3.366, 3.359, 3.363, 3.356, 3.343, 3.353, 3.354, 3.346, 3.332};

In[20]:= \[Zeta] = {3.64539, 3.66719, 3.58475, 3.7045, 3.64828, 3.66286, 3.62385,
   3.67652, 3.61252, 3.70674};

(*Fermi level position in the bulk*)
In[21]:= bulk\[Xi] = (k T/e) Log[Nc/nbulk]

Out[21]= 0.027879

(*Valence band bending*)
In[22]:= Vbb = Abs[Eg - bulk\[Xi] - \[Zeta]]

Out[22]= {0.331269, 0.329069, 0.253629, 0.369379, 0.320159, 0.347739, 0.298729, \
0.350399, 0.294399, 0.402619}

(*width of accumulation region*)
In[23]:= w = Table[Sqrt[(2 \[Epsilon]ZnO \[Epsilon]0 Vbb[[i ]]) /(
   e nbulk)], {i, 1, 10}]*10^9

Out[23]= {17.7449, 17.6859, 15.5268, 18.7378, 17.4448, 18.1807, 16.8509, 18.2501, \
16.7283, 19.5628}

In[24]:= r = d/2;

In[25]:= \[CapitalDelta]r = \[CapitalDelta]d/2;
```

Load files and gate voltages

```
In[26]:= dirpath = (*directory path*)

(*folder and sample names*)

In[27]:= folders = {"1_APTES", "2_GA", "3_AB", "4_BSA", "5_AG", "6_EDAC_AB",
```

```
"7␣EDAC␣BSA", "8␣EDAC␣AG", "9␣Control␣1", "10␣Control␣2"};

(*number of files*)

In[28]:= nof = Length[folders];

In[29]:= path = Table[StringJoin[dirpath, folders[[ i ]]], {i, 1, Length[folders]}];

In[30]:= files = Table[FileNames["*.csv", path[[i ]]], {i, 1, Length[folders]}];

In[31]:= alldata = Table[Map[Import, files[[i ]]], {i, 1, Length[folders]}];

(*number of samples*)

In[32]:= nos = Length[alldata[[1]]]

Out[32]= 41

(*number of measurements*)

In[33]:= nom = Length[alldata[[1, 1]]] - 1

Out[33]= 100

(*sample names*)

In[34]:= letters = Table[
  Characters[
   StringReplace[
    files [[ i ]], {path -> "", "Vg.csv" -> "", "\NW␣" -> "", "␣" -> "" }]][[
  All, 2 ;;]], {i, 1, nof}];

(*import gate voltagess from file names*)

In[35]:= vg = ToExpression[
  Table[Table[StringJoin[letters[[i, x, 1 ;;]]], {x, 1, nos}], {i, 1, nof}]];

IdsVds plots fits

(*transconductance data*)

In[36]:= tddata = Table[
  Table[{vg[[i, x]], alldata[[i, x, y, 1]], alldata[[i, x, y, 2]]}, {x, 1,
    nos}, {y, 2, nom + 1}], {i, 1, nof}];

(*sorted transconductance data*)

In[37]:= stddata = Table[Sort[tddata[[i ]]], {i, 1, nof}];

(*IV fits *)

In[38]:= fits = Table[
  Table[Fit[stddata[[j, i, All, 2 ;; 3]], {x}, x], {i, 1, nos}], {j, 1,
   nof}];

In[39]:= resistance = 1/fits*x;

In[40]:= resistivity = Table[resistance[[i ]]*( d[[i]]^2 \[Pi])/(4 L[[i ]]), {i, 1, nof}];
```

Sigmoid–Boltzmann fits and calculate transconductance and threshold (Vth) for all Vds

```
(*sigmoid–bolzmann function*)

In[41]:= model = ((A1 − A2)/(1 + E^((x − xo)/dx))) + A2

Out[41]= A2 + (A1 − A2)/(1 + E^((x − xo)/dx))

(*nonlinear fits and fitting parameters*)

In[42]:= nlfitparameters =
  Table[Table[
    NonlinearModelFit[stddata[[j, All, i, {1, 3}]], model, {A1, A2, xo, dx},
      x]["BestFitParameters"], {i, 1, nom}], {j, 1, nof}];

In[43]:= nlfits = Table[
   Table[NonlinearModelFit[stddata[[j, All, i, {1, 3}]],
     model, {A1, A2, xo, dx}, x], {i, 1, nom}], {j, 1, nof}];

(* fit 1sigma confidence intervals using exponential functions*)

In[44]:= nlfits68 =
  Table[Table[
    nlfits [[j, i]]["MeanPredictionBands", ConfidenceLevel -> .68], {i, 1,
     nom}], {j, 1, nof}];

(* list of gate voltages*)

In[45]:= vgs = Range[−20, 20, 1];

(*tables containing 1sigma confidence intervals as a function of gate voltage*)

In[46]:= lsamplenlconfits =
  Table[Table[
    Transpose[{vgs, nlfits68[[j, i]][[1]] /. x -> vgs}], {i, 1, nom}], {j, 1,
    nof}];

In[47]:= usamplenlconfits =
  Table[Table[
    Transpose[{vgs, nlfits68[[j, i]][[2]] /. x -> vgs}], {i, 1, nom}], {j, 1,
    nof}];

(*sigmoid–bolzmann fits to 1sigma confidence intervals*)

In[48]:= lowerconfit =
  Table[Table[
    NonlinearModelFit[lsamplenlconfits[[j, i]], model, {A1, A2, xo, dx},
     x], {i, 1, nom}], {j, 1, nof}];

In[49]:= upperconfit =
  Table[Table[
    NonlinearModelFit[usamplenlconfits[[j, i]], model, {A1, A2, xo, dx},
     x], {i, 1, nom}], {j, 1, nof}];

(*sigmoid–bolzmann parameters*)

In[50]:= vars = {A1, A2, xo, dx}
```

```
Out[50]= {A1, A2, xo, dx}

(*parameters that describe the 1sigma confidence intervals fits*)

In[52]:= lowervars =
  Table[Table[
    Table[vars[[c]] /. lowerconfit[[j, i]]["BestFitParameters"], {c, 1,
      Length[vars]}], {i, 1, nom}], {j, 1, nof}];

In[53]:= uppervars =
  Table[Table[
    Table[vars[[c]] /. upperconfit[[j, i]]["BestFitParameters"], {c, 1,
      Length[vars]}], {i, 1, nom}], {j, 1, nof}];

In[54]:= avevars = Table[
   Table[Table[
     vars[[c]] /. nlfitparameters[[j, i]], {c, 1, Length[vars]}], {i, 1,
     nom}], {j, 1, nof}];

In[55]:= splitdifvars = (uppervars - lowervars/2) + lowervars;

In[56]:= lowerparams =
  Table[Table[
    Table[lowerconfit[[j, i]]["ParameterTable"][[1, 1, c + 1, 2]], {c, 1,
      4}], {i, 1, nom}], {j, 1, nof}];

In[57]:= upperparams =
  Table[Table[
    Table[upperconfit[[j, i]]["ParameterTable"][[1, 1, c + 1, 2]], {c, 1,
      4}], {i, 1, nom}], {j, 1, nof}];

In[58]:= aveparams =
  Table[Table[
    Table[nlfits[[j, i]]["ParameterTable"][[1, 1, c + 1, 2]], {c, 1, 4}], {i,
     1, nom}], {j, 1, nof}];

(*tables of parameters that describe the 1sigma confidence intervals*)

In[59]:= A1stdev = Table[
   Table[Mean[{Abs[aveparams[[j, i, 1]] - upperparams[[j, i, 1]]],
      Abs[aveparams[[j, i, 1]] - lowerparams[[j, i, 1]]]}], {i, 1, nom}], {j,
    1, nof}];

In[60]:= A2stdev = Table[
   Table[Mean[{Abs[aveparams[[j, i, 2]] - upperparams[[j, i, 2]]],
      Abs[aveparams[[j, i, 2]] - lowerparams[[j, i, 2]]]}], {i, 1, nom}], {j,
    1, nof}];

In[61]:= xostdev = Table[
   Table[Mean[{Abs[aveparams[[j, i, 3]] - upperparams[[j, i, 3]]],
      Abs[aveparams[[j, i, 3]] - lowerparams[[j, i, 3]]]}], {i, 1, nom}], {j,
    1, nof}];

In[62]:= dxstdev = Table[
   Table[Mean[{Abs[aveparams[[j, i, 4]] - upperparams[[j, i, 4]]],
      Abs[aveparams[[j, i, 4]] - lowerparams[[j, i, 4]]]}], {i, 1, nom}], {j,
    1, nof}];

(*transcondutance*)
```

```
In[63]:= trans = ((-A1 + A2)/(4 dx));

In[64]:= (* differentiate model to get the transconductance*)

In[65]:= dtrans = D[model, x];

(* fit to linear region*)

In[66]:= linfit = ((-A1 + A2)/(4 dx))*x + (2 A1 dx + 2 A2 dx + A1 xo - A2 xo)/(4 dx);

In[67]:= linfits = Table[
  Table[ linfit /. nlfitparameters[[j, i ]], {i, 1, nom}], {j, 1, nof }];

(*maximal transconductance values*)

In[68]:= maxgm = Table[
  Table[trans /. nlfitparameters[[j, i ]], {i, 1, nom}], {j, 1, nof }];

(*threshold voltages*)

In[69]:= vth = Table[
  Table[Solve[ linfits [[ j, i ]] == A1 /. nlfitparameters[[j, i ]], x ], {i, 1,
    nom}], {j, 1, nof }];
```

Calculate gate capacitance, total charge and carrier concentration

```
In[70]:= (*Calculating the gate capacitence on a given nanowire*)

In[71]:= Cg = Table[(2*
     Pi*\[Epsilon]SiO2*\[Epsilon]0)/(Log[(((d[[s]]/2) + h)/(d[[s]]/2)) +
      Sqrt[(((d[[s]]/2) + h)/(d[[s]]/2))^2 - 1]])*L[[s ]], {s, 1, nof }];

In[72]:= vthv = Transpose[(x /. vth) ];

(*total charge in the NWs*)

In[73]:= Qtot[Vg_, s_] := Transpose[Cg[[s]]*Abs[Vg - vthv[[All, s ]]]][[1]]

(*carrier concentration*)

In[74]:= n[Vg_, s_] := Qtot[Vg, s ]/(e*Pi*(d[[s ]]/2)^2*L[[s ]])

(*table of carrier concentrations at 0.1V*)

In[75]:= N100mV1 = Table[n[0, i][[56]], {i, 1, 10}]

Out[75]= {3.88527*10^23, 4.94078*10^21, 3.44767*10^22, 6.30666*10^24, 2.55662*10^23,
  7.91407*10^23, 4.92167*10^23, 4.37887*10^23, 3.98075*10^22, 2.12112*10^24}

(*table of carrier concentrations at 10V*)

In[76]:= Table[n[10, i ][[56]], {i, 1, 10}]*10^-6

Out[76]= {1.5636*10^17, 1.29698*10^18, 1.48803*10^18, 7.38558*10^18, 1.49078*10^18,
  1.35195*10^18, 1.25859*10^18, 1.01032*10^18, 2.88765*10^17, 3.24774*10^18}

(*extract relevant samples for fitting *)
```

```
In[77]:= N100mV = N100mV1[[{4, 5, 6, 7, 8, 10}]]

Out[77]= {6.30666*10^24, 2.55662*10^23, 7.91407*10^23, 4.92167*10^23, 4.37887*10^23,
 2.12112*10^24}

In[78]:= \[Xi]1 = Abs[Eg - \[Zeta]]

Out[78]= {0.30339, 0.30119, 0.22575, 0.3415, 0.29228, 0.31986, 0.27085, 0.32252, \
0.26652, 0.37474}

(*extract relevant samples for fitting *)

In[79]:= \[Xi] = \[Xi ]1[[{4, 5, 6, 7, 8, 10}]]

Out[79]= {0.3415, 0.29228, 0.31986, 0.27085, 0.32252, 0.37474}

(*table of \[Xi] as a function of carrier concentration*)

In[80]:= plotNvs\[Xi] = Table[{N100mV[[i]], \[Xi ][[ i ]]}, {i, 1, 6}];
```

Fit to transfer characteristics:

```
(*define JD approximation*)

In[81]:= \[Xi]modelacc =
  k T/e (Log[n0/Nc] + 1/Sqrt[8] (n0/Nc) - (3/16 - Sqrt[3]/9) (n0/Nc)^2) + c;

(* fit to table of \[Xi] as a function of carrier concentration*)

In[82]:= fitacc = NonlinearModelFit[plotNvs\[Xi], \[Xi]modelacc, {c}, n0];

In[83]:= fitacc ["BestFitParameters"]

Out[83]= {c -> 0.34499}

(*substract c from all samples to get corrected value of \[Xi]*)

In[84]:= \[Xi] - c /. fitacc ["BestFitParameters"]

Out[84]= {-0.00348992, -0.0527099, -0.0251299, -0.0741399, -0.0224699, 0.0297501}

In[85]:= Show[ListPlot[plotNvs\[Xi], PlotStyle -> PointSize[0.02]],
 Plot[ fitacc [n0], {n0, 0, 1*10^26}], AxesOrigin -> {0, 0}]

Out[85]= (*JD fit *)
```

Uncertainties

```
(*parameters at Vds = 0.1V for uncertainty calculations*)

In[86]:= A1a = aveparams[[All, 56, 1]];

In[87]:= A2a = aveparams[[All, 56, 2]];

In[88]:= x0a = aveparams[[All, 56, 3]];
```

```
In[89]:= dxa = aveparams[[All, 56, 4]];

In[90]:= \[CapitalDelta]gm =
 Table[1/4 \[Sqrt](1/(dxa[[
        i ]])^4 ((A1a[[i ]] - A2a[[i ]])^2 dxstdev[[i,
        56]]^2 + (A1stdev[[i, 56]]^2 +
        A2stdev[[i, 56]]^2) (dxa[[i ]])^2)), {i, 1, 10}]

Out[90]= {2.09777*10^-9, 2.79865*10^-6, 0.0000191567, 1.39096*10^-9, 2.43587*10^-9,
 6.46601*10^-9, 2.46277*10^-10, 5.19737*10^-9, 2.81245*10^-7, 1.322*10^-10}

In[91]:= \[CapitalDelta]vth =
 Table[Sqrt[4*dxstdev[[i, 56]]^2 + xostdev[[i, 56]]^2], {i, 1, 10}]

Out[91]= {0.347037, 0.479392, 0.257182, 5.51792, 0.699908, 0.697698, 0.0825912, \
0.576821, 0.286013, 0.278282}

In[92]:= d1 = Table[(2 \[Pi] \[Epsilon]SiO2 \[Epsilon]0)/
   Log[(h + r[[ i ]]) /r[[ i ]] + Sqrt[((h + r[[ i ]]) /r[[ i ]]) ^2 - 1]], {i, 1, 10}];

In[93]:= d2 = Table[(-2 \[Pi] \[Epsilon]SiO2 \[Epsilon]0 L[[ i ]]) /(r[[
      i ]] Sqrt[(h (h + 2 r[[ i ]]) )/
      r[[ i ]]^2] (Log[
        1 + h/r[[ i ]] + Sqrt[(h (h + 2 r[[ i ]]) )/(r[[ i ]]) ^2]])^2), {i, 1, 10}];

In[94]:= d3 = Table[(2 \[Pi] \[Epsilon]SiO2 \[Epsilon]0 L[[
      i ]] h)/(r[[ i ]]^2 Sqrt[(h (h + 2 r[[ i ]]) )/
      r[[ i ]]^2] (Log[
        1 + h/r[[ i ]] + Sqrt[(h (h + 2 r[[ i ]]) )/(r[[ i ]]) ^2]])^2), {i, 1, 10}];

In[95]:= \[CapitalDelta]cg = Sqrt[(d1)^2 \[CapitalDelta]L^2 + (d2)^2 \
\[CapitalDelta]h^2 + (d3)^2 \[CapitalDelta]r^2]

Out[95]= {1.04458*10^-17, 1.64234*10^-17, 2.96845*10^-17, 2.95709*10^-17,
 2.32338*10^-17, 1.72915*10^-17, 2.92272*10^-17, 3.35373*10^-17,
 6.24537*10^-17, 2.8607*10^-17}

In[96]:= vtha = Table[x /. vth[[ i, 56, 1]], {i, 1, 10}];

In[97]:= dcgt = Table[((Abs[
        vtha[[ i ]]]) /(\[Pi] e r[[ i]]^2 L[[ i ]]) )^2 \[CapitalDelta]cg[[
      i ]]^2, {i, 1, 10}];

In[98]:= dlt = Table[((-Cg[[i ]] Abs[
         vtha[[ i ]]]) /(\[Pi] e r[[ i]]^2 L[[ i]]^2))^2 \[CapitalDelta]L[[
      i ]]^2, {i, 1, 10}];

In[99]:= drt = Table[((-2 Cg[[i ]] Abs[vtha[[i ]]]) /(\[Pi] e r[[ i]]^3 L[[
        i ]]) )^2 \[CapitalDelta]r[[ i ]]^2, {i, 1, 10}];

In[100]:= dvtht = Table[((Cg[[i ]]) /(\[Pi] e r[[ i]]^2 L[[ i ]]) )^2 \[CapitalDelta]vth[[
      i ]]^2, {i, 1, 10}];

In[101]:= \[CapitalDelta]n = Sqrt[dcgt + dlt + drt + dvtht]

Out[101]= {3.66572*10^22, 6.19455*10^22, 3.82918*10^22, 1.17344*10^24, 1.01245*10^23,
 1.62335*10^23, 7.43474*10^22, 7.96154*10^22, 2.85604*10^22, 2.03639*10^23}
```

Figure B.1 shows the transfer characteristics and Boltzmann-Sigmoid fits at $V_{ds} = 0.1$ V. Using *Mathematica*, Boltzmann-Sigmoid functions were fitted to all 100 I_{ds}–V_g curves in order to compute a threshold voltage over the whole range of V_{ds} (−1 V to 1 V). The variation of V_{th} with V_{ds} is plotted in figure B.2.

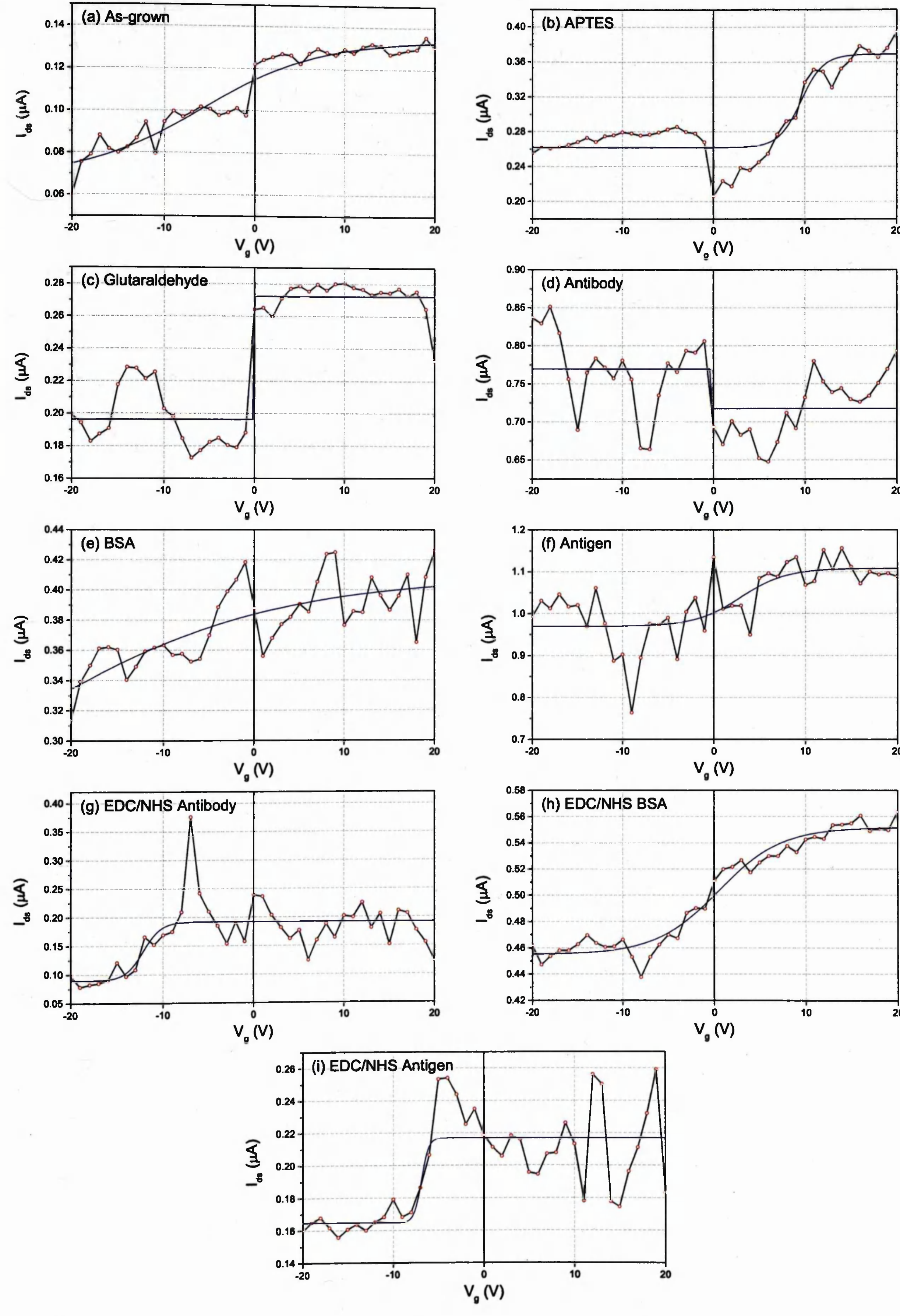

Figure B.1: Transfer characteristics at $V_{ds} = (0.1\,\text{V})$

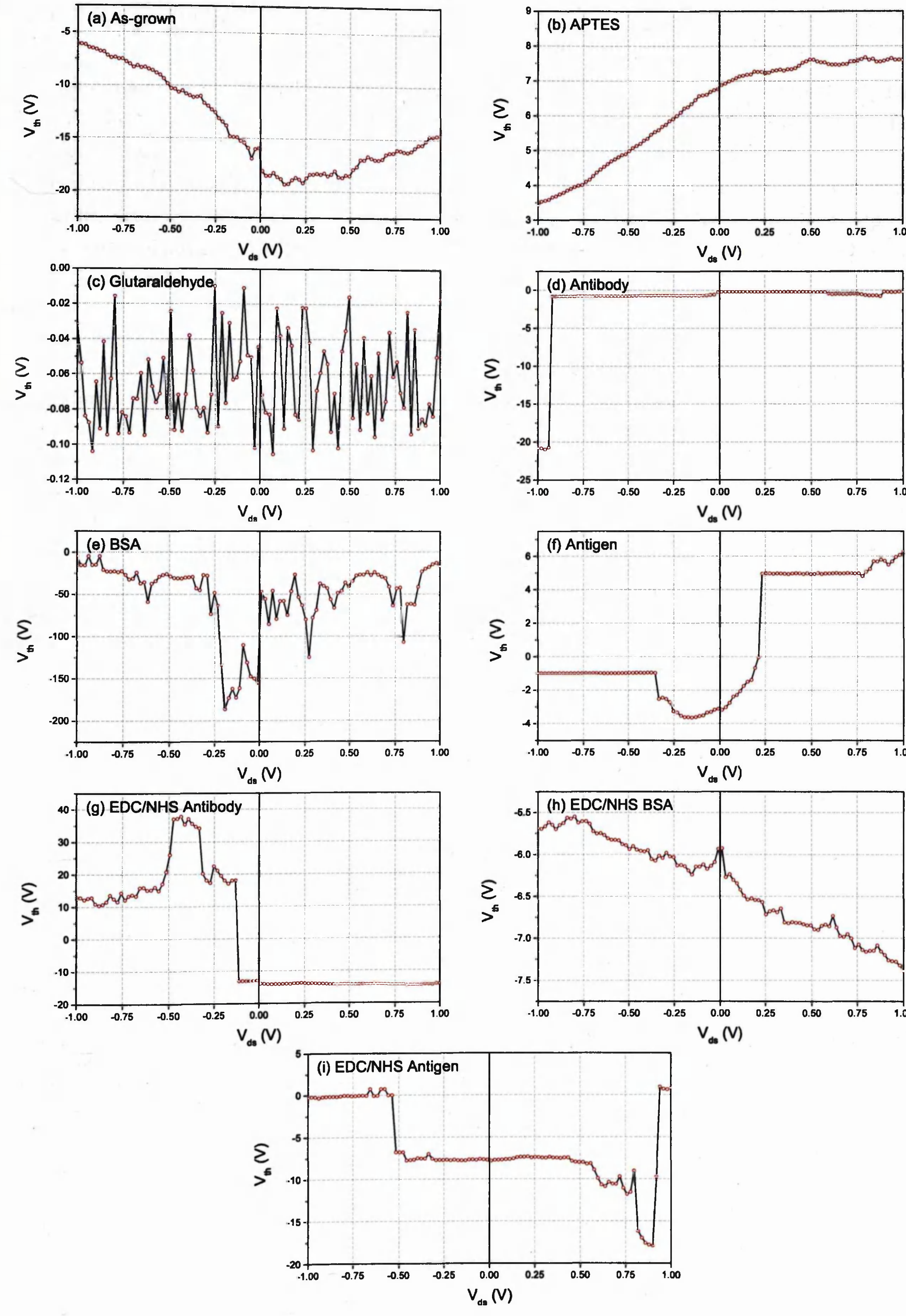

Figure B.2: Threshold voltage as a function of drain-source voltage.

B.2 Propagation of Uncertainty

Equation 5.4 gives the form of the Boltzmann-Sigmoid function used to fit the transfer characteristics shown in section B.1. The fitting parameters are A_1 and A_2, which determine the initial and final values of I_{ds} (off-state and on-state drain source current), x_0, which is the position of the centre of the linear region, and dx, which is the time constant determining the gradient of the linear fit. The corresponding uncertainty in each value can be obtained by taking the difference between the parameters that describe the curve bounding the 1σ confidence interval and the fit to the transfer characteristics, e.g.

$$\Delta A_1 = \left| A_{1(1\sigma)} - A_{1(\text{fit})} \right| . \tag{B.1}$$

An example of the 1σ confidence bands given by the "NonlinearModelFit" command in *Mathematica* are shown in figure B.3. The uncertainties in the fitted parameters can be used to calculate the propagated uncertainties in the maximum transconductance, threshold voltage and carrier concentration.

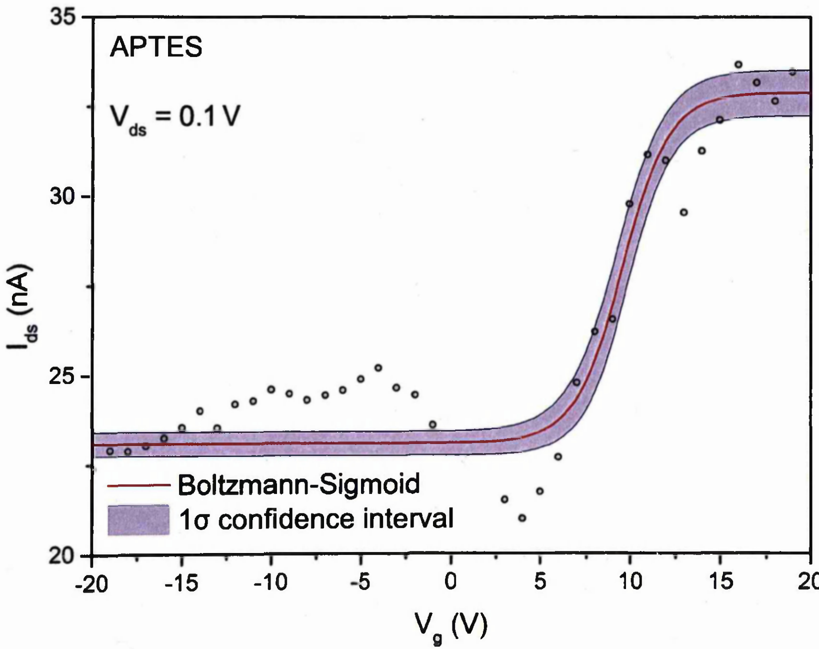

Figure B.3: I_{ds}–V_g plot for APTES treated NW with V_{ds} = 0.1 V. The blue bands show the 1σ (68%) confidence interval.

Assuming independent variables, the variance formula for the function $f(x_1, x_2, ..., x_n)$ is given by:

$$\Delta f = \sqrt{\sum_{i=1}^{n} \left(\frac{\partial f}{\partial x_i} \right)^2 \Delta x_i^2} \tag{B.2}$$

where Δf is the standard deviation in function f and Δx_i is the standard deviation in independent variable x_i. The maximum value for the transconductance, g_m, is determined from the fitted

Boltzmann-Sigmoid parameters using the following equation:

$$g_m = \frac{-A_1 + A_2}{4\mathrm{dx}}. \tag{B.3}$$

Using equation B.2, the uncertainty in the maximum transconductance is given by:

$$\Delta g_m = \sqrt{\left(\frac{-1}{4\mathrm{dx}}\right)^2 \Delta A_1^2 + \left(\frac{1}{4\mathrm{dx}}\right)^2 \Delta A_2^2 + \left(\frac{A_1 - A_2}{4\mathrm{dx}}\right)^2 \Delta \mathrm{dx}^2}, \tag{B.4}$$

which simplifies to:

$$\boxed{\Delta g_m = \frac{1}{4}\sqrt{\frac{(A_1 - A_2)^2 \Delta \mathrm{dx}^2 + \left(\Delta A_1^2 + \Delta A_2^2\right)\mathrm{dx}^2}{\mathrm{dx}^4}}} \tag{B.5}$$

The threshold voltage V_{th} is calculated using:

$$V_{th} = -2\mathrm{dx} + x_0. \tag{B.6}$$

Using the variance formula, the uncertainty is then simply:

$$\boxed{\Delta V_{th} = \sqrt{4\Delta \mathrm{dx}^2 + \Delta x_0^2}} \tag{B.7}$$

In order to calculate the carrier concentration, the gate-NW capacitance must be known, which is calculated using an analytical model for a metallic cylinder on an infinite plane of dielectric [214]. Using this model, the gate capacitance C_g is given by:

$$C_g = \frac{2\pi\varepsilon_{\mathrm{SiO_2}}\varepsilon_0 L}{\mathrm{Log}\left[\frac{h+r}{r} + \sqrt{\left(\frac{h+r}{r}\right)^2 - 1}\right]} \tag{B.8}$$

The measurement uncertainties in dielectric thickness, NW length and NW radius are designated Δh, ΔL and Δr, respectively. In the case of NW length and radius, the range of values from repeated SEM measurements are used for ΔL and Δr. The thickness of the dielectric layer was measured using cross-sectional SEM, and the uncertainty was given an upper bound of $\Delta h = \pm 5\,\mathrm{nm}$, due to some variation in the oxide thickness across the sample. The uncertainty in the relative and absolute permittivity are assumed to be negligible, thus terms in the variance formula containing $\Delta\varepsilon$ may be neglected. The uncertainty in C_g can then be calculated using:

$$\boxed{\Delta C_g = \sqrt{\left(\frac{\partial C_g}{\partial L}\right)^2 \Delta L^2 + \left(\frac{\partial C_g}{\partial h}\right)^2 \Delta h^2 \left(\frac{\partial C_g}{\partial r}\right)^2 \Delta r^2}} \tag{B.9}$$

where:

$$\frac{\partial C_g}{\partial L} = \frac{2\pi\varepsilon_{SiO_2}\varepsilon_0}{\text{Log}\left[\frac{h+r}{r} + \sqrt{\left(\frac{h+r}{r}\right)^2 - 1}\right]} \tag{B.10}$$

$$\frac{\partial C_g}{\partial h} = \frac{-2\pi\varepsilon_{SiO_2}\varepsilon_0 L}{r\sqrt{\frac{h(h+2r)}{r^2}}\text{Log}\left[1 + \frac{h}{r} + \sqrt{\frac{h(h+2r)}{r^2}}\right]^2} \tag{B.11}$$

$$\frac{\partial C_g}{\partial r} = \frac{2\pi\varepsilon_{SiO_2}\varepsilon_0 Lh}{r^2\sqrt{\frac{h(h+2r)}{r^2}}\text{Log}\left[1 + \frac{h}{r} + \sqrt{\frac{h(h+2r)}{r^2}}\right]^2} \tag{B.12}$$

The carrier concentration at gate voltage V_g is then determined from the gate capacitance and threshold voltage using:

$$n = \frac{C_g\left|V_g - V_{th}\right|}{e\pi r^2 L}. \tag{B.13}$$

At $V_g = 0\text{V}$ the equation can be simplified to:

$$n = \frac{C_g\left|V_{th}\right|}{\pi e r^2 L}, \tag{B.14}$$

giving an uncertainty in the carrier concentration of:

$$\boxed{\Delta n = \sqrt{\left(\frac{\left|V_{th}\right|}{\pi e r^2 L}\right)^2 \Delta C_g^2 + \left(\frac{-C_g\left|V_{th}\right|}{\pi e r^2 L^2}\right)^2 \Delta L^2 + \left(\frac{-2C_g\left|V_{th}\right|}{\pi e r^3 L}\right)^2 \Delta r^2 + \left(\frac{C_g}{\pi e r^2 L}\right)^2 \Delta V_{th}^2}} \tag{B.15}$$

assuming negligible uncertainty in the elementary charge e.

References

[1] H.Morkoc. U.Ozgur, Ya.I. Alivov, C.Liu, A.Teke, M.A.Reshchikov, S.Dogan, V.Avrutin, S.J. Cho. A comprehensive review of ZnO materials and devices. *Journal of Applied Physics*, 98(4):041301, 2005.

[2] Chegnui Bekeny, Tobias Voss, Houcem Gafsi, Jurgen Gutowski, Bianca Postels, Marc Kreye, and Andreas Waag. Origin of the near-band-edge photoluminescence emission in aqueous chemically grown ZnO nanorods. *Journal of Applied Physics*, 100(10):104317, 2006.

[3] Zhong Lin Wang. Nanostructures of zinc oxide. *Materials Today*, (June):26–33, 2004.

[4] Richard a. Brown, Jon E. Evans, Nathan a. Smith, Afshin Tarat, Daniel R. Jones, Chris J. Barnett, and Thierry G. G. Maffeis. The effect of metal layers on the morphology and optical properties of hydrothermally grown zinc oxide nanowires. *Journal of Materials Science*, 48(14):4908–4913, March 2013.

[5] Shu-Te Ho, Chiu-Yen Wang, Hsiang-Lin Liu, and Heh-Nan Lin. Catalyst-free selective-area growth of vertically aligned zinc oxide nanowires. *Chemical Physics Letters*, 463(1-3):141–144, September 2008.

[6] Jong Seok Jeong and Jeong Yong Lee. Investigation of initial growth of ZnO nanowires and their growth mechanism. *Nanotechnology*, 21(47):475603, November 2010.

[7] S N Cha, B G Song, J E Jang, J E Jung, I T Han, J H Ha, J P Hong, D J Kang, and J M Kim. Controlled growth of vertically aligned ZnO nanowires with different crystal orientation of the ZnO seed layer. *Nanotechnology*, 19(23):235601, June 2008.

[8] Tomas Bryllert, Lars-Erik Wernersson, Truls Löwgren, and Lars Samuelson. Vertical wrap-gated nanowire transistors. *Nanotechnology*, 17(11):S227–S230, June 2006.

[9] Hyun Jin In, Christopher R Field, and Pehr E Pehrsson. Periodically porous top electrodes on vertical nanowire arrays for highly sensitive gas detection. *Nanotechnology*, 22(35):355501, September 2011.

[10] Hee Han, Jungkil Kim, Ho Sun Shin, Jae Yong Song, and Woo Lee. Air-bridged Ohmic contact on vertically aligned si nanowire arrays: application to molecule sensors. *Advanced materials (Deerfield Beach, Fla.)*, 24(17):2284–8, May 2012.

[11] Mohammad M a Hakim, Marta Lombardini, Kai Sun, Francesco Giustiniano, Peter L Roach, Donna E Davies, Peter H Howarth, Maurits R R de Planque, Hywel Morgan, and Peter Ashburn. Thin film polycrystalline silicon nanowire biosensors. *Nano letters*, 12(4):1868–72, April 2012.

[12] Pierce Protein Biology. http://www.piercenet.com/product/nhs-sulfo-nhs/, June 2014.

[13] Clariant GmbH. AZ® 6600 series product data sheet. Available at: http://www.microchemicals.com/micro/az_6600_series.pdf, 2014.

[14] Clariant GmbH. AZ® nLOF™ 2000 series i-line photoresists (datasheet). Available at: http://www.microchemicals.com/micro/AZ_nLOF2000_bulletin.pdf, 2014.

[15] Omicron Nanotechnology. Nanoprobe. Available at: http://www.omicron.de/en/products/uhv-nanoprobe/instrument-concept, 2014.

[16] S. Tanuma, C. J. Powell, and D. R. Penn. Calculations of electron inelastic mean free paths. IX. Data for 41 elemental solids over the 50 eV to 30 keV range. *Surface and Interface Analysis*, 43(3):689–713, March 2011.

[17] Chi-chang Wu, Tung-ming Pan, Chung-shu Wu, Li-chen Yen, and Cheng-keng Chuang. Label-free Detection of Prostate Specific Antigen Using a Silicon Nanobelt Field-effect Transistor. *International Journal of Electochemical Science*, 7:4432–4442, 2012.

[18] Pierce Protein Biology. http://www.piercenet.com/product/nhs-sulfo-nhs/, June 2014.

[19] Yue Liu, Yueming Li, Xue-Mei Li, and Tao He. Kinetics of (3-aminopropyl)triethoxylsilane (APTES) silanization of superparamagnetic iron oxide nanoparticles. *Langmuir : the ACS journal of surfaces and colloids*, 29(49):15275–82, December 2013.

[20] Jayeeta Lahiri, Sanjaya Senanayake, and Matthias Batzill. Soft x-ray photoemission of clean and sulfur-covered polar ZnO surfaces: A view of the stabilization of polar oxide surfaces. *Physical Review B*, 78(15):155414, October 2008.

[21] By Noriko Saito, Hajime Haneda, Takashi Sekiguchi, Naoki Ohashi, Isao Sakaguchi, and Kunihito Koumoto We. Low-Temperature Fabrication of Light-Emitting Zinc Oxide Micropatterns Using Self-Assembled Monolayers. *Advanced Materials*, 8603(6):418–421, 2002.

[22] J.Y Lee, Y.S Choi, J.H Kim, M.O Park, and S Im. Optimizing n-ZnO/p-Si heterojunctions for photodiode applications. *Thin Solid Films*, 403-404:553–557, February 2002.

[23] Michael H Huang, Samuel Mao, Henning Feick, Haoquan Yan, Yiying Wu, Hannes Kind, Eicke Weber, and Richard Russo. Room-Temperature Ultraviolet Nanowire Nanolasers. *Science*, 292:1897–1899, 2001.

[24] Yuanhua Lin, Zhongtai Zhang, Zilong Tang, Fangli Yuan, and Jinlin Li. Characterisation of ZnO-based Varistors Prepared from Nanometre Precursor Powders. *Advanced Materials for Optics and Electronics*, (January 1999):194–198, 2000.

[25] K Weigenrieder. Conductivity model for sputtered ZnO-thin film gas sensors i ii : I. *Thin Solid Films*, 300:30–41, 1997.

[26] R N Koch, M H; Timbrel, P Y; Lamb. The influence of film crystallinity on. *Semiconductor Science and Technology*, 10:2–7, 1995.

[27] H Rensmo, K Keis, H Lindstro, A Solbrand, A Hagfeldt, S Lindquist, L N Wang, and M Muhammed. High Light-to-Energy Conversion Efficiencies for Solar Cells Based on Nanostructured ZnO Electrodes. *Journal of Physical Chemistry B*, 101:2598–2601, 1997.

[28] Dae-yong Son, Jeong-hyeok Im, Hui-seon Kim, and Nam-gyu Park. 11% E ffi cient Perovskite Solar Cell Based on ZnO Nanorods: An E ff ective Charge Collection System. *Journal of Physical Chemistry C*, 118, 2014.

[29] Chennupati Jagadish and Stephen J. Pearton, editors. *Zinc Oxide Bulk, Thin Films and Nanostructures: Processing, Properties and Applications*. Elsevier Ltd., 2006.

[30] Peng Wang, Changlian Jin, Xuefeng Wu, Huahan Zhan, Yinghui Zhou, Huiqiong Wang, and Junyong Kang. Quality improvement of ZnO thin layers overgrown on Si(100) substrates at room temperature by nitridation pretreatment. *AIP Advances*, 2(2):022139, 2012.

[31] G Brauer, J Kuriplach, C C Ling, and a B Djurišić. Activities towards p -type doping of ZnO. *Journal of Physics: Conference Series*, 265:012002, January 2011.

[32] K. Vanheusden, W. L. Warren, C. H. Seager, D. R. Tallant, J. a. Voigt, and B. E. Gnade. Mechanisms behind green photoluminescence in ZnO phosphor powders. *Journal of Applied Physics*, 79(10):7983, 1996.

[33] Zhong Lin Wang. Zinc oxide nanostructures : growth , properties and applications. *Journal of Physics: Condensed Matter*, 16:829–858, 2004.

[34] A F Kohan, G Ceder, D Morgan, and Chris G Van De Walle. First-principles study of native point defects in ZnO. 61(22):19–27, 2000.

[35] Anderson Janotti and Chris G. Van de Walle. Native point defects in ZnO. *Physical Review B*, 76(16):165202, October 2007.

[36] J E Stehr, S L Chen, S Filippov, M Devika, N Koteeswara Reddy, C W Tu, W M Chen, and I a Buyanova. Defect properties of ZnO nanowires revealed from an optically detected magnetic resonance study. *Nanotechnology*, 24(1):015701, January 2013.

[37] Anderson Janotti and Chris G Van de Walle. Fundamentals of zinc oxide as a semiconductor. *Reports on Progress in Physics*, 72(12):126501, December 2009.

[38] Magnus Willander, Omer Nur, Jamil Rana Sadaf, Muhammad Israr Qadir, Saima Zaman, Ahmed Zainelabdin, Nargis Bano, and Ijaz Hussain. Luminescence from Zinc Oxide Nanostructures and Polymers and their Hybrid Devices. *Materials*, 3(4):2643–2667, April 2010.

[39] X.M. Fan, J.S. Lian, Z.X. Guo, and H.J. Lu. Microstructure and photoluminescence properties of ZnO thin films grown by PLD on Si(111) substrates. *Applied Surface Science*, 239(2):176–181, January 2005.

[40] Jongmin Lim, Kyoungchul Shin, Hyoun Woo Kim, and Chongmu Lee. Effect of annealing on the photoluminescence characteristics of ZnO thin films grown on the sapphire substrate by atomic layer epitaxy. *Materials Science and Engineering: B*, 107(3):301–304, March 2004.

[41] K H Tam, C K Cheung, Y H Leung, a B Djurisić, C C Ling, C D Beling, S Fung, W M Kwok, W K Chan, D L Phillips, L Ding, and W K Ge. Defects in ZnO nanorods prepared by a hydrothermal method. *The journal of physical chemistry. B*, 110(42):20865–71, October 2006.

[42] Li-li Yang, Jing-hai Yang, Dan-dan Wang, Yong-jun Zhang, Ya-xin Wang, Hui-lian Liu, Hou-gang Fan, and Ji-hui Lang. Photoluminescence and Raman analysis of ZnO nanowires deposited on Si(100) via vapor–liquid–solid process. *Physica E: Low-dimensional Systems and Nanostructures*, 40(4):920–923, February 2008.

[43] Yinyan Gong, Tamar Andelman, Gertrude F. Neumark, Stephen O'Brien, and Igor L. Kuskovsky. Origin of defect-related green emission from ZnO nanoparticles: effect of surface modification. *Nanoscale Research Letters*, 2(6):297–302, June 2007.

[44] P.S. Xu, Y.M. Sun, C.S. Shi, F.Q. Xu, and H.B. Pan. The electronic structure and spectral properties of ZnO and its defects. *Nuclear Instruments and Methods in Physics Research Section B: Beam Interactions with Materials and Atoms*, 199:286–290, January 2003.

[45] Cheol Hyoun Ahn, Young Yi Kim, Dong Chan Kim, Sanjay Kumar Mohanta, and Hyung Koun Cho. A comparative analysis of deep level emission in ZnO layers deposited by various methods. *Journal of Applied Physics*, 105(1):013502, 2009.

[46] Thierry Pauport. *Toward Functional Nanomaterials*. Springer US, New York, NY, 2009.

[47] Ajay Kushwaha, Himanshu Tyagi, and M. Aslam. Role of defect states in magnetic and electrical properties of ZnO nanowires. *AIP Advances*, 3(4):042110, 2013.

[48] Su Kim Min, Gug Yim Kwang, Young Cho Min, Leem Jae-Young, Lee Dong-Yul, Soo Kim Jin, Su Kim Jong, and Son Jeong-Sik. Post-Annealing Effects on the Structural and the Optical Properties of ZnO Thin Films Grown by Using the Hydrothermal Method. *Journal of the Korean Physical Society*, 58(3):515, March 2011.

[49] S. a. Studenikin, Nickolay Golego, and Michael Cocivera. Fabrication of green and orange photoluminescent, undoped ZnO films using spray pyrolysis. *Journal of Applied Physics*, 84(4):2287, 1998.

[50] Gui-Yang Huang, Chong-Yu Wang, and Jian-Tao Wang. First-principles study of diffusion of oxygen vacancies and interstitials in ZnO. *Journal of physics. Condensed matter : an Institute of Physics journal*, 21(19):195403, May 2009.

[51] R. Elilarassi and G. Chandrasekaran. Influence of Co-doping on the structural, optical and magnetic properties of ZnO nanoparticles synthesized using auto-combustion method. *Journal of Materials Science: Materials in Electronics*, 24(1):96–105, October 2012.

[52] Cheng-Ying Chen, Ming-Wei Chen, Jr-Jian Ke, Chin-An Lin, José R. D. Retamal, and Jr-Hau He. Surface effects on optical and electrical properties of ZnO nanostructures. *Pure and Applied Chemistry*, 82(11):2055–2073, January 2010.

[53] Bixia Lin, Zhuxi Fu, and Yunbo Jia. Green luminescent center in undoped zinc oxide films deposited on silicon substrates. *Applied Physics Letters*, 79(7):943, 2001.

[54] Jinzhang Liu, Soonil Lee, Y H Ahn, Ji-Yong Park, and Ken Ha Koh. Tailoring the visible photoluminescence of mass-produced ZnO nanowires. *Journal of Physics D: Applied Physics*, 42(9):095401, May 2009.

[55] R. a. Powell and W. E. Spicer. Photoemission studies of the cesiation of ZnO. *Journal of Applied Physics*, 48(10):4311, 1977.

[56] Fred S Hickernell. Post-deposition annealing. pages 489–492, 1981.

[57] a. Tarat, R. Majithia, R.a. Brown, M.W. Penny, and K.E. Meissner. Synthesis of nanocrystalline ZnO nanobelts via pyrolytic decomposition of zinc acetate nanobelts and their gas sensing behavior. *Surface Science*, 606(7-8):715–721, April 2012.

[58] W. I. Park, D. H. Kim, S.-W. Jung, and Gyu-Chul Yi. Metalorganic vapor-phase epitaxial growth of vertically well-aligned ZnO nanorods. *Applied Physics Letters*, 80(22):4232, 2002.

[59] By Won, Il Park, Gyu-chul Yi, Miyoung Kim, and Stephen J Pennycook. ZnO Nanoneedles Grown Vertically on Si. (24):1841–1843, 2002.

[60] Gaëlle Amiri, Ahmed Souissi, Nadia Hanèche, Christèle Vilar, Alain Lusson, Vincent Sallet, and Pierre Galtier. Synthesis and characterization of core-shell ZnO/ZnSe nanowires grown by MOCVD. *Physica Status Solidi (B)*, 2136(10):n/a–n/a, September 2013.

[61] Hironori Fujisawa, Yuta Iwamoto, Seiji Nakashima, and Masaru Shimizu. Fabrication of PZT/ZnO Core-Shell Nanowires by Metalorganic Chemical Vapor Deposition. *2012 Fifth International Conference on Emerging Trends in Engineering and Technology*, pages 57–60, November 2012.

[62] Christopher B Jacobs, M Jennifer Peairs, and B Jill Venton. Review: Carbon nanotube based electrochemical sensors for biomolecules. *Analytica chimica acta*, 662(2):105–27, March 2010.

[63] Yun Wang and John T. W. Yeow. A Review of Carbon Nanotubes-Based Gas Sensors. *Journal of Sensors*, 2009:1–24, 2009.

[64] Aleksandr V Eletskii. Carbon nanotube-based electron field emitters. *Physics-Uspekhi*, 53(9):863, 2010.

[65] Phaedon Avouris, Marcus Freitag, and Vasili Perebeinos. *Carbon-Nanotube Optoelectronics*, volume 111 of *Topics in Applied Physics*. Springer Berlin Heidelberg, 2008.

[66] Bell Telephone Laboratories and Murray Hill. HYDROTHERMAL GROWTH OF LARGE SOUND CRYSTALS Hydrothermal Growth of Large Sound Crystals. *Journal of The American Ceramic Society*, 12(1):9–12, 1964.

[67] Zhong Lin Wang. ZnO nanowire and nanobelt platform for nanotechnology. *Materials Science and Engineering: R: Reports*, 64(3-4):33–71, April 2009.

[68] Umasankar Yogeswaran and Shen-ming Chen. A Review on the Electrochemical Sensors and Biosensors Composed of Nanowires as Sensing Material. *Sensors (Basel, Switzerland)*, pages 290–313, 2008.

[69] Jin-Ho Choy, Eue-Soon Jang, Jung-Hee Won, Jae-Hun Chung, Du-Jeon Jang, and Young-Woon Kim. Hydrothermal route to ZnO nanocoral reefs and nanofibers. *Applied Physics Letters*, 84(2):287, 2004.

[70] Zhengquan Li, Yujie Xiong, and Yi Xie. Selected-control synthesis of ZnO nanowires and nanorods via a PEG-assisted route. *Inorganic chemistry*, 42(24):8105–9, December 2003.

[71] Jinmin Wang and Lian Gao. Wet chemical synthesis of ultralong and straight single-crystalline ZnO nanowires and their excellent UV emission properties. *Journal of Materials Chemistry*, 13(10):2551, 2003.

[72] Bin Liu and Hua Chun Zeng. Hydrothermal synthesis of ZnO nanorods in the diameter regime of 50 nm. *Journal of the American Chemical Society*, 125(15):4430–1, April 2003.

[73] Sunil K Arya, Shibu Saha, Jaime E Ramirez-Vick, Vinay Gupta, Shekhar Bhansali, and Surinder P Singh. Recent advances in ZnO nanostructures and thin films for biosensor applications: review. *Analytica chimica acta*, 737:1–21, August 2012.

[74] Zhiqing Zhang and Jin Mu. Hydrothermal synthesis of ZnO nanobundles controlled by PEO-PPO-PEO block copolymers. *Journal of colloid and interface science*, 307(1):79–82, March 2007.

[75] Y. C. Kong, D. P. Yu, B. Zhang, W. Fang, and S. Q. Feng. Ultraviolet-emitting ZnO nanowires synthesized by a physical vapor deposition approach. *Applied Physics Letters*, 78(4):407, 2001.

[76] R. S. Wagner and W. C. Ellis. Vapor-Liquid-Solid Mechanism of Single Crystal Growth. *Applied Physics Letters*, 4(5):89, 1964.

[77] Soumen Dhara and P K Giri. ZnO Nanowire Heterostructures : Intriguing Photophysics and Emerging Applications. *Revoews in Nanoscience and Nanotechnology*, 2(3):1–24, 2013.

[78] R.B. Saunders, E. McGlynn, M. Biswas, and M.O. Henry. Thermodynamic aspects of the gas atmosphere and growth mechanism in carbothermal vapour phase transport synthesis of ZnO nanostructures. *Thin Solid Films*, 518(16):4578–4581, June 2010.

[79] Ruth B. Saunders, Enda McGlynn, and Martin O. Henry. Theoretical Analysis of Nucleation and Growth of ZnO Nanostructures in Vapor Phase Transport Growth. *Crystal Growth & Design*, 11(10):4581–4587, October 2011.

[80] Shu-Te Ho, Kuan-Chiao Chen, Hsiang-An Chen, Hsin-Yu Lin, Chun-Yuan Cheng, and Heh-Nan Lin. Catalyst-Free Surface-Roughness-Assisted Growth of Large-Scale Vertically Aligned Zinc Oxide Nanowires by Thermal Evaporation. *Chemistry of Materials*, 19(16):4083–4086, August 2007.

[81] Shu-Yi Liu, Tao Chen, Jing Wan, Guo-Ping Ru, Bing-Zong Li, and Xin-Ping Qu. The effect of pre-annealing of sputtered ZnO seed layers on growth of ZnO nanorods through a hydrothermal method. *Applied Physics A*, 94(4):775–780, November 2008.

[82] Alex M. Lord, Michael B. Ward, Jonathan E. Evans, Philip R. Davies, Nathan a. Smith, Thierry G. Maffeis, and Steve P. Wilks. Enhanced Long-Path Electrical Conduction in ZnO Nanowire Array Devices Grown via Defect-Driven Nucleation. *The Journal of Physical Chemistry C*, page 140902114013008, September 2014.

[83] Jun Liu, Juncong She, Shaozhi Deng, Jun Chen, and Ningsheng Xu. Ultrathin Seed-Layer for Tuning Density of ZnO Nanowire Arrays and Their Field Emission Characteristics. *The Journal of Physical Chemistry C*, 112(31):11685–11690, August 2008.

[84] Shou-yi Chang, Nai-hao Yang, Yi-chung Huang, and Chia-feng Lin. Oriented Growth of ZnO Nanorod Arrays on Ultraviolet-Activated Low-Temperature Cured Seed Layers. pages 1–8.

[85] Mi Xiao and Makoto Kuwabara. Effect of Seed Layer on the Orientation of Zinc Oxide Film on Silicon Substrate. *Journal of Materials Sciences & Technology*, 21(6):887–890, 2005.

[86] Pai-chun Chang, Zhiyong Fan, Dawei Wang, Wei-yu Tseng, Wen-an Chiou, Juan Hong, and Jia G Lu. ZnO Nanowires Synthesized by Vapor Trapping CVD Method. *Chemistry of Materials*, (13):5133–5137, 2004.

[87] Richard G. Hobbs, Nikolay Petkov, and Justin D. Holmes. Semiconductor Nanowire Fabrication by Bottom-Up and Top-Down Paradigms. *Chemistry of Materials*, 24(11):1975–1991, June 2012.

[88] Alex M Lord, Thierry G Maffeis, Alex S Walton, Despoina M Kepaptsoglou, Quentin M Ramasse, Michael B Ward, Jürgen Köble, and Steve P Wilks. Factors that determine and limit the resistivity of high-quality individual ZnO nanowires. *Nanotechnology*, 24(43):435706, November 2013.

[89] Daniel Kälblein, R Thomas Weitz, H Jens Böttcher, Frederik Ante, Ute Zschieschang, Klaus Kern, and Hagen Klauk. Top-gate ZnO nanowire transistors and integrated circuits with ultrathin self-assembled monolayer gate dielectric. *Nano letters*, 11(12):5309–15, December 2011.

[90] Y Huang, X Duan, Q Wei, and C M Lieber. Directed assembly of one-dimensional nanostructures into functional networks. *Science (New York, N.Y.)*, 291(5504):630–3, January 2001.

[91] Wenzhuo Wu, Xiaonan Wen, and Zhong Lin Wang. Taxel-addressable matrix of vertical-nanowire piezotronic transistors for active and adaptive tactile imaging. *Science (New York, N.Y.)*, 340(6135):952–7, May 2013.

[92] Sepideh Gorji Ghalamestani, Sofia Johansson, B Mattias Borg, Erik Lind, Kimberly a Dick, and Lars-Erik Wernersson. Uniform and position-controlled InAs nanowires on 2" Si substrates for transistor applications. *Nanotechnology*, 23(1):015302, January 2012.

[93] Ping-Hung Yeh, Zhou Li, and Zhong Lin Wang. Schottky-Gated Probe-Free ZnO Nanowire Biosensor. *Advanced Materials*, 21(48):4975–4978, December 2009.

[94] Y Cui, Q Wei, H Park, and C M Lieber. Nanowire nanosensors for highly sensitive and selective detection of biological and chemical species. *Science (New York, N.Y.)*, 293(5533):1289–92, August 2001.

[95] Gengfeng Zheng, Fernando Patolsky, Yi Cui, Wayne U Wang, and Charles M Lieber. Multiplexed electrical detection of cancer markers with nanowire sensor arrays. *Nature biotechnology*, 23(10):1294–301, October 2005.

[96] Fernando Patolsky, Gengfeng Zheng, Oliver Hayden, Melike Lakadamyali, Xiaowei Zhuang, and Charles M Lieber. Electrical detection of single viruses. *Proceedings of the National Academy of Sciences of the United States of America*, 101(39):14017–22, September 2004.

[97] Robert Kelsall. *Nanoscale Science and Technology*. John Wiley & Sons, Inc., 2005.

[98] V. Dugas. *Use of Organosilanes in Biosensors*. Nova Science Publishers, Inc., 2010.

[99] Alain Carré, William Birch, and Valérie Lacarrière. Glass substrates modified with organosilanes for DNA immobilization. *Silanes and Other Coupling Agents*, 4:1–14, 2007.

[100] Jooran Lee, Sunyoung Choi, Seon Joo Bae, Seok Min Yoon, Joon Sig Choi, and Minjoong Yoon. Visible light-sensitive APTES-bound ZnO nanowire toward a potent nanoinjector sensing biomolecules in a living cell. *Nanoscale*, 5(21):10275–82, November 2013.

[101] Sandeep Kumar Vashist. Comparison of 1-Ethyl-3-(3-Dimethylaminopropyl) Carbodiimide Based Strategies to Crosslink Antibodies on Amine-Functionalized Platforms for Immunodiagnostic Applications. *Diagnostics*, 2(4):23–33, August 2012.

[102] Beibei Zhang, Tao Kong, Wenzhi Xu, Ruigong Su, Yunhua Gao, and Guosheng Cheng. Surface functionalization of zinc oxide by carboxyalkylphosphonic acid self-assembled monolayers. *Langmuir : the ACS journal of surfaces and colloids*, 26(6):4514–22, March 2010.

[103] *Crosslinking Reagents - Technical Handbook*, volume 1. Pierce Biotechnology, Inc., 2006.

[104] *Thermo Scientific Particle Technology Product Catalog and Technical Reference Guide*. Thermo Scientific, 2011.

[105] Clariant GmbH. General Properties of AZ®/ TI Photoresists. Available at: http://www.microchemicals.com/micro/introduction.pdf, 2014.

[106] Samantha Grist, Jasbir N. Patel, Moeed Haq, Bonnie L. Gray, and Bozena Kaminska. Effect of surface treatments/coatings and soft bake profile on surface uniformity and adhesion of su-8 on a glass substrate. *Proc. SPIE*, 7593, 2010.

[107] MicroChemicals GmbH. Softbake of Photoresist Films. Available at: http://www.microchemicals.com/technical_information/softbake_photoresist.pdf, 2014.

[108] MicroChemicals GmbH. Lift-off processes with photoresists. Available at: http://www.microchemicals.com/technical_information/lift_off_photoresist.pdf, 2014.

[109] MicroChemicals GmbH. Solvents: Theory and application. Available at: http://microchemicals.com/technical_information/solvents.pdf, 2014.

[110] Kazuo Sat, Mitsuhiro Shikida, Yoshihiro Matsushima, Takashi Yamashiro, Kazuo Asaumi, Yasuroh Iriye, and Masaharu Yamamoto. Characterization of orientation-dependent etching properties of single-crystal silicon : effects of KOH concentration. 61:87–93, 1998.

[111] Irena Zubel. Silicon anisotropic etching in alkaline solutions III : On the possibility of spatial structures forming in the course of Si ž 100 / anisotropic etching in KOH and KOH q IPA solutions. pages 116–125, 2000.

[112] Kirt R Williams, Senior Member, Kishan Gupta, Student Member, and Matthew Wasilik. Etch Rates for Micromachining Processing — Part II. *Journal of Microelectromechanical Systems*, 12(6):761–778, 2003.

[113] Shigeru Lee, Ji-Myon and Kim, Kyoung-Kook and Hyun, Chan-Kyung and Tampo, Hitoshi and Niki. zno wet etch.pdf. *Journal of nanoscience and nanotechnology*, 6(11):3364–3368, 2006.

[114] Tao Zhang, Lei Sun, Dedong Han, Yi Wang, and Ruqi Han. Surface uniform wet etching of ZnO films and influence of oxygen annealing on etching properties. *2011 6th IEEE International Conference on Nano/Micro Engineered and Molecular Systems*, pages 626–629, February 2011.

[115] C.J Huang, Y.K Su, and S.L Wu. The effect of solvent on the etching of ITO electrode. *Materials Chemistry and Physics*, 84(1):146–150, March 2004.

[116] Stephen M. Rossnagel et al. *Handbook of Plasma Processing Technology*. Noyes Publications, 1990.

[117] Werner Kern. *Handbook of Semiconductor Wafer Cleaning Technology*. Noyes Publications, 1993.

[118] K Kanaya Okayama and S. Penetration and energy-loss theory of electrons in solid targets. *Journal of Physics D: Applied Physics*, 43(5):43–58, 1972.

[119] Albert Einstein. Über einen die Erzeugung und Verwandlung des Lichtes betreffenden heuristischen Gesichtspunkt. *Annalen der Physik*, (17):132–148, 1905.

[120] T. Koopmans. Über die Zuordnung von Wellenfunktionen und Eigenwerten zu den Einzelnen Elektronen Eines Atoms. *Physica*, 1:104–113, 1934.

[121] B.D.F.L. Claude Cohen-Tannoudji. *Quantum Mechanics Volume 2*. Hermann, 1991.

[122] Masaru Kuno. *Introductory Nanoscience: Physical and Chemical Concepts*. Garland Science, 2012.

[123] Yefan Chen, D. M. Bagnall, Hang-jun Koh, Ki-tae Park, Kenji Hiraga, Ziqiang Zhu, and Takafumi Yao. Plasma assisted molecular beam epitaxy of ZnO on c -plane sapphire: Growth and characterization. *Journal of Applied Physics*, 84(7):3912, 1998.

[124] Charles Kittel. *Introduction to Solid State Physics*. John Wiley & Sons, Inc., 8th edition, 2004.

[125] Vd Mote, Y Purushotham, and Bn Dole. Williamson-Hall analysis in estimation of lattice strain in nanometer-sized ZnO particles. *Journal of Theoretical and Applied Physics*, 6(1):6, 2012.

[126] Alex Lord. Vertically aligned zinc oxide nanowires grown by vapour transport on single crystal silicon substrate. Master's thesis, Swansea University, 2009.

[127] Jonathan Evans. Vertically aligned zinc oxide nanowire growth in silicon micro-trenches. Master's thesis, Swansea University, 2010.

[128] Alex Lord. *Electronic and Structural properties of Au contacts on ZnO Nanowires*. PhD thesis, Swansea University, 2012.

[129] Woo-young Kim, Soon-wook Kim, Dae-hwang Yoo, Eui Jung Kim, and Sung Hong Hahn. Annealing Effect of ZnO Seed Layer on Enhancing Photocatalytic Activity of ZnO / TiO 2 Nanostructure. *International Journal of Photoenergy*, 2013, 2013.

[130] Jaejin Song and Sangwoo Lim. Effect of Seed Layer on the Growth of ZnO Nanorods. *The Journal of Physical Chemistry C*, 111(2):596–600, January 2007.

[131] Maryam Roozbehi, Parvaneh Sangpour, Ali Khademi, and Alireza Z. Moshfegh. The effect of substrate surface roughness on ZnO nanostructures growth. *Applied Surface Science*, 257(8):3291–3297, February 2011.

[132] Nathan a. Smith, Jon E. Evans, Daniel R. Jones, Alex M. Lord, and S.P. Wilks. Growth of ZnO nanowire arrays directly onto Si via substrate topographical adjustments using both wet chemical and dry etching methods. *Materials Science and Engineering: B*, 193:41–48, March 2015.

[133] Rob Legtenberg, Henri Jansen, Meint De Boer, and Miko Elwenspoek. Anisotrapic Reactive Ion Etching of Silicon Using SF6 / O2 / CHF3 Gas Mixtures. 142(6), 1995.

[134] M. Li, G.-C. Wang, and H.-G. Min. Effect of surface roughness on magnetic properties of Co films on plasma-etched Si(100) substrates. *Journal of Applied Physics*, 83(10):5313, 1998.

[135] Richard Petri, Pascal Brault, Olivier Vatel, Daniel Henry, Elie Andre, Philippe Dumas, and Franck Salvan. Silicon roughness induced by plasma etching. *Journal of Applied Physics*, 75(11):7498, 1994.

[136] E Gogolides. Si etching in high-density SF6 plasmas for microfabrication: surface roughness formation. *Microelectronic Engineering*, 73-74:312–318, June 2004.

[137] Hsu-Cheng Hsu, Ching-Sheng Cheng, Chia-Chieh Chang, Song Yang, Chen-Shiung Chang, and Wen-Feng Hsieh. Orientation-enhanced growth and optical properties of ZnO nanowires grown on porous silicon substrates. *Nanotechnology*, 16(2):297–301, February 2005.

[138] Ilan Shalish, Henryk Temkin, and Venkatesh Narayanamurti. Size-dependent surface luminescence in ZnO nanowires. *Physical Review B*, 69(24):245401, June 2004.

[139] S. J. Fang, W. Chen, T. Yamanaka, and C. R. Helms. Comparison of Si surface roughness measured by atomic force microscopy and ellipsometry. *Applied Physics Letters*, 68(20):2837, 1996.

[140] Wen-Ting Chiou, Wan-Yu Wu, and Jyh-Ming Ting. Growth of single crystal ZnO nanowires using sputter deposition. *Diamond and Related Materials*, 12(10-11):1841–1844, October 2003.

[141] J. Venables. Nucleation and growth of thin films. *Reports on Progress in Physics*, 47:399–459, 1984.

[142] Guo Zhong, Jie Li, Qingmei Su, Gaohui Du, and Bingshe Xu. Temperature-dependent controlled preparation of ZnO nanostructures and their photoluminescence properties. *Materials Letters*, 65(4):670–673, February 2011.

[143] Yu Yang, Sreenivas Jayaraman, Do Young Kim, Gregory S. Girolami, and John R. Abelson. Crystalline texture in hafnium diboride thin films grown by chemical vapor deposition. *Journal of Crystal Growth*, 294(2):389–395, September 2006.

[144] Aurelien Habrioux, Walter Vogel, Maxime Guinel, Laure Guetaz, Karine Servat, Boniface Kokoh, and Nicolas Alonso-Vante. Structural and electrochemical studies of Au-Pt nanoalloys. *Physical chemistry chemical physics : PCCP*, 11(18):3573–9, May 2009.

[145] Bertram Eugene Warren. *X-ray Diffraction*. Courier Dover Publications, 1969.

[146] a. Khorsand Zak, W.H. Abd. Majid, M.E. Abrishami, and Ramin Yousefi. X-ray analysis of ZnO nanoparticles by Williamson–Hall and size–strain plot methods. *Solid State Sciences*, 13(1):251–256, January 2011.

[147] Nanda Shakti. *Synthesis, Characterization and Probable Applications of Nanostructured Zinc oxide Thin Films*. PhD thesis, Indian School of Mines, 2013.

[148] Z Cao. Woodhead Publishing, 20011.

[149] Alex M Lord, Thierry G Maffeis, Alex S Walton, Despoina M Kepaptsoglou, Quentin M Ramasse, Michael B Ward, Jürgen Köble, and Steve P Wilks. Factors that determine and limit the resistivity of high-quality individual ZnO nanowires. *Nanotechnology*, 24(43):435706, November 2013.

[150] Paul Erhart and Karsten Albe. Diffusion of zinc vacancies and interstitials in zinc oxide. *Applied Physics Letters*, 88(20):201918, 2006.

[151] Sai-Chang Liu and Jih-Jen Wu. Low-temperature and catalyst-free synthesis of well-aligned ZnO nanorods on Si (100). *Journal of Materials Chemistry*, 12(10):3125–3129, September 2002.

[152] P Ke, B Pre, A Perez, G Guiraud, and J Lebrusq. Nanostructured silicon films obtained by neutral cluster depositions. *The Journal of Chemical Physics*, 107(23):10278–10287, 1997.

[153] Claus Klingshirn, Robert Hauschild, Johannes Fallert, and Heinz Kalt. Room-temperature stimulated emission of ZnO: Alternatives to excitonic lasing. *Physical Review B*, 75(11):115203, March 2007.

[154] Optically Pumped, Ultraviolet Lasing, From Zno, Elsevier Science, Zno Material Gan, Wurtzite Wurtzite Lattice, From Landolt-btrnstein, and New York. t Pergamon. *Solid State Communications*, 99(12):873–875, 1996.

[155] Lukas Schmidt-mende and Judith L Macmanus-driscoll. defects , and devices ZnO has received much attention over the past few years because. *Materials Today*, 10(5):40–48, 2007.

[156] M.-W. Ahn, K.-S. Park, J.-H. Heo, J.-G. Park, D.-W. Kim, K. J. Choi, J.-H. Lee, and S.-H. Hong. Gas sensing properties of defect-controlled ZnO-nanowire gas sensor. *Applied Physics Letters*, 93(26):263103, 2008.

[157] Ping-Jian Li, Zhi-Min Liao, Xin-Zheng Zhang, Xue-Jin Zhang, Hui-Chao Zhu, Jing-Yun Gao, K Laurent, Y Leprince-Wang, N Wang, and Da-Peng Yu. Electrical and photoresponse properties of an intramolecular p-n homojunction in single phosphorus-doped ZnO nanowires. *Nano letters*, 9(7):2513–8, July 2009.

[158] H Y Lin, C L Cheng, Y Y Chou, L L Huang, Y F Chen, and K T Tsen. Enhancement of band gap emission stimulated by defect loss. *Optics express*, 14(6):2372–9, March 2006.

[159] Dake Wang and Nicholas Reynolds. Photoluminescence of Zinc Oxide Nanowires: The Effect of Surface Band Bending. *ISRN Condensed Matter Physics*, 2012:1–6, 2012.

[160] Morten Madsen, Kuniharu Takei, Rehan Kapadia, Hui Fang, Hyunhyub Ko, Toshitake Takahashi, Alexandra C Ford, Min Hyung Lee, and Ali Javey. Nanoscale semiconductor "X" on substrate "Y"–processes, devices, and applications. *Advanced materials (Deerfield Beach, Fla.)*, 23(28):3115–27, July 2011.

[161] Cheng-Liang Hsu, Shoou-Jinn Chang, Yan-Ru Lin, Jyh-Ming Wu, Tzer-Shen Lin, Song-Yeu Tsai, and I-Cherng Chen. Indium-diffused ZnO nanowires synthesized on ITO-buffered Si substrate. *Nanotechnology*, 17(2):516–519, January 2006.

[162] F. Kurdesau, G. Khripunov, a.F. da Cunha, M. Kaelin, and a.N. Tiwari. Comparative study of ITO layers deposited by DC and RF magnetron sputtering at room temperature. *Journal of Non-Crystalline Solids*, 352(9-20):1466–1470, June 2006.

[163] Dong-Hau Kuo and Bo-Jie Chang. Growth Behaviors of ZnO Nanorods Grown with the Sn-Based Bilayer Catalyst-Covered Substrates. *Journal of Nanomaterials*, 2011:1–9, 2011.

[164] O. Krause, H. Ryssel, and P. Pichler. Determination of aluminum diffusion parameters in silicon. *Journal of Applied Physics*, 91(9):5645, 2002.

[165] Gyu-Chul Yi, Chunrui Wang, and Won Il Park. ZnO nanorods: synthesis, characterization and applications. *Semiconductor Science and Technology*, 20(4):S22–S34, April 2005.

[166] A R Phani, M Passacantando, L Lozzi, and S Santucci. Structural characterization of bulk ZnWO 4. *Journal of Materials Science*, 35:4879–4883, 2000.

[167] Byung Oh Jung, Ju Ho Lee, Jeong Yong Lee, Jae Hyun Kim, and Hyung Koun Cho. High-Purity Ultraviolet Electroluminescence from n-ZnO Nanowires/p+-Si Heterostructure LEDs with i-MgO Film as Carrier Control Layer. *Journal of The Electrochemical Society*, 159(2):H102, 2012.

[168] Eric W Petersen, Edward M Likovich, Kasey J Russell, and Venkatesh Narayanamurti. Growth of ZnO nanowires catalyzed by size-dependent melting of Au nanoparticles. *Nanotechnology*, 20(40):405603, October 2009.

[169] J Y Kim, H W Shim, and E Suh. Catalytic Growth and Optical Characterization of ZnO Nanowire on Silicon and Sapphire. *Journal of the Korean Physical Society*, 44(1):137–139, 2004.

[170] Chia Ying Lee, Tseung Yuen Tseng, Seu Yi Li, and Pang Lin. Growth of Zinc Oxide Nanowires on Silicon (100). *Tamkang Journal of Science and Engineering*, 6(2):127–132, 2003.

[171] Susie Eustis, Douglas C Meier, Michael R Beversluis, and Babak Nikoobakht. Analysis of copper incorporation into zinc oxide nanowires. *ACS nano*, 2(2):368–76, February 2008.

[172] B. E. Sernelius, K.-F. Berggren, Z.-C. Jin, I. Hamberg, and C. G. Granqvist. Band-gap tailoring of zno by means of heavy al doping. *Phys. Rev. B*, 37:10244–10248, Jun 1988.

[173] Do-Joong Lee, Ki-Ju Kim, Soo-Hyun Kim, Jang-Yeon Kwon, Jimmy Xu, and Ki-Bum Kim. Atomic layer deposition of Ti-doped ZnO films with enhanced electron mobility. *Journal of Materials Chemistry C*, 1(31):4761, 2013.

[174] D. Paul Joseph and C. Venkateswaran. Bandgap Engineering in ZnO By Doping with 3d Transition Metal Ions. *Journal of Atomic, Molecular, and Optical Physics*, 2011:1–7, 2011.

[175] K. Srinivasarao, G. Srinivasarao, K. V. Madhuri, K. Krishna Murthy, and P. K. Mukhopadhyay. Preparation and Characterization of R.F. Magnetron Sputtered Mo:ZnO Thin Films. *Indian Journal of Materials Science*, 2013:1–7, 2013.

[176] Jin Chen, Jinhai Tang, Feng Yan, and Huangxian Ju. A gold nanoparticles/sol-gel composite architecture for encapsulation of immunoconjugate for reagentless electrochemical immunoassay. *Biomaterials*, 27(10):2313–21, April 2006.

[177] Bo Zhang, Qiongguo Mao, Xue Zhang, Tianlun Jiang, Ming Chen, Fan Yu, and Weiling Fu. A novel piezoelectric quartz micro-array immunosensor based on self-assembled monolayer for determination of human chorionic gonadotropin. *Biosensors and Bioelectronics*, 19(7):711–720, February 2004.

[178] CLARICE R. WEINBERG A LLEN J. WILCOX, DONNA DAY BAIRD. Time of implantation of the conceptus and loss of pregnancy. *The New England Journal of Medicine*, 340(23), 1999.

[179] Mary C. Territo Dennis Albert Casciato. *Manual of Clinical Oncology*. Lippincott Williams & Wilkins, 2009.

[180] E Mcca and J P Wightman. Determination of the Concentration of Surface Hydroxyl Groups on Metal Oxide Films by a Quantitative XPS Method. *Surface and Interface Analysis*, 564(March):549–564, 1998.

[181] Chuan Liang Feng, Zhihong Zhang, Renate Fo, Wolfgang Knoll, G Julius Vancso, and Holger Scho. Reactive Thin Polymer Films as Platforms for the Immobilization of Biomolecules. *Biomacromolecules*, 6:3243–3251, 2005.

[182] F. Baldini. *Optical Chemical Sensors*. Springer, 2004.

[183] Robert M. Giuliano Francis A. Carey. *Organic Chemistry*. McGraw-Hill, 2010.

[184] Ying Wan, Yan Su, Xinhua Zhu, Gang Liu, and Chunhai Fan. Development of electrochemical immunosensors towards point of care diagnostics. *Biosensors & bioelectronics*, 47:1–11, September 2013.

[185] N-terminal Asp and These Nmr. Proton NMR studies of bovine serum albumin Assignment of spin systems. *European Journal of Biochemistry*, 643(2):631–643, 1992.

[186] J. Zhou, N. S. Xu, and Z. L. Wang. Dissolving Behavior and Stability of ZnO Wires in Biofluids: A Study on Biodegradability and Biocompatibility of ZnO Nanostructures. *Advanced Materials*, 18(18):2432–2435, September 2006.

[187] Nikhil R Jana, Hsiao-Hua Yu, Emril Mohamed Ali, Yuangang Zheng, and Jackie Y Ying. Controlled photostability of luminescent nanocrystalline ZnO solution for selective detection of aldehydes. *Chemical communications (Cambridge, England)*, (14):1406–8, April 2007.

[188] Jason W Soares, James E Whitten, Daniel W Oblas, and Diane M Steeves. Novel photoluminescence properties of surface-modified nanocrystalline zinc oxide: toward a reactive scaffold. *Langmuir : the ACS journal of surfaces and colloids*, 24(2):371–4, January 2008.

[189] Sofia Teixeira, G. Burwell, a. Castaing, D. Gonzalez, R.S. Conlan, and O.J. Guy. Epitaxial graphene immunosensor for human chorionic gonadotropin. *Sensors and Actuators B: Chemical*, 190:723–729, January 2014.

[190] C. D. Wagner. *Practical Surface Analysis*, volume 1. J. Wiley and Sons, 1990.

[191] Siegfried Hofmann. *Auger- and X-Ray Photoelectron Spectroscopy in Materials Science*. Springer, 2013.

[192] S Tanuma and T Kimura. Quantitative Auger and X-ray Photoelectron Analysis of Au-Cu Alloys with Three Kinds of Relative Sensitivity Factors. *Journal of Surface Analysi*, 10(2), 2003.

[193] Andreas Skallberg. *Synthesis and functionalization of Gd-based nanoparticles for MRI contrast enhancement*. PhD thesis, Linköping, 2009.

[194] Z H Ibupoto, N Jamal, K Khun, and M Willander. Sensors and Actuators B : Chemical Development of a disposable potentiometric antibody immobilized ZnO nanotubes based sensor for the detection of C-reactive protein. *Sensors & Actuators: B. Chemical*, 166-167:809–814, 2012.

[195] T.G.G. Maffeis, M.W. Penny, a. Castaing, O.J. Guy, and S.P. Wilks. XPS investigation of vacuum annealed vertically aligned ultralong ZnO nanowires. *Surface Science*, 606(1-2):99–103, January 2012.

[196] D. Byrne, E. McGlynn, M.O. Henry, K. Kumar, and G. Hughes. A novel, substrate independent three-step process for the growth of uniform ZnO nanorod arrays. *Thin Solid Films*, 518(16):4489–4492, June 2010.

[197] O. Lupan, T. Pauporté, I.M. Tiginyanu, V.V. Ursaki, V. Şontea, L.K. Ono, B. Roldan Cuenya, and L. Chow. Comparative study of hydrothermal treatment and thermal annealing effects on the properties of electrodeposited micro-columnar ZnO thin films. *Thin Solid Films*, 519(22):7738–7749, September 2011.

[198] Seokhwan Bang, Seungjun Lee, Joohyun Park, Soyeon Park, Wooho Jeong, and Hyeongtag Jeon. Investigation of the effects of interface carrier concentration on ZnO thin film transistors fabricated by atomic layer deposition. *Journal of Physics D: Applied Physics*, 42(23):235102, December 2009.

[199] Kathleen L Purvis, Gang Lu, Jeffrey Schwartz, and Steven L Bernasek. Surface Characterization and Modification of Indium Tin Oxide in Ultrahigh Vacuum. *Journal of the American Chemical Society*, (30):1808–1809, 2000.

[200] Lee-Jene Lai, Yaw-Wen Yang, Yao-Kwang Lin, Li-Ling Huang, and Yi-Heui Hsieh. Surface characterization of immunosensor conjugated with gold nanoparticles based on cyclic voltammetry and X-ray photoelectron spectroscopy. *Colloids and surfaces. B, Biointerfaces*, 68(2):130–5, February 2009.

[201] Hyung Jin Kim, In-Seob Bae, Sang-Jin Cho, Jin-Hyo Boo, Byung-Cheo Lee, Jinhee Heo, Ilsub Chung, and Byungyou Hong. Synthesis and characteristics of NH2-functionalized polymer films to align and immobilize DNA molecules. *Nanoscale research letters*, 7(1):30, January 2012.

[202] Nicholas D. Spencer. *Tailoring Surfaces: Modifying Surface Composition and Structure for Applications in Tribology, Biology and Catalysis.* World Scientific Publishing, 2011.

[203] Y Y Tay, T T Tan, M H Liang, F Boey, and S Li. Specific defects, surface band bending and characteristic green emissions of ZnO. *Physical chemistry chemical physics : PCCP*, 12(23):6008–13, June 2010.

[204] Tery L. Barr and Sudipta Seal. Nature of the use of adventitious carbon as a binding energy standard. *Journal of Vacuum Science Technology A: Vacuum, Surfaces, and Films*, 13(3):1239–1246, May 1995.

[205] C Serre, A Pe, J R Morante, V Heera, W Skorupa, Y Pacaud, R Ko, and I Introduction. Ion-beam synthesis of amorphous SiC films : Structural analysis and recrystallization. *Journal of Applied Physics*, 79(May):6907–6913, 1996.

[206] Cheng-Ying Chen, Jose Ramon Duran Retamal, I-Wen Wu, Der-Hsien Lien, Ming-Wei Chen, Yong Ding, Yu-Lun Chueh, Chih-I Wu, and Jr-Hau He. Probing surface band bending of surface-engineered metal oxide nanowires. *ACS nano*, 6(11):9366–72, November 2012.

[207] Xiang Liu. Growth mechanism and properties of ZnO nanorods synthesized by plasma-enhanced chemical vapor deposition. *Journal of Applied Physics*, 95(6):3141, 2004.

[208] Alex M. Lord, Thierry G. Maffeis, Martin W. Allen, David Morgan, Philip R. Davies, Daniel R. Jones, Jonathan E. Evans, Nathan a. Smith, and Steve P. Wilks. Surface state modulation through wet chemical treatment as a route to controlling the electrical properties of ZnO nanowire arrays investigated with XPS. *Applied Surface Science*, 320:664–669, November 2014.

[209] Ayan Kar, Ke-Bin Low, Michael Oye, Michael a. Stroscio, Mitra Dutta, Alan Nicholls, and M. Meyyappan. Investigation of Nucleation Mechanism and Tapering Observed in ZnO Nanowire Growth by Carbothermal Reduction Technique. *Nanoscale Research Letters*, 6(1):3, August 2010.

[210] R. J. Cobley, R. a. Brown, C. J. Barnett, T. G. G. Maffeis, and M. W. Penny. Quantitative analysis of annealed scanning probe tips using energy dispersive x-ray spectroscopy. *Applied Physics Letters*, 102(2):023111, 2013.

[211] Chia-Ling Hsu. *Fabrication and Characterisation of ZnO Nanowire Transistors*. VDM Publishing, 2008.

[212] Woong-Ki Hong, Dae-Kue Hwang, Il-Kyu Park, Gunho Jo, Sunghoon Song, Seong-Ju Park, Takhee Lee, Bong-Joong Kim, and Eric a. Stach. Realization of highly reproducible ZnO nanowire field effect transistors with n-channel depletion and enhancement modes. *Applied Physics Letters*, 90(24):243103, 2007.

[213] Kowk K. Ng S. M. Sze. *Physics of Semiconductor Devices*. John Wiley & Sons, Inc., 2007.

[214] D R Khanal and J Wu. Gate coupling and charge distribution in nanowire field effect transistors. *Nano letters*, 7(9):2778–83, September 2007.

[215] U.A.Bakshi A.P.Godse. *Electronic Circuits and Appliations*. Technical Publications, 2009.

[216] Woong-ki Hong, Jung Inn Sohn, Dae-kue Hwang, Soon-shin Kwon, Gunho Jo, Sunghoon Song, Seong-min Kim, Hang-ju Ko, Seong-ju Park, Mark E Welland, and Takhee Lee. Tunable Electronic Transport Characteristics of Nanowire Field Effect Transistors 2008. *Nano Letters*, 8(3):950–956, 2008.

[217] Josh Goldberger, Donald J Sirbuly, Matt Law, and Peidong Yang. ZnO Nanowire Transistors. *Journal of Physical Chemistry B*, (100):9–14, 2005.

[218] Ivan Mora-Sero, Francisco Fabregat-Santiago, Benjamin Denier, Juan Bisquert, Ramon Tena-Zaera, Jamil Elias, and Claude Levy-Clement. Determination of carrier density of ZnO nanowires by electrochemical techniques. *Applied Physics Letters*, 89(20):203117, 2006.

[219] W. B. Joyce and R. W. Dixon. Analytic approximations for the Fermi energy of an ideal Fermi gas. *Applied Physics Letters*, 31(5):354, 1977.

[220] E. H Rhoderick and R. H Williams. *Metal-semiconductor contacts.* Oxford [England] : Clarendon Press ; New York : Oxford University Press, 1988.

[221] M. W. Allen and S. M. Durbin. Influence of oxygen vacancies on Schottky contacts to ZnO. *Applied Physics Letters*, 92(12):122110, 2008.

[222] X. Lin, X. B. He, T. Z. Yang, W. Guo, D. X. Shi, H.-J. Gao, D. D. D. Ma, S. T. Lee, F. Liu, and X. C. Xie. Intrinsic current-voltage properties of nanowires with four-probe scanning tunneling microscopy: A conductance transition of ZnO nanowire. *Applied Physics Letters*, 89(4):043103, 2006.

[223] Michael C.P. Wang and Byron D. Gates. Directed assembly of nanowires. *Materials Today*, 12(5):34–43, May 2009.

[224] Dong Chan Kim, Byung Oh Jung, Yong Hun Kwon, and Hyung Koun Cho. Highly Sensible ZnO Nanowire Ultraviolet Photodetectors Based on Mechanical Schottky Contact. *Journal of The Electrochemical Society*, 159(1):K10, 2012.

[225] a C E Chia and R R LaPierre. Contact planarization of ensemble nanowires. *Nanotechnology*, 22(24):245304, June 2011.

[226] R. Konenkamp, Robert C. Word, and C. Schlegel. Vertical nanowire light-emitting diode. *Applied Physics Letters*, 85(24):6004, 2004.

[227] Wenzhuo Wu, Xiaonan Wen, and Zhong Lin Wang. Taxel-addressable matrix of vertical-nanowire piezotronic transistors for active and adaptive tactile imaging. *Science (New York, N.Y.)*, 340(6135):952–7, May 2013.

[228] Xianying Wang, Kanguk Kim, Yinmin Wang, Michael Stadermann, Aleksandr Noy, Alex V Hamza, Junhe Yang, and Donald J Sirbuly. Matrix-assisted energy conversion in nanostructured piezoelectric arrays. *Nano letters*, 10(12):4901–7, December 2010.

[229] Chu-yeu Peter Yang and Liwei Lin. VERTICAL INTEGRATION OF ZNO NANOWIRES INTO ASYMMETRIC PT / ZNO / TI SCHOTTKY UV PHOTODIODES. *MEMS 2011*, pages 1382–1385, 2011.

[230] Benjamin M. Curtin, Eugene W. Fang, and John E. Bowers. Highly Ordered Vertical Silicon Nanowire Array Composite Thin Films for Thermoelectric Devices. *Journal of Electronic Materials*, 41(5):887–894, February 2012.

[231] B. S. Simpkins, P. E. Pehrsson, and a. R. Laracuente. Electronic conduction in GaN nanowires. *Applied Physics Letters*, 88(7):072111, 2006.

[232] Ludovic Dupré, Thérèse Gorisse, Angélique Letrouit Lebranchu, Thomas Bernardin, Pascal Gentile, Hubert Renevier, and Denis Buttard. Ultradense and planarized antireflective vertical silicon nanowire array using a bottom-up technique. *Nanoscale research letters*, 8(1):123, January 2013.

[233] R. a. Kraya and L. Y. Kraya. The role of contact size on the formation of Schottky barriers and ohmic contacts at nanoscale metal-semiconductor interfaces. *Journal of Applied Physics*, 111(6):064302, 2012.

[234] Leonard J. Brillson and Yicheng Lu. ZnO Schottky barriers and Ohmic contacts. *Journal of Applied Physics*, 109(12):121301, 2011.

[235] a Wierzbicka, Z R Zytkiewicz, S Kret, J Borysiuk, P Dluzewski, M Sobanska, K Klosek, a Reszka, G Tchutchulashvili, a Cabaj, and E Lusakowska. Influence of substrate nitridation temperature on epitaxial alignment of GaN nanowires to Si(111) substrate. *Nanotechnology*, 24(3):035703, January 2013.